Lappeenrannan teknillinen yliopisto
Lappeenranta University of Technology

Jussi Puranen

INDUCTION MOTOR VERSUS PERMANENT MAGNET SYNCHRONOUS MOTOR IN MOTION CONTROL APPLICATIONS: A COMPARATIVE STUDY

Thesis for the degree of Doctor of Science (Technology) to be presented with due permission for the public examination and criticism in the Auditorium 1382 at Lappeenranta University of Technology, Lappeenranta, Finland on the 5th of December, 2006, at noon.

Acta Universitatis
Lappeenrantaensis
249

ISBN 952-214-296-4
ISBN 952-214-297-2 (PDF)
ISSN 1456-4491

Lappeenrannan teknillinen yliopisto
Digipaino 2006

ABSTRACT

Jussi Puranen

Induction motor versus permanent magnet synchronous motor in motion control applications: a comparative study

Lappeenranta 2006

147 p.
Acta Universitatis Lappeenrantaensis 249
Diss. Lappeenranta University of Technology
ISBN 952-214-296-4, ISBN 952-214-297-2 (PDF), ISSN 1456-4491

High dynamic performance of an electric motor is a fundamental prerequisite in motion control applications, also known as servo drives. Recent developments in the field of microprocessors and power electronics have enabled faster and faster movements with an electric motor. In such a dynamically demanding application, the dimensioning of the motor differs substantially from the industrial motor design, where feasible characteristics of the motor are for example high efficiency, a high power factor, and a low price. In motion control instead, such characteristics as high overloading capability, high-speed operation, high torque density and low inertia are required.

The thesis investigates how the dimensioning of a high-performance servomotor differs from the dimensioning of industrial motors. The two most common servomotor types are examined; an induction motor and a permanent magnet synchronous motor. The suitability of these two motor types in dynamically demanding servo applications is assessed, and the design aspects that optimize the servo characteristics of the motors are analyzed. Operating characteristics of a high performance motor are studied, and some methods for improvements are suggested. The main focus is on the induction machine, which is frequently compared to the permanent magnet synchronous motor. A 4 kW prototype induction motor was designed and manufactured for the verification of the simulation results in the laboratory conditions.

Also a dynamic simulation model for estimating the thermal behaviour of the induction motor in servo applications was constructed. The accuracy of the model was improved by coupling it with the electromagnetic motor model in order to take into account the variations in the motor electromagnetic characteristics due to the temperature rise.

Keywords: Induction motor, permanent magnet synchronous motor, servomotor, motion control

UDC 621.313.333 : 681.587.7

Acknowledgements

This research work has been carried out during the years 2003-2006 in the Department of Electric Engineering of Lappeenranta University of Technology (LUT). The project was financed by Carelian Drives and Motor Centre (CDMC), which is the research centre of ABB Companies and LUT.

I wish to thank all the people involved in the process, especially Professor Juha Pyrhönen, the supervisor of this thesis, for giving me the opportunity to carry out this research work and also for his valuable comments and corrections throughout the work.

I also wish to thank D.Sc. Markku Niemelä for his valuable suggestions and especially for the guidance during the measurements in the laboratory. I also thank the laboratory personnel Martti Lindh, Harri Loisa and Jouni Ryhänen for practical arrangements in the laboratory.

Many thanks are due to all the people involved in Motion Control project during the latest years, and also for all the people working in Rotatek Finland Oy for giving me the opportunity to finish this work during the year 2006.

Special thanks are due to PhD Hanna Niemelä for her professional help to improve the language of this work.

I am also very grateful to the pre-examiners of this thesis, Professor emeritus Tapani Jokinen and Professor Alexander Mikerov for their valuable comments and corrections.

Financial support by the Finnish Cultural Foundation is gratefully acknowledged.

I am deeply indebted for my parents Eila and Eero, for their support and for providing me a good basis for life.

And finally, warm thanks for Johanna for all the time we have had together, and for giving me strength and motivation for this work.

Lappeenranta, October 2006 *Jussi Puranen*

CONTENTS

SYMBOLS AND ABBREVIATIONS

Roman letters

a	Tangential length of the skewing along the stator or the rotor surface
A	Area
A_b	Cross-sectional area of the rotor bar
A_r	Cross-sectional area of the end ring between two bars
A_s	Linear current density
B	Magnetic flux density
c_{th}	Specific thermal capacitance
C_{th}	Thermal capacitance
d	Thickness
D_{ag}	Air gap diameter
D’	Average end ring diameter
E	Average distance of the end winding from the stack
E_m,	Induced air gap voltage
E_{PM}	PMSM no-load voltage
f	Frequency
f_{slot}	Slot fill factor
$f_{s,max\text{-}cp}$	Maximum stator frequency at constant power range
F	Rod equivalent conductivity factor
h	Height
h_c	Convection factor
H	Magnetic field strength
H_c	Coercive field strength
$\boldsymbol{i}_d$	Current vector direct-axis component
$\boldsymbol{i}_m$	Magnetizing current vector
$\boldsymbol{i}_q$	Current vector quadrature-axis component
$\boldsymbol{i}_r$	Rotor current vector
$\boldsymbol{i}_s$	Stator current vector
I_m	Magnetizing current RMS value
I_s	Stator current RMS value
J	Current density, inertia
k_b	Friction factor
k_c	Carter’s coefficient
k_e	Excess-loss coefficient
k_f	Lamination stacking factor
k_h	Hysteresis coefficient
k_r	Skin effect factor
k_{stray}	Additional loss coefficient
l	Length
l_b	Length of the rotor bar
l_r	Length of the end ring segment between two bars
$L’$	Stack effective length
L	Inductance, length
$L’_{r\sigma}$	Rotor leakage inductance reduced to the stator

L'_s	Stator transient inductance
L_d	Direct-axis inductance
L_m	Magnetizing inductance
L_n	Slot leakage inductance
L_q	Quadrature-axis inductance
L_r	Rotor inductance
L_s	Stator inductance
L_{sc}	Short-circuit inductance
$L_{s\sigma}$	Stator leakage inductance
L_w	End winding leakage inductance
L_δ	Harmonic leakage inductance
L_z	Tooth-tip leakage inductance
L_χ	Skew leakage inductance
m	Mass, phase number
n_r	Rotor speed
n_s	Synchronous speed
N	Turns in series in the winding
Nu	Nusselt's number
p	Number of pole pairs, power density
P	Power
Pr	Prandtl's number
q	Number of slots per pole per phase
Q	Number of slots
r	Radius
R	Resistance, Radial conductivity factor, Reluctance
Re	Reynold's number
R_{Fe}	Iron loss resistance
R'_r	Rotor resistance reduced to the stator
R_s	Stator resistance
R_{th}	Thermal resistance
s	Slip
t	Time
T	Temperature, Torque
Ta	Taylor's number
$\boldsymbol{u}_m$	Air gap voltage vector
$\boldsymbol{u}_r$	Rotor voltage vector
$\boldsymbol{u}_s$	Stator voltage vector
U_m	Air gap voltage RMS value
U_s	Stator voltage RMS value
w	Width
W	Coil span, Coil hotspot-to-mean temperature ratio
x	Distance

Greek letters

α	Angular acceleration, arithmetic flux density value, resistance thermal expansion factor
γ	Angle between rotor and stator flux-linkage vectors
δ	Physical air gap length, skin depth
δ'	Average electric air gap length
δ_a	Load angle
δ_{eff}	Effective air gap length
ε	Emissivity
θ_k	Harmonic phase angle at k^{th} harmonic
Θ	Magneto-motive force
λ_E	End winding axial leakage factor
λ_N	Slot leakage factor
λ_{th}	Heat transfer coefficient
λ_W	End winding tangential leakage factor
μ	Dynamic viscosity
μ_0	Vacuum permeability
μ_r	Relative permeability
ν	Ordinal of harmonic frequency, circumferential speed
ξ_1	Fundamental winding factor
ξ_ν	Winding factor for ν^{th} harmonic frequency
ρ	Density, electrical resistivity
σ	Conductivity
σ_{SB}	Stefan-Boltzmann's coefficient
σ_{Tan}	Tangential tension
σ_δ	Harmonic leakage factor
τ_p	Pole-pitch
φ	Phase angle, angle
Φ	Magnetic flux
Φ_{th}	Heat flux
χ	Skew leakage factor, ratio of the rotor length to diameter
$\boldsymbol{\psi}_m$	Magnetizing flux-linkage vector
$\boldsymbol{\psi}_{PM}$	Permanent magnet flux-linkage vector
$\boldsymbol{\psi}_r$	Rotor flux-linkage vector
$\boldsymbol{\psi}_s$	Stator flux-linkage vector
ω	Angular frequency
ω_r	Rotor angular frequency
ω_s	Stator angular frequency
Ω	Mechanical angular velocity

Subscripts

d	Direct-axis
em	Electromagnetic
EMF	electro-motive force
loss	Loss
max	Maximum value
mech	mechanical
min	Minimum value
n	Nominal
q	Quadrature-axis
r	Rotor
Rad	Radial
s	Stator
Tan	Tangential
th	Thermal

Acronyms

ABB	Asea Brown Boveri
AC	Alternating Current
DC	Direct Current
DTC	Direct Torque Control
BLDC	Brushless Direct Current Motor
EMF	Electro-Motive Force
FEM	Finite Element Method
IGBT	Insulated Gate Bipolar Transistor
IEC	The International Electrotechnical Commission
IM	Induction Machine
MMF	Magneto-motive force
NdFeB	Neodymium-Iron-Boron
PM	Permanent Magnet
PMDC	Permanent Magnet Direct Current
PMSM	Permanent Magnet Synchronous Machine
PWM	Pulse Width Modulation
RMS	Root Mean Square
SMPMSM	Surface-Magnet Permanent Magnet Synchronous Machine

1. INTRODUCTION

The word ‘servo’ originates from the Latin word ‘servus’ meaning a slave (Fowler 1988); in a motion control system, a servomotor is an actuator that executes tasks requested by the user, process control etc. A servo drive is a generic term for automated motion control systems, where the position of the load is controlled by controlling the movement – rotational or linear – of an actuator. There is neither a clear definition for the servomotor, nor a specification how it differs from the conventional motors, but servomotors are often regarded as capable of high dynamic performance. The power range of servomotors varies from fractional kW range up to hundreds of kilowatts. Low-power servomotors are used for example in cars, in machine tools, and in different kinds of valves, while high power servomotors are used for instance in paper machines, elevators, and hoisting machines. The servomotors are, however, typically below 100 kW range, usually only some tens of kilowatts at maximum. Also, below 1 kW range, servomotors can often be special machines, such as stepper or linear motors. The scope of this work are the AC servomotors having a classical three-phase winding in the stator, producing a rotating magnetic field, and the machines below 1 kW power range are excluded from this work.

Servo systems can be grouped into three main categories by their operating principle: hydraulic, pneumatic, and electric servos, while the latter is in the focus of this study. Hydraulic servos use pressurized oil to create motion, and the torque and the speed can be controlled by controlling the pressure and the flow rate of the oil. Although the power densities are extremely high, the accuracy of the speed and position control is poor and the speed is low. Also oil leakages and fire hazard may cause problems in certain applications. Such applications can typically be found in food and beverage industry. Also the arrangement of pressurization network is usually both difficult and expensive. The operating principle and characteristics of pneumatic servos are basically the same as in the hydraulic ones, but they have significantly lower power densities, and they are mainly used in low-power applications, where oil leakages and fire hazard are not tolerated. Electric servomotors are by far the most rapidly increasing group due to huge developments in the field of electric drive technology during the latest decades. An electrical servo system comprises four main parts: a power converter, a motor, a feedback device and a load. With modern closed-loop control, extremely high dynamic performance is possible with high efficiency. Typical applications are robots, conveyors, auxiliary motors in automobile industry, machine tools, lifts, and so on. Although the proper control of an electric drive is as vital as the characteristics of the motor itself in order to achieve a good dynamic performance, the focus of this work is solely on the servo machine design aspects. There are, however, two doctoral theses in progress within the same project that study the control-based optimization methods of the servo drives. Table 1.1 in the following page lists some characteristics of hydraulic, pneumatic, and electric servos.

Table 1.1. Benefits and drawbacks of various servo systems.

Actuator type	**Benefits**	**Drawbacks**	**Examples**
Electric motor	•Excellent dynamics •Mature technology •Simple wiring •Wide product variety •Several suppliers available •High speeds possible •Excellent efficiency	•Expensive •Lower torque or force density than in hydraulic systems •Requires lots of sensors	•Machine tools •Conveyors •Lifts and hoists •Robotics •Extruders •Automated warehousing
Hydraulic motor	•Easy to apply •High torques available •Centralized power source •Easy to use •High force density	•Arrangement of pressurization network •Audible noise •Accurate speed control difficult •Slow positioning •Oil leakages •Poor efficiency •Fire hazard •Regular maintenance required	•Lifts (low rise) •Pumps •Linear motion •Valves •Metal punching •Heavy machinery
Pneumatic motor	•Low cost •Easy to use •Requires little maintenance •Centralized power source	•Arrangement of pressurization network •Audible compressor noise •Accurate speed control difficult •Poor efficiency •Low force density •Non-linear due to air compressibility	•Valves •Food and packaging applications •Fire-hazardous motion control applications

In general, hydraulic servo systems are mainly used in applications, where high forces are required per small unit volume, as for instance in metal punching. This is because the force densities of hydraulic systems are substantially higher than with electric motors. Even in lower force density hydraulic systems, such as in vehicle brakes, the operating pressure can typically be 2000 kPa, that is, 2000 kN/m^2. The tangential stress acting in the air gap of an electric machine without forced cooling ranges typically between 5−30 kN/m^2, which makes it approximately 1 per cent compared to the value of the lightest hydraulic systems. The operating pressure of a hydraulic system in heavy machinery can typically be 7000−42000 kN/m^2, although due to the advances in materials and design, there is a trend towards higher pressures, up to 100 000 kN/m^2. With titanium hardware, operating pressures even up to 350 000 kN/m^2 are possible, which is a four decades higher value than with electric machines regardless of the cooling arrangement. With through ventilated air or hydrogen cooling or direct water cooling methods, tangential stresses of electric machines can be increased only up to 50−100 kN/m^2. It should be borne in mind that by using a gearing, the torques of electric motors can naturally be increased, if necessary. However, in most of the motion control applications, positioning accuracy is required rather than high force

densities, which makes an electric motor a feasible solution thanks to its advantageous characteristics. Figure 1.1 shows two motion control applications. The first one is a very common servo application – an industrial robot suitable for e.g. arc welding, spraying, material handling, etc., and the second one is an elevator hoisting machine. Although the elevators are not often referred as servos, they are, however, very similar applications, where the cycle contains acceleration, constant speed, and deceleration phases, after which the load is accurately positioned.

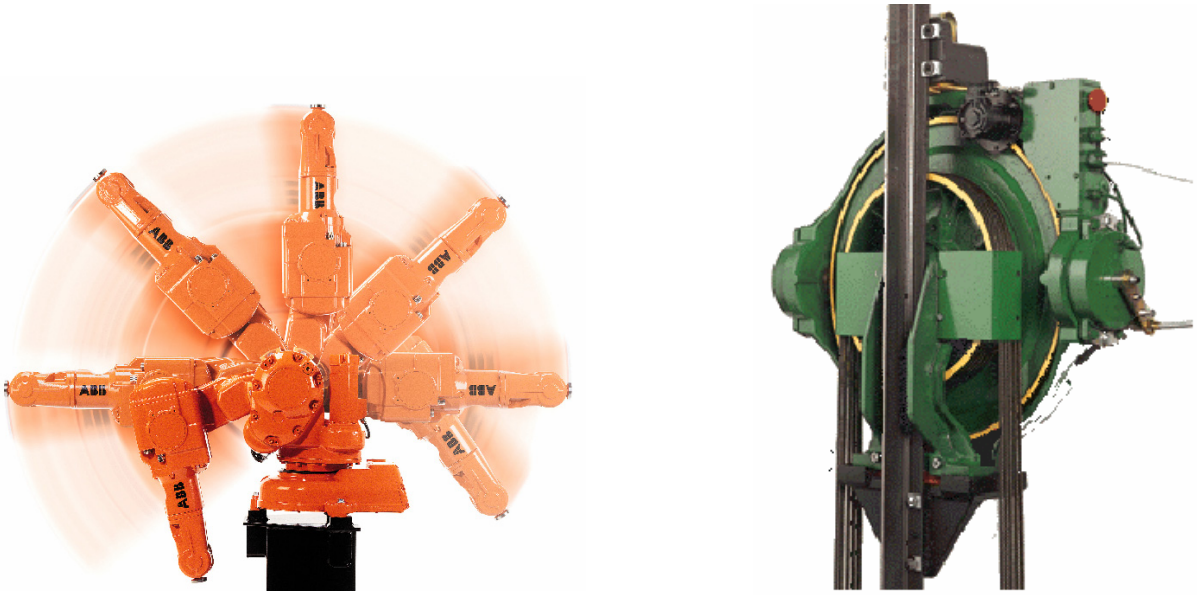

a) b)

Figure 1.1. Two motion control applications of different kinds. a) An industrial robot containing six permanent magnet synchronous motors (PMSMs), and b) KONE Ecodisc® elevator hoisting machine, which is an axial-flux permanent magnet synchronous motor (www.abb.com, www.kone.com).

The industrial robot in Fig. 1.1 a) requires a high torque response, which makes the low inertia and high momentary torque critical parameters, while for an elevator hoisting machine, inertia of the motor is not critical at all due to huge load inertia. More important is the torque smoothness, which is required to guarantee a comfortable ride for the passengers. Depending on the application, the load may limit the acceleration rate, for example, if fragile pieces are moved with an industrial robot. On the other hand, overloading capability can temporarily be used to avoid the over-dimensioning of the elevator motor, which seems to be the case with the crane motors, too.

First electric servo systems were all DC drives, since the DC motor was for a long time the only motor type capable of high dynamic performance. Regardless of its certain drawbacks – namely a complex construction (especially with a fully compensated machine), lower efficiency than in the AC machines, and high cost – the torque control of the DC motor has nevertheless always been very straightforward, as the air gap flux and the torque can be controlled separately. However, the DC machine requires regular maintenance due to its carbon brushes. Its overloading capability is also poor due to the mechanical commutator, which is not capable of commutating high currents. Further, its rotor construction limits the maximum speed, and if high-speed operation is required, some special measures must be adopted to ensure adequate mechanical ruggedness. Starting in the

1960s, development on permanent magnet (PM) materials, power switches, and microprocessors made it possible to utilize also AC in the speed control of electrical machines. This way, it was possible to get rid of the brushes by electronically commutating the current from one phase to another. The first brushless machines were three-phase PM machines with rectangular-shaped stator voltage, although the back-EMF waveform ranged from sinusoidal to trapezoidal. Although the direction of the current of these machines varied, their control was yet quite similar to the control of DC machines. Nowadays, these machines are often referred to as permanent magnet DC motors (PMDC) or brushless DC motors (BLDC), although the use of terminology is still very confusing and depends largely on the source.

The first speed-controlled AC drives with sinusoidal excitation were synchronous machines (SM), since early inverter topologies based on mercury-arc switches were not capable of handling reactive power. A milestone in the field of speed control of AC machines was the invention of the cycloconverter capable of reactive power handling in the early 1930s. This enabled also the use of induction machines in the speed control, although the dynamic performance and the stability of the machines were very poor. Induction machines were more robust and cheaper, and unlike the synchronous machines, they did not have the problem of losing synchronism. The introduction of the space vector theory for multi-phase AC machines by Kovács and Rácz (1959), and the theory of pulse width modulation (PWM) for AC drives in 1964 finally made it possible for AC motors to be used also in speed controlled drives (Stemmler 1994). This was also due to the introduction of the silicon power switches in the 1950s, which made it possible to switch higher and higher currents and voltages faster and faster. Despite all these developments, these early speed controlled AC drives were basically frequency controlled (u/f –control) and consequently, their dynamic performance still lagged DC drives until the early 1970s. Field-oriented control (later referred as vector control) of AC machines, pioneered by Blaschke (1972), made it possible to achieve equal – or even better – dynamic performance of AC drives compared to DC drives. This was due to a fact that their fundamental operation principle is the same, that is, decoupling of flux- and torque-producing currents. Vector control, however, required large computing resources due to continuous modelling of the machine's electromagnetic state, and therefore it was first applied only in high-power applications, where the extra cost was justified. Fast development in the field of microprocessors and the introduction of ASIC (application specific integrated circuit) in the early 1980s finally made it possible to achieve excellent dynamic performance with the AC drive also in low-volume applications and also in a lower power range, such as in servo applications.

Due to their good characteristics, such as the efficiency and the torque smoothness, the AC machines soon gained ground from different kinds of DC motor topologies in motion control applications, despite the fact that a well-designed DC machine often produced smooth torque. The first AC servo drives often utilized the squirrel-cage induction machine because the electrically excited synchronous machines were excluded from low-power servo applications, and the control theory of PMSMs was not fully developed yet. The squirrel-cage IM is extremely robust and cheap, and its overloading capability (and consequently the field weakening characteristics) is good. However, its main problem is an always lagging power factor, which means that it can produce typically only 70−90 % of the torque produced by a comparable PMSM with the same current. Due to the introduction of the NdFeB (Neodymium-Iron-Boron) magnets and the vector control methods for PMSMs in the early 1990s, during the past decade, PMSM has become more common in dynamically demanding applications than IM. Because of the rotor permanent magnetization of PMSMs, a physically smaller motor and an inverter with a smaller current rating

can be chosen. With the surface-magnet permanent magnet synchronous machines (SMPMSMs) the overloading capability is inherently very good, as will be shown later in this work. This is especially important in motion control, where the overloading capability can be utilized to obtain rapid acceleration rates. The most common material in modern high performance PM machines is NdFeB, because it can have a very high energy product, which leads to a high remanence flux density and a high coercive field strength. NdFeB magnets with remanence flux density of 1.5 T are commercially available, but their maximum operating temperature must be limited below 100 °C. In motors instead, magnets with lower remanence flux density, but better thermal characteristics are usually required. The temperature dependence of both the remanence flux density and the coercive field strength are the major drawbacks of modern NdFeB magnets. As the remanence flux density decreases due to the temperature rise, more stator current is required to produce the given torque, which further increases the heating of the machine. Further, as the coercive field strength decreases, the so-called knee-point, where the irreversible demagnetization of the magnets starts to take place, occurs at lower negative field strength values. Figure 1.2 shows the demagnetization flux density-magnetic field strength *BH* curves of the modern NdFeB magnets at different temperatures, where these two phenomena are visible.

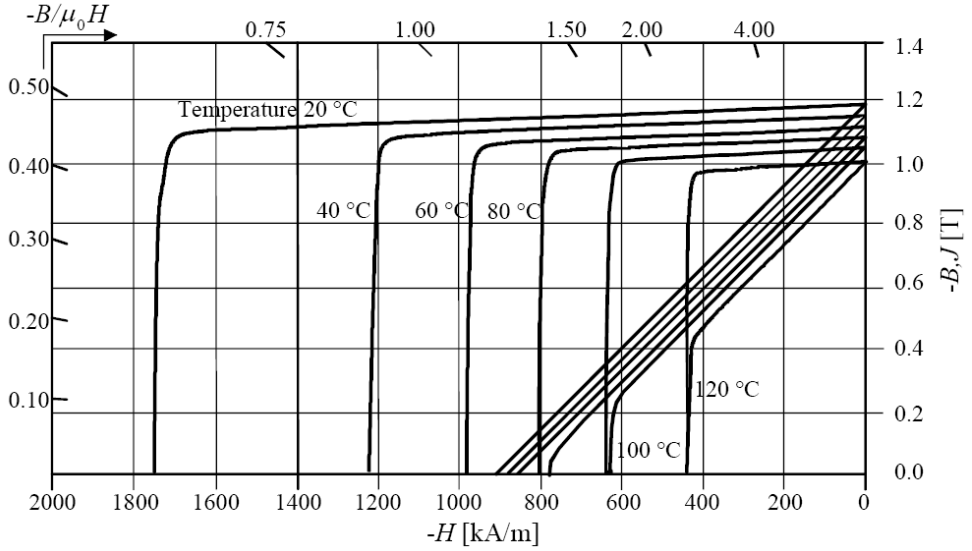

Figure 1.2. *BH* and *JH* curves of NdFeB magnets in the second quadrant. An increase of 100 °C in the temperature decreases the remanence flux density by almost 20 %. Also the so-called knee-point, where the polarization *J* is lost and the irreversible demagnetization starts to take place, occurs at lower demagnetizing field strengths *H* as the temperature increases (Neorem).

As it can be seen in Fig. 1.2, the knee-point, where the irreversible demagnetization starts to take place occurs at -1700 kA/m at the 20 °C temperature, but already slightly under -400 kA/m when the temperature is raised to 120 °C. Further disadvantages of NdFeB magnets are the sensitivity of the magnets to corrosion and the fact that they are very brittle and can therefore crack easily if exposed to mechanical shocks or to tensile stress. In addition to the strong dependence of the PMSM characteristics on temperature, usually the biggest drawback of a PMSM drive system in general is the lack of proper field weakening. Because of the constant flux set by the magnets, and the very weak armature reaction of surface magnet permanent magnet synchronous motors (SMPMSM), the field weakening is very difficult and also impractical. There would be very little current left to produce torque, while most of the current is consumed in demagnetization. If a high-

speed operation is required, the motor nominal point must therefore be located close to the maximum speed, and further, surface magnets may require for instance a fibre glass band for attachment. Although the magnet-retaining band prevents the magnets from detaching, it degrades the heat dissipation of the magnets. Although the fundamental flux in the rotor of PM machines is constant, the inverter supply generates high-frequency time harmonics in the air gap flux in addition to the spatial permeance harmonics due to the slotting and the winding harmonics which in turn result from a discrete distribution of the winding in the slots. Different harmonic flux waves induce eddy currents in the magnets and in the magnetic circuit material under the magnets causing them to heat.

The major advantages of induction machines are the good field weakening performance and the robust construction of the rotor, which both favour high-speed operation. If field weakening can be utilized, the gain in the motor physical size can be significant compared to a PMSM. A high overloading capability is a prerequisite for good field weakening characteristics of the induction machine. This is also a fundamental requirement for high dynamic performance. By optimizing the pull-out torque of an IM, both a good dynamic performance and high-speed operation can be achieved. As will be shown later, high flux densities should be used to obtain high dynamic performance. A high flux density decreases the power factor due to increased magnetizing current. If the motor must operate in saturation, the increase in the magnetizing current is large. However, by properly adjusting the motor flux as a function of the load, the characteristics of the motor, such as the power factor as well as the efficiency can be significantly increased. With a proper design, the overloading capability of an induction motor can be increased, and with a proper flux control strategy, its torque-to-current ratio can be improved. With its high overloading capability, good field weakening performance and only a little lower torque-to-current ratio, it can compete against PMSMs, which currently dominate the motion control industry.

1.1 Motion control requirements and applications

Figure 1.3 illustrates a schematic diagram of a basic servo control. The servo control is traditionally based on a cascade control, where the position reference for the position controller is fed by the user or by a higher-level controller, which controls the whole process. Next to a position controller there is a speed controller, and after that a current controller, which controls the current of the motor to produce an adequate movement of the rotor. As a feedback device, an incremental encoder or a resolver (especially with PMSMs) is typically used. The power converter in Fig. 1.3 is nowadays typically a voltage source inverter with IGB transistors in the power stage, and the motor is a brushless AC motor.

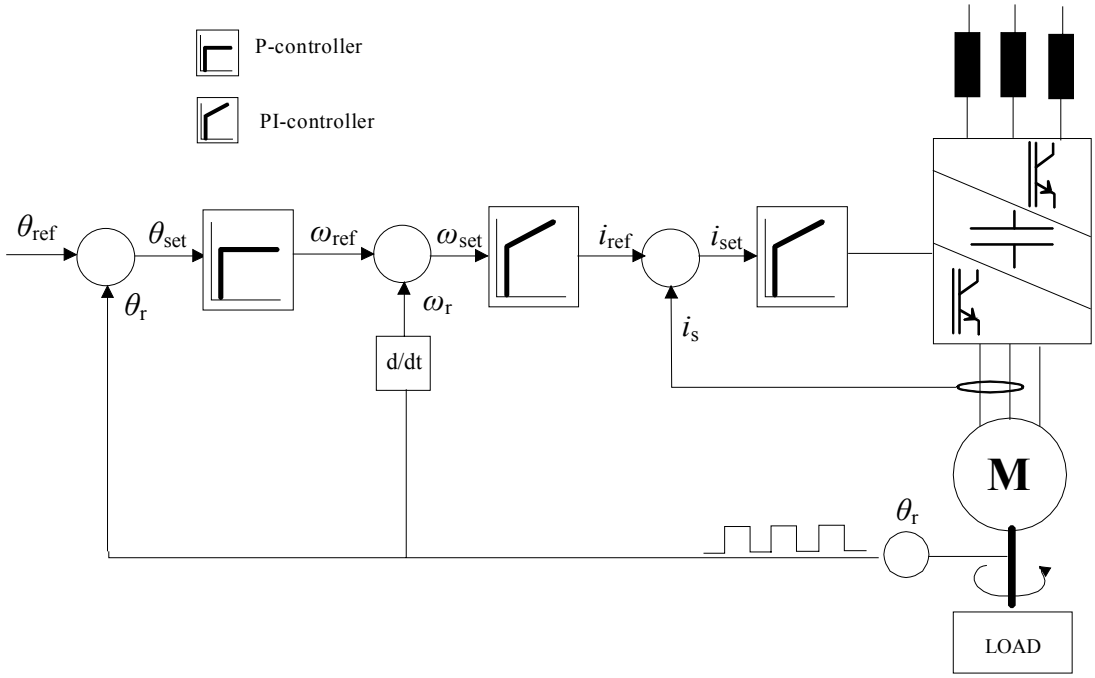

Figure 1.3. Schematic diagram of a servo control. The movement of the motor is controlled by controlling the voltage and the frequency of the motor. A position feedback-device is always required to obtain good positioning accuracy.

There are no specific definitions for the term 'servo', and basically, it can refer to any application, in which the motion is controlled with a motor and some kind of a controller. For instance an electric cam is a very simple servo application, while more demanding applications of servos are those in which the *position* of the load must be accurately controlled, as in conveyors, in robots, in elevators, in pick-and-place machines, in extruders, and in winders. Table 1.2 lists some of the most common and more demanding servo applications. Later, the most important requirements for servo applications are discussed in brief.

Table 1.2. Some of the most common servo applications and their requirements (Drury 2001).

Application	**Requirements**
Cast tube spinner	High accelerating torque, four-quadrant operation
Machine tool spindle drive	High-speed operation, smooth torque
Extruder	High overloading at start-up, difficult environment
Calendar	200% braking torque
Automated warehousing	Four-quadrant operation, high overloading torque.
Lift and hoist	High overloading, smooth torque, four-quadrant operation, 90−200 starts/hour with 200% torque at start-up.
Printing press	Field weakening, four-quadrant operation, smooth torque at low speeds
Winders and reels	Field weakening, four-quadrant operation
Test rigs	Field weakening, smooth torque and speed

1.1.1 Overloading capability

Figure 1.4 shows a very typical load cycle of a servo application, which can be applied for instance in pick-and-place machines, cranes, and elevators. First, the motor is rapidly accelerated with high torque to a constant speed, at which only small torque is required. In elevators, however, the maximum acceleration−deceleration rate is often limited. After the constant speed phase, high braking torque is required to rapidly decelerate the motor into the desired position. Typically the speed of the motor must be altered smoothly by limiting the initial acceleration to avoid jerking, which could cause some mechanical damage to the application. The speed curve in Fig. 1.4 is said to have an "S-profile".

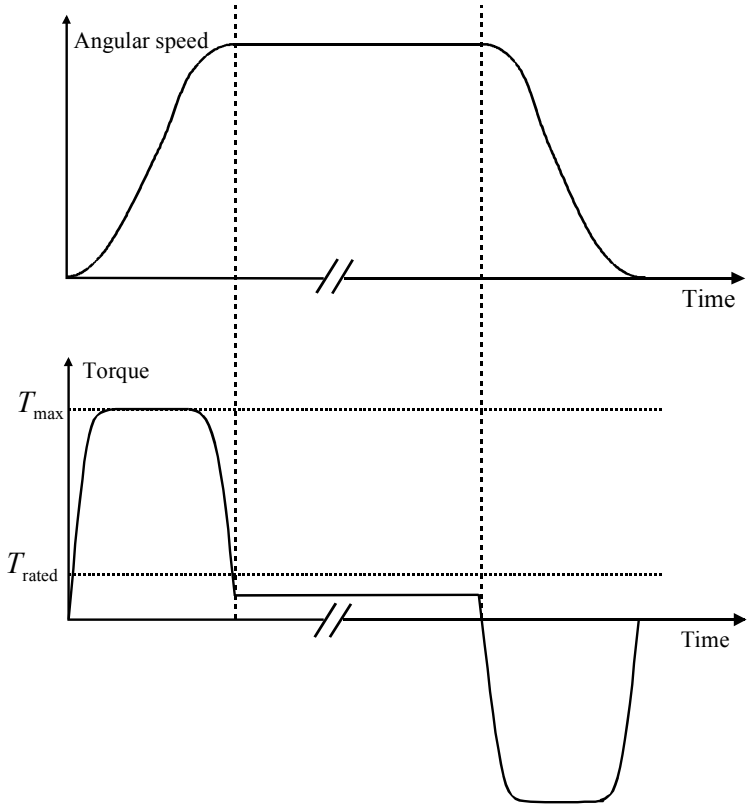

Figure 1.4. Typical load cycle of a servo application (e.g. a pick-and-place machine). By limiting the acceleration rates, jerking can be avoided. A consequent speed profile (in the upper figure) is called an "S-profile". If the overloading of the motor can be utilized during the acceleration, sizing of the motor can be significantly reduced.

As the acceleration and the deceleration phases in Fig. 1.4 are typically much shorter compared to the constant speed phase, the sizing of the motor can be reduced by occasionally utilizing the overloading capability of the motor. The duration of the overloading period is limited both by the frequency converter current rating, and by the motor pull-out torque. The thermal time constants of the power IGB transistors, used commonly in modern inverters, are very short. This means that the overloading capability of the inverter is negligible compared to the overloading capability of the motor. The inverter can typically provide for instance 150 % current for the duration of only few seconds. This means that the inverter must be oversized compared to the motor, which is naturally always a technical and economical compromise. An inverter with a larger current rating is more expensive, but a smaller motor can be chosen if the overloading capability is utilized. If the

inverter current rating is matched near to the motor rating, a low dynamic performance of the drive follows, as there is no "torque reserve" during fast loading transients. Especially, with low inertia loads, overloading capability of the motor is important, as the motor own inertia becomes dominant, and the utilization of the overloading capability occasionally can lead to a physically smaller motor.

Besides the inverter current rating, the overloading capability could be also limited by the motor pull-out torque. The pull-out torque is the maximum torque the motor can provide with the given voltage. The pull-out torques of industrial induction motors typically vary between 1.6 and 3 per-unit value (1.6 p.u. is the minimum value defined by the standard IEC60034-1), while the pull-out torque of PM machines largely depends on the machine topology. For the salient-pole synchronous machines (PMSM servos can be grouped into this category) the standard defines the minimum of 50 % excess torque. With buried magnet machines, the overloading capability is often poor, and if a surface magnet construction is used, the per-unit pull-out torque can be even 4−6 p.u. due to low d-axis inductances. A high pull-out torque in addition to a low inertia and a high torque-to-current ratio compared to induction machines makes the SMPMSM feasible in motion control applications.

As the electromagnetic torque is proportional to the current, and the copper losses proportional to the current squared, heavy overloading causes excessive heating on the stator. For example, loading the machine with a 4 p.u. torque causes 16-fold copper losses in the stator windings. This can rapidly cause thermal failure in the stator winding insulation, and consequently, a turn-to-turn or turn-to-ground short-circuit. That is why temperature monitoring is almost without exception used in servo drives, either with thermistors or with temperature sensors. A thermistor is a passive protecting device, which is used to disconnect the motor from the inverter if the temperature increases too high. A temperature sensor is simply a measuring device based on the measurement of resistance, which changes as a function of temperature. In an inverter, there is some kind of protection function, which uses the temperature information and for instance limits the motor current if necessary. Temperature signals are usually wired in parallel inside the cable from the speed-feedback device, and no separate cabling is required. In this study, an analytic model for the transient heat transfer of an induction machine is presented in Chapter 4, in which the temperatures in different parts of the machine are calculated by using the motor loss components as inputs.

1.1.2 Rotor inertia

Besides by utilizing the overloading capability of the motor, high acceleration and deceleration rates can be achieved if the inertia of the motor-load combination is low. However, for control purposes in highly dynamic applications, the ratio of the load inertia-to-motor inertia should be close to unity, and as a rule of thumb, it can be stated that the ratio should not exceed 5 (Armstrong Jr. 2001). Due to too high a mismatch between the load and the motor inertia, the gains in the control loop must be set low to avoid dynamic instability. Low gains in the controllers cause poor dynamic performance to the entire drive system. Hence, low-inertia motors should be used only with low-inertia loads. The inertia of the rotor can be decreased by decreasing the diameter and, correspondingly, by increasing the length of the rotor. Torque T of a rotor may be considered a result of the tangential stress σ_{Tan} on the rotor surface A_{rotor}

$$T = r_{\mathrm{rotor}} \sigma_{\mathrm{Tan}} A_{\mathrm{rotor}} \quad . \tag{1.1}$$

For constant torque, the product $r_{\text{rotor}} A_{\text{rotor}}$ should be kept constant (if the tangential stress is constant). This means that as the length of the rotor is increased, the radius can be decreased as $r_{\text{rotor}} \propto L^{-1/2}$ in order to keep the product $r_{\text{rotor}} A_{\text{rotor}}$ constant. The inertia of the rotor therefore decreases inversely proportional to the rotor length in the case of constant torque. Although the amount of the copper slightly increases with the rotor length, the ratio of the length of the end turn to the active part of the copper decreases. According to Levi (1984), an optimal ratio to minimize the turn length can be expressed as a function of the motor pole pair number p

$$\chi_{\text{opt}} = \frac{L'}{D_{\text{ag}}} \approx \frac{\pi}{2} p^{-\frac{2}{3}} \quad . \tag{1.2}$$

Equation (1.2) states that the higher the pole pair number, the shorter the rotor should be compared to the air gap diameter. Servomotors are very often of four- or six-pole constructions; that is, their optimal rotor length-to-diameter ratio, according to Levi, is between 0.76−0.99. Because the rotor inertia should be matched to the load inertia, the longer rotor with smaller inertia is not necessarily better. Often there are different kinds of servomotors available from the same manufacturer; ones with the low inertia and ones with the higher. The ratio can be up to 2−3 for the low inertia motors, and less than one for the motors with higher inertia.

1.1.3 Torque quality

An important requirement in motion control is the quality of the torque, which basically means that the generated torque should be as smooth as possible. For example, the performance specifications of the servomotors embedded in equipment ranging from the machining tools and the conveyor lines to the robots and the satellite dishes require minimization of all sources of a pulsating torque. In high-grade elevators, the maximum allowed torque ripple is 0.5 % of the rated torque (Laurila 2004). Torque ripples in electrical machines are caused in general by the air gap flux time- and space-dependent harmonics, where the first one is caused by the inverter supply switching operation, and the second by the motor itself. With PM machines, there may occur also so-called cogging torque, which is caused by the tendency of the PM rotor to align itself into positions, in which the reluctance of the flux path is locally minimized. Even though the rotor would be fully non-salient, there is always a reluctance difference in different directions due to the distribution of teeth and slots in the stator. Space harmonics can be further divided into those caused by the discrete distribution of the stator winding in the slots (winding harmonics) and those caused by the permeance variations in the air gap caused by the stator (and rotor) slotting. In general, the higher is the slots per pole per phase number q, the smaller is the winding harmonic content. The pole number of electrical machines must be chosen according to the desired speed range. With a fixed phase number, this means that the higher the slot number of the stator Q_{s}, the more sinusoidal is the air gap flux distribution and the smaller is the harmonic content. The majority of servomotors are physically small-diameter machines, that is, there is a limitation for the maximum value of Q_{s}. A three-phase motor with 36 stator slots having four or six poles is a very common solution used in motion control, and the number of slots per pole per phase of such motors is, in this case, 2 or 3.

The permeance harmonics in the air gap flux distribution are caused by the slotting, that is, there is always a local permeance minimum under each slot opening, where the flux density sags. The wider the slot opening, the deeper is the sag under the slot and vice versa, but unfortunately, choosing narrow slot openings rapidly increases the slot and the tooth-tip leakage flux. This is a problem especially with induction machines, as their overloading capability is inversely proportional to the leakage inductance, which makes the selection of the slot opening dimensions a compromise between the permeance harmonics and the overloading capability. Air gap permeance harmonics also strongly induce eddy currents on the rotor surface of an induction machine and also on the magnets of PMSMs. The electric conductivity of for instance the NdFeB magnets is only a decade smaller than that of iron, which means that the high-frequency flux pulsations effectively induce eddy currents on solid magnets. Consequent heating of the magnets decreases their remanence flux density, which increases the stator current to compensate the decreased torque. This further increases the heat generation in the machine, and the remanence can drop even more. Besides the fact that the heating decreases the remanence flux density, it also brings the knee-point in the permanent magnet material *BH* curve closer to the operating point. If, for example due to a short-circuit, the magnet demagnetizing field strength exceeds the value at the knee-point, irreversible demagnetization of the magnets will occur (especially with surface-magnet PMSMs).

Due to these reasons, semi-open slots are used with both PM and induction machine stators. Sometimes even semi-magnetic slot wedges are applied to close the stator slots, although this is quite an expensive and rare solution. This is mainly used with high-speed machines, as the smooth stator bore can significantly reduce the windage losses. Also the effects of the air gap flux harmonics are far more critical at high-speed machines. On the rotor of the induction machines, however, closed rotor slots are often preferred mainly due to manufacturing reasons. If a die-casting process is applied in the rotor manufacturing, closed rotor slots prevent the cast from spilling outside the rotor. It must be noted, however, that the iron bridge above the rotor slots is made very thin, which means that it saturates heavily even at normal operation and appears magnetically open. In this work, a copper-cage rotor with fully open rotor slots is studied.

The cogging torque of PM machines can be sensed by rotating the shaft manually, and it occurs even when there is no current flowing in the stator. This topic has been widely studied during the latest decade, and numerous methods have been proposed to reduce the cogging torque. Traditional skewing of either the stator slots or the magnets usually by one slot-pitch is a very common and also effective method to reduce the cogging torque (although it helps also with the torque ripple generated by the air gap harmonics). Other suggested methods to reduce cogging torque are for example (Hendershot and Miller 1994; Li and Slemon 1988):

- Using increased length of the air gap
- Using fractional slots/pole
- Using larger number of slots/pole
- Decreasing the width of the slot openings or using semi-magnetic slot wedges
- Chamfering the magnets
- Using dummy slots in the stator

Using the increased air gap length to decrease the cogging will increase the amount of the PM material, because low permeability of the air will rapidly increase the required MMF. Fractional

slot/pole design will make the machine design more complicated, and it also leads to a higher harmonic content of the air gap flux. It was shown by Salminen (2004), however, that with a proper design, the torque ripple of a fractional slot machine can be kept small. If the slot openings with decreased widths or even with semi-magnetic slot wedges are applied, the tooth-tip and the slot-leakage inductance will increase thus decreasing the torque production capability of the motor. Chamfering of the magnets, however, is a very effective and common method to decrease the cogging torque. Magnets with chamfered edges will produce a more sinusoidal air gap flux density distribution, although the average flux density value over one pole-pitch will slightly decrease. The idea of using dummy slots between real slots in the stator is based on the fact that the frequency of the cogging torque increases, while the amplitude decreases. Dummy slots, however, complicate the manufacturing of the stator, and can increase the permeance losses in the magnets. It is also possible to decrease the cogging torque not only by the proper machine design, but also by modulating the inverter current waveform; numerous papers have been written on this topic, as well as on the other control-based methods.

1.2 Common motor types in motion control

The first speed-controlled drive was introduced over 100 years ago by Harry Ward Leonard in his paper "Volts versus ohms – speed regulation of electric motors". The rotating rectifier consisted of a grid-supplied induction machine that rotated a DC generator. By adjusting the magnetization of the DC generator, controllable DC voltage was available for the speed control of a DC motor. Although three machines were required, it was at the time the only possibility to realize a speed controlled drive. When the transistors and first micro-processors were introduced, chopper technologies such as the PWM enabled the accurate speed control of DC machines. Brushless DC motors with permanent magnets in the rotor were also introduced in the early 1960s, but since there were not powerful enough PM materials available yet, their power range was limited typically below 10 kW. Typical applications for brushless DC motors were small machine tools, tape recorders, and robotics. For higher-power speed-controlled applications, brushed DC motor was for a long time the only solution. Until the early 1980s, when high energy density NdFeB magnets were introduced, it was possible to get rid of the brushes also at the higher power range up to hundreds of kWs by using a brushless DC motor. Later on, the introduction of the field-oriented control for machines made it possible to use AC machines in demanding speed-controlled applications. First, the speed-controlled AC drives were induction motor drives, but as the vector control for PMSMs was introduced in the early 1990s, they soon started to gain ground from the DC motors and have dominated in the motion control industry ever since. The trend in the motion control nowadays is clearly towards the brushless AC machines with sinusoidal excitation, which, in practice, means that a permanent magnet synchronous motor or an induction motor must be used.

It can be concluded that the brushed DC motors dominated the speed controlled drives in the 1960s and 70s, and the brushless DC motors in the 1980s. Since the early 1990s, PMSMs have dominated the motion control industry to the present, and, according to the current trend, there seems to be no end for that. Induction motors have always been a minority in the motion control, and they are mainly used in applications, where the field weakening can be utilized to avoid the over-sizing of the drive, which would be the case with PMSMs. The most common motor types are presented below.

1.2.1 Brushed DC motor

DC motor was for a long time the only motor type available to convert electrical power into mechanical power, and due to its straightforward operating characteristics and simple and stable control, it is still being used to some extent in speed-controlled applications. The speed of the motor is controlled by controlling the armature voltage, and the torque by the armature current, that is, the flux and the torque can easily be controlled separately. This is the main principle on which all the modern AC control methods nowadays rely. The first DC motors were controlled with some chopper technology, such as the pulse width modulation (PWM). Network-connected thyristor bridges were mainly used in higher power range, typically in a variety of applications such as in printing and paper industry, passenger lifts, and any kinds of drives subjected to high transient loading, such as in rolling mills. Chopper technology was mainly used in the lower power range, such as in machine tool applications. Development in permanent magnet materials introduced a permanent magnet DC (PMDC) motor, in which the stator excitation coil was replaced by permanent magnets. Some advantages in using permanent magnet excitation were decreased copper losses, higher power density, and a smaller torque ripple at low speeds. Using permanent magnet material in the magnetic circuit causes a low armature inductance and hence a low armature reaction. Extremely linear speed-torque characteristics of the motor, which result from the permanent magnet-provided constant field flux at all speeds, makes the control of the PMDC very straightforward; the speed of the motor is controlled by simply adjusting the armature DC voltage. PMDC machines were, however, limited to the lower power range due to the absence of the proper magnets until the 1980s. Typical applications of PMDC were low-voltage battery-powered applications, such as machine tools, automotive auxiliary drive applications, and solar-powered applications. Above the 10 kW range, the separately excited DC motor was the only solution, as it provided high dynamic performance especially when fully compensated.

Although the separately excited DC motor suits extremely well to servo applications thanks to its dynamic performance, the major problem is the mechanical commutator and the carbon brushes, which require regular maintenance. The commutator also degrades the overloading capability of the machine. Good commutation, which means armature current reversal in a single armature coil without sparking at the brushes, is extremely important to prevent the premature brush failure. There is a physical limit to the speed and to the power, at which the current can be commutated. This limit is often expressed as a product of the mechanical power and speed; a widely accepted value for this product is 3 TW/min (Drury 2001). If this limit is excessively exceeded, a ring of heavy sparking runs around the commutator circumference. This is known as a brush fire or a brush flashover, and it will rapidly destroy the brushes and the commutator. If the commutation limit has to be exceeded, several armatures on a single shaft are required, which makes the drive more complex and expensive. There still are numerous applications, in which the most demanding motion control is realized with a brushed DC motor, because when properly maintained, the DC motor has a dynamic performance equal to the modern vector controlled AC drive with a notably simpler control. Therefore it is not surprising that even today, in the literature, the word “servo motor” often refers to a brushed DC motor.

1.2.2 Brushless DC motor (BLDC)

A brushless DC motor (BLDC), introduced in 1962 by T.G.Wilson and P.H.Trickey in “DC Machine with Solid State Commutation” (Wilson 1962), has a classic three-phase stator, and the rotor has surface magnets that produce rectangular air gap flux distribution. The stator may have a distributed or a concentrated winding, although the latter one is more often preferred. The motor is

driven by rectangular or trapezoidal voltage strokes coupled with the given rotor position. The voltage strokes must be properly applied between the phases, so that the angle between the stator flux and the rotor flux is kept close to 90° to get the maximum generated torque. The position sensor required for the commutation can be very simple, since only six pulses per revolution (in a three-phase machine) are required. Typically, the position feedback is comprised using three Hall effect sensors aligned with the back-EMF of the motor. Figure 1.5 a) shows the geometry of the machine and b) the stator current- and the back-EMF waveforms.

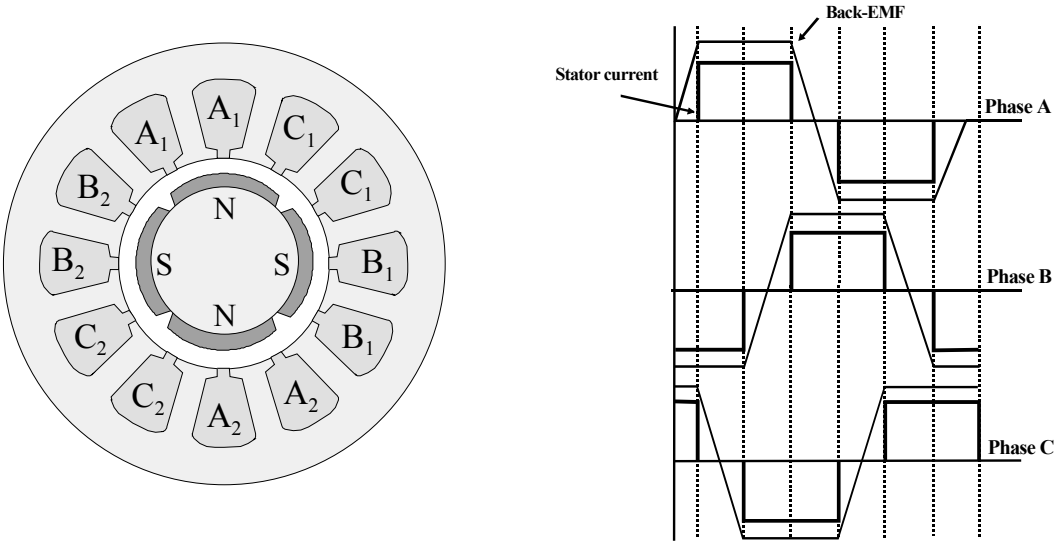

a) b)

Figure 1.5. The geometry and the operating principle of the BLDC motor. a) Four-pole brushless DC motor with three-phase concentrated winding. b) Phase-current and back-EMF waveforms in an ideal case. In a real motor, the switching of the stator current between the phases is never simultaneous, which easily causes significant torque ripple with this motor type.

According to Crowder (1995), with equal air gap peak flux densities and equal RMS currents, a BLDC can produce 47 % more torque than a comparable PMSM with sinusoidal air gap flux density distribution. This is because both the average flux density in one pole area and the RMS value of the current will be higher with the BLDC because of the rectangular air gap flux density and the stator current distribution. Of course, in order to produce a rectangular flux distribution in the air gap, a BLDC requires more PM material in the rotor. If the amount of PM material in both machines is chosen equal, the PMSM produces slightly higher torque with equal RMS current than the BLDC (Crowder 1995).

Although the control principle and the construction of the converter power stage of the BLDC motor are relatively simple, high torque ripple is generated even by small delay errors in the commutation, when the square wave current is switched from one the phase to another. With real switches, the commutation requires always a finite time, which can be seen in the torque ripple. More torque ripple is generated if either the current or the back-EMF waveform deviates from rectangular, or if the currents in each phase differ by the amplitude. The torque ripple of BLDC machines is their biggest drawback; as a result, this motor type is often used in high-speed and high-inertia applications, where the mechanics of the system effectively filter the high-frequency ripple out. If a smooth torque at lower speeds is required, AC motors with sinusoidal excitation are

commonly preferred, which often leads to the selection of a permanent magnet synchronous motor.

1.2.3 Permanent magnet synchronous motor (PMSM)

In principle, the construction of a permanent magnet synchronous machine does not differ from that of the BLDC, although distributed windings are more often used. However, while the excitation current waveform was rectangular with a BLDC, sinusoidal excitation is used with PMSMs, which eliminates the torque ripple caused by the commutation. PMSMs are typically fed by voltage source inverters, which cause time-dependent harmonics on the air gap flux. Permanent magnet synchronous machines can be realized with either embedded or surface magnets on the rotor, and the location of the magnets can have a significant effect on the motor's mechanical and electrical characteristics, especially on the inductances of the machine. As the relative permeability of the modern rare-earth magnets, such as the NdFeB is only slightly above unity, the effective air gap becomes long with a surface magnet construction. This makes the direct-axis inductance very low, which has a substantial effect on the machine's overloading capability, and also on the field-weakening characteristics. As the pull-out torque is inversely proportional to the d-axis inductance, the pull-out torque becomes very high. Typically, the per-unit values of the d-axis synchronous inductances of the SMPMSM servos vary between 0.2−0.35 p.u., and consequently the pull-out torque is in the range of 4−6 p.u., which makes them well suitable in motion control applications. The drawback of a low L_d –value is the very short field weakening range, as the armature reaction with a surface magnet construction is very weak. This means that a high demagnetizing stator current component would be required to decrease the air gap flux, and consequently, there would be very little current left on the q-axis to produce the torque. Direct-axis inductance of a machine having embedded magnets becomes high, as the rotor magnets per pole form a parallel connection for the flux, while with a surface magnet construction they are connected in series. With equivalent magnets, the rotor reluctance of the surface-magnet construction is therefore double compared to an embedded-magnet construction, and the inductance is inversely proportional to the reluctance. With embedded-magnets, the direct-axis inductance is further increased because of the higher rotor leakage flux. Three basic configurations of PMSMs are shown in Fig. 1.6.

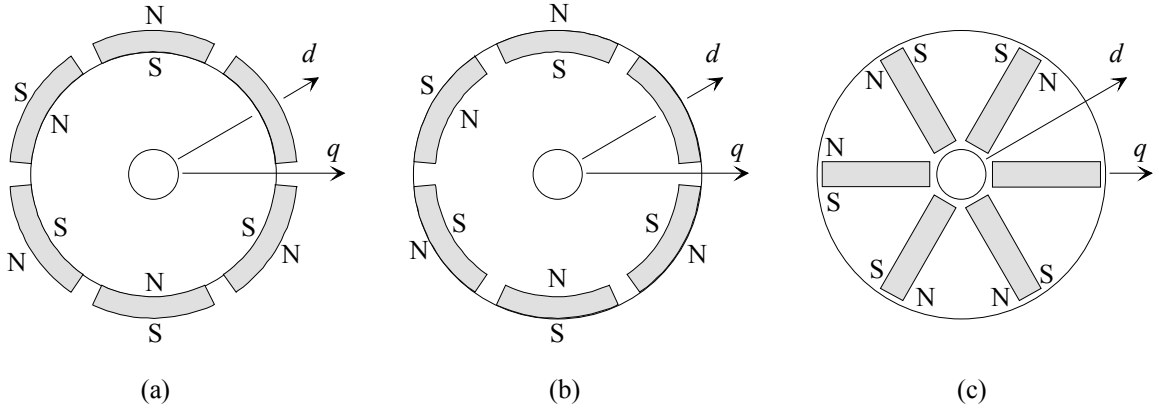

Figure 1.6. The most common PM rotor constructions. a) Non-salient surface magnet rotor. Due to high d-axis reluctance, L_d is low and consequently the pull-out torque high. b) Salient pole surface magnet rotor with inset magnets, which is basically the same as a), but this type produces also some reluctance torque. c) Embedded magnets in the rotor, which has a high L_d value, and consequently a poor overloading capability, but a lot better field weakening characteristics than with the surface magnet constructions. Typically the construction of the PMSM servomotor is somewhere between a) and b), and the q-axis inductance is larger. Industrial PMSMs often represent the type c). (Naumanen 2005)

In addition to the good overloading capability, another reason that makes the surface magnet construction favourable in servo applications is the lower inertia. With multi-pole machines, the rotor and the stator yokes can be made very thin, and all the additional iron can be removed from the rotor to provide a lower inertia. These large holes also improve the heat transfer from the rotor, as the high frequency flux pulsations generate heat on the magnets and on the rotor iron. As the servomotors must typically rotate very fast, gluing does usually not suffice in attaching the magnets on the surface of the rotor, and some non-magnetic material, such as a stainless steel cylinder or a fibre-glass band must be used to support the magnets. The problem in using steel is that it is a highly conductive material, and the air gap harmonics strongly generate losses and consequently heat in it. Therefore, a fibre-glass band or a plastic cylinder is more often used for the magnet retaining. Unfortunately, electrical insulators are also thermal insulators, which means that their thermal conductivity for the heat generated in the rotor iron and in the magnets is poor. The temperature rise of the magnets decreases their remanence flux density, and consequently the torque production.

The rotor in Fig. 1.6 b) with inset surface magnets has better mechanical characteristics, but on the other hand, it has higher leakages between two adjacent magnets. In addition to the higher leakage, the torque production decreases more as the motor must operate at higher pole angle due to increased q-axis inductance compared to a non-salient rotor. Typically, the construction of commercial servomotors is somewhere between a) and b) in Fig. 1.6, that is, the magnets are slightly embedded in the rotor. This improves the mechanical strength of the rotor and introduces a reluctance difference-based term in the torque. According to measurements made at LUT for eight different commercial servomotors in the power range of 3−5 kW, the values for the q-axis inductances were 10−20 % higher than the values in the d-direction (Naumanen 2005).

With buried magnets and flux concentration, a sinusoidal air gap flux density distribution is possible with simple rectangular magnets. A sinusoidal air gap flux distribution significantly decreases the cogging torque especially with low-speed multi-pole machines that have a low number of slots per poles per phase number q. Also, it is possible to increase the air gap flux density beyond the remanence flux density of the magnets with a flux concentration arrangement, and the machine can produce more torque at a given volume. This is especially desirable in low-speed applications, such as in wind generators and in propulsion motors (ABB Azipod®) where the space is limited. As the direct-axis inductance is typically high with a buried magnet construction, the overloading capability will be poor, which makes this motor type incompetent in motion control applications. Typically, the embedded v-shape magnet machine can have L_d approx. 0.7 p.u, which means only 1.4 p.u. overloading capability according to the load-angle equation of a synchronous machine with the assumption that $E_{PM} = u_s = 1$ p.u. and $L_d = L_q$. If there is a reluctance difference in the machine, the maximum torque can be somewhat larger. It must, however, be borne in mind that despite the embedded magnets, it is of course possible to increase the physical air gap large enough, and thereby to decrease the direct axis inductance of the machine remarkably from the value given above. However, the consumption of the magnet material is increased remarkably in such a case.

1.2.4 Induction motor

Induction machines are by far the largest group of all industrial electrical machines, converting approximately 70−80 % of all electrical energy into mechanical form. It has a very robust rotor

construction, which makes it suitable for high-speed applications, and further, with a proper design, it can have good overloading and field weakening characteristics. The theory of induction machines is old and well-known, and therefore, both motors and inverters are widely available from numerous manufacturers from fractional kW machines up to MW range. The induction motor is also known as the asynchronous motor, which derives from the fact that the rotor is always lagging the stator magnetic field. The difference is called the slip, and it is a fundamental characteristic in the operation of an induction motor. The slip is problematic in drives where a high dynamic performance is required, as it degrades the transient response of the motor for instance during stepwise loading variations. Also the rotor copper losses are directly proportional to the slip. The slip can be decreased by reducing the rotor resistance, and also by using a higher air gap flux density.

The biggest drawback of the induction machine is the always lagging power factor, because the machine is magnetized from the stator, in other words, there is a magnetizing current flowing in the stator winding even at no-load conditions. This means that less torque is available with a given current than for example with a PMSM, or alternatively, more current is required to produce an equal torque, which leads to an inverter with a higher current rating. With four-pole industrial induction machines, the power factor typically varies between 0.8−0.9, but with low-power induction machines, it can be notably lower. The power factor of an induction machine is directly connected to the magnetizing inductance L_m (Vogt 1996)

$$\cos(\varphi) \propto L_\mathrm{m} = \frac{E_\mathrm{m}}{\omega_\mathrm{s} I_\mathrm{m}} = \frac{E_\mathrm{m} m \xi_1 N 2\sqrt{2}}{\omega_\mathrm{s} \Theta_\mathrm{tot} \pi p} \quad , \tag{1.3}$$

where φ is the phase-angle, E_m the induced phase-voltage, m the phase number, ξ_1 the fundamental winding factor, N the number of turns, ω_s the stator angular frequency, I_m the RMS-magnetizing current, Θ_tot the magneto-motive force and p the number of pole pairs. With PMSM servomotors, the number of pole pairs p is often chosen to be 3 or 4, as it is possible to use a rotor with a larger diameter in a given frame. This is because the stator yoke can be made thinner, as the number of pole pairs increases. The limiting factor in choosing the number of the pole-pairs with PMSMs, is typically the leakage flux between two adjacent magnets. The increased rotor diameter can be seen in an increased output torque, and also on the amount of the copper, as a higher p leads to relatively shorter end windings. Consequently, the resistance and the mass of the motor slightly decrease. Although the same applies, in principle, also to the induction machines, increasing the pole-pair number introduces a problem, as the magnetizing inductance decreases according to Eq. (1.3). This can be explained by the fact that as the p increases, the share of the air gap reluctance from the entire flux path reluctance per pole increases, in other words, the air gap reluctance becomes more and more dominant with an increasing p. The power factor of the induction machines is therefore inversely proportional to the pole number squared

$$\cos(\varphi) \propto \frac{1}{(2p)^2} \quad . \tag{1.4}$$

With PMSMs, it is also possible to use higher flux densities than with IMs, as the slight saturation does not affect significantly on the machine characteristics. This is convenient, as the output torque of electrical machines is proportional to the air gap flux density squared. A PMSM with a

high air gap flux density also requires less stator current to produce the given torque, which means that there is a trade-off between the copper and the permanent magnet material. A lower stator current effectively decreases the stator copper losses, which are proportional to the current squared. This can have a significant effect on the thermal dimensioning of PMSMs, and could explain for instance why most commercial PMSM servos are fully closed with no integrated fan on the shaft. Induction servomotors are typically through-blown and thereby require a separate fan on the non-drive end. Using a high air gap flux density with induction machines to improve the performance introduces a problem, as the permeability of the iron decreases rapidly when the iron-core starts to pass into saturation. This increases the magneto-motive force, and can be seen in the decreased magnetizing inductance according to Eq. (1.3). An increased magnetizing current can be seen in increased copper losses, and also iron losses are increased, as they are proportional to the flux density squared.

These problems can be partially solved, if the flux of the induction motor is dynamically adjusted as a function of the loading torque. For example, in a load cycle shown in Fig. 1.4, a high air gap flux density is applied during the acceleration to provide the required overloading torque, and during the constant speed phase, the flux density is decreased to decrease the stator current and the losses of the machine. If the motor is dimensioned to operate at heavy saturation, decreasing the flux density back to the linear region of the *BH* curve can have a substantial effect on the magnetizing current. When driving the motor with a decreased flux, the torque decreases proportionally to the flux density squared. This significantly reduces the transient response of the motor for instance when a torque stroke occurs on the shaft. Too low a flux level could therefore cause the motor to stall if the load torque exceeds the pull-out torque. Basically, this means that it is necessary to know the instant at which the loading variation takes place, or in general, the load-cycle has to be known in order to utilize the dynamic flux control with induction motor. Dynamic flux control of an induction machine is studied in Chapter 3 in more detail. With a proper design, also the overloading capability of an induction motor can be increased close to the values of surface-magnet PMSMs. Since such a design inherently leads to good field weakening characteristics, an induction motor can be a respectable choice also in motion control applications. The focus of this thesis is to study the suitability and design aspects of the induction motor in motion control applications.

Table 1.3 lists the main benefits and drawbacks of the motor types discussed above.

Table 1.3. Features of various motor types in motion control applications

	Brushed DC motor	**BLDC motor**	**PMSM**	**IM**
Benefits	•Good controllability •Linear torque-current curve •Low torque ripple	•High power density and torque-to-inertia ratio •Good heat dissipation→good overloading capability	•Smooth torque possible •High efficiency •High torque/volume •High pull-out torque possible •Good heat dissipation→good overloading capability	•Excellent dynamics with proper control •High speed operation possible •Low price and simple construction •Durable •Several suppliers available
Drawbacks	•Low reliability •Requires maintenance •Low overloading capability •Low heat dissipation	•Expensive •Torque ripple •Danger of demagnetization of the magnets •Poor field weakening	•Expensive •Danger of demagnetization of the magnets •Poor field weakening	•Complicated control •Always lagging power factor •Low efficiency with lighter loads

1.3 Outline of the thesis

The main objective of this thesis is to study the suitability and the characteristics of an induction motor in dynamically demanding drives, often referred to as servo drives. Induction machine properties in dynamic applications are compared to permanent magnet synchronous machines. Typically, a surface magnet PMSM is selected instead of an IM because of its good overloading capability and higher torque-per-volume and torque-to-current ratio, which lead to a compact construction and a smaller inverter. The thesis addresses methods by which the dynamic performance of an induction motor can be improved with design and dimensioning aspects. Also the parasitic effects due to the performance optimization techniques, such as an increased torque ripple, a low efficiency, and a poor power factor are studied. Countermeasures to overcome these problems are introduced. It will be shown that with a proper design and an adequate flux level control strategy, the performance characteristics of an induction motor can be significantly enhanced. Analytical (Matlab/Simulink®) and numerical (Flux2D®) methods are applied in the theoretical analysis. The theoretical results are verified with a newly designed six-pole copper-cage induction motor in the laboratory.

The thesis is divided into five chapters. The theoretical background, the goals, and the motivation for this work are introduced in Chapter 1. In Chapter 2, the basic dimensioning of the PMSM and

the IM in high performance drives is given. Also a prototype motor used in the laboratory measurements is introduced in Chapter 2. In Chapter 3, design aspects of an induction motor that have to be adopted to improve its dynamic performance in order to be able to compete with the dynamic performance of the PMSMs are introduced. The most important are the leakage inductance minimization techniques, as the pull-out torque of an induction motor is inversely proportional to its leakages. Also a flux control strategy, which correctly balances the dynamic performance and running characteristics, is introduced in Chapter 3. Chapter 4 focuses on the dynamic thermal modelling of an induction motor with a coupled electromagnetic-thermal model. An analytical thermal network model for the induction motor is introduced. It is then connected to the analytical electromagnetic motor model of an IM. In such a way, the accuracy of the modelling can be improved, as the coupled model is thereby capable of correctly modelling the effects of the temperature rise on the motor's electric characteristics, such as the resistance variation due to temperature. Variations of the stator and rotor resistances affect the losses, the slip, and the pull-out torque of the motor, which are all taken into account in the model. The model is realized in Simulink™, and the results are verified in the laboratory with the prototype motor. Chapter 5 provides a summary of the work, and presents ideas for further investigation.

1.4 Scientific contribution

Different kinds of dynamically high-performance motion control applications where so-called servo drives are utilized are growing in popularity in the manufacturing industry. This thesis is related to the Motion Control project by ABB Drives, in which the focus was to carry out a comprehensive analysis regarding the electric motion control applications from both the drive and the motor point of view. Hence, being part of a larger project – divided into several parts, the focus of this text is on the motor of the electric servo systems. Other parts of this project deal with the control and the modelling of the frequency converter, and are therefore out of the scope of this thesis.

Experts in the field generally think that a servo motor has a low inertia and a high torque. There is, however, currently very little public information available on the exact design aspects of AC servomotors, and the vast majority of the research seems to focus on the control of servomotors, not on the motor itself; in projects that focus on the motor part of the servo systems, the motor is very often a PM machine, typically a PMSM. This thesis clarifies the main design principles of a servomotor and also some motor drive details. The scientific contributions of this thesis can be summarized as follows:

1. Differences in the dimensioning of an industrial motor and a servomotor were investigated and reported. The most important difference when comparing these two machines is the overloading capability.

2. Dimensioning aspects and performance characteristics of an induction motor and a permanent magnet synchronous motor in servo applications were studied and the analysis results reported.

3. Optimization possibilities in the induction motor design in order to improve its "servo characteristics", such as the overloading and the field weakening capability, were analyzed.

4. Dynamic flux-level control of a highly saturable induction motor was investigated to improve the operating characteristics and the thermal loadability of such a machine. A flux-level control strategy is suggested.

5. Computationally fast analytical model was developed to model the dynamic heat transfer of an induction machine. The model was implemented as a novel *coupled* electromagnetic-thermal model to increase the accuracy. The thermal model was also simplified in order to find a version that could be implemented in a servo drive embedded system. There was no significant difference between the two models, which favours the use of the simplified model during the design stage.

6. A prototype induction motor was designed and constructed, and was then used in the verification of the simulation tools. Comparison of the simulated and the measured results proved that the simulations tools were valid.

The first items in the above list focus on studying the dimensioning differences between a servomotor and an industrial motor. The main design principles of a servomotor are defined. There is no generally accepted public definition for a servomotor, and often the difference compared to a regular motor can be only an advertisement slogan. Therefore, the approach selected in this thesis was to find out the fundamental requirements for servo applications, and to study how the motor must be designed and dimensioned to meet these requirements.

The second part studies the dimensioning and the operating characteristics of an induction motor and a permanent magnet synchronous motor in these kinds of high-performance drives. Although the induction motor is very robust and cheap, it has a well-known theory, and it is by far the most common motor type used in the industry compared to the PMSM, it is yet far less often used in servo applications.

The third part studies the design aspects of the induction motor that must be adopted to improve its servo characteristics, such as the pull-out torque and the field weakening performance. Also dynamic flux-level control was investigated in order to improve the running characteristics of a highly saturable induction motor and to improve also the thermal loadability. The analysis was carried out mainly by using FEM as it correctly models the non-linear behaviour of the iron. The results were verified in the laboratory with a newly designed prototype induction motor.

Lastly, a computationally fast dynamic heat transfer model for the induction servomotor was developed, which can be used in the dimensioning of the servo drive system. Emphasis was particularly on the transient modelling, as the utilization of a motor overloading capability is used to obtain high acceleration and deceleration rates. In order to increase the accuracy, the model was implemented as a coupled electromagnetic-thermal model, where the effects of the heating on the motor parameters, such as on the resistances can be taken into account in the electromagnetic part of the model.

Comprehensive analysis and simulations were carried out by using both analytical and numerical tools. Simulations were verified in the laboratory with a commercial PMSM servo motor and a newly designed IM prototype.

2. SIZING AND PERFORMANCE OF AN IDUCTION MOTOR AND A PERMANENT MAGNET SYNCHRONOUS MOTOR IN SERVO DRIVES

The two most commonly used motor types in servo applications are the permanent magnet synchronous motor (PMSM) and the induction motor (IM). The purpose of this chapter is to provide information about the dimensioning and the performance of these two motor types in dynamically demanding servo applications. As it was stated in the first chapter, the focus is on the 1−100 kW power range. The goal is to study how the dimensioning of servomotors differs from industrial motor design, and further, to find out how the dimensioning of a high performance PMSM relates to the dimensioning of a comparable IM. According to Vas (1998), a servomotor should meet the following requirements

- High air gap flux density
- High power-to-weight ratio
- Large torque-to-inertia ratio
- Smooth torque operation (also at low speeds)
- Accurate torque control at zero speed
- High-speed operation
- High overloading torque
- High efficiency and high power factor
- Compact design

Nearly all the requirements seem to prefer a PMSM instead of an IM, with the exception of a requirement of the high-speed operation, which might be problematic due to limited field weakening capability of PMSMs. In somewhat older literature (for instance Vas 1998) when comparing a permanent magnet synchronous motor to an induction motor, it is often claimed that an induction motor can have a higher air gap flux density. This is a quite obsolete argument, because with modern high energy density magnets, air gap flux densities well beyond 1 T are possible, even without the flux concentration. Of course, the induction motor can be dimensioned to any desired flux density level, but in general, fundamental air gap flux densities beyond 0.9−1.0 T should be avoided to prevent the excessive saturation of the iron path. High flux densities will saturate the iron path of a PMSM as well, which will lead to an increased need for magneto-motive force (mmf) as the permeability of the iron decreases. Therefore more PM material must be used to supply the extra mmf, and this, in fact, seems to be the case with commercial PMSM servos. High dynamic performance is obtained by using high flux densities, and the increased need for mmf is covered simply by substantially increasing the amount of the PM material. The tangential stress $\sigma_{\tan}$ that produces the torque in cylindrical electric machines is proportional to the product of the stator linear current density A_s and the air gap flux density B_δ

$$\sigma_{\tan} \cong A_s B_\delta \quad . \tag{2.1}$$

With modern NdFeB –permanent magnets, air gap flux densities B_δ up to 1 T and even beyond are possible. Such values together with high linear current densities lead to high tangential stresses and thus to a high torque density. In principle, the required copper mass in PMSM is lower than in IM because of the magnetization, and inversely, with equal amount of copper, a PMSM produces more torque. High air gap flux density (in PMSM) also results in lower stator copper losses and lower inverter current rating, although the stator iron losses are increased approx. proportionally to

the flux density squared (Deng 1999). Further, the losses generated in the stator iron are easier to dissipate than those generated in the windings, as there is (thermally) a highly resistive path from the winding to the ambient through different kinds of insulations and material boundary sections. Lower losses, of course, mean that more torque is available from a given frame size. With rotor surface magnets, the overloading capability of the motor is inherently high (typically over 4 p.u.), and also the minimization techniques of the cogging torque are well-known (different cogging torque minimization techniques were shortly introduced in Chapter 1). However, with a surface magnet construction, especially the high-speed operation might be problematic due to poor field weakening performance. Also the mechanical construction of the PMSM rotor with surface magnets is less robust than with an IM. If considerable torque is to be produced at both low and high speeds, usually the induction motor is a better solution, and can lead to a significantly smaller motor physical size. This is because of the good field weakening characteristics of an induction motor. The IM field weakening will be studied in Chapter 3 in more detail. The sizing and the performance of these two motor types are studied in this chapter with two case examples. The PMSM studied is an ABB 8C series six-pole servomotor with surface magnets on the rotor. Characteristics and main dimensions of the motor are shown in Table 2.1.

Table 2.1. Main dimensions and motor parameters of the PMSM used in the study

Dimension	**Value**	**Name-plate values**	**Value**
Stator outer diameter	136.0 mm	Rated voltage	330 V
Stator inner diameter	80.0 mm	Rated current	8.7 A
Rotor outer diameter	79.0 mm	Rated frequency	125 Hz
Rotor inner diameter	58.0 mm	Number of pole-pairs	3
Stack length	153.0 mm	Rated torque	15 Nm
Stator slots	36	Insulation class	F
Magnet thickness in the middle	8.0 mm		
Magnet thickness on the edge	5.0 mm		
Stator yoke thickness	8.5 mm		
Rotor yoke thickness (d-axis)	3.5 mm		
Rotor yoke thickness (q-axis)	11.5 mm		
Magnet width	150 °(electric)		

The induction motor was realized by removing the PM rotor and designing and constructing a copper-cage rotor for this existing stator. Clearly, an induction motor constructed into an existing frame of a PMSM cannot compete against the original PMSM, and the goal of this work is not to compare these two exact machines against each others, either. The goal is to provide general information how these two machine types are dimensioned in such high performance applications, and how the sizing differs from that of industrial machines. Motors are thereby mainly used to verify the simulation tools, which are then used for analysis in Chapters 3 and 4.

The frequency converter used in the laboratory tests was ABB's ACS800 with PMSM and IM software. As the PMSMs are by far the fastest growing group in different kinds of motion control applications, the basic dimensioning of a PMSM servo is first introduced. It is also studied how it differs from an industrial PMSM. Then, the characteristics and the dimensioning of an induction motor are studied more closely to evaluate the suitability, the characteristics, and pros and cons of an IM in servo drives.

2.1 Dimensioning of a high performance PMSM

Industrial permanent magnet synchronous motors may have a low pull-out torque, typically well below 2 p.u.. This is because very often industrial PMSMs have buried magnets in the rotor, for example in V-shape, and buried magnets usually result in higher direct-axis inductance and thus in a low pull-out torque. The buried magnet construction is, however, mechanically favourable, since simple rectangular magnets can be used. The buried magnets are also well protected electro-magnetically, chemically, and mechanically. The protection during possible short-circuits is good, as the surrounding iron guides the flux to pass the magnets, so that the magnetic field strength may not exceed the demagnetizing value. Also rotor pole surfaces can be easily manufactured to shapes that result in a sinusoidal air gap flux density distribution. With an adequate design the torque ripple of the machine is also minimized. Surface-magnet constructions are also used especially in low-speed industrial PM machines, as the gluing of the magnets is then adequate for attaching the magnets due to low rotor peripheral speed. The drawback in a surface magnet construction is that curved magnets are required to obtain a smooth air gap. With surface magnets, the armature reaction is small, and problems might arise if the field weakening is to be utilized. With industrial motors, however, this is rarely the case. Because of the relatively high price of the rare-earth magnets, the amount of the PM material is always both a technological and economical compromise, which often leads to thin magnets. For example, in an industrial PMSM with embedded magnets studied by Heikkilä (2002) (45 kW, 600 rpm), the thickness of the magnets was only 6 mm, although the machine had a 716 Nm rated torque and the air gap diameter of 250 mm. With surface magnets mounted on the rotor, the consumption of the PM material is less than with embedded magnets; first of all, because the leakage flux of the magnets is lower as there is no ferromagnetic path for the flux enclosure at the edges of the magnet. And secondly, reduced quadrature magnetizing inductance decreases the armature reaction, which leads to a decreased pole angle and an increased torque. The problem with surface magnets is, especially in difficult environments, that the IP class of the motor should be high, for the small ferromagnetic particles (for instance iron dust) and the moisture not to enter the rotor. When the NdFeB -magnets are exposed to hydrogen (water), the phenomenon called white corrosion occurs, and the PM material turns to white powder and looses its properties (Kurronen 2003). Although magnets are practically always either coated or phosphated for this reason, the moisture should be kept outside the machine. In addition to good thermal characteristics of a PMSM, this is probably the second reason why PMSM servos are usually fully closed constructions (IP 54 or higher).

High performance of a PMSM can be obtained by using a large amount of PM material on the rotor. On the rotor of the ABB servomotor used in the study, the thickness of the magnets (8 mm) was approx. 20 % of the rotor radius. Compared to Heikkilä's motor, the relative magnet thickness (ratio of the magnet width to the rotor radius) is 3.5-fold. Most industrial motors operate in continuous cycles, where neither the overloading capability nor the fast torque response is essential. Instead, more important design aspects are for example low manufacturing costs. As the price of the NdFeB magnets in particular is relatively high, it is practical to use less PM material in industrial machines. As the thickness of the magnets decreases, the magneto-motive force (mmf) of the magnets Θ_{PM} decreases also

$$\Theta_{\mathrm{PM}} = H_{\mathrm{c}} l_{\mathrm{PM}} \quad , \tag{2.2}$$

where H_{c} is the magnet coercive field strength and l_{PM} the magnet thickness. Typically, the thickness of the magnets is large compared to the length of the physical air gap, and thus the total

reluctance of the flux path is chiefly caused by the magnets. The air gap magnetic flux Φ_δ created by the magnets can be expressed as

$$\Phi_\delta = \frac{\Theta_{\mathrm{PM}}}{R_{\mathrm{PM}} + R_\delta + R_{\mathrm{Fe}}} = \frac{H_{\mathrm{c}} l_{\mathrm{PM}}}{\frac{l_{\mathrm{PM}}}{\mu_{\mathrm{r,PM}} \mu_0 L' w_{\mathrm{PM}}} + R_\delta + R_{\mathrm{Fe}}} \quad , \tag{2.3}$$

where R_{PM} is the reluctance of the magnet, R_δ the air gap reluctance, R_{Fe} the iron reluctance, $\mu_{\mathrm{r,PM}}$ the magnet relative permeability, μ_0 the vacuum permeability, and w_{PM} the magnet width. Air gap reluctance between the magnets and the stator can be calculated from

$$R_\delta = \frac{\delta_{\mathrm{eff}}}{\mu_0 L \tau_{\mathrm{p}}} \quad , \tag{2.4}$$

where δ_{eff} is the effective air gap length (excluding the magnets) and τ_{p} the pole-pitch. However, because the magnet width is always less than the pole-pitch, the air gap reluctance between the stator and the magnets in such a case is somewhat higher than the value given by Eq. (2.4). The reluctance of the iron R_{Fe} is usually very small compared to that of the air gap or the magnets, unless the flux path heavily saturates. As the reluctance of the magnets decreases with the thickness, the air gap flux – and consequently the air gap flux density – will decrease only slightly, because the iron path and air gap reluctances remain approximately constant. However, there is a knee-point, after which the flux density collapses, if the thickness of the magnets is further decreased. This is illustrated in Fig. 2.1. The air gap flux density B_δ can be calculated

$$B_\delta = \frac{\Phi_\delta}{\alpha L \tau_{\mathrm{p}}} \quad , \tag{2.5}$$

where the coefficient α is the arithmetic average of the flux density distribution in one pole area and L the stack length. For a surface magnet machine with a constant air gap length, the coefficient can be assumed to be the ratio of the width of the magnets to the pole-pitch. With embedded magnets and sinusoidal air gap flux distribution, it can be approximated to be $2/\pi$ for an unsaturated machine. Figure 2.1 shows how the air gap flux density of ABB PMSM servo behaves as a function of the magnet thickness at four different effective air gap lengths, based on the analytical equations shown above. Since the exact PM material of the motor was not known, the values of Neorem 495a NdFeB magnets were used in the calculation. The coercive field strength of this material is 830 kA/m, and the relative permeability 1.1. The physical air gap length of the motor was 0.5 mm, and the thickness of the fibre-glass band was approximately 0.3 mm. Effective air gap excluding the magnet thickness can thus be estimated to be near 1.0 mm. Air gap reluctance used in Fig. 2.1 was calculated by using Eq. (2.4), and therefore the flux density values can be slightly lower in reality.

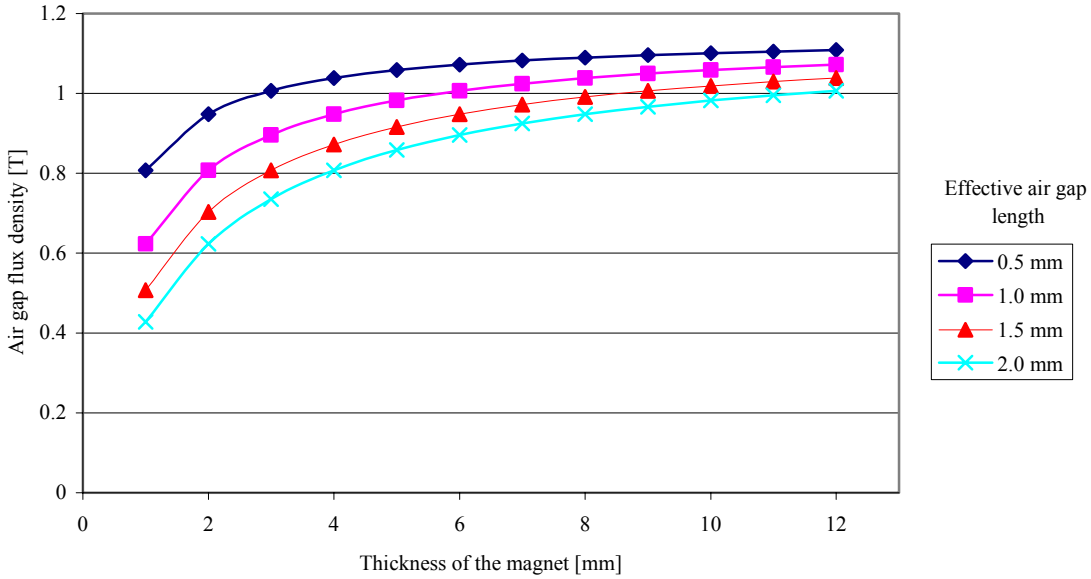

Figure 2.1. Effect of the magnet thickness on the air gap flux density at different effective air gap lengths (excluding the magnet thickness). The PMSM used in the study had 8 mm thick magnets. The effect of the magnet thickness is relatively small on the flux density, with the exception of the smallest values of magnet thicknesses. Values are analytically calculated with the above presented equations.

According to simulations with FEM, the PMSM fundamental wave air gap flux density was 0.99 T, which is approx. 0.05 T less than with analytical calculations. Part of the mmf, however, goes for harmonic flux densities, and also because the PM material used in the motor was unknown, the coercive field strength can be somewhat less than with Neorem 495a magnets. Basically, the thickness of the magnets could be reduced (from 8 mm) near the knee-point in Fig. 2.1 (to approx. 4 mm), without significantly decreasing the air gap flux density of the motor. For example, cutting the thickness of the magnets from 10 mm to 5 mm decreases the air gap flux density only by 0.1 T. To compensate this, only approx. a 10 % higher stator current is required to produce the same torque. This explains why industrial motors usually have a minimum amount of the magnetic material in the rotor; equal torque production capability can be obtained by slightly increasing the amount of the copper and the current rating of the machine. As a consequence of the decreased PM material amount the back-EMF E_{PM} will slightly decrease

$$E_{\mathrm{PM}} = \frac{\xi_1 N \omega_s \Phi_\delta}{\sqrt{2}} \quad , \tag{2.6}$$

where ξ_1 is the fundamental winding factor, N the number of turns and ω_s the electrical angular frequency. Although the air gap flux density and the back-EMF are affected only slightly, decreasing the magnet thickness has a substantial effect on the direct-axis magnetizing inductance L_{md}

$$L_{\mathrm{md}} = \frac{m}{2}\frac{4}{\pi}\alpha\mu_0 \frac{1}{2p}\frac{\tau_{\mathrm{p}}}{\left(\delta_{\mathrm{eff}} + l_{\mathrm{PM}}\right)} L'\left(\xi_1 N\right)^2 \quad , \tag{2.7}$$

Where m is the phase number, α is the arithmetic average of the flux density distribution in one pole area, τ_p the pole-pitch, δ_{eff} the effective air gap length (excluding the magnets), L' the stack electromagnetic length, ξ_1 the fundamental winding factor, and N the number of series connected wires. The inductances thus behave in an (inversely) similar manner to the air gap flux density as a function of the magnet thickness (illustrated in Fig. 2.3). The effective air gap δ_{eff} in Eq. (2.7) includes the increase in the air gap length due to the slotting and the saturation of the iron. The effect of the slotting can be taken into account by multiplying the physical air gap δ with the Carter's coefficient k_C

$$\delta' = k_C \delta \quad , \tag{2.8}$$

where δ' is the average electric air gap length. Air gap is further electromagnetically increased due to the saturation of the iron, and the effective air gap δ_{eff} includes both of these phenomena. The electromagnetic torque of a permanent magnet synchronous motor can be expressed using the phase back-EMF induced by the magnets E_{PM}, the stator phase voltage U_s, and the d- and q-axis inductances

$$T_{em} = \frac{m}{2\pi n_s}\left[\frac{E_{PM}U_s}{\omega_s L_d}\sin(\delta_a) + \frac{U_s^2}{2}\left(\frac{1}{\omega L_q} - \frac{1}{\omega L_d}\right)\sin(2\delta_a)\right] \quad , \tag{2.9}$$

where n_s is the synchronous speed, L_q the q-axis synchronous inductance, L_d the d-axis one, and δ_a is the load angle measured between the phasors E_{PM} and U_s. The direct-axis synchronous inductance L_d is a sum of the d-axis magnetizing inductance and a stator leakage inductance

$$L_d = L_{md} + L_{s\sigma} \quad . \tag{2.10}$$

The first part in Eq. (2.9) is the fundamental torque, and the second part represents the reluctance torque due to saliency. PMSMs often exhibit the so-called inverse saliency, which means that the inductance in q-direction is higher than in d-direction. As a result, the load angle during the rated operation increases, and also the pull-out torque is obtained at a power angle greater than 90°. The effect of the saliency ratio for the torque production of the motor is shown in Fig. 2.2 for the PMSM used in this study (the motor parameters are presented in Table 2.1).

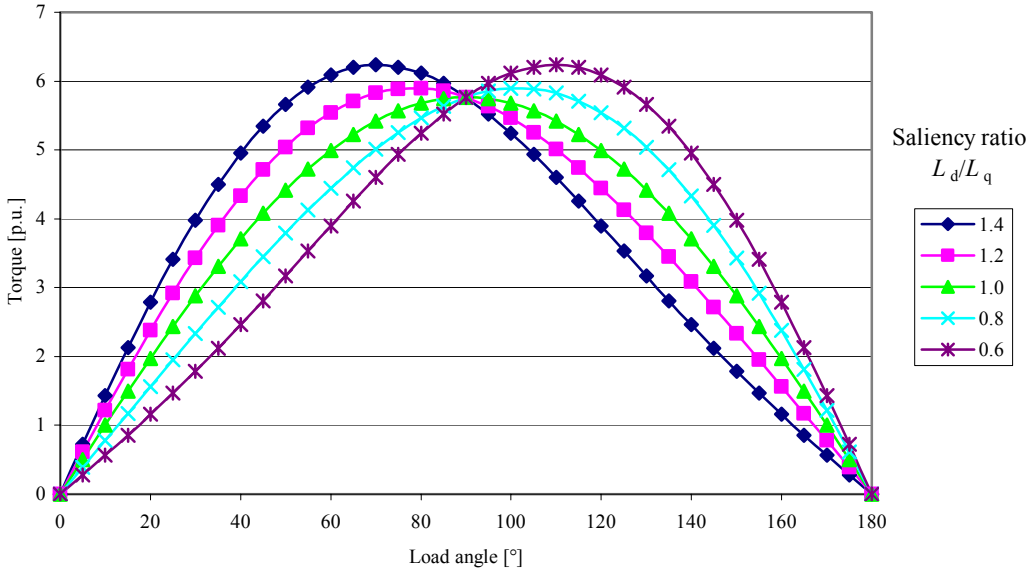

Figure 2.2. Torques of a PMSM with L_d = 0.16 p.u, E_{PM} = 0.91 p.u., and U_s = 1.0 p.u. as a function of the load angle at different saliency ratios. According to measurements made at LUT, the L_d/L_q –ratio for commercial servomotors is typically 0.8-0.9.

When the thickness of the magnets decreases, also the back-EMF decreases (Eq. 2.6), while the direct-axis inductance increases (Eq. 2.7). This causes the torque production capability of the PMSM to decrease, which means that the pull-out torque decreases, and the rated torque is obtained at a higher load angle. A higher load angle degrades the torque stiffness of the motor, which in practice means that the dynamic stability reduces. In some PMSM servomotors, there is a steel cage similar to squirrel-cage machines in the rotor to mechanically strengthen the rotor, but it also acts as damper winding, and could therefore improve the dynamic response of the machine during transients (it also enables the direct grid-connection of such a motor if necessary). In Fig. 2.3, the pull-out torques ($L_d = L_q$) and d-axis synchronous inductances (Eq. 2.7) are plotted as a function of the magnet thickness for four different air gaps calculated analytically.

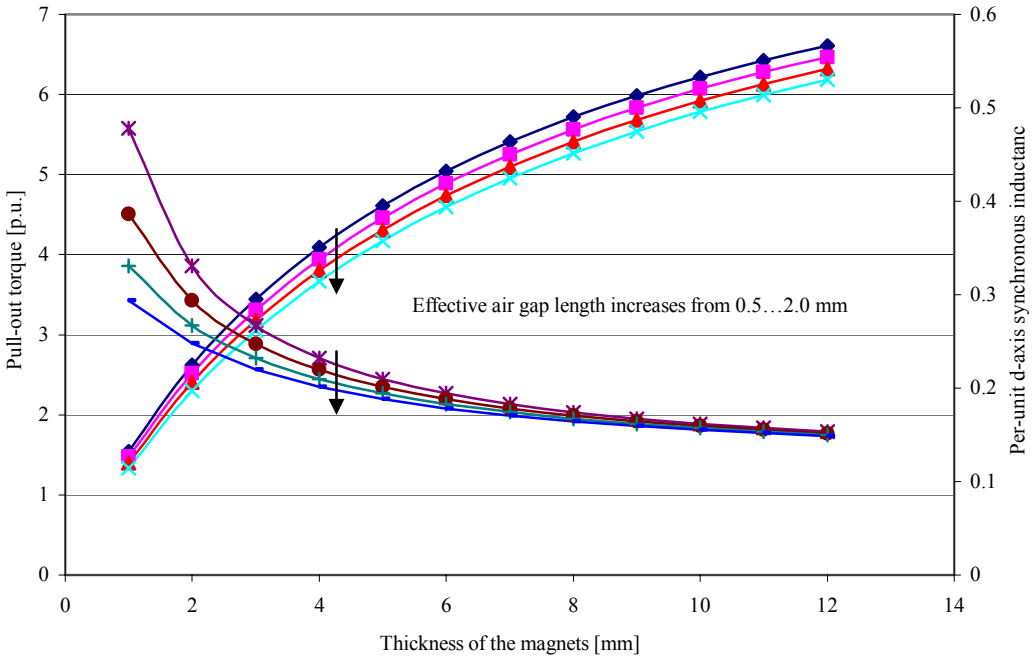

Figure 2.3. Pull-out torques (increasing monotonously with magnet thickness) and d-axis inductances (decreasing monotonously with magnet thickness) as a function of the magnet thickness of the PMSM used in the study, at four different air gap sizes (U_N and I_N are assumed constants).

It must be borne in mind that the low values of the per-unit inductances in Fig. 2.3 are also, to a large degree, caused by the voltage and the current ratings of the motor. Because of the high air gap flux density, a low number of stator winding turns in series are needed, and the current density is consequently low. The inductance base value is defined as

$$L_{\text{base}} = \frac{U_N}{\sqrt{2}\omega_s I_N} \quad . \tag{2.11}$$

As the stator voltage of a machine with a high air gap flux density is high, and the current low, the inductance base-value becomes high, resulting thus in low direct-axis inductance per-unit values.

By using thick rare-earth magnets on the rotor surface, a high air gap flux density, low inductances, and consequently a high torque can be obtained. As the thickness of the magnets increases, the direct-axis synchronous inductance rapidly decreases, approaching asymptotically the value of the stator leakage inductance. A low value of L_d will provide a high pull-out torque in addition to a low value of the load angle during rated operation, both being fundamental requirements for a high dynamic performance. As the thickness of the magnets is increased, the effect of the leakage term in the synchronous inductance becomes more dominating as the magnetizing inductance term decreases. This emphasizes the leakage minimization design aspects with such PMSMs with thick magnets. With embedded magnet machines, the leakage term can be typically 10−20 % of the value of a synchronous inductance, while with the PMSM used in this study, the ratio is approx. 65 %. Further, the thicker the magnets, the smaller is the effect of the physical air gap on the motor characteristics, which favours the possibility to increase the air gap length in certain applications for mechanical reasons. Inversely, with industrial PMSMs with significantly thinner magnets, the effect of the air gap is much more dominating, and should be

kept as small as possible. By increasing the length of the air gap, and not the magnets, the d-axis inductance can be decreased, but clearly the torque production capability would deteriorate, as more and more mmf in the air gap is required.

The flowchart in Fig. 2.4 summarizes the various interactions when optimizing the dynamic performance of a PMSM. A similar chart for an induction motor is presented at the end of Chapter 3, as its focus is on the optimization of the induction motor dynamic performance.

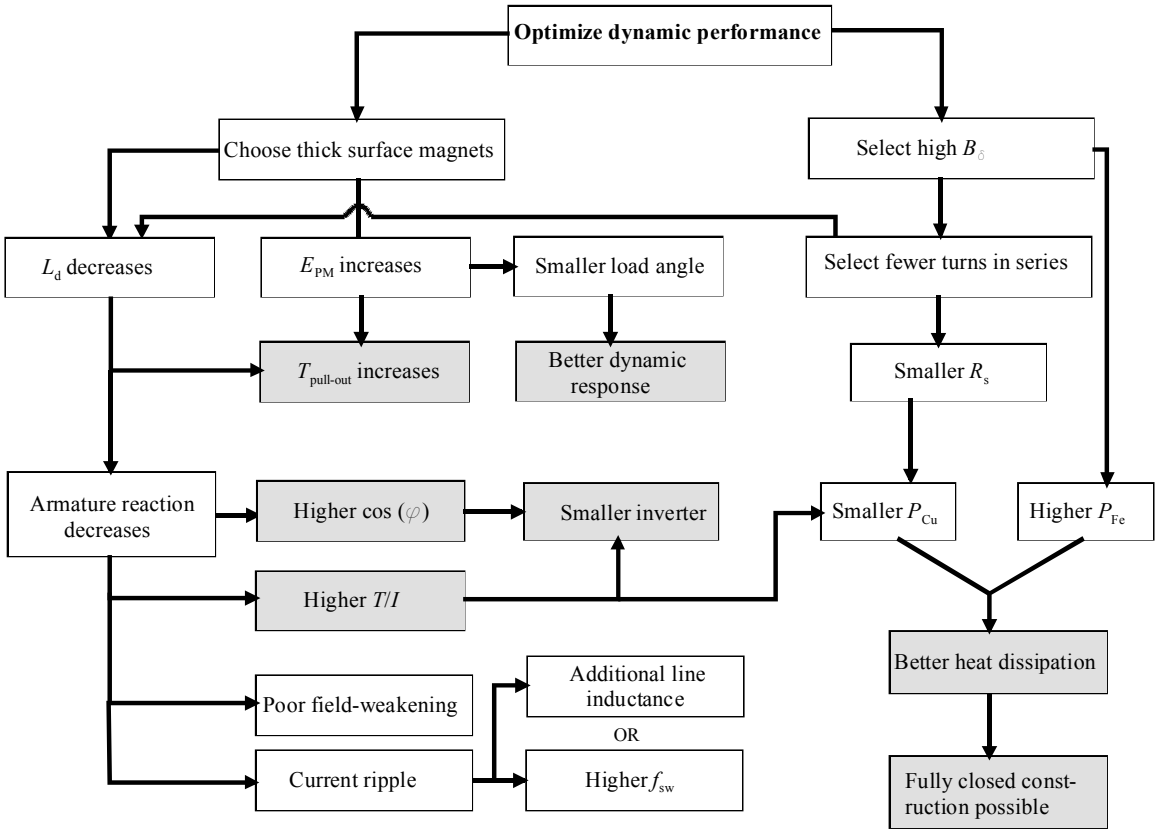

Figure 2.4. Different interactions in the optimization process of a permanent magnet synchronous motor.

2.2 Motors used in the study

The original motor used in the study was ABB's 8C-series six-pole PMSM (DSM-2-24-20k.9b-130), which has surface-magnets on the rotor, attached with a surrounding glass-fibre band. The magnets are slightly chamfered on the edges to provide a more sinusoidal air gap flux density distribution, in order to obtain a low cogging torque. Also, according to Slemon (1994) chamfering of the magnet edges decreases the stator iron losses, as nearly rectangular PM flux distribution would cause higher losses at the magnet edges. There are large axial holes in the rotor to reduce the inertia and also to enhance the cooling of the rotor. Although there is a DC field in the rotor, air gap flux harmonics are present because of the inverter supply. The slotting and the discrete distribution of the stator winding cause their own harmonic components in the air gap. Harmonic flux components penetrate also the iron beneath the magnets due to the relatively high skin depth of NdFeB magnets, defined as

$$\delta = \sqrt{\frac{2}{\omega\mu\sigma}} \quad , \tag{2.12}$$

where ω is the angular frequency, μ the permeability and σ the conductivity of the material. The skin depth is for example with NdFeB magnets as high as 20 mm at the frequency of 1000 Hz, because of the low permeability ($\mu_r \approx 1.05-1.2$) and fairly low resistivity ($\rho \approx 1.5$ μΩm). This causes the harmonic flux components to penetrate through the magnets to the rotor core. Heating takes also place in the rotor core (even though made of laminations), which has poor heat dissipation outwards due to the magnet-retaining glass-fibre band. The large rotor core holes can therefore effectively increase the heat transfer from the rotor to the end caps and further to the ambient.

As one of the main goals of this thesis is to study the suitability of an induction motor in servo applications, a prototype motor was designed, constructed, and used for studying the phenomena related for instance to magnetic saturation, heat transfer, and flux control, etc. of a real motor. The goal of the design was not to build an ultimate induction servomotor, but rather to verify the different simulation tools used in this study, both analytical and numerical. A copper-cage rotor was then designed for the existing frame of the PMSM servo. Copper was used in the rotor cage material to obtain a low slip, and consequently, low rotor ohmic losses. The stator had 36 slots, and the rotor slot number was chosen to be 30. The leakage inductance of the rotor was minimized by using rectangular, 3-mm-wide and 10-mm-deep fully open slots (the dimensioning of the prototype is discussed in Chapter 3 in more detail). Figure 2.5 shows the original PM rotor, and the newly designed copper-cage rotor.

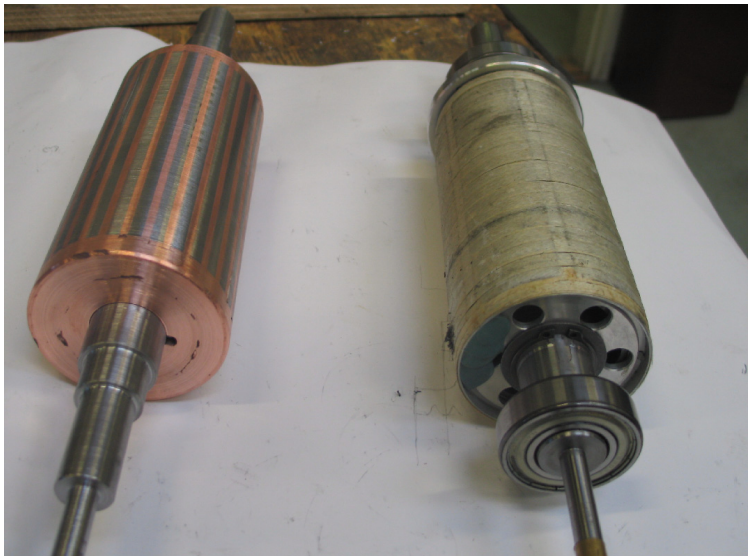

Figure 2.5. The rotors of the two motor types used in this study. On the left, there is the newly designed copper-cage rotor, and on the right the original PM rotor. The PM rotor is surrounded by a fibre-glass band to provide large enough mechanical strength.

Figure 2.6 shows the cross-sectional geometries and the magnetic field distributions at the rated point for both of these motors. In the PM rotor, the rotor yoke is very thin (especially on the d-

axis), and there are large segments of air beneath the yoke. The cage-rotor has rectangular, open slots in the rotor, which minimize the leakage inductance of the rotor.

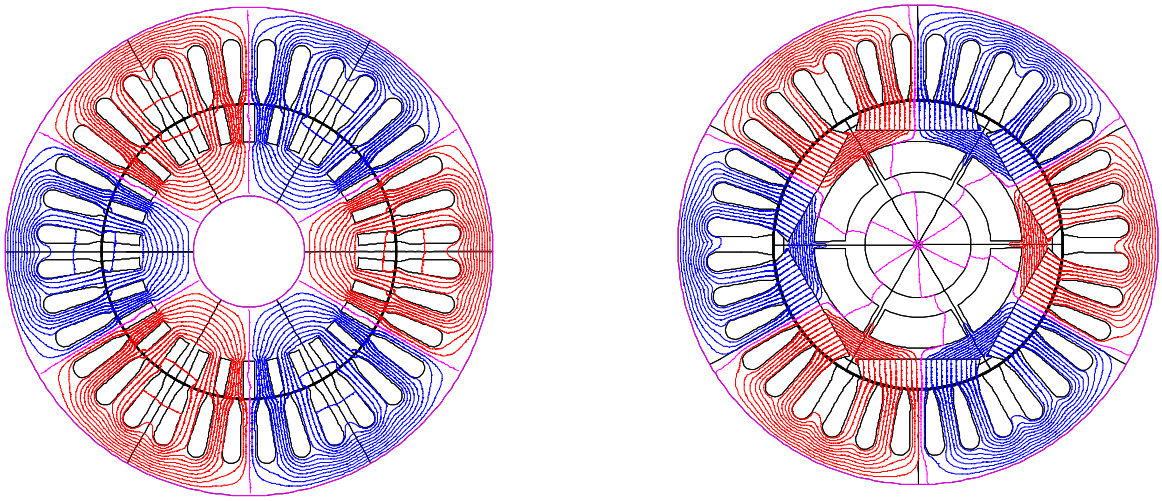

a) b)

Figure 2.6. Cross-sectional geometries and magnetic field distributions at the rated points of the two motors. a) The induction motor and b) the permanent magnet synchronous motor. Beneath the PMSM yoke there are thick segments of air, and beneath those, there is again a ring of electrical steel between the air and the shaft. The inner yoke is for manufacturing reasons only.

Figure 2.6 illustrates the actual thickness of the magnets compared to the physical size of the motor. The thickness of the magnets is approx. 8 mm, which is significantly higher than in the case of an industrial motor of equal size. Also we can see that the rotor inertia is far lower with the PMSM because of the large holes in the core. The only possibility to reduce the inertia of the cage rotor would be to remove some steel near the shaft, which would have only a slight effect on the inertia. The density of the NdFeB magnets ($\rho \approx 7400$ kg/m^3) is approx. 5 % lower than the density of steel ($\rho \approx 7800$ kg/m^3), while the density of copper ($\rho \approx 8960$ kg/m^3) is approx. 15 % higher. With aluminium bars in the rotor, the situation would be more even, although the slip would consequently increase due to higher rotor resistance. Figure 2.7 shows the air gap flux density distributions for these two motors over 360° mechanical degrees.

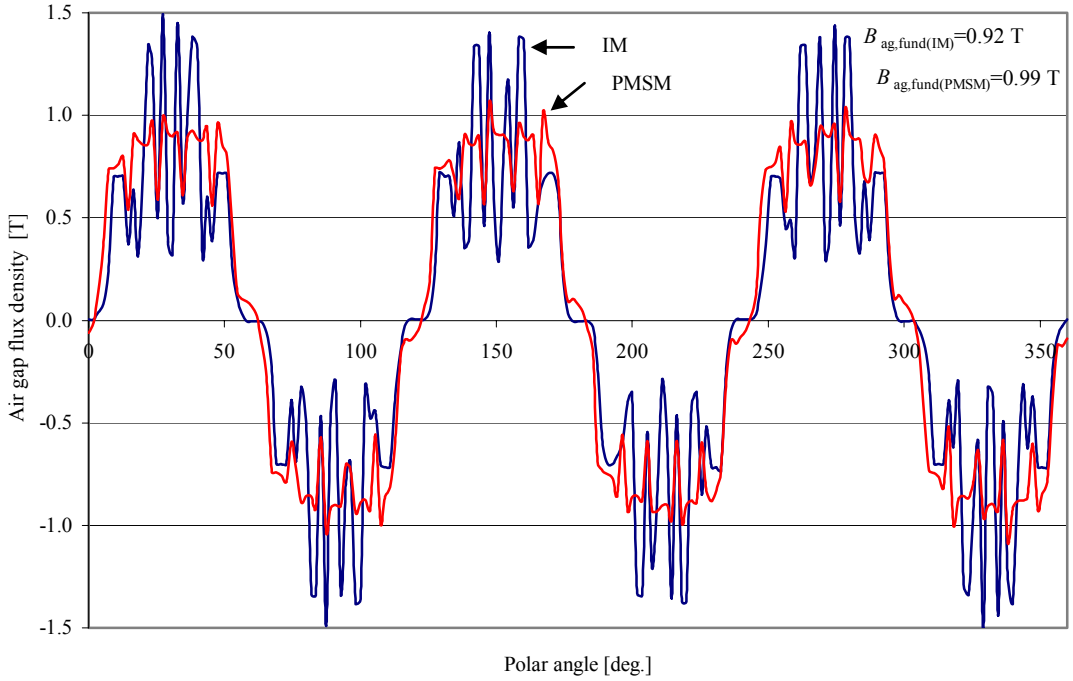

Figure 2.7. Air gap flux density distributions for the two motors calculated with FEM. The air gap flux density fundamental is approx. 1 T for the PMSM and 0.92 T for the IM. The lower value for the induction motor is caused mainly by the higher harmonic content due to fully open slots of the cage rotor.

As it can be seen in Fig. 2.7, the flux densities for the machines are near 1 T, which means that ferromagnetic parts of the motor are operated in partial saturation. Although the increased need for the mmf due to the saturation can be produced with the PMSM by adding more PM material, it has to be provided from the supply with the induction motor. This substantially deteriorates the characteristics of an IM, and the flux density should be lowered or the dimensions of the motor increased. Consequently, this would result in a poorer torque response or a lower torque density. With full flux applied to IM, the stator current was nearly doubled compared to the current of the PMSM at the rated torque, and consequently, the power factor remained below 0.5 (which is only partially explained by the fact that the motor is a six-pole motor). The stator copper losses were large, and the torque-to-current ratio was poor. PMSM servomotors are often six- or eight-pole machines, because with a high amount of poles, a narrower stator yoke is required, and hence with a given frame size, the diameter of the rotor can be increased to produce more torque. Induction servomotors are usually four-pole machines to maintain an adequate power factor.

Table 2.2 shows the characteristics of the two motors. The values for the induction motor are expressed at three operating points. The first column for the induction motor, “PMSM flux”, shows the values at the rated flux of the original PMSM, which is clearly too high for the induction motor. The values in the second column “Optimized flux” are expressed for the rated 15 Nm torque, but lowering the flux level to the point where the current has a minimum value. The third column “Thermal rated” represents the true rated values for the induction motor, which occurs when the stator current has the same value as the original PMSM. It can be seen that if the torque is de-rated by 60 %, and the air gap flux decreased by 50 %, equal current density in the stator will occur, and the motor can be estimated to operate with this torque continuously.

Although there are losses in the rotor with the induction motor, the stator iron losses have decreased by 75 % due to a 50 % smaller flux level. Characteristics of the prototype induction motor are shown in appendix A in more detail.

Table 2.2. Rated values and motor parameters of the two motors. Values for the induction motor are shown at three different operating points. The last column represents the "true" rated values for the induction motor with equal cooling.

	Unit	**PMSM**	**IM**		
			PMSM flux level	**Optimized flux**	**Thermal rated**
Number of pole-pairs		3	3	3	3
Rated torque	[Nm]	15	15	15	6.5
Synchronous frequency	[Hz]	125	125	125	125
Stator voltage	[V]	330	330	248	169
Stator current at rated load	[A]	8.7	17.8	14.2	8.8
Stator resistance (@T=20°C)	[Ω]	0.53	0.53	0.53	0.53
Stator leakage inductance	[mH]	2.5	2.5	2.5	2.5
Magnetizing inductance	[mH]	2.5	16.2	18.2	19.1
Rotor leakage inductance	[mH]	N.A.	1.5	1.5	1.5
Air gap flux density (U_N, f_N)	[T]	0.99	0.92	.70	.51
Power factor		.95	.45	.73	.72
Electrical efficiency	[%]	92.3	84.3	85.5	87.3
Slip	[%]	-	1.7	3.0	2.4*
Power	[kW]	3.93	3.86	3.81	1.66
T_{max}/T_N at nominal flux	[p.u.]	5.4	4.4	2.5.	2.8*

*Refferred to 6.5 Nm

Table 2.2 shows how the induction motor torque should be heavily de-rated not to exceed the thermal limits because of the significantly lower efficiency, or inversely, forced cooling should be arranged to achieve the same torque as from the PMSM. Even if the flux of the induction motor is optimized, the current is still 5.5 A higher, which in this case means approx. 2.7-fold copper losses (stator iron losses have decreased approx. by a factor of 0.5). As there are also copper losses in the rotor of the induction motor, it is clear that the heat dissipation must be improved with additional cooling device. During the measurements, pressurized air was used for cooling for the prototype IM, which seemed to be suffice. Commercial induction servomotors are very often equipped with a separate fan mounted on the non-drive end, while PMSM servomotors are usually cooled only by natural convection and are often fully closed. Therefore, a difference in the physical size between an IM and PMSM with equal power might not necessarily be significant. A drawback in using an external fan is the increased motor length; furthermore, also some additional power supply will be required. Chapter 3 discusses how the characteristics of such a highly saturable motor can be improved by adjusting the flux level. Later in this chapter, it is studied how well a four-pole induction machine could compete with the original six-pole PMSM.

2.3 Characteristics and the suitability of an induction motor and a permanent magnet synchronous motor for servo applications

In servo applications, a large speed and torque variation of the motor are required. Almost zero speed is required at the end of the deceleration phase, when the motor is crawling to the desired position. During a positioning sequence in the constant speed phase, the speed should be as high as possible with regard to the mechanical boundary conditions to minimize the cycle times. Depending on the application, the utilization of the motor field weakening capability might also be required. Correspondingly, only a fraction of the rated torque is required during the constant speed running typically only to overcome the system friction. And during the acceleration and the deceleration phases, a high overloading torque is applied. Due to the different implementations of the magnetization of these two motor types, the torque-speed characteristics differ notably from each other. Due to the surface magnets in the PMSM, the high overloading capability results, and the torque production capability of the motor depend only slightly on the speed and on the degree of the load, while the drawback is the extremely limited field weakening range. By optimizing the design procedure of an induction motor, high overloading capability and consequently good field weakening characteristics can be obtained. A drawback of an IM is the highly non-linear behaviour of the torque production capability as a function of the load level.

When a high dynamic performance is required, it is practical to use as high an air gap flux density as possible, within the boundary conditions. A high air gap flux density will decrease the load angle with the PMSM, and decrease the slip with the IM. This will improve the dynamic response and the stability of the motor during fast loading transients. For the induction motor, a low slip also decreases the rotor losses. The drawback in using high flux densities is that the permeability of ferromagnetic materials is non-linearly inversely proportional to the flux density. This means that the magnetizing inductance will start to decrease due to saturation, if the flux density is increased. In an induction machine, a large magnetizing inductance is a benefit. With PMSMs, a small magnetizing inductance is beneficial; it is reached by using thick high energy-density magnets. Figure 2.8 shows the flux density distribution in one pole area of the PMSM; we can see that the flux densities in the iron are higher than with standard industrial machines. In particular, the rotor flux density in the quadrature direction is approximately 2.0 T, which will saturate the iron and decrease the q-axis inductance.

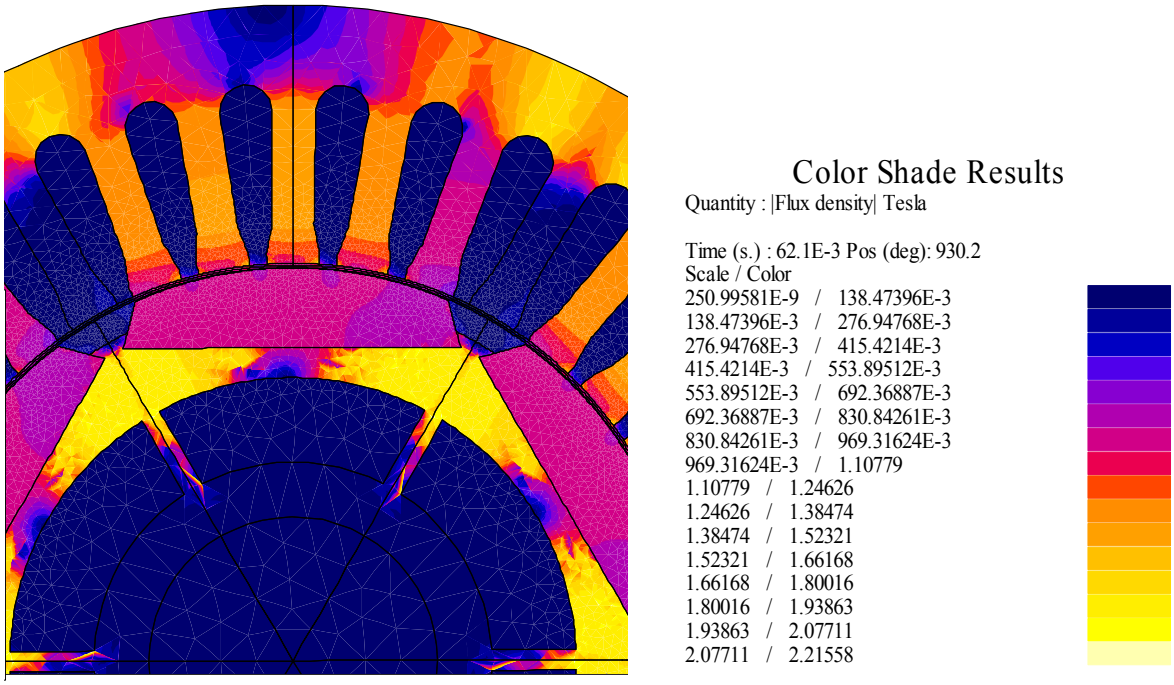

Figure 2.8. Flux density distribution of the ABB 8C PMSM servomotor in one pole area calculated with FEM in 2D. The iron path of the motor is dimensioned to operate in a high degree of saturation, which is compensated by increasing the permanent magnet material amount. The magnets are chamfered on the edges to provide more sinusoidal air gap flux density distribution. The remanence flux density of the magnets is approximated to be 1.1 T in the calculations.

Figure 2.8 shows how the iron path of the motor is heavily saturated, as the saturation flux density with conventional electrical steels varies between 1.6−1.8 T. Particularly the rotor core iron in the quadrature-axis area is heavily saturated, as the flux densities are approx. 2.0 T. This decreases the q-axis inductance, and consequently the q-axis armature reaction. Figure 2.8 shows that although the d-axis is not saturated, the rotor yoke in that direction is very narrow, and as the relative permeability of the thick magnets is close to unity, the synchronous inductance in the d-direction becomes lower than in the q-direction. According to the measurements made at LUT, the inductance values in the d –direction are typically 10−20 % lower than in the q-direction. Measurements were carried out for 8 commercial PM servomotors in the power range of 3−5 kW. There was not a single motor, in which the d-axis inductance would have been higher than the q-axis one.

2.3.1 Operating characteristics of the motors as a function of load and speed

Compared to the induction machine, the characteristics of the PMSM depend far less on the load level, and the stator current is (nearly) a linear function of torque. An induction motor, however, is highly non-linear due to the magnetization from the stator, which significantly decreases the characteristics of the motor to deteriorate as the torque decreases. Basically the power factor and the torque-to-current ratio of an induction motor approach zero with the torque, if the losses are neglected. A further advantage of the PMSM is that by controlling the (negative) d-axis current, the power factor and the torque-to-current ratio can be easily optimized if necessary. The rated power factor of the surface magnet PMSMs is typically well beyond 0.9, and can be set to unity by

increasing the negative d-axis current. The power factor is also sensitive to the voltage level since the armature reaction of the machine is very low. When driving a low inductance PMSM, it is important to use a correct flux level in order to maintain the power factor at an acceptable level.

Another control method of PMSM is the so-called $i_d = 0$ control (also known as the minimum current control), where the d-axis current component is set to zero. Although this minimizes the current, it will give a lower power factor and requires usually a higher stator voltage, which means that the voltage reserve is smaller. Usually the $i_d = 0$ control is preferred with low-inductance surface magnet PMSMs due to the low armature reaction. Figure 2.9 shows these two control methods of the PMSM with vector diagrams.

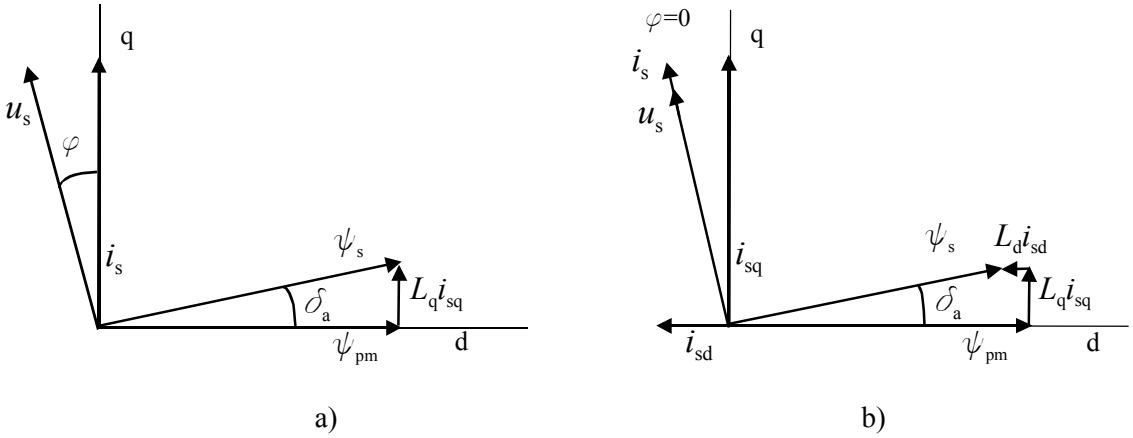

Figure 2.9. Vector diagrams of the PMSM with two different control methods. a) $i_d = 0$ control, where all the current is on the q-axis to produce torque. The stator current is minimized, but the power factor is lagging. b) $\cos(\varphi) = 1$ control, where the negative d-axis current sets the phase angle to zero. The total current is somewhat higher, but the voltage is consequently lower.

Depending on the amount of the negative d-axis current, the stator current of the PMSM can vary significantly from the nameplate value of the motor, which can confuse the user. There seem to be no commonly accepted method among the manufacturers for expressing the rated current of the motor. At partial loads, the characteristics of the PMSM are good because of the very small armature reaction, which means that both the phase and the load angles are small. As the loading increases, the armature reaction starts to increase the phase angle, and both the power factor and the torque-to-current ratio start to decrease. Figure 2.10 shows the vector diagrams of a PMSM with $L_d = L_q = 0.20$ p.u. at 50 % torque and at 200 % torque.

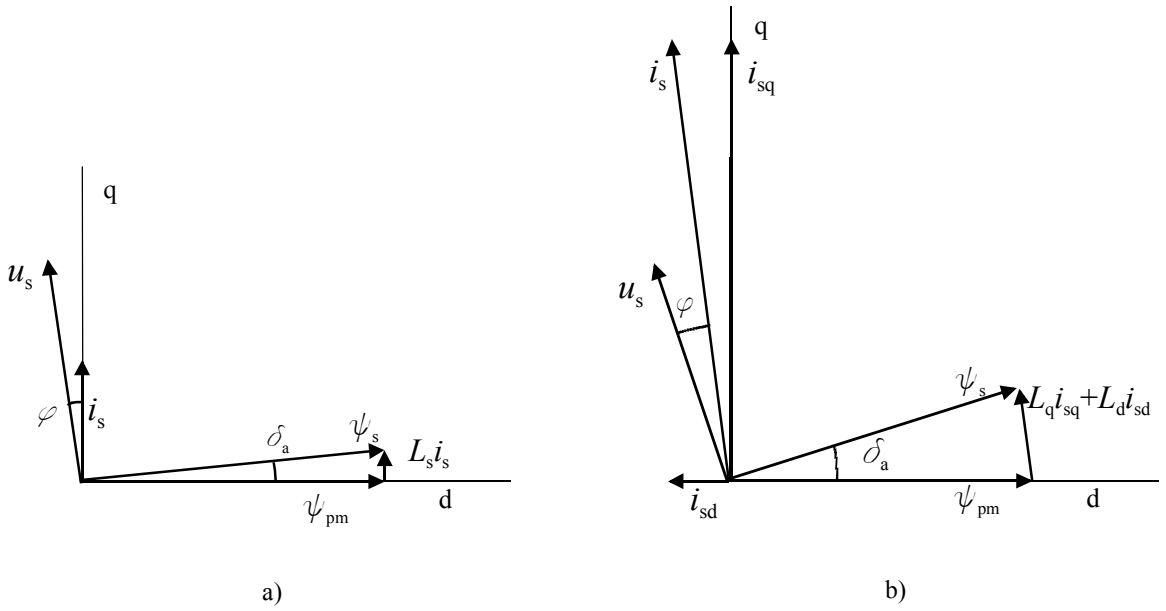

Figure 2.10. Vector diagrams of the PMSM ($L_d = L_q = 0.20$ p.u.) a) at 50 % torque and b) at 200 % torque. When the inductances are low, the power factor remains high at partial loads even with $i_d = 0$ control, but at high loadings, a demagnetizing current is required for power factor compensation.

During the constant-speed operation in typical servo applications, the loading torque is typically only from some percents to tens of per cents of the rated torque (only to compensate the friction). With such a load, the operation characteristics of an induction motor with full flux are very poor, because only a fraction of the stator current then produces the torque, while the rest goes for the magnetization. With larger two-pole motors, the magnetization current can be typically 20−50 % of the rated stator current, but as the pole-number increases, the share of the magnetization current increases with it, because the ratio of the length of the air gap the pole-pitch increases. Further, if the machine is designed for higher flux densities to provide a better dynamic performance, the saturation of the iron will decrease the magnetizing inductance, which will further increase the need for the magnetizing current. Basically, the magnetizing current is determined from the *BH* curve, where the flux density is a direct function of the stator voltage. At the normal operation range, the magnetizing inductance is nearly independent of the torque, but at high overloads, the magnetizing inductance starts to decrease proportionally to torque. This is because the flux lines cross the air gap in a skewed angle, and the main flux starts also to straighten through the slots, and thus there is a significant increase of the air in the main flux path. This was shown by Nerg et al. (2004). In their case, the magnetizing inductance was decreased by 23 %, when the torque of a 30 kW four-pole industrial induction motor was 300 %. The torque production capability of an induction motor is further decreased at high overloads, as the increased stator voltage loss will decrease the air gap flux. However, as the loading increases, the magnetizing current remains nearly constant, while the torque producing current increases, and thereby both the power factor and the torque-to-current ratio will increase with the loading. The situation is opposite to a PMSM, where the increasing armature reaction due to increasing torque tends to increase the phase angle between the current and the voltage (with constant flux). Figure 2.11 shows the vector diagrams for the prototype induction motor at the rated speed with the loadings 25 % and 200 % of the rated torque. At 25 % load torque, the angle between the current and the voltage is close to 90° due to small rotor current, but at 200 % load torque, the phase angle has decreased significantly.

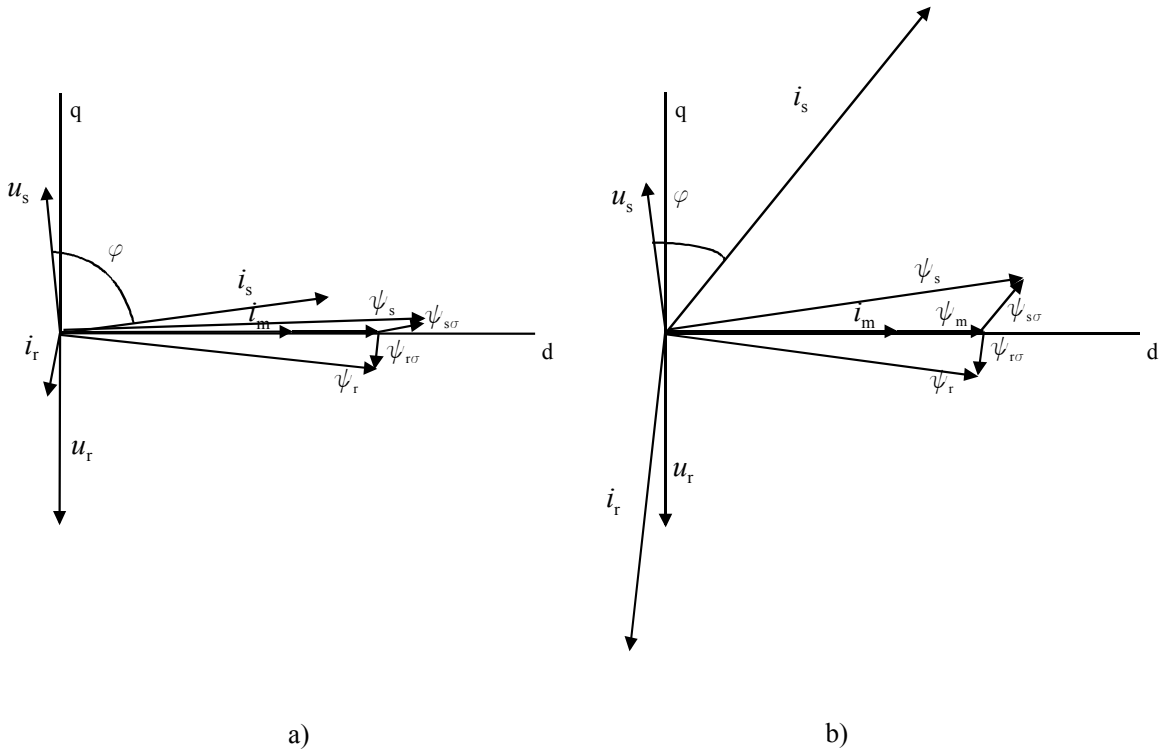

Figure 2.11. Vector diagram of the prototype induction motor at the rated speed and flux a) operating at 25 % torque and b) at 200 % torque. Unlike with the PMSM, the power factor of an induction machine increases as the torque increases.

Figure 2.12 illustrates FEM-calculated power factors for the prototype induction motor as a function of the torque at four different speeds; 50 %, 100 %, 150 %, and 200 %. Also the power factor of the PMSM construction is shown with the assumption of $i_d = 0$ control. While the power factor of an induction motor increases up to a certain point as the torque increases, the power factor of the PMSM decreases with the torque. The power factor of the PMSM could be easily increased by using a demagnetizing current, but this of course would decrease the torque production. It must be noted, that the situation in Fig. 2.12, where the PMSM operates at 4 p.u. torque is impossible near the rated speed, because higher than the rated stator voltage would then be required due to the high armature reaction.

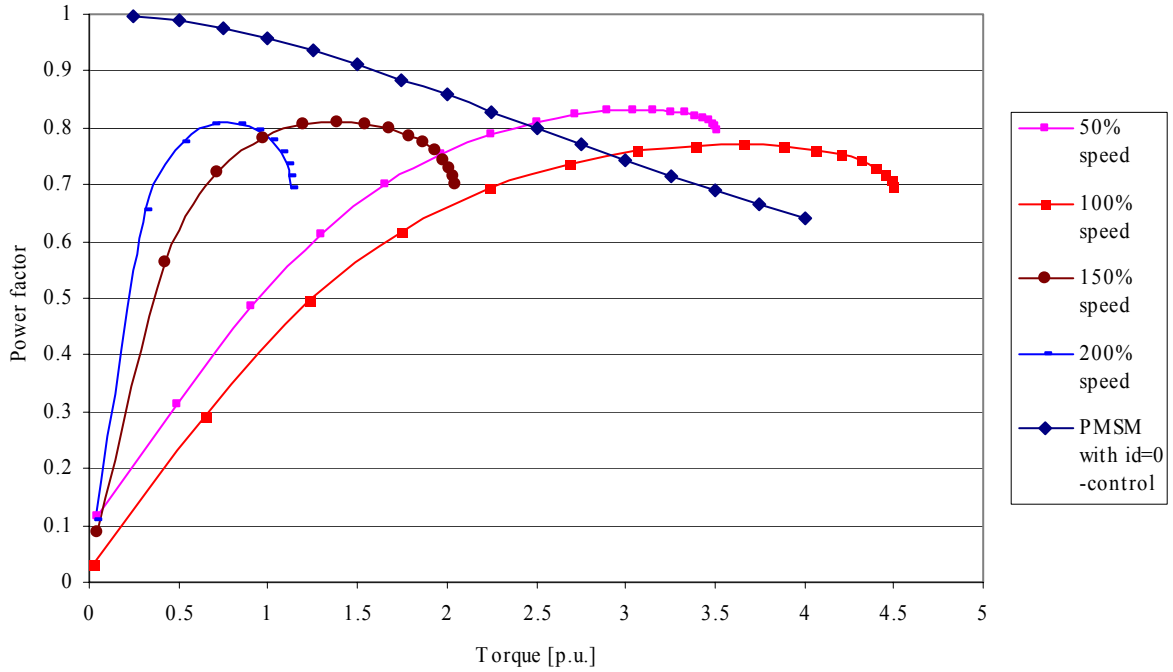

Figure 2.12. Simulated (FEM) power factors of the prototype induction motor as a function of torque at different speeds (rated flux). As the torque increases, the power factor increases up to a certain point. In the field weakening, the power factor increases substantially due to the decreased flux. The lowest power factor occurs at the rated speed. Also the power factor of the PMSM with $i_d = 0$ control is shown.

As can be seen in Fig. 2.12, the power factor of induction motor increases up to a certain point as the torque increases, but increasing the torque beyond this point will start to decrease the power factor again. At no-load, the stator current vector equals the magnetizing current vector (if the losses are neglected), and the angle between the current and the flux linkage would be zero. Figure 2.13 shows the FEM-calculated power factors of the prototype induction motor as a function of the speed. Calculations are carried out at different torque levels, ranging from 20 % up to 200 % torque.

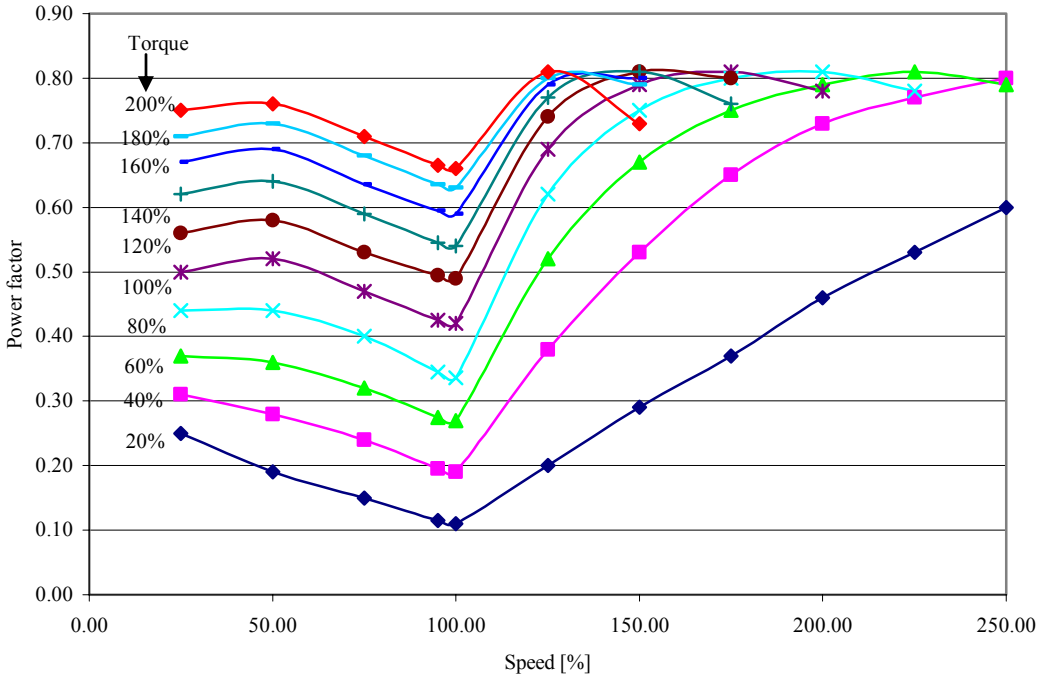

Figure 2.13. Power factors of the prototype IM as a function of speed at different torque levels (from 20 % up to 200 %). The power factor has the lowest value at the rated speed. The values are calculated with FEM at the rated flux (after the base speed the flux naturally decreases from the rated value).

Figure 2.13 shows that the power factor of an induction machine increases as the motor enters the field weakening region. The phenomenon is emphasized with this particular machine because of the saturation in the normal flux range. It must be also noted that as the speed decreases below the base-speed and the torque is kept constant, the power factor starts to increase up to a certain point indicating that there is a similar maximum point for the power factor below the base speed.

Figure 2.14 shows the torque-to-current ratios of the prototype induction motor as a function of torque with speed as a parameter. In general, the higher the speed or the torque, the better are the characteristics of the motor. The values for the 150 % and 200 % speeds are low in the figure, because the motor operates in the field weakening, and hence the torque production capability has consequently decreased. Therefore, for example, the maximum value of T/I ratio at 200 % speed (0.79 Nm/A) means a better torque production than for example the maximum value at rated speed (1.47 Nm/A). The torque-to-current ratio of the PMSM is approx 1.7 Nm/A according to the nameplate values. It must be also remembered, that the torque production capability of a surface magnet PMSM will deteriorate rapidly when the motor enters the field weakening. Field weakening is discussed in more detail in Chapter 3.

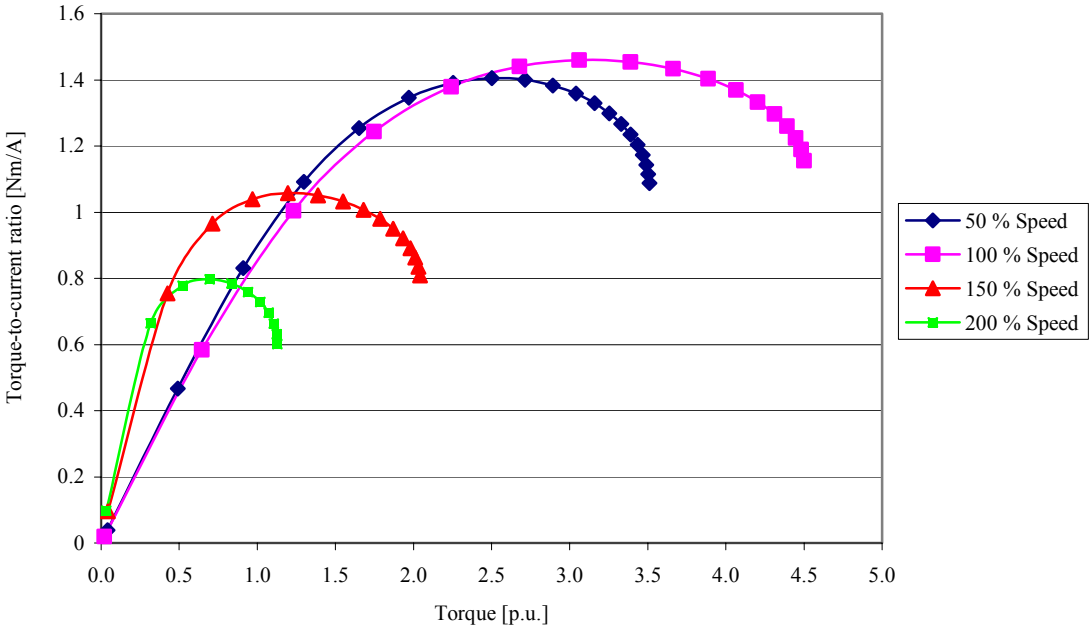

Figure 2.14. Torque-to-current ratios of the prototype as a function of torque (at rated flux). Because the magnetizing current remains approximately constant for the given speed, the ratio increases with the torque up to a certain point. In the full flux area, the ratio for the PMSM is approx. 1.7 Nm/A according to a nameplate values of the motor. The maximum speed of the PMSM is approx. 120 % at no load.

2.4 Four-pole induction machine

High torque density or high torque-to-current ratio is a fundamental requirement of a servomotor. PMSM with surface magnets has a high power factor, and thus both the motor and the inverter are physically smaller. With induction motors, there are three problems related to the motor dimensioning in high-performance applications, which make the induction motor a less competent alternative. The first one derives from the fact that the majority of servomotors are some tens of kWs at maximum. The smaller is the physical size of an induction motor, the smaller is the magnetizing inductance, as the air gap becomes more and more dominating when the motor diameter is decreased. An increased magnetizing current leads to an increased slot cross-sectional area, which can be seen in the increased motor physical size. Secondly, in high-performance applications, a high air gap flux density is required, which further decreases the power factor due to the saturation of the flux path. And thirdly, to optimize the torque density of the motor, several pole-pairs are beneficial to minimize the stator yoke thickness. For example, PMSM servomotors have often 3 or 4 pole-pairs. Small induction motors cannot be designed for high pole numbers, since the magnetizing inductance would collapse. The dynamic flux level control, which improves the running characteristics of an induction motor is presented in Chapter 3; below, it will be shortly discussed, how much the motor characteristics will improve if the pole number is decreased (from 6 to 4 of the prototype motor).

Calculations for the induction motor presented in this chapter were carried out for a highly saturable six-pole motor. A six-pole induction motor typically has a low magnetizing inductance, which, in this case is further decreased by the saturation. By decreasing the pole number down to

four, the magnetizing inductance increases, but the flux per pole will increase by 50 %. This means that a larger cross-sectional area for the flux is required. With six-pole machines, the flux densities in the rotor are typically very moderate, as a certain rotor diameter is required to provide adequate torque. However, as the flux densities in the stator were high already with a six-pole construction, at least a thicker stator yoke is required to prevent the excessive saturation. This will increase the outer diameter of the machine.

The magnetizing inductance of an AC machine with a uniform air gap can be expressed as follows (Vogt 1996)

$$L_{\mathrm{m}} = \frac{m}{\pi} \frac{\mu_0}{\delta_{\mathrm{eff}}} DL' \left(\frac{N}{p} \right)^2 \xi_1^2 \quad , \tag{2.13}$$

where m is the phase number, μ_0 the vacuum permeability, D the stator bore diameter, L' the stator stack effective length, N the number of turns per phase, p the number of pole pairs, and ξ_1 the fundamental winding factor. According to Eq. (2.13), decreasing the number of pole pairs from 3 to 2 will increase the magnetizing inductance by 125 % if other parameters are held constant. For the magnetizing reactance, this means an increase of 83 % if the speed of the motor is kept constant (frequency decreases). The fundamental winding factor, defined for the machine without short-pitching, is

$$\xi_1 = \frac{2\sin\left(\frac{\pi}{2m} \right)}{\frac{Q_{\mathrm{s}}}{mp} \sin\left(\frac{\pi p}{Q_{\mathrm{s}}} \right)} \quad , \tag{2.14}$$

which remains approximately constant (decreases from 0.966 to 0.960). The number of turns per phase in the winding can be expressed with the induced voltage E, fundamental winding factor ξ_1, and the maximum value of the flux per pole $\hat{\Phi}$

$$N = \frac{\sqrt{2}E}{2\pi f \xi_1 \hat{\Phi}} \quad . \tag{2.15}$$

Reducing the pole number will decrease the frequency for a given speed, and increase the pole flux, defined as

$$\hat{\Phi} = \alpha \hat{B}_\delta \tau_{\mathrm{p}} L' \quad . \tag{2.16}$$

As the increased pole flux and the decreased frequency cancel each other in Eq. (2.15), the number of turns remains constant. This is very convenient, since the magnetizing inductance is inversely proportional to the pole number squared, and on the other hand the leakages are affected only slightly. Slot and tooth-tip leakages are not affected at all, and the end-winding leakage inductance increases slightly as the coil span increases. The air gap leakage describes the space harmonics caused by the slotting that induce fundamental frequency components into the winding. Therefore,

the definition of the air gap leakage is similar to that of the magnetizing inductance, and it is inversely proportional to the number of pole pairs squared.

The characteristics of a prototype motor with four poles (instead of six) were calculated with FEM. First it was studied, whether it is possible to improve the characteristics simply by increasing the height of the stator yoke (while keeping the rotor size constant) until the yoke flux density decreased below saturation. This, however, seemed to decrease the stator current at the rated point only slightly, which implies that the large magnetizing current is caused by the teeth saturation in the stator and in the rotor, because the flux density in the rotor yoke was only slightly above 1 T even with a four-pole construction. A more effective method for increasing the torque production would be to increase the rotor diameter, as the torque increases proportional to rotor radius squared. By keeping the voltage (and the number of turns) constant, the air gap flux density decreases, which, in theory, should compensate the improved torque production. However, as teeth flux densities in both the stator and in the rotor decrease, the magnetizing current also decreases. Calculations were carried out for four different stator outer diameters; 140, 150, 160 and 170 mm (the original outer diameter of the stator was 132 mm). For each stator, the rotor diameter was increased from the original value (79.4 mm). The goal was to answer the question "How much larger will an induction motor have to be to produce an equal torque with equal current and voltage?". The currents and the power factors are shown in Fig. 2.15.

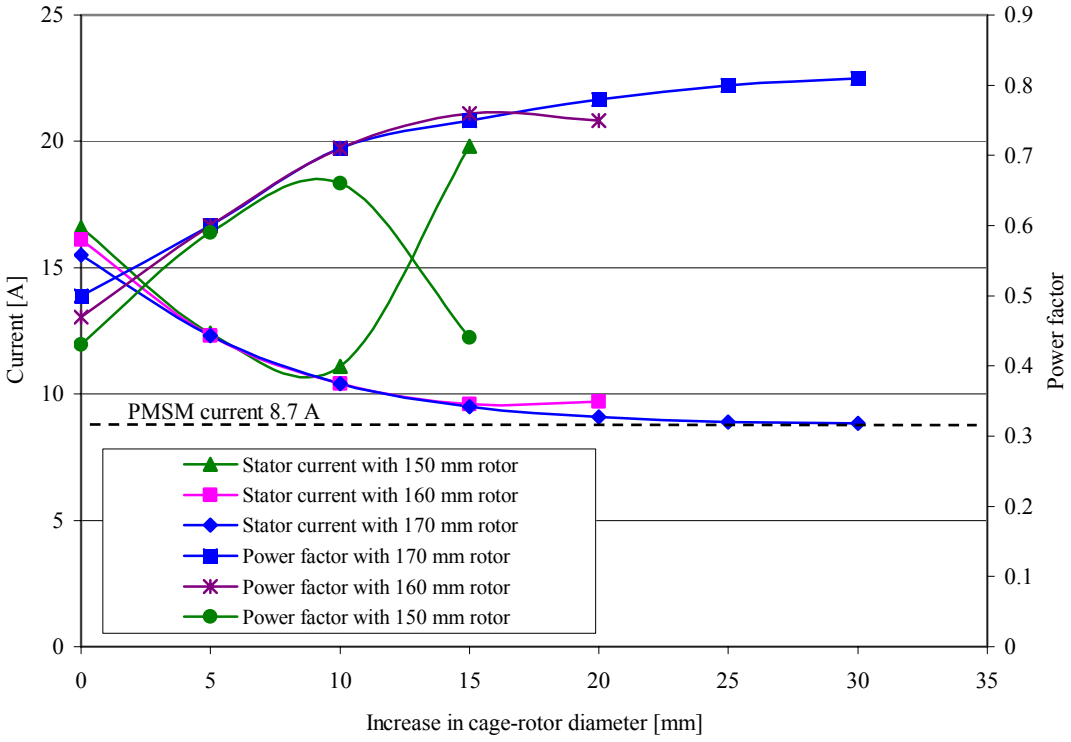

Figure 2.15. Stator currents and power factors of the four-pole induction motor constructions, when the rotor outer diameters of both the stator and rotor were varied to find out a construction which would be equivalent with the original PMSM (rated current, voltage and torque). The diameter of the original motor was 132 mm. It is also apparent how small the effect is on the stator current, if only the stator yoke thickness is increased (zero on the x-axis).

In Fig. 2.15, the stator voltage and the number of turns have been kept as constants, which will mean that the air gap flux density decreases as the rotor size increases. According to calculations, increasing the outer diameter of the stator by 38 mm (while simultaneously increasing the rotor diameter by 25−30 mm) would result in an equal stator current compared to the original PMSM. Of course, the power factor would be lower (approx. 0.8). Also a 160-mm outer diameter would result in only a 1 A larger current compared to a PMSM, and also in a moderate power factor. Thus, with an induction motor, basically a 30 mm larger outer diameter is required for equal torque production compared to a PMSM. In this case, 30 mm equals approx. 20 %. It must be noted, however, that this ratio applies only for the machines of this size. In general, the larger is the motor torque (physical size), the smaller is the difference in physical sizes between an induction motor and a permanent magnet synchronous motor. This is because the induction motor magnetizing inductance increases with the physical size. It must be also noted, that by properly dimensioning the PMSM, its power factor can be chosen unity, while the power factor of the IM is always lagging. With equal machine size, the torque-to-current ratio of the induction motor is thereby always lower than with the permanent magnet synchronous motor, and the induction motor therefore is larger. The purpose of the previous analysis was just to clarify the difference in sizes of the two machine types in this particular case.

2.5 Conclusion

In this chapter, the dimensioning of an induction motor and a permanent magnet synchronous machine in dynamically demanding applications was studied. When the PMSM has thick surface magnets on the rotor, high overloading capability will result. Also the rated torque-to-current ratio of such a motor is high because of the high air gap flux density. Because the synchronous inductance of such a machine is low, the machine can be controlled in $i_d = 0$ mode, while simultaneously obtaining a high power factor. And lastly, PMSM servomotors can be realized as 4-8 pole constructions, which makes the outer diameter of the machine smaller because of the thin stator yoke. If an induction machine is dimensioned to equal flux density levels, the saturation of the iron substantially deteriorates the characteristics of the motor (power factor, efficiency and torque-to-current ratio). Further, it is not practical to dimension a small power induction machine to a pole number higher than four, which indicates that a thicker stator yoke, and therefore a larger outer diameter is required. According to calculations performed in this study, at least 20 % larger outer diameter with an induction machine is required to produce an equal torque for the given current as with a PMSM. The deeper is the degree of saturation with the induction motor, the higher is the ratio. This suggests a dynamic flux level control, which will be discussed in Chapter 3.

3. MOTOR CHARACTERISTICS

It was shown in Chapter 2 that a PMSM servomotor equipped with thick surface magnets inherently has a high pull-out torque as the d-axis inductance becomes low. A further advantage in using surface magnets and a small amount of rotor iron is the decreased inertia. Surface magnets contribute to the low inertia, because their density is lower than the density of iron, and also the lowest possible amount of magnet material is needed when the surface installation is used. These three features make the SMPMSM very feasible in dynamically demanding applications, compared for example to induction machines. Typically, the pull-out torques of industrial induction machines are in the range of 1.6−3 p.u.. Higher torques, however, are available, if the flux density level is increased, as the electromagnetic torque is proportional to the air gap flux density squared. Unfortunately, it is often impractical to design an induction machine with a high flux density level, as the saturation of the iron path will have a substantial effect on the motor characteristics, such as on the power factor and on the efficiency. An induction motor drive inverter must have a higher current rating than a PMSM drive inverter (nominal voltages being commensurable). Besides of increasing the flux level of the (induction) machine, another approach would be to maximize the torque production capability by minimizing the parasitic leakage fluxes, which, in practice yields to the minimization of the leakage inductances. As also this approach has its drawbacks, such as an increased harmonic content of the air gap and a decreased power factor, the compromise would be to moderately use both of these methods.

The measures to increase the pull-out torque of an induction motor are studied in this chapter. The motor under study is the prototype motor introduced in Chapter 2. The induction motor was realized by removing the rotor from the PM servomotor and designing and constructing a copper-cage rotor for this existing stator. Therefore it operates in quite a heavy saturation. Saturation causes an increase in the magnetizing current due to the decreased magnetizing inductance, which can be seen in increased losses and a poorer torque-to-current ratio. By controlling the flux level of the motor in an advanced way, the drawbacks caused by saturation can be, to a large degree, prevented.

The focus of this chapter is first to discuss the increasing of the overloading capability of an induction motor close to the values of PM servos, and second to study the characteristics of such a motor. Also the field weakening of the induction motor is studied in more detail, as it is closely related to the overloading capability. Depending on the application, the physical size of the motor drive can be significantly decreased, if the field weakening of the motor can be utilized. Finally, it is studied how the flux of an induction motor should be controlled as a function of the load torque in order to improve the running characteristics of a pull-out-optimized induction motor.

3.1 Overloading capability

Servo drives are often applications, in which objects are to be moved very quickly from point to point; therefore, high acceleration and deceleration rates are a fundamental requirement in motion control. An increased drive performance results in lower cycle times and therefore in lower production costs. Since fast acceleration rates are required, the motor should have a high torque and a low moment of inertia, since their ratio defines the rate of the angular acceleration according to Newton’s second law of motion

$$\alpha = \frac{T}{J} \quad , \tag{3.1}$$

where α is the angular acceleration, T the torque, and J the moment of inertia. It is a common method in motion control to utilize all the torque available, which is typically limited by the frequency converter current rating rather than by the pull-out torque of the motor itself. If the over dimensioning of the frequency converter compared to the motor can be justified for instance by the lower production costs, the pull-out torque of the motor can then become the bottleneck of the system. For example, a frequency converter having a double current rating compared to the motor can provide even a four-fold short-time motor current for a rapid acceleration. If the pull-out torque of the motor is for instance 2−3 p.u. (a typical value for industrial induction motors) it cannot produce the maximum torque even though it would be available from the frequency converter. By optimizing the overloading capability of the motor – that is, the pull-out torque – a dynamically higher performance is then available.

According to Maxwell's tension theory, the torque generating tangential tension $\sigma_{\tan}$ component in the air gap of an electric machine can be expressed with the magnetic field strength radial and tangential components H_{rad} and $H_{\tan}$

$$\sigma_{\tan} = \mu_0 H_{\mathrm{rad}} H_{\tan} \quad , \tag{3.2}$$

where μ_0 is the vacuum permeability. The tangential component of the magnetic field strength on the stator or the rotor surface is produced by the linear current density acting on the surface. The tangential tension can then be expressed in the form

$$\sigma_{\tan} = \frac{B_{\mathrm{rad}} B_{\tan}}{\mu_0} \quad , \tag{3.3}$$

where B_{rad} and $B_{\tan}$ are the air gap flux density radial and tangential components, respectively, related by

$$B_\delta = \sqrt{B_{\mathrm{rad}}^2 + B_{\tan}^2} \quad . \tag{3.4}$$

The electromagnetic torque T_{em} of the machine can be calculated by integrating Eq. (3.3) around the rotor surface

$$T_{\mathrm{em}} = \frac{L'}{\mu_0} \int_0^{2\pi} B_{\mathrm{rad}} B_{\tan} r_\delta^2 \, \mathrm{d}\varphi \quad , \tag{3.5}$$

where L' is the electromagnetic length of the stack, r_δ is the mean air gap radius, and φ the polar angle. In no-load condition, there is only the radial component present, but as the torque starts to increase, the flux lines cross the air gap in a skewed angle, which means that also a tangential component of the air gap flux exists and the machine generates torque. At the same time, the radial component starts to decrease, and according to Eq. (3.5), the maximum value of the

electromagnetic torque is obtained when the two components are equal. This is called the pull-out point, and the consequent torque the pull-out torque. If the load torque is further increased, the torque production starts to decrease, and the so-called pull-out (or the breakdown) occurs, after which the motor stalls to zero speed.

In practice, the pull-out torque of AC machines is largely determined by the inductances. With non-salient pole PMSMs, the pull-out torque is inversely proportional to the synchronous inductance L_d, while with induction motors, the pull-out torque is approx. inversely proportional to the short-circuit inductance L_{sc}, which is a sum of the stator and the rotor leakages

$$L_{sc} = L_{s\sigma} + L'_{r\sigma} \quad . \tag{3.6}$$

A motor designer can therefore influence the pull-out torque by the motor design. In PM rotors, the permanent magnet material may be attached on the rotor surface, or embedded in the rotor body. Often the surface magnet construction yields to a lower L_d and therefore a higher $T_{pull\text{-}out}$ than the embedded magnet construction, as it was explained in Chapter 2. Of course, it would be possible to decrease the inductances of a machine with embedded magnets by increasing the thickness of the magnets or by increasing the air gap length (which is quite unpractical), and thus to achieve a high pull-out torque. Such a design, however, is rarely practical, as it significantly increases the amount of the magnetic material in the machine. With induction machines, the situation is much more complicated, as the design procedure that minimizes the leakages has many drawbacks, such as an increased torque ripple and a lower power factor.

3.1.1 Overloading capability of an induction motor

The pull-out torque of an induction motor can be derived from the common simplified equivalent circuit of an induction motor, shown in Fig. 3.1. It assumes that the air gap voltage equals the terminal voltage, and there is no voltage drop in the stator. Especially, as the servomotors are always controlled with a frequency converter, and the motor operates in the linear part of the torque-speed curve, the resistive voltage loss remains small.

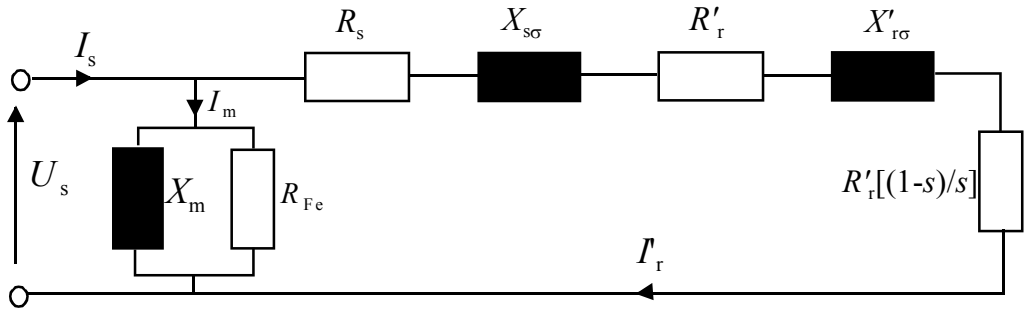

Figure 3.1. Simplified equivalent circuit of an induction motor.

The air gap power is converted to ohmic losses in R_r' and to mechanical power P_{mech} in the apparent resistance R_r'[(1-s)/s]. The motor electromagnetic torque T_{em} can thereby be expressed as

$$T_{em} = \frac{P_{mech}}{\Omega} = \frac{mR_r^{'}\left(\frac{1-s}{s}\right)I_r^{'2}}{(1-s)\frac{\omega_s}{p}} = \frac{mR_r^{'}I_r^{'2}}{s\frac{\omega_s}{p}} \quad , \tag{3.7}$$

where ω_s is the stator angular frequency, m is the phase number, R_r' the rotor resistance referred to the stator, s the per unit slip, p the number of pole pairs and Ω the mechanical angular velocity. The rotor current I_r' can be expressed

$$I_r^{'} = \frac{U_s}{\sqrt{\left(R_s + \frac{R_r^{'}}{s}\right)^2 + \left(\omega_s L_{s\sigma} + \omega_s L_{r\sigma}^{'}\right)^2}} \quad , \tag{3.8}$$

and the electromagnetic torque T_{em} (Engelmann and Middendorf 1995)

$$T_{em} = \frac{mp}{\omega_s}\frac{\frac{R_r^{'}}{s}U_s^2}{\left(R_s + \frac{R_r^{'}}{s}\right)^2 + \left(\omega_s L_{s\sigma} + \omega_s L_{r\sigma}^{'}\right)^2} \quad . \tag{3.9}$$

The maximum value for the torque with a given voltage U_s – the pull-out torque $T_{pull\text{-}out}$ – is given, when the derivative of Eq. (3.9) with respect to R'_r/s is set to zero. The value for the pull-out slip is thereby

$$s_{pull-out} = \frac{R_r^{'}}{\sqrt{R_s^2 + \omega_s^2\left(L_{s\sigma} + L_{r\sigma}^{'}\right)^2}} \quad . \tag{3.10}$$

By substituting Eq. (3.10) into the equation of the electromagnetic torque, an equation for the pull-out torque can be written as

$$T_{pull-out} = \frac{mp}{2\omega_s}\frac{U_s^2}{R_s + \sqrt{R_s^2 + \omega_s^2\left(L_{s\sigma} + L_{r\sigma}^{'}\right)^2}} \quad . \tag{3.11}$$

The pull-out torque of an induction motor is therefore inversely proportional to the stator resistance and the leakage inductances of the stator and the rotor, and directly proportional to the stator voltage squared. In practice, the per-unit resistance is far lower than the per-unit leakages, and thus no big mistake is made if the stator resistance is ignored. In order to increase the pull-out torque, the motor should be designed to have low leakage inductances, as will be discussed.

3.1.2 Induction motor leakage calculation

All the flux-components that do not contribute to the electromechanical energy conversion belong to leakage fluxes. According to Richter (1954), they can be divided into five components:

- the harmonic leakage inductance L_δ
- the coil end leakage inductance L_w
- the tooth tip leakage inductance L_z
- the skew leakage inductance L_χ
- the slot leakage inductance L_n

The total leakage inductance of the machine is the sum of these

$$L_\sigma = L_\delta + L_w + L_z + L_\chi + L_n \quad . \tag{3.12}$$

Besides that the leakages decrease the torque production capability of the motor by lowering the fundamental air gap flux density, they also contribute to the motor losses by inducing losses into the ferromagnetic parts of the machine, often regarded as additional losses. The loss calculation of the machine is discussed in Chapter 4 in more detail. In practice, the same methods that are used to optimize the characteristics, such as the efficiency and the torque ripple usually have a undesirable side-effect to increase the leakages, and thus to decrease the electromagnetic coupling between the stator and the rotor. The leakage flux components are shortly introduced below.

Harmonic leakage inductance L_δ

The harmonic leakage (referred also as the air gap leakage) takes into account the discrete distribution of the stator and rotor windings in slots, which causes the air gap mmf curve to be stepwise rather than sinusoidal. This will introduce harmonic components in the air gap flux. The harmonic leakage inductance describes the amount of these harmonic fluxes, and it can be expressed as a fraction of the machine's magnetizing inductance L_m using an air gap leakage factor σ_δ

$$L_\delta = \sigma_\delta L_m \quad . \tag{3.13}$$

The leakage factor σ_δ can be defined as

$$\sigma_\delta = \sum_{\substack{\nu=-\infty \\ \nu \neq 1}}^{\nu=\infty} \left(\frac{\xi_\nu}{\nu \xi_{\nu 1}} \right)^2 \quad , \tag{3.14}$$

where ν is the ordinal of a harmonic frequency, and ξ_ν the corresponding winding factor. As the harmonic leakage depends on the winding factors of the higher harmonics, it is strongly dependent on the winding layout. In general, the higher the number of slots per pole per phase q, the more sinusoidal the mmf distribution and the lower the harmonic leakage inductance. Most servomotors are physically small machines, the stator slot number of which is typically 36−48 and the pole number often 4−6, which means that q is often 2−4. Short-pitching of the winding is an effective

method to decrease the harmonic leakage; Fig. 3.2 shows the harmonic leakage factors of a three-phase winding as a function of the short pitching W/τ_p with q as a parameter.

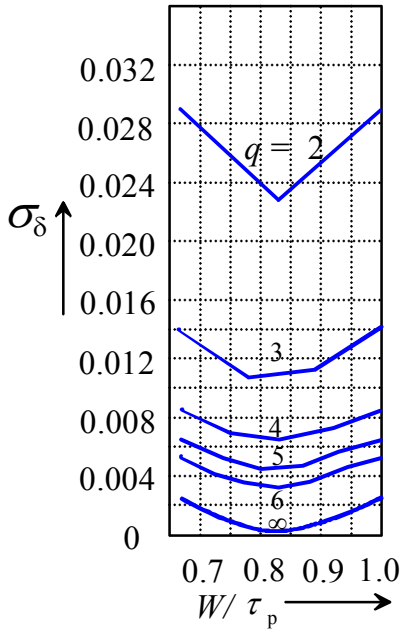

Figure 3.2. Harmonic leakage factor of a three-phase winding as a function of the coil span W, the number of slots per pole per phase as a parameter. Short-pitching of $W/\tau_p = 5/6$ has the most favorable effect on the harmonic leakage factor (Vogt 1996).

As it can be seen in Fig. 3.2, in order to minimize the harmonic leakage, the stator winding should have at least 3 slots per pole per phase (e.g. a three-phase-, four-pole machine with 36 slots in the stator), and in addition, short-pitching should be applied. As the short-pitching will decrease the coil span, also the end leakage and resistance are slightly decreased.

Coil end leakage inductance L_w

Currents at the end windings of the stator and the rotor create a flux distribution in the end section of the machine, which induces eddy-currents to the neighboring ferromagnetic parts. Due to complex geometries and different winding layouts, an exact solution of the end region fields is impossible without effective numerical methods in three dimensions. The end winding leakage, however, can be approximated with an equation given by Richter (1954)

$$L_{ew} = \frac{4m}{Q_s} q N^2 \mu_0 \left(2E\lambda_E + W\lambda_w\right) \quad , \tag{3.15}$$

where m is the phase number, Q_s the number of the stator slots, q the number of slots per pole per phase, and N the number of turns in series per phase. E is the axial distance of the end winding from the stack, and W the coil span. λ_E and λ_W are empirical factors that depend on the winding layout, for example, for a 3-phase, double-layer stator winding with a squirrel-cage rotor, $\lambda_E = 0.50$ and $\lambda_E = 0.20$. For the cage-rotor, the end ring leakage can be approximated with an equation given by Levi (1984)

$$L_{\mathrm{er}} = \mu_0 \frac{Q_{\mathrm{r}}}{mp^2} \frac{1}{3} \left(\frac{L_{\mathrm{bar}}}{L'} - 1 + \upsilon \frac{\pi D'}{2p} \right) \quad , \tag{3.16}$$

where L_{bar} is the length of rotor bars, L' the effective stack length, D' the average end ring diameter, and $\upsilon = 0.36$ when $p = 1$ and else $\upsilon = 0.18$. Coil end leakages usually are minimized by nature, as it is always beneficial to keep the dimensions of the end windings as small as possible; furthermore, the (stator) end winding is often surrounded by air, and therefore it is located relatively far from the ferromagnetic stack. The use of short-pitching further decreases the stator end winding leakage as the coil span decreases.

Tooth tip leakage inductance L_{z}

Tooth-tip leakage is caused when the slot mmf creates a potential difference on teeth located at opposite sides of the slot, and the flux lines close through tooth-tips in the air gap outside the slot opening. Richter (1967) defines the tooth-tip leakage

$$L_{\mathrm{z}} = \frac{4m}{Q} N^2 \mu_0 L' \left(\frac{5 \frac{\delta}{w_{\mathrm{so}}}}{5 + 4 \frac{\delta}{w_{\mathrm{so}}}} \right) \quad , \tag{3.17}$$

where w_{so} is the width of the slot opening and δ is the length of the air gap. The term in parentheses represents the tooth-tip leakage coefficient. Eq. (3.17) shows that the smaller the air gap, and the wider the slot openings, the smaller is the tooth-tip leakage. Therefore, slots with wide openings should be applied. An increased slot opening width, however, will increase, especially in short air gap machines, the air gap harmonic content as will be shown later.

Skew leakage inductance L_{χ}

Skewing of the rotor or the stator slots usually by one slot-pitch is a very effective method to reduce the effects of the air gap flux permeance and winding harmonics, which cause torque ripple and audible noise in the machine. Skewing, unfortunately, weakens the electromagnetic coupling between the rotor and the stator, as a part of the flux created by the stator does not penetrate the rotor winding. This part is the skew leakage, and the corresponding leakage inductance can be defined as a fraction of the magnetizing inductance

$$L_{\chi} = \left(1 - \chi^2\right) L_{\mathrm{m}} = \left[1 - \left(\frac{\sin\left(\nu \frac{\pi a}{2 \tau_{\mathrm{p}} \pi} \right)}{\left(\nu \frac{\pi a}{2 \tau_{\mathrm{p}} \pi} \right)} \right)^2 \right] L_{\mathrm{m}} \quad , \tag{3.18}$$

where τ_{p} is the pole-pitch, a the tangential length of the skewing along the stator or the rotor surface, L_{m} the magnetizing inductance, and ν the ordinal of harmonic. Although the skew leakage is the third major leakage term in electrical machines, its decreasing effect on the torque ripple is so significant that it is almost without exception used also in servomotors.

Slot leakage inductance L_n

The slot leakage flux is created by the slot current, when some of the flux lines close through the slot without crossing the air gap and linking the stator and the rotor electromagnetically. According to Richter (1954), the slot leakage inductance can be defined as

$$L_n = \frac{4m}{Q}\mu_0 L' N^2 \lambda_N \quad , \tag{3.19}$$

where m is the phase number, Q the number of the slots, L' the effective stack length, and N the number of turns in series in phase. Coefficient λ_N is the slot leakage factor (also referred as the permeance coefficient), which is defined entirely by the slot geometry. Figure 3.3 illustrates the dimensions used in the determination of the slot permeance coefficient of a single layer winding for different slot shapes.

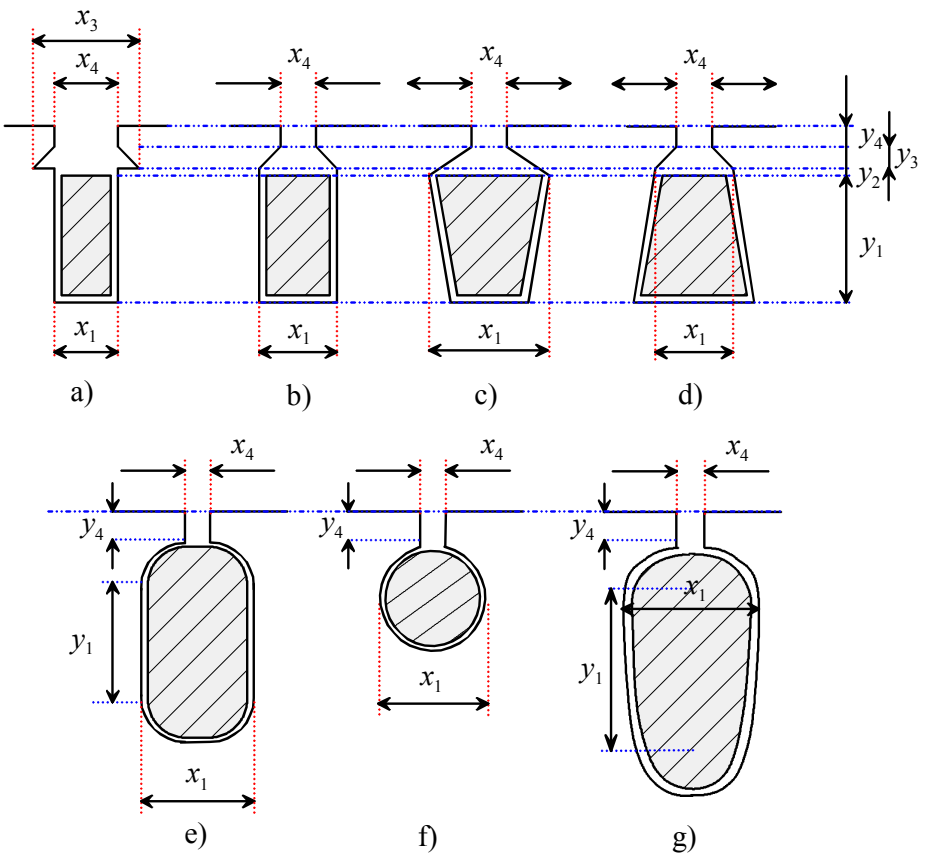

Figure 3.3. Dimensions of different slot geometries used in the determination of the slot leakage coefficient.

There are numerous equations for different slot shapes in the literature; for example Vogt (1996) and Richter (1954) have presented equations for the most common slot types. Slot leakage factors for slots in Fig. 3.3 a), b), c) and d) can be defined as

$$\lambda_N = \frac{y_1}{3x_1} + \frac{y_2}{x_1} + \frac{y_4}{x_4} + \frac{y_3}{x_1 - x_4}\ln\left(\frac{x_1}{x_4}\right) \quad . \tag{3.20}$$

According to Jokinen (1979), the slot leakage factor for the slot shapes in Fig. 3.3 e), f) and g) is

$$\lambda_N = \frac{y_1}{3x_1} + \frac{y_4}{x_4} + 0.66 \quad . \tag{3.21}$$

Industrial induction machines often have closed rotor slots due to the rotor manufacturing process (die-casting), which makes the rotor slot leakage factor strongly dependent on the degree of the saturation of the iron bridge above the slot. Accurate analytical determination of the slot leakage in such a case is practically impossible, and numerical methods should be applied. For double layer windings, equations for the slot leakage factors have been presented for instance by Jokinen (1979).

Figure 3.4 shows the leakage inductances of a 30 kW, four-pole standard industrial induction motor (ABB M2BA -series), calculated with the equations presented above from the motor dimensional data. The slot leakage and the harmonic leakage are the dominating leakage components, while the end winding and the tooth-tip components are the minor ones.

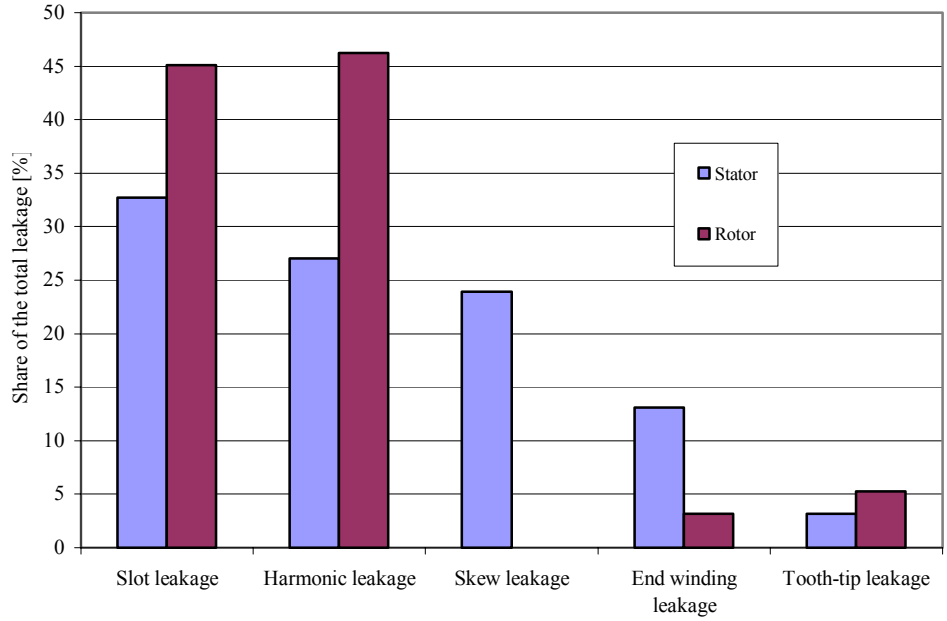

Figure 3.4. Analytically calculated leakage inductance distributions for standard industrial cage-rotor induction motor calculated with equations given above. Rotor leakage values are referred to the stator. The motor is an ABB 30 kW, 50 Hz four-pole machine.

The dominant slot leakage term can be explained by the shape of the slot openings. Very often, semi-closed slots are used in the stator and fully closed in the rotor to keep the harmonic content of the air gap flux density distribution small. A low harmonic content of the air gap flux will decrease the torque ripple and increase the efficiency of the machine, which are critical design parameters in most S1 (continuous duty) drives, while the overloading capability rarely has any significance. A minimum value for the pull-out torque of an induction machine, defined by the standard IEC60034-1 to be 1.6 p.u., is often sufficient for industrial S1 drives. The designer of such a machine can thereby optimize for example the efficiency and the torque ripple at the expense of

increased leakage inductance. However, when the machine should have a high torque output during the overloading as well as in the continuous state, the methods for minimizing the leakage should be searched for. Unfortunately, such a design will easily lead to the deterioration of the other motor characteristics. The effects of the leakage minimization techniques on the motor characteristics are discussed below.

Equations (3.12)−(3.21) and Fig. 3.4 suggest that the most effective ways to decrease the total leakage would be to try to influence the slot, the harmonic and the skew leakage terms. As the servomotors should usually exhibit a smooth torque, and as the skewing is a very effective method to decrease the torque ripple, only the first two methods will be left to minimize the total leakage. An effective method to decrease the harmonic leakage is to use at least 3 slots per pole per phase in the stator winding, and in addition short-pitching, as it can be seen in Fig. 3.2. The short-pitching will slightly decrease also the end winding leakage. As the end winding leakage is a minor component, the effect on the total leakage is far below this. According to Eq. (3.13), the use of short pitching will decrease the harmonic leakage inductance approx. by 25 %, which makes the total stator leakage to decrease by approximately 11 % (this includes also the decrease in the end winding leakage). Although the short-pitching makes the manufacturing of the winding more complicated, it should yet be carefully considered because of its many advantages. It will not only effectively decrease the total leakage, but it will also decrease the air gap harmonic content and therefore it will decrease the torque ripple and the high-frequency pulsating losses occurring on the iron surfaces. A further advantage is the shorter coil span, which will decrease the size of the end winding in addition to a slightly lower stator resistance. As the short-pitching is a fairly simple and a well-known method, it is not discussed here in more detail. In the following, the minimization of the total leakage by minimizing the slot leakage is discussed instead.

3.1.3 Induction motor slot leakage minimization

According to Eq. (3.19), the slot leakage is a function of the slot geometry and inversely proportional to the number of the slots Q, if the phase number, the stack length, and the number of series-connected conductors N are fixed. The ratio of the slot leakage factor to the number of the slots λ_N/Q therefore defines the slot leakage. As the slot leakage flux is directly proportional to the slot current, and the slot current is inversely proportional to the number of the slots, the slot leakage could be decreased by increasing the number of slots Q. Increasing the rotor or the stator slot number, however, means that the width of the slots should be simultaneously decreased in order to keep the teeth flux density constant (i.e., below saturation level). Thereby, the depth of the slots should be increased while increasing the slot number for the slot current density to remain constant. Such a design will inevitably increase the slot leakage factor, which means that the ratio λ_N/Q remains approximately constant, and the number of slots has no influence on the slot leakage. This can be seen in Fig. 3.5. It must also be borne in mind that increasing the slot number will decrease the slot cross-sectional area, which means that the slot fill factor decreases due to increased amount of insulation material needed in the slot.

In the design stage of the prototype motor, different rotor constructions were studied; Fig. 3.5 shows the pull-out torques for eight different rotors, each one having an equal total amount of copper in the rotor. Due to manufacturing reasons, simple rectangular rotor bars were used (and the target of 4 p.u. pull-out torque was obtained with a geometry of this kind). The effect of the slot number on the pull-out torque was calculated with four different rotor slot numbers in two

different ways. The first set of calculations was carried out by maintaining a constant slot leakage factor λ_N, while simultaneously increasing Q. In practice, this means that the radial and tangential rotor slot dimensions are decreased by the same factor (as Q increases, the area per slot can be decreased to obtain a constant current density). Although such a design will increase the pull-out torque, it soon leads to a situation, where the excessive tooth saturation causes the magnetizing current to strongly increase. By increasing the rotor slot number from 30 up to 54, and by keeping the constant slot leakage factor, the pull-out torque of the prototype induction motor increases approximately by 15 %. If also the stator slot dimensions were modified in the same way, the effect on the pull-out would be less than twice the above- mentioned 15 %, as the share of the stator slot leakage on the total leakage is typically larger in the rotor than in the stator.

The second set of calculations were carried out by similarly increasing the rotor slot number, but keeping the rotor slot height constant while decreasing the width to obtain constant current density. Therefore constant tooth flux density results, but consequently, the leakage factor increases and the effect on the pull-out torque is negligible according to FEM calculations. These two sets of calculations are shown in Fig. 3.5 (Note that the two cases, where $Q_r = 30$, are identical).

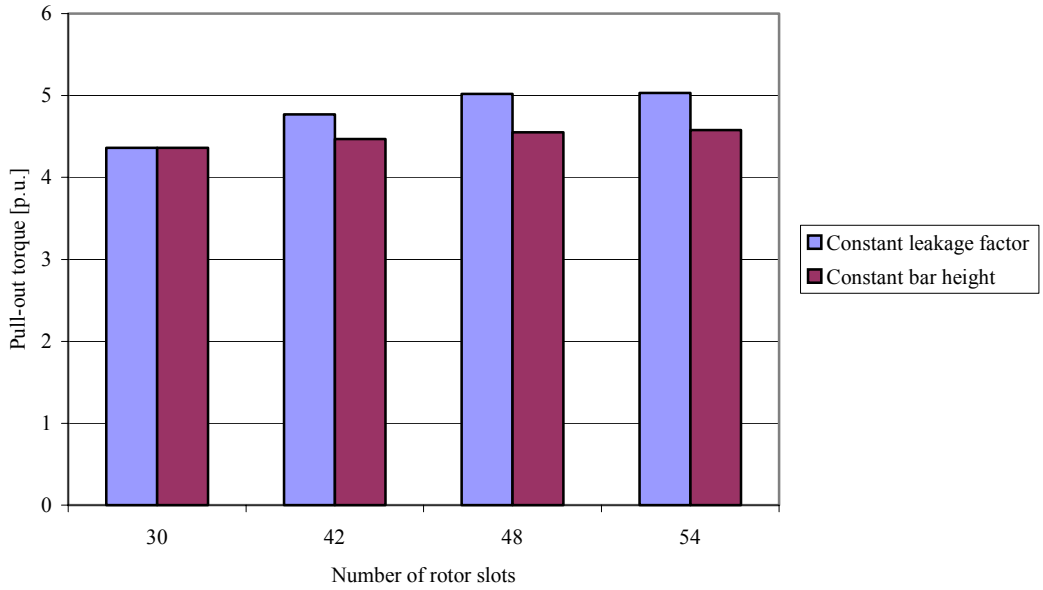

Figure 3.5. Pull-out torques with different rotor slot numbers, calculated with FEM, as the amount of copper in each eight cases is the same. Keeping the relative dimensions of the slot constant while simultaneously increasing Q_r ("constant leakage factor" in the figure) will increase the pull-out torque, but it will soon lead to excessive tooth saturation. The tooth saturation can be avoided by simultaneously decreasing the slot width as Q_r increases, but in such a case, the increased slot leakage factor causes the effect on the total pull-out torque to be negligible.

Figure 3.5 implies that the pull-out torque can be increased by keeping the slot leakage factor constant and by increasing the slot number. Such a design, however, will soon lead to increased tooth saturation. Tooth saturation could be partially diminished, and at the same time a constant leakage factor could be maintained, if it were possible to decrease the slot cross-sectional area. This, however, will require more efficient cooling, as the slot current density will consequently

increase. Improved cooling, would, of course, increase the continuous torque, too, and therefore only the absolute pull-out would increase, not the per-unit value. It must also be noted, that increasing the slot number decreases also the harmonic leakage, which is a significant leakage component. Further, a higher slot number will result in a more sinusoidal magneto-motive force distribution, which decreases the torque ripple of the machine.

As increasing the pull-out torque by increasing the slot number is not possible, the only possibility would be to directly decrease the slot leakage factor λ_N. According to Eq. (3.20) and Fig. 3.3, the larger the dimensions of the slot in the tangential direction and the smaller in the radial direction the smaller is the leakage factor, and consequently the higher is the pull-out torque. Equation (3.20) also implies that only the air gap side of the slot has a notable influence on the slot leakage factor, and thus the slot dimensions on the air gap side should be chosen wide, while having narrow slots on the bottom. Such as design is favourable in the rotor, as it leads to the commonly applied constant tooth width. In order to obtain constant-width teeth on the stator side, wider slot bottoms should be chosen. Wider slot bottoms are, certainly, not harmful from the leakage point of view. The slot dimensions and the geometry are mainly determined by the following factors: the slot cross-sectional area depends on the current density allowed and therefore on the type of the cooling. Tangential dimensions of the slot are determined by the allowed tooth flux density, which can be typically 2.0−2.2 T at maximum, depending on the lamination material. The slot opening geometry has a substantial effect on the slot leakage, and also on the tooth-tip leakage, although it is typically a minor term. The slot opening region is typically determined by the allowed torque ripple; wide slot openings will effectively decrease the leakage, but as a drawback, more harmonics are generated in the air gap flux. In addition, wide slot openings will cause higher permeance fluctuations under each slot, thus increasing the harmonic losses.

Small leakage factor will result, when wide rectangular slots in Fig. 3.6 a) with fully open slot-openings are applied, as there is only the first term in Eq. (3.20) left. It would be possible to further increase the pull-out torque by choosing a constant tooth flux density in the rotor, as the slot width near the air gap then becomes large thus decreasing the slot leakage factor (of course the slot openings would then be semi-closed). The reason why this geometry was not used here was that the target of 4 p.u. pull-out torque was obtained by using simple radially insertable rectangular bars. Further on, such “mummy bars” would have to be inserted axially in the slots from the stack end, which means that there would have to be certain clearance between the rotor bars and the iron to enable inserting of the bars. Such clearance could easily cause vibrations and problems with mechanical integrity especially in high-speed applications. Traditionally, cage rotors manufactured by die-casting utilize this slot geometry. Although simple rectangular slots can be used in the rotor, a slot wedge is probably required in the stator to keep the conductors in the slot. A common solution would then be to use the construction shown in Fig. 3.6 b), which is typical in high-voltage machines. The drawback with both of these geometries is the increased eddy-current losses in conductors. This is due to a fact that with fully open slots, the flux penetrates to the slot in the middle, and then turns into the teeth. Especially when conductors have large diameter, the eddy-current losses can be high. On the other hand, the servomotors usually utilize small-diameter round wire, and thus the eddy-current losses can be assumed small. It must be noted, however, that the FEM software used in this work (Flux2D®) does not take this phenomenon into account. A further problem with both of these constructions, in which the slots are made fully open, is the increased air gap harmonic content and also the increased equivalent length of the air gap, as the Carter’s coefficient increases; this can be seen in the increased magnetizing current. Semi-closed slot

openings and the use of semi-magnetic slot wedges are effective methods to reduce the air gap harmonics, but unfortunately they increase the leakage fluxes at the slot opening regions. As there is a clear trade-off between the torque ripple and the leakage flux, it is the designer's task to correctly balance these. The balancing depends greatly on the application. For example, when the load has a high inertia, as with electric working machines, such as load haul trucks, log stackers, and container lift trucks, there is a requirement of a very high pull-out torque, whereas the smoothness of torque is not so vital a parameter, as the mechanics effectively filter the torque ripple out. When both high pull-out and low torque ripple are required, it would be beneficial to use special-shaped semi-magnetic slots, where the width of the tooth-tip decreases towards the radial centreline of the slot, Fig. 3.6 c). The dimensioning of the tooth-tip should be such that during the normal operation, the slot current will not saturate the tooth tips, and hence the slot leakages are higher, but consequently the air gap flux harmonic content lower. During overloading, a high slot current will saturate the tooth-tips, and the slot opening seems magnetically more open thus increasing the pull-out torque. Also the eddy-current losses in conductors will be smaller with this construction. The drawback is naturally the higher harmonic content of the air gap flux during overloading.

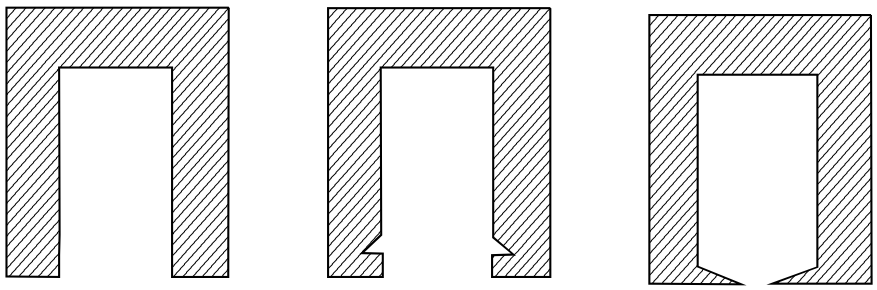

a) b) c)

Figure 3.6. Different slot shapes with low leakage coefficient. a) The lowest leakage is achieved with wide rectangular and fully open slots, although it leads to a higher torque ripple. b) The same as previous, but ready to be equipped with the slot wedge, and thus it can be applied to the stator as well. c) Semi-closed slot, with variable-height tooth-tips. During the normal operating conditions, the slot leakage is higher but the air gap harmonics lower, and as the tip saturation virtually opens the slot more during the overloading, the pull-out torque is increased.

Figures 3.7 to 3.11 show the flux distributions of the prototype during the overloading (T_{load} = 2.0 p.u.) and the consequent slot leakage flux densities for five different slot geometries. The flux densities were calculated with FEM through the centreline of the slot, at the tooth where the peak flux passes (the middle rotor tooth in Figs. below). First the calculations were carried out for 1.5mm×20mm rectangular rotor slots with fully closed and fully open slots. After that, the leakage coefficient was cut into half with 3mm×10mm slots (equal cross-sectional area), and the calculations were carried out with three different slot opening shapes; closed, semi-closed and fully open. The stator was the same in all calculations, and only the shape of the rotor slots was varied. In order to get comparable values, all the calculations were carried out at 2.0 p.u. overloading torque, which means that the rotor slot current is approximately the same.

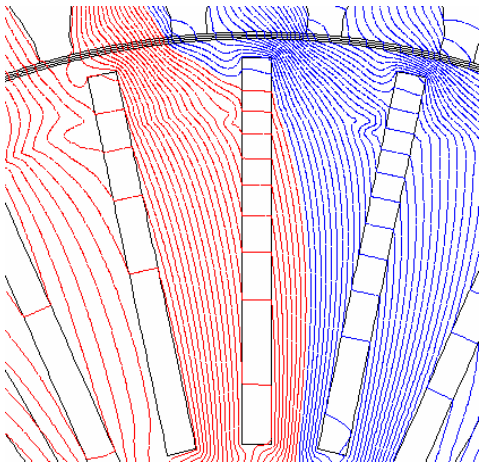

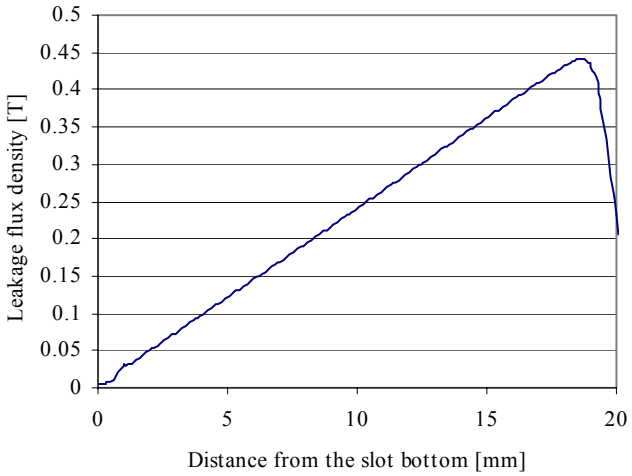

a) b)

Figure 3.7. Flux distribution of the prototype motor with 1.5mm×20mm fully closed rotor slots. a) The flux distribution at the main flux path, and b) the leakage flux density through the tooth where the flux density is at highest (the middle slot in the figure). Because the slot leakage of such a construction is high, the motor operates near by the pull-out point. The stator current at 2.0 p.u. torque is 31.2 A and the slip 8.2 %. The pull-out torque is 2.05 p.u..

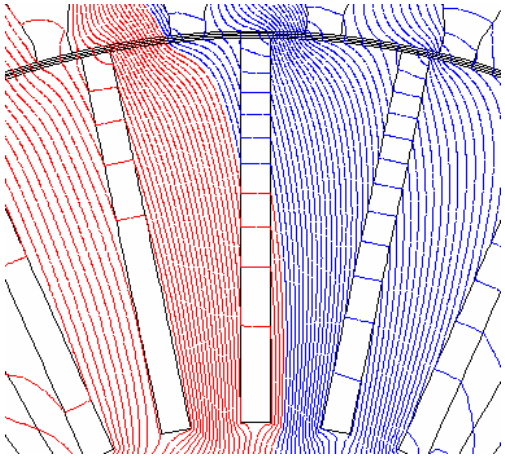

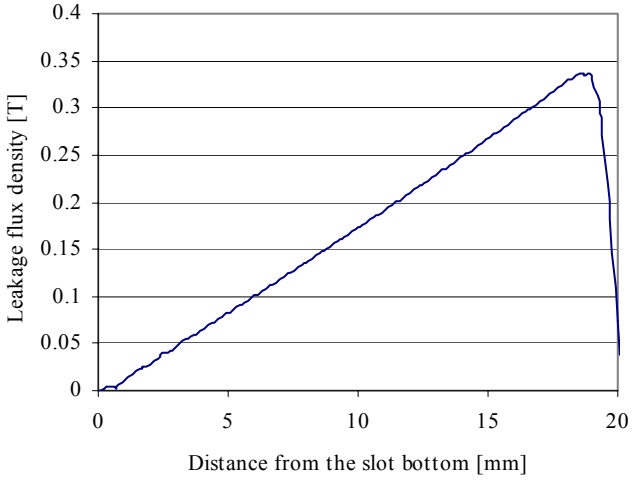

a) b)

Figure 3.8. The same motor as in Fig. 3.7, but with fully open slots. The slot leakage is notably lower, and consequently the pull-out torque higher (2.8 p.u.). The stator current is 25.5 A and the slip 4.9 % (at 2.0 p.u. torque)

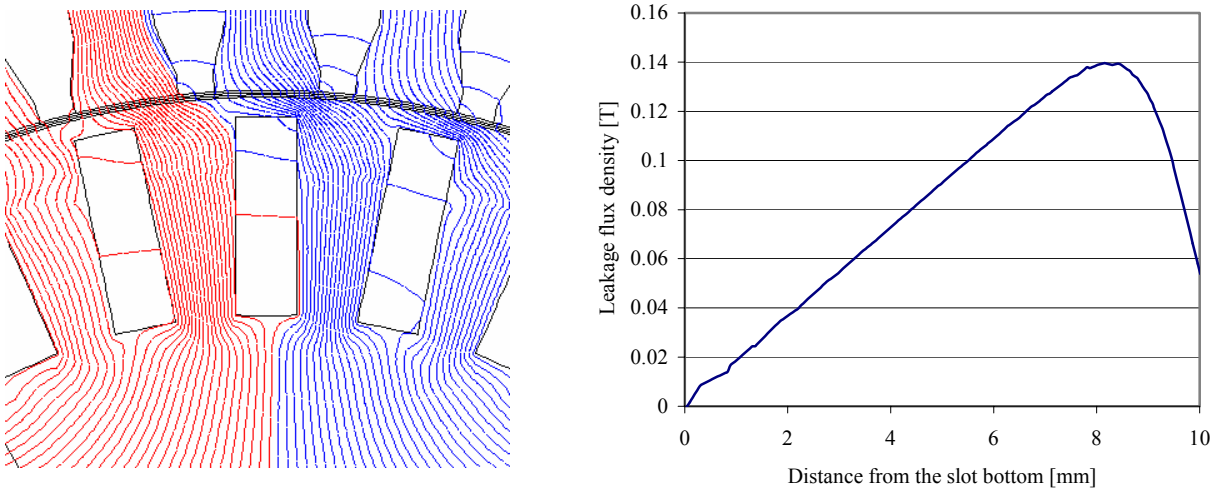

a) b)

Figure 3.9. A motor with a low slot leakage coefficient and with closed rotor slots. There is excessive saturation in the iron bridge above the slot. The pull-out torque is 3.3 p.u. The stator current is 23.6 A and the slip 4.6% (at 2.0 p.u. torque)

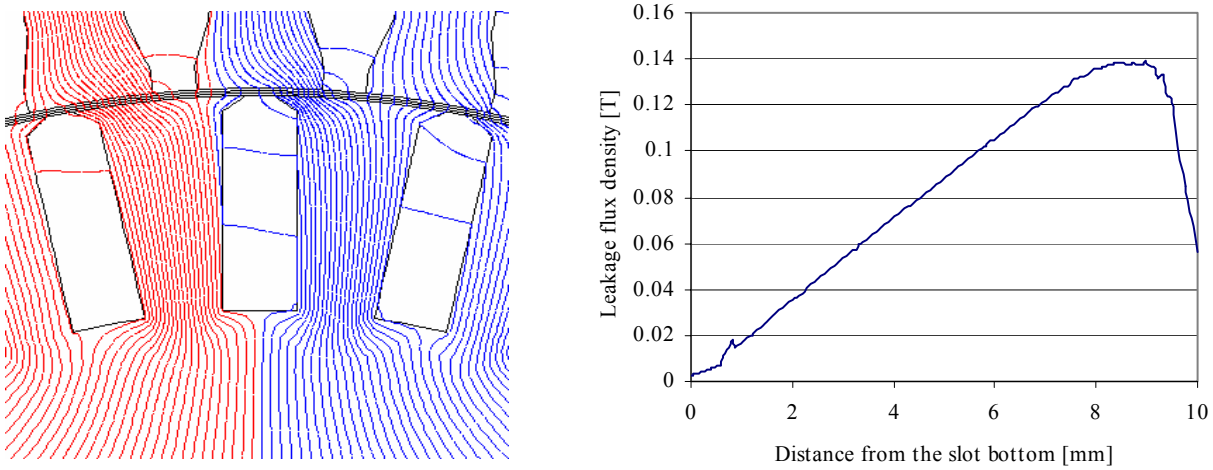

a) b)

Figure 3.10. A motor with a low slot leakage coefficient and semi-closed slots. The rotor tooth-tips saturate heavily during overloading causing the width of the slot opening to virtually increase, and thus increasing the pull-out torque, which is 4.1 p.u. for this motor type. The stator current is 22.6 A, and the slip 3.9 % (at 2.0 p.u. torque)

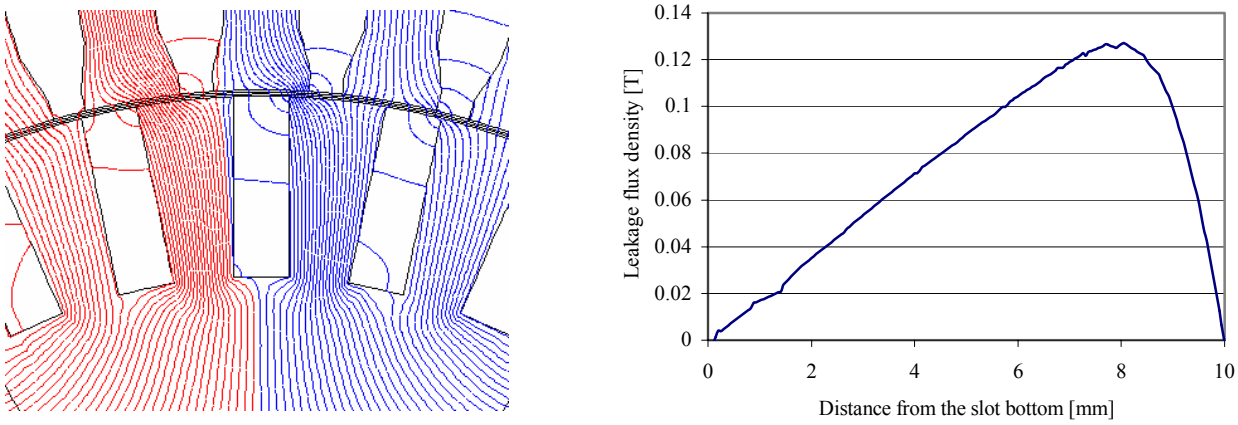

a) b)

Figure 3.11. A motor with a low slot leakage coefficient and fully open slots. The leakages are slightly lower than with the same motor with semi-closed slots, and consequently the pull-out is only slightly higher, 4.3 p.u.. This was also the prototype construction. The stator current is 23.2 A and the slip 3.7 % (at 2.0 p.u. torque).

Figures 3.7−3.11 indicate that in order to achieve a high pull-out torque, the most straightforward method is to use wide and shallow fully- or semi-open slots. In this case, the difference in the pull-out torques of the motors in Figs. 3.10 and 3.11 (3×10mm semi- or fully-open slots) is quite a small. This suggests the use of semi-closed slots, as the air gap flux harmonic content is lower. Further, when semi-closed slots are used, the rotor is more robust, as the bars are more firmly attached. It might be possible to further optimize the tooth-tips to produce a higher pull-out torque with even lower air gap harmonic content. Table 3.1 shows the characteristics of these five motor constructions at the rated and pull-out points.

Table 3.1. Characteristics of the five motor configurations at the rated and the pull-out points calculated with FEM.

Rotor configuration	Rated current [A]	Rated slip [%]	Efficiency at rated point [%]	Pull-out torque [p.u.]	Pull-out slip [%]	Torque/current at the pull-out point [Nm/A]
20mm×1.5mm closed slots	17.8	2.77	83.1	2.1	7.98	0.97
20mm×1.5mm open slots	18.5	2.05	83.7	2.8	10.3	1.05
10mm×3mm closed slots	15.9	2.10	85.5	3.3	14.0	1.04
10mm×3mm semi-closed slots	17.2	1.78	84.6	4.1	15.9	1.12
10mm×3mm open slots	18.3	1.67	84.3	4.4	17.2	1.12

Figure 3.12 shows the pull-out torques for different slot geometries calculated with FEM for the 4 kW prototype with the copper-cage rotor. The stator is the existing one from a PMSM servo (Q_s = 36). The rotors slots in Fig. 3.12 are rectangular, fully open slots with constant width 3 mm in each case. The pull-out torques were calculated as a function of the rotor slot height (for constant slot width, the slot leakage factor increases as the slot height increases), and also with three different slot opening geometries. Semi-open slots were the ones presented in Fig. 3.10, and closed slots those in Fig. 3.9. The pull-out of the motor with semi-closed slots can be affected by modifying the slot opening regions (the width of the slot opening and the height of the tooth-tip). It is a compromise between the air gap harmonics and the pull-out torque. The prototype was realized with the width of the rotor slots of 3 mm and the height of 10 mm, because the goal was to achieve 4.0 p.u. pull-out torque.

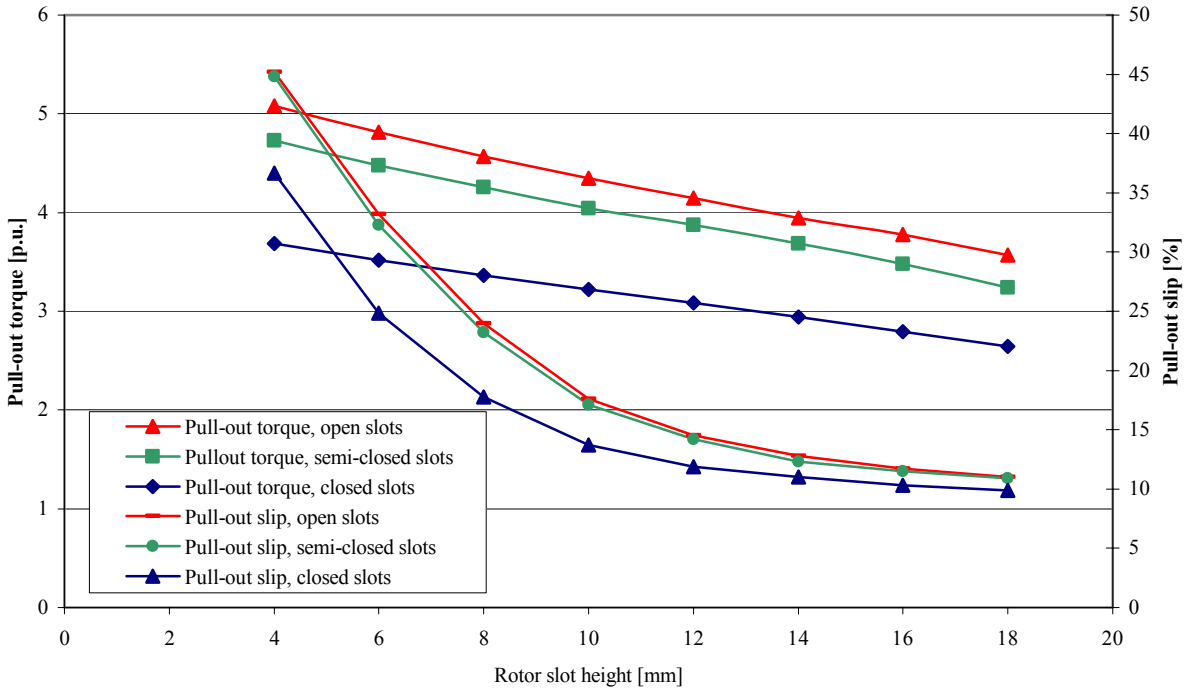

Figure 3.12. Pull-out torques and pull-out slips for different rotor slot geometries; the width of the slot is constant 3 mm in each case, and the height is varied. Three different slot opening geometries were calculated; fully closed, semi-closed and fully open. Fully open slots give the highest pull-out torque, although it is only slightly higher than with semi-closed ones.

The boundary conditions for the dimensions of the slot in the radial direction come from the maximum allowed continuous current density. In the tangential direction, the width of the slot is limited by the tooth flux density, which can be set to approx. 2−2.2 T at maximum with typical electric steels. Too deep a saturation rapidly decreases the power factor and increases the iron losses. The boundary condition for the slot opening width comes from the torque ripple allowed; the wider the slot openings, the higher the torque ripple. Also harmonics losses due to permeance harmonics under each slot increase as the slot width of the slot opening increase; and therefore also the desired efficiency limits the selection of the slot opening region. Thereby, the following procedure could be used in order to maximize the pull-out torque:

1. Set the width of the slots so that the maximum allowed tooth-flux density is obtained.
2. Set the height of the slot so that the maximum allowable slot current density is reached (E.g $J_{max} \approx 8$ A/mm^2 for air cooling).
3. Increase the width of the slot opening until the allowed cogging is exceeded or until the losses due to permeance harmonics are at the maximum value (Priority depends on the application)

3.1.4 Harmonic analysis for different slot shapes

The geometry of an induction motor slot opening has a substantial effect on the pull-out torque of the machine; the wider the slot opening, the higher the pull-out torque. The drawback in using an increased slot opening width are the increased permeance fluctuations in the air gap. Under each slot opening, there exists a local permeance minimum, which depends on the width of the slot opening. The wider the slot opening, the deeper is the sag in the flux density under it, and the larger spatial harmonics are generated in the air gap flux. This results in torque ripple, and therefore there is a clear trade-off between the pull-out torque and the torque quality. Figure 3.13 shows the calculated air gap harmonic content of the prototype induction motor with FEM for the same five rotors shown in Figs. 3.7−3.11.

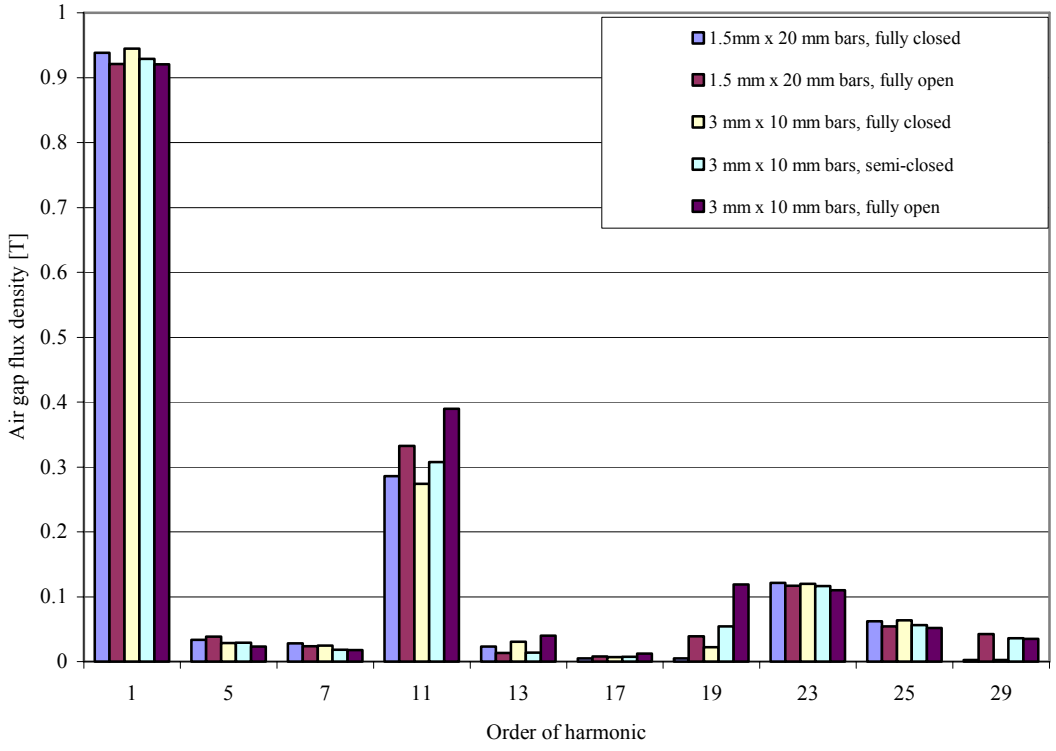

Figure 3.13. The air gap flux density harmonics with different rotor constructions ($Q_s = 36$, $Q_r = 30$). The rotor, which has the closed 3mm×10mm rotor bars, gives the highest flux density fundamental, and also the smallest low order harmonics (5th, 7th and 11th), which are the most harmful ones. Its pull-out torque is, however, low (3.25 p.u.) compared to the same rotor with semi-or fully open rotor slots. There is no significant difference in the harmonic behavior between different rotors, with the exception of the 11th and 19th harmonic on the rotor with fully open 3mm×10mm bars.

Figure 3.13 shows that the design which gives the highest pull-out torque also results in a higher harmonic content (3 mm×10 mm bars, fully open); especially the 11^{th} and the 19^{th} harmonics are significantly larger with such a design. By using semi-closed slots with a variable tooth height in the rotor, these harmonics can be effectively reduced, even though the pull-out torque is decreased only by approx. 5 %. By carefully designing the tooth-tips, it is possible to decrease the harmonic content further while increasing the pull-out torque. As stated earlier, the dimensions of the tooth-tips should be chosen in such a way that the overloading current will saturate them and thus to magnetically open them more. During normal operation, the flux flowing in teeth will cause a more sinusoidal air gap flux distribution, although the leakages are larger.

Figure 3.14 presents the harmonics of the prototype motor, which has 3mm×10mm rotor bars with fully open slots. The harmonics are calculated as a function of slip with FEM. As the slip increases, the flux lines cross the air gap in a skewed angle, and the flux distribution gets distorted as the slip increases. The air gap flux distortion can be seen in an increased harmonic content of the air gap flux, which causes more torque ripple and audible noise, but what is more important, it decreases the flux fundamental wave. The fundamental wave is further decreased during overloading, as the stator over current will cause a larger voltage drop in the stator. As the fundamental air gap flux thus decreases approximately linearly as the slip increases, the "torque reserve" of the motor starts also to decrease approximately proportional to the slip squared. This can be seen in the curvature of the speed-torque curve towards the pull-out point. When the pull-out point is reached, the fundamental wave has decreased to a value where its radial and tangential components are equal, and the flux crosses the air gap approx. in a 45° angle. As the 5^{th} and the 7^{th} harmonics are not clearly visible in Fig. 3.14, and as they are typically the most harmful ones, they are shown separately in Fig. 3.15.

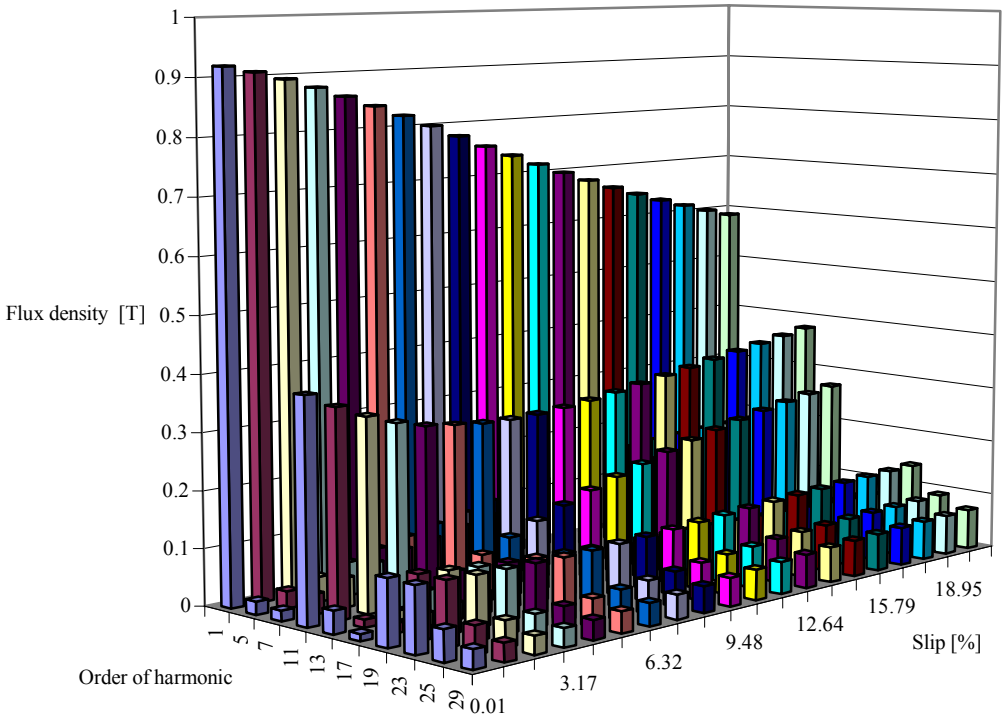

Figure 3.14. Simulated air gap flux harmonics of the prototype as a function of slip ($Q_s = 36$, $Q_r = 30$). As the slip increases, the air gap flux distortion increases the amplitudes of the air gap harmonics, and thereby decreases the fundamental wave. The fundamental wave is further decreased, as the stator voltage losses increase as a function of the stator current. The pull-out occurs at the slip s = 17.2 %.

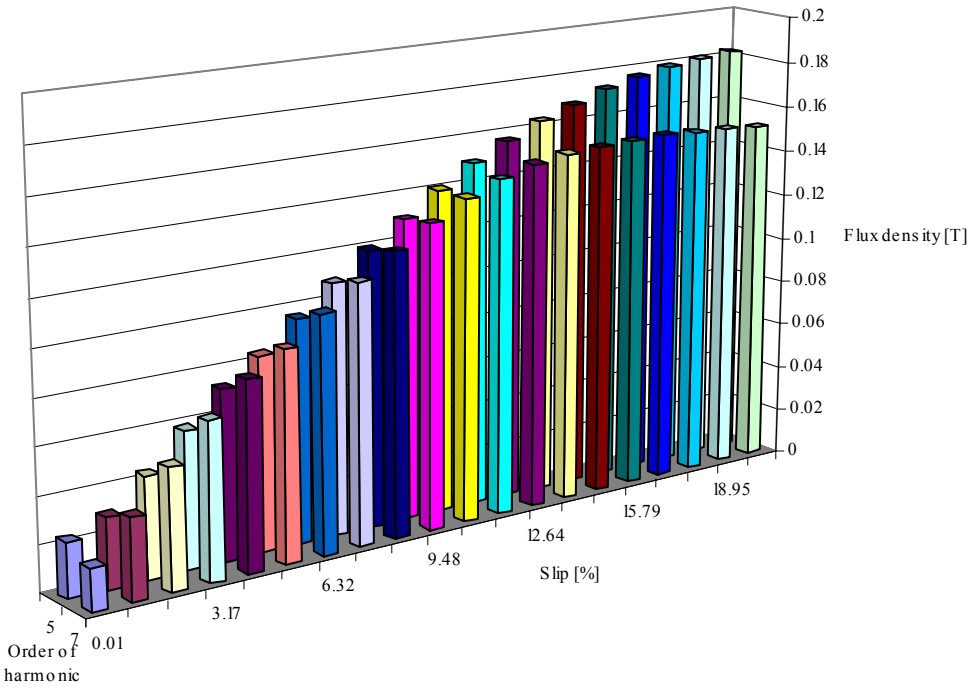

Figure 3.15. The 5th and the 7th harmonic of the air gap flux density as a function of the slip (Q_s=36, Q_r=30).

3.2 Field weakening

In a typical motion control application, the motor must frequently rotate very fast, for example during the constant speed phase of the positioning, or in a spindle drive. The maximum speed required by the system can be obtained either by dimensioning the rated speed of the motor to the vicinity of the maximum speed, or alternatively, the field weakening of the motor can be utilized. The *u*/*f* ratio, which defines the flux linkage, starts to decrease when the maximum inverter output voltage is reached and the speed is further increased. As the torque requirement at a high speed is often low, the utilization of the field weakening can considerably reduce the dimensioning of the drive. This is because the rated point of the motor can then be chosen at a lower speed, and the motor can thereby produce a higher torque at the low speed region with the given power.

Field weakening with PM machines has typically been problematic due to the constant flux set by the magnets, and the problem is further complicated when the surface magnets are used. This is because the armature reaction is very weak, which means that a high demagnetizing current would be required to produce the demagnetizing field. A high negative i_d-component leads to increased copper losses, but what is more important, only a small amount of current handling capacity is left for the machine's q-axis to produce torque. For example, with PMSM having a per-unit value 0.20 of the d-axis inductance, rated negative d-axis current would decrease the air gap flux only by 20 %. This means that the rated speed can be exceeded only by 20 %, after which the motor cannot produce torque anymore, and thus the motor can operate with 20 % over speed at no-load only. If the PMSM must operate at speeds higher than the rated one, the dimensioning of the motor must be changed in such a way that the rated speed increases, which will, as a drawback, decrease the rated torque for given output power. In practice, extending the speed range means rewinding the stator to have fewer turns in series. This is illustrated in Fig. 3.16 with an induction machine and a PMSM having $L_d = 0.20$ p.u. It is assumed that the PMSM can produce 20 % more torque with the given current than the induction machine because of the PM magnetization. If no field weakening range – or only a very short one – is required, the PMSM seems to be a more feasible solution compared to the induction machine, but if the speed range extension is required, the situation becomes totally different as the torque production capability of the PMSM decreases. If the speed range of the PMSM is extended by 20 %, it has approximately the same rated torque as with an induction motor with the assumption of 20 % higher torque-to-current ratio. In Fig. 3.16, the current for each PMSM operating points was the same.

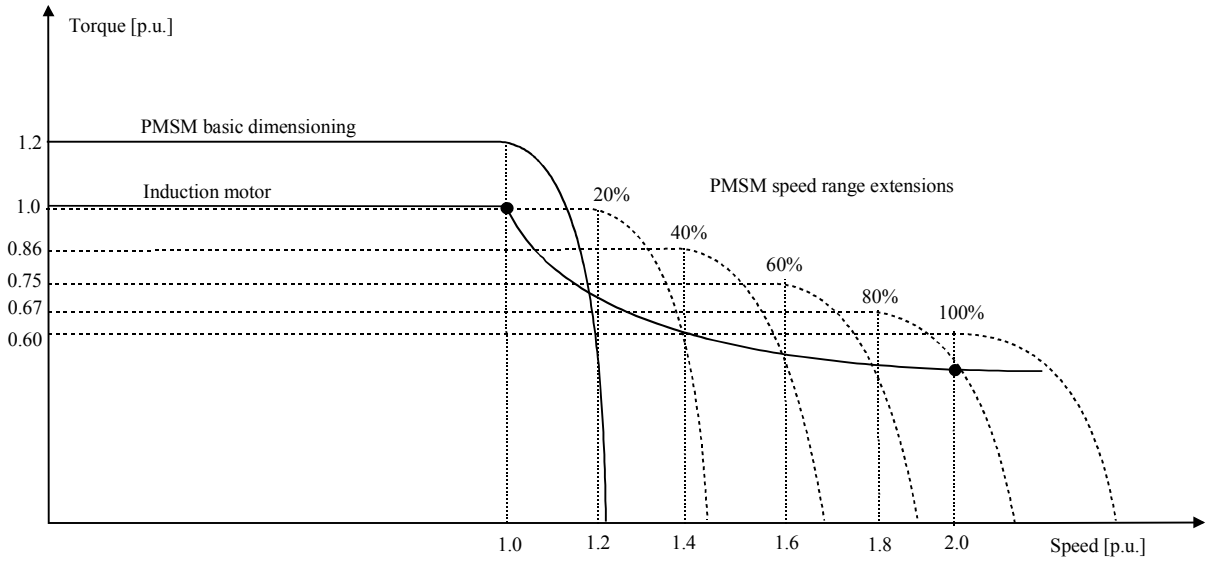

Figure 3.16. Comparison of the dimensioning of a SMPMSM and an induction motor in a drive where high-speed operation is required. It is assumed that the SMPMSM can, at the constant field range, produce a 20 % higher torque with the given current than the induction motor. The SMPMSM seems to be a more feasible solution only if no field weakening is required. Rewinding the SMPMSM to a higher speed will deteriorate the rated torque, and thus make the IM a more feasible solution.

Figure 3.16 shows how the torque production capability of a PMSM deteriorates if the motor has to be dimensioned to higher speeds, while the utilization of the induction motor field weakening has significant advantages on the torque production capability at low speeds. For example, if the motor must provide a 0.50 p.u. torque at 2.0 p.u. speed – which means rated power – the rated speed of the PMSM must be located to approx. 1.80 p.u. (compared to the IM rated speed). Such a dimensioning will result in nearly 70 % higher rated torque of an induction motor compared to a PMSM having $L_\mathrm{d} = 0.20$ per-unit value. In Fig. 3.16, it is assumed that the induction motor current is approx. 20 % larger than the PMSM current, which is the case if the induction motor power factor is approx. 0.80 (and the PMSM $\cos(\varphi) \approx 1$). With saturable induction machines – particularly if multiple pole pairs is used – the power factor, however, is much lower, and consequently the current higher than 20 % of the PMSM current. At the end of this chapter, it is discussed how the poor torque-to-current ratio of such a motor can be improved with proper flux control.

The field weakening of a PMSM may be conveniently studied with the so-called current-limit circle and the voltage-limit ellipses. During the field weakening, the proportion of the resistive voltage drop of the stator voltage is negligible. The equation for the stator voltage u_s can then be written in the form

$$u_\mathrm{s} = \sqrt{\left(\omega_\mathrm{s}\psi_\mathrm{PM} + \omega_\mathrm{s}L_\mathrm{d}i_\mathrm{d}\right)^2 + \left(\omega_\mathrm{s}L_\mathrm{q}i_\mathrm{q}\right)^2} \quad , \tag{3.22}$$

where ω_s is the electrical angular frequency, ψ_PM the PM flux linkage, L_d and L_q the synchronous inductances in the d- and q-directions, respectively, and i_d and i_q the stator currents in the d- and q-axes, respectively. The stator voltage u_s is limited by the supply and the inverter voltage rating,

$$u_s \leq u_{max} \quad . \tag{3.23}$$

By substituting Eq. (3.23) into (3.22), squaring and dividing by ω_s squared, an equation for the voltage-limit ellipse is given in the form

$$(\psi_{PM} + L_d i_d)^2 + (L_q i_q)^2 = \left(\frac{u_{max}}{\omega_s}\right)^2 \quad . \tag{3.24}$$

The stator current i_s is limited by the inverter current rating, and by dividing it into d- and q-components, an equation for the current-limit circles can be written as

$$i_d^2 + i_q^2 \leq i_{max}^2 \quad . \tag{3.25}$$

Equations (3.24) and (3.25) define entirely the allowed current vectors in the i_d-i_q plane, as the current vector must in all conditions fulfil both of these equations. In Fig. 3.17, the voltage-limit ellipses and the current-limit circle are plotted in the i_d-i_q plane.

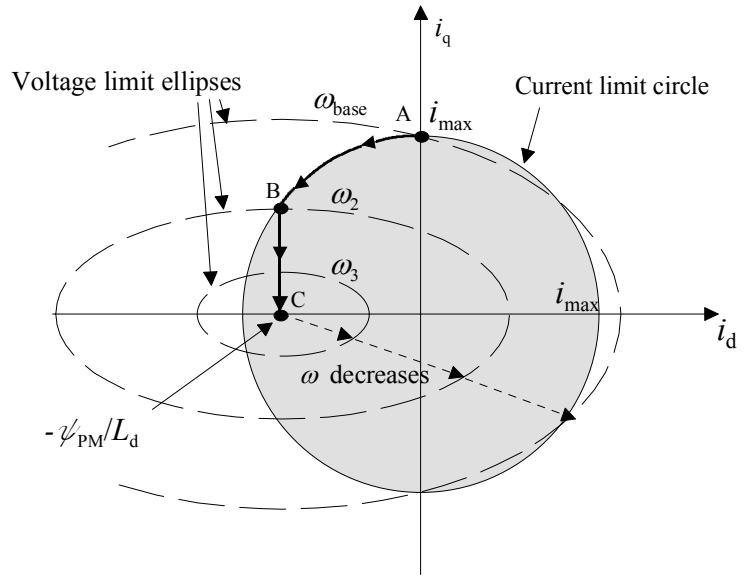

Figure 3.17. Current-limit circle and voltage-limit ellipses of the PMSM. Different ellipses represent different speeds (the speed increases towards the point C). In the figure $\omega_{base}<\omega_2<\omega_3$, and the maximum torque is always obtained by using as high a q-axis current component as possible. The maximum torque trajectory between the points A and C is marked with an arrowed line.

From zero up to the base speed ω_{base}, the operation of the motor is limited by the current limit circle, not by the voltage limit ellipses. Below the base speed, the voltage increases linearly, and the maximum torque is obtained at point A, where all the current is on the q-axis of the machine. The situation corresponds to the $i_d = 0$ control. The base speed is thereby defined as

$$\omega_{\text{base}} = \frac{u_{\text{max}}^2}{\sqrt{\left(\psi_{\text{PM}} + L_{\text{d}} i_{\text{d}}\right)^2 + \left(L_{\text{q}} i_{\text{q}}\right)^2}} \quad . \tag{3.26}$$

Between the points A and B both the current and the voltage are at their maximum values, and the maximum torque can be obtained, if the current vector follows the intersecting trajectory of the voltage-limit ellipse and the current-limit circle up to the point B. This explains why the torque production of a PMSM typically collapses so rapidly after the base speed. Right after the base speed, the q-axis current decreases only slightly, but as the field weakening proceeds deeper, the i_{q} must be decreased faster and faster, and consequently the torque collapses. Beyond the point B, the current-limit circle will not limit the drive any longer, and the maximum torque can be obtained by setting the i_{q} to a maximum value with regard to voltage-limit ellipse. Between the points B and C, the maximum torque can be obtained if the demagnetizing current is set constant, and the q-axis current is decreased linearly with the voltage limit ellipse. Therefore, also the total current decreases from the rated value. In general, to produce the maximum torque during the field weakening, the q-axis current should be always set as high as possible with these two boundary conditions. Point C is the theoretical upper limit for the field weakening, where the torque production capability of the motor reaches zero. The location of the point C is defined by the machine's d-axis inductance L_{d} and the PM flux linkage ψ_{PM}

$$i_{\text{d}} = -\frac{\psi_{\text{PM}}}{L_{\text{d}}} \quad , \tag{3.27}$$

and it determines to a large degree the field weakening characteristics of the PMSM. The higher the machine's d-axis inductance and the smaller the PM flux linkage, the closer to the origin the point C is located. With industrial PM machines having embedded magnets, the per-unit value for Eq. (3.27) can be below unity, and the point C is located inside the current-limit circle, as illustrated in Fig. 3.17. The field weakening characteristics of such a motor are good, but as a drawback, due to the smaller PM flux linkage, the torque density is typically lower.

PMSMs with surface magnets have low direct-axis inductances, and further, if high dynamic performance is required, thick magnets are applied, which makes the PM flux linkage high and further decreases the L_{d} value. Due to these factors combined, the field weakening characteristics of such a machine are poor, since according to Eq. (3.27), the point C is then located far on the left outside the current limit circle. With such a motor, the speed range beyond point B in Fig. 3.17 is not possible, as the torque production capability goes to zero already at the point B. The point B is located on the i_{d}-axis, and the demagnetizing current equals the rated one. No current capacity is left for the q-axis to produce torque. The situation is illustrated in Fig. 3.18. The lower the L_{d} value of the machine and the higher the PM flux linkage, the sooner the point B is reached, and the narrower is the field weakening range of the motor.

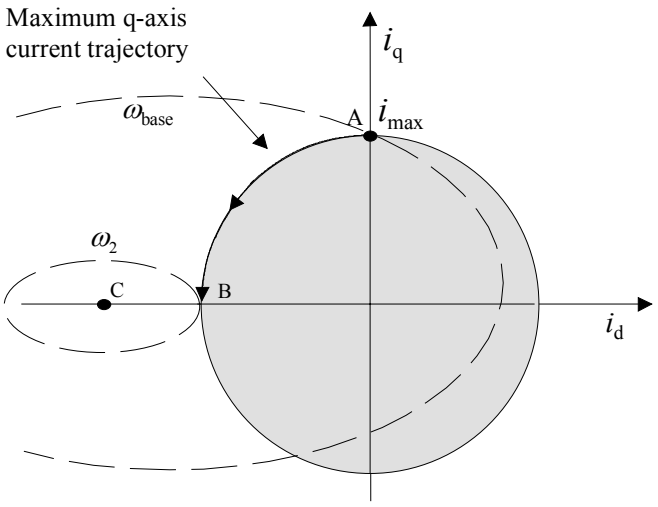

Figure 3.18. Current-limit circle and voltage limit ellipses for a PMSM with surface magnets and low d-axis inductance. The torque production of the machine drops to zero at point B, and the speed range beyond ω_2 cannot be obtained. This is the case with most PMSM servomotors.

Speed ω_2, where the torque production goes to zero can be expressed as

$$\omega_2 = \frac{u_{max}}{\psi_{PM} - L_d i_{max}} \quad . \tag{3.28}$$

In Eq. (3.28) the minus sign is used, because the demagnetizing current is negative. According to the measurements made at LUT for eight commercial PMSM servomotors, the back-electromotive forces varied between 0.8−1.08 p.u., and the d-axis inductances between 0.15−0.35 p.u.. The field weakening range for such motors becomes therefore very short. For example, if the machine has ψ_{PM} 0.90 p.u. and the L_d 0.25 p.u., the speed at which the motor torque production goes to zero is slightly above 1.5 p.u.. It must be noted, however, that the machine can operate at this speed only at no-load, and the torque production starts to rapidly decrease beyond the base speed. It should be remembered though, that often the rated voltage of a PMSM servo is somewhat lower than the grid voltage (400 VAC in Finland), for example 330 V (which is the case with the PMSM servo studied here). This gives the possibility to increase the motor voltage, if necessary during the field weakening. Increasing the voltage from 330 V up to 400 V will therefore increase the constant flux range by approx. 20 %. Figure 3.19 illustrates the analytically calculated field weakening characteristics of non-salient pole PMSMs with different L_d values.

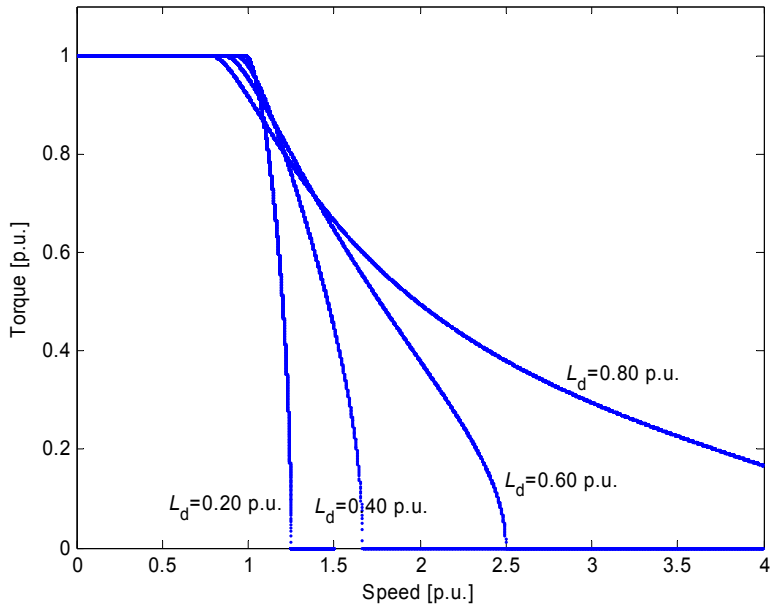

Figure 3.19. Field weakening characteristics of PMSMs with $L_d = L_q$ and $\psi_{PM} = 0.98$ p.u.. $i_s = 1.0$ p.u.. The higher the direct-axis inductance, the better is the torque production capability during the field weakening. If ψ_{PM} equalled to $L_d i_d$, in theory, infinite constant speed region would result.

Figure 3.19 shows that although the field weakening characteristics of PMSMs with low L_d are poor, they can produce somewhat higher rated power, because the rated torque can be produced at somewhat higher speed than with a PMSM having a higher L_d. Controversially, this would mean that if the two machines have equal rated speeds, the one with the lower L_d can produce a higher torque at the rated speed. The situation is illustrated in Fig. 3.20 by similarly illustrating the motor output powers.

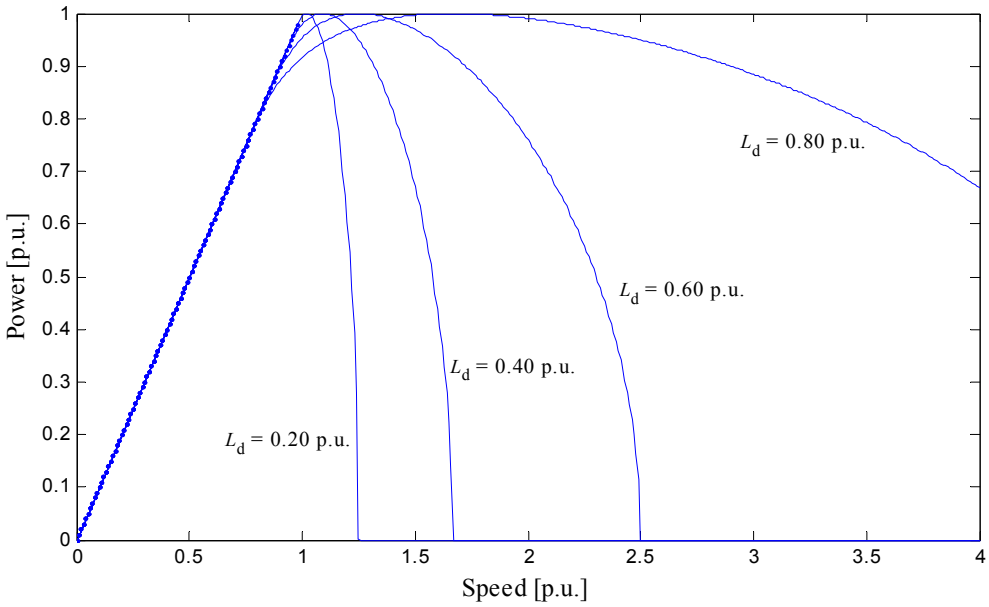

Figure 3.20. Output power of PMSMs with $L_d = L_q$ and $\psi_{PM} = 0.98$ p.u. and $i_s = 1$ p.u.. Because of the lower power factor (if $i_d = 0$), PMSM with a higher L_d value cannot produce as high power at the rated speed as the one having a lower L_d. It must be noted that below the rated speed, where the output powers are equal, the machine with the highest L_d value draws the largest apparent power due to poorest power factor (voltage is higher). The curves are calculated analytically, and the stator resistive voltage loss is neglected.

Higher armature reaction of a PMSM with a higher L_d value causes that the stator flux linkage amplitude of such a machine – and consequently the stator voltage – is higher, and therefore such a machine reaches sooner the inverter limit voltage. At that point (=base speed), the torque starts to decrease, as a part of the current is required on the d-axis for demagnetization. Beyond the base speed, the current vector starts to rotate towards the negative d-axis, while the stator voltage vector rotates towards the positive q-axis, which means that the power factor starts to rapidly increase as the speed is further increased. This explains why the output power still increases beyond the base speed. At the point where the two vectors are overlapping, the machine produces the maximum output power ($u_s = i_s = 1.0$ p.u., $\cos(\varphi) = 1$). Beyond this point, the power factor is capacitive and the output power starts to decrease. The smaller is the L_d value, the sooner after the base speed the maximum power point (=unity power factor point) occurs, as the power factor of such a machine is near unity even at the rated operating region. As it can be seen in Fig. 3.20, with a PMSM having $L_d = L_q = 0.20$ p.u., the point is practically the same as the rated speed, while with a PMSM having $L_d = L_q = 0.80$ p.u., the maximum power is obtained approx. at 1.7 p.u. speed. The situation is illustrated in Fig. 3.21 with the vector diagrams for the non-salient PMSMs having 0.20 p.u. and 0.80 p.u. synchronous inductances and operating at equal voltage and current (=1.0 p.u.). In here, the term "field weakening" corresponds to the situation, where the negative d-axis current component exists. PMSMs having low d-axis inductance can be operated in such a way, that only beyond the base-speed, the demagnetizing current component is applied, but PMSMs having higher inductances, this may not be practical because of the higher stator current. With such machines having high L_d, demagnetizing stator current is often used even below the base speed to increase the power factor. In such a case, the machine operates in "field weakening" already below the base speed.

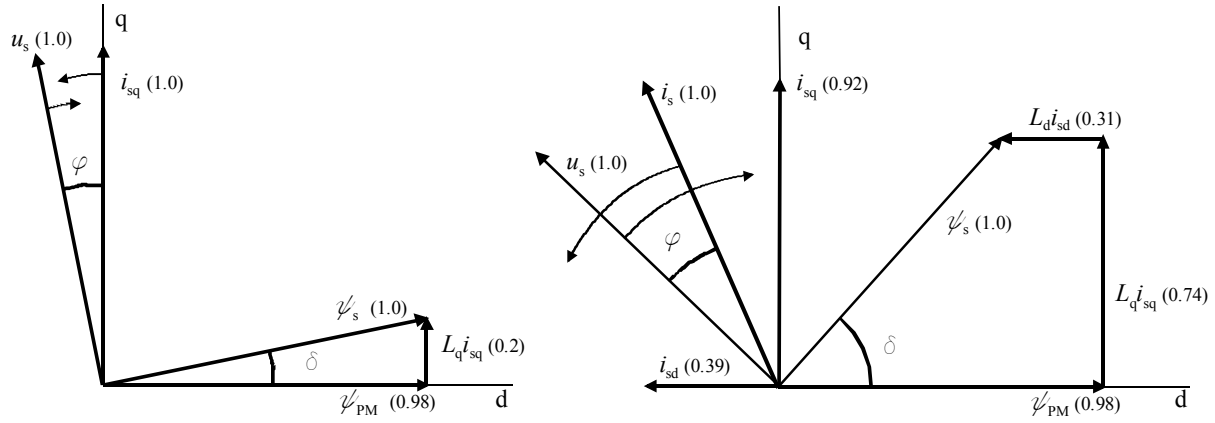

Figure 3.21. Non-salient PMSMs having synchronous inductances a) 0.20 p.u. and b) 0.80 p.u. operating at equal voltage and current (=1.0 p.u.). Because of the higher armature reaction, the machine in Fig. b) is already in the field weakening region to keep the stator voltage below unity, and thus it can produce less torque than the machine in Fig. a). The arrows indicate the direction of rotation of the current and the voltage vectors during field weakening.

As it can be seen in Fig. 3.21, a PMSM having higher inductances must enter the field weakening region earlier than a machine having lower ones, if the maximum limit voltages and the currents are equal. The output power of the machine having higher inductances increases far beyond the base speed, as the power factor starts to increase. In practice, this means that the torque decreases slower than the speed increases. Maximum output power is obtained at unity power factor, when the voltage and the current vectors are overlapping. The same phenomenon occurs also with the machine having low inductances, but it is far more unnoticeable, as the maximum output power condition occurs only slightly beyond the base speed.

3.2.1 Induction motor field weakening

With modern vector controlled induction motors drives, the flux of the motor can be controlled, which enables the utilization of the field weakening. When the voltage reaches the maximum value defined by the supply and the speed is further increased, the air gap flux starts to decrease in proportion to the frequency, which is known as field weakening. The field weakening of induction motors can be analyzed by using vector diagrams, shown in Fig. 3.22.

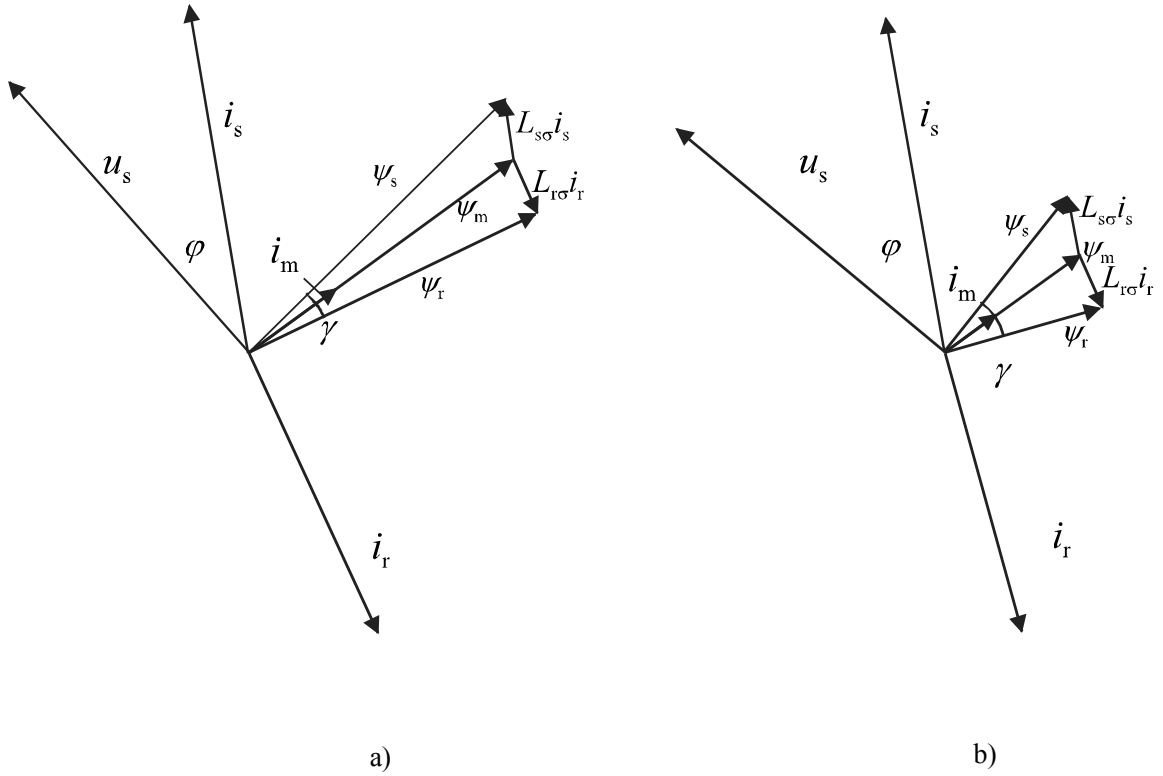

Figure 3.22. Vector diagrams of an induction machine, $L_{s\sigma} = 0.2$, $L_{r\sigma} = 0.2$, $L_m = 3$ a) Motor operating at its rated point at rated torque and at rated current. The angle γ between the rotor flux linkage vector ψ_r and the stator flux linkage vector ψ_s is relatively small. b) Induction motor operating at its rated current at twice its rated speed. As the stator flux linkage vector ψ_s has decreased to a half of the rated value, but the leakage fluxes $L_{s\sigma}i_s$ and $L_{r\sigma}i_r$ have remained somewhat constant, the angle γ has increased significantly, and the motor is operating near by its pull-out point.

Figure 3.22 clearly shows the significance of the leakage inductances for the field weakening characteristics of an induction motor. As the motor enters the field weakening, its stator flux ψ_s starts to decrease inversely proportional to the frequency, and the angle γ between the stator and the rotor flux linkage vectors starts to increase as the leakages remain approximately constant. The field weakening region can be further divided into two sub-regions. The region, where the torque decreases inversely proportional to the frequency, is called the constant power region, as the power is a product of the torque and the angular velocity. Equation (3.11) earlier stated that the pull-out torque decreases in proportion to the frequency squared, which means that also the pull-out slip decreases proportionally to the frequency squared during the field weakening. At the constant power region, the per unit slip remains approximately constant, which means that the slip that produces the constant power starts to approach the decreasing pull-out slip as the speed increases. At the point where the slip equals the pull-out slip, the angle γ is approximately 45°. In order to avoid the pull-out of the motor from occurring, beyond this point the torque of the motor must be decreased in proportion to the frequency squared, and thereby the operation is limited by the pull-out torque instead of the thermal limits. This operating range, where the torque must be decreased proportionally to the frequency squared is called the high-speed region. In practice, there has to be a safety margin between the pull-out slip and the operating slip.

In practice, the motor can produce a slightly higher than the rated power during the field weakening. This is mainly because of the decreasing flux level, which means that the required magnetizing current decreases as the speed increases (and the flux decreases). Further, if the motor is dimensioned to a high flux density level to provide a high dynamic performance (such as servomotors), the decrease in the magnetizing current can be significant when the iron path returns to the linear region in the *BH* curve. As the magnetizing current decreases, more current capacity is left for the machine's q-axis to produce torque, and therefore the motor can produce a higher than the rated power with the rated current. Further, if there is an integrated fan on the shaft, the cooling of the motor improves during the field weakening (although the cooling device itself somewhat increases the losses as the speed increases). Also the convection heat transfer coefficients from the rotor surface increase, due to increased peripheral speed of the rotor. In Fig. 3.23, three operation regions of an induction motor are illustrated with the standard 30 kW, four-pole cage induction motor discussed previously. It must be borne in mind that with standard machines, the speed range is typically limited by the mechanical robustness of the rotor rather than by the pull-out torque (the maximum allowed speed is given by the manufacturer).

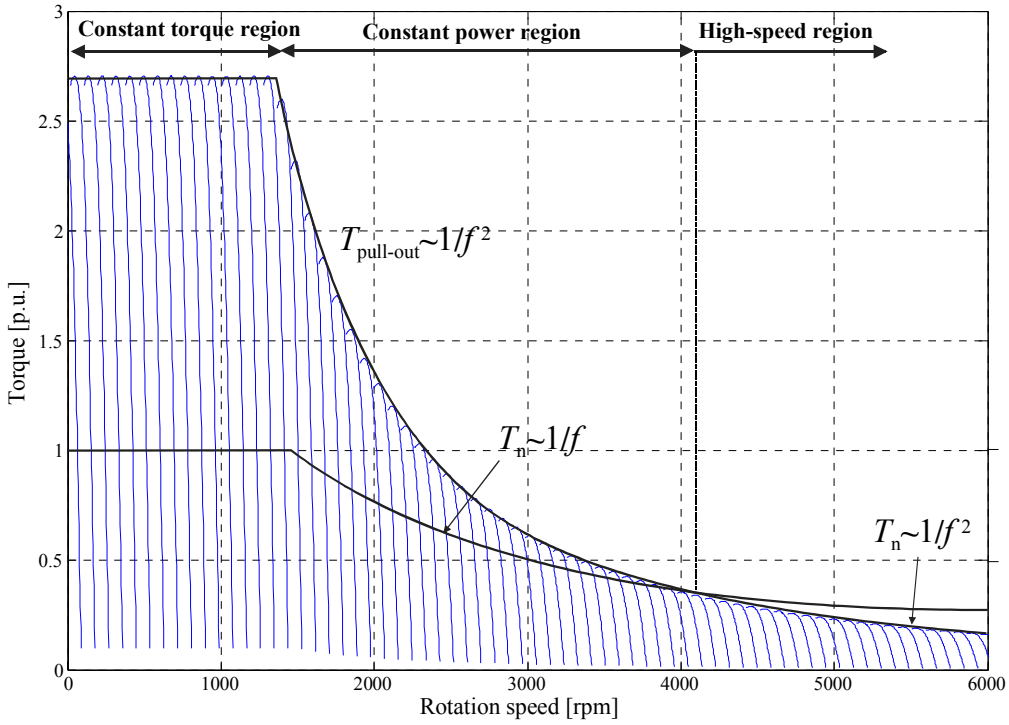

Figure 3.23. Different operating regions of a standard 30 kW four-pole induction motor calculated analytically using the single-phase equivalent circuit. L_{sc} = 0.36, L_m = 3. The value of the pull-out torque is approx. 2.7 p.u.. The constant power region ends at the point, where the pull-out torque has decreased so low that it equals the constant power curve.

The higher the leakages of an induction motor, the sooner the armature reaction causes the angle between the stator and the rotor flux linkage vectors to reach the value of 45°, which is the end of the constant power range. By minimizing the motor leakages with the techniques presented earlier, the pull-out torque can be increased, which consequently yields to an extended constant power range. It is particularly the pull-out torque of the motor that defines the length of the constant

power range. The frequency, at which the pull-out torque equals the constant power producing torque, is the theoretical maximum frequency of the constant power region. The constant power producing torque decreases inversely proportional to the frequency, and the pull-out torque inversely proportional to the frequency squared, and by setting them equal

$$\frac{f_{\mathrm{n}}}{f_{\mathrm{s,max-cp}}} T_{\mathrm{n}} = \left(\frac{f_{\mathrm{n}}}{f_{\mathrm{s,max-cp}}} \right)^2 T_{\mathrm{pull-out}} \quad , \tag{3.29}$$

where f_{n} is the rated frequency, $f_{\mathrm{s,max\text{-}cp}}$ the maximum constant power frequency, T_{n} the constant power producing torque, and $T_{\mathrm{pull\text{-}out}}$ the pull-out torque. By solving the maximum constant power stator frequency $f_{\mathrm{s,max\text{-}cp}}$

$$f_{\mathrm{s,max-cp}} = f_{\mathrm{n}} \frac{T_{\mathrm{pull-out}}}{T_{\mathrm{n}}} \ , \tag{3.30}$$

it is evident that the per unit pull-out torque directly defines the length of the constant power range of an induction motor. For example, an induction motor having a per unit pull-out torque of 4.0 p.u. can produce the rated power even at a speed, which is four times the rated speed. Figure 3.24 illustrates the FEM calculated slip and torque values for the constant power and pull-out operations of the prototype motor.

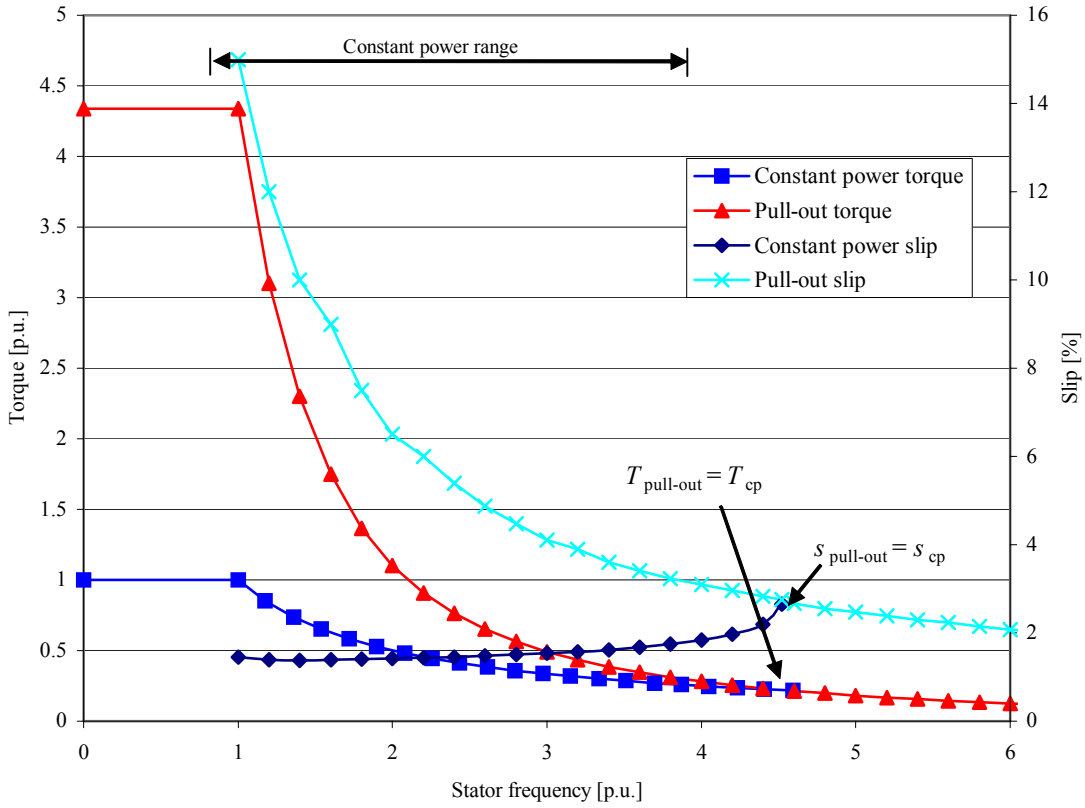

Figure 3.24. Torque characteristics of the prototype motor during the field weakening calculated with FEM. The maximum frequency, at which the motor can still produce its nominal power, is approximately 4.4 times the nominal frequency. The per-unit pull-out of the motor is also 4.4 times the rated torque. The constant power producing slip is not constant, as it theoretically should be, but it slightly increases with the increasing frequency.

Leakage inductances are therefore extremely important parameters in applications, in which both high overloading capability and field weakening are required, as they define the pull-out torque and the length of the constant power range of an induction motor. Figure 3.25 shows the analytically calculated torque-speed curves of the prototype induction motor in two cases to illustrate the significance of the leakage inductances for both the overloading capability and for the field weakening characteristics. Figure 3.25 a) shows the curves of the prototype motor, while Fig. 3.25 b) illustrates the same motor with all the slot (stator and rotor) radial dimensions doubled and tangential ones cut into half. This means that the slot leakage factors have approximately quadrupled, which implies that the total leakage will be nearly double. Consequently, the effect on the pull-out torque and on the constant power range is approximately the same. Of course, doubling the slot depth would lead to an increased stator outer diameter; therefore, the following figures are here only to illustrate the significance of the (slot) leakage.

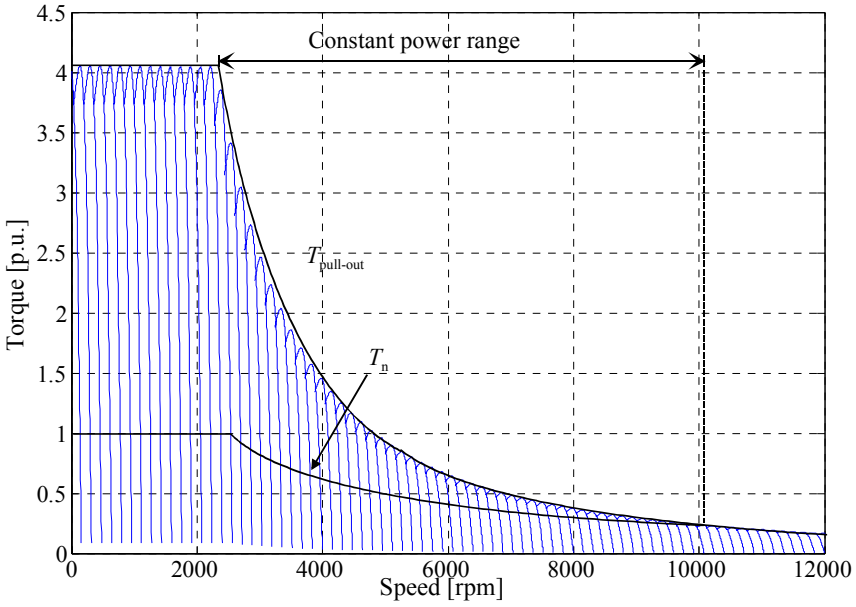

a)

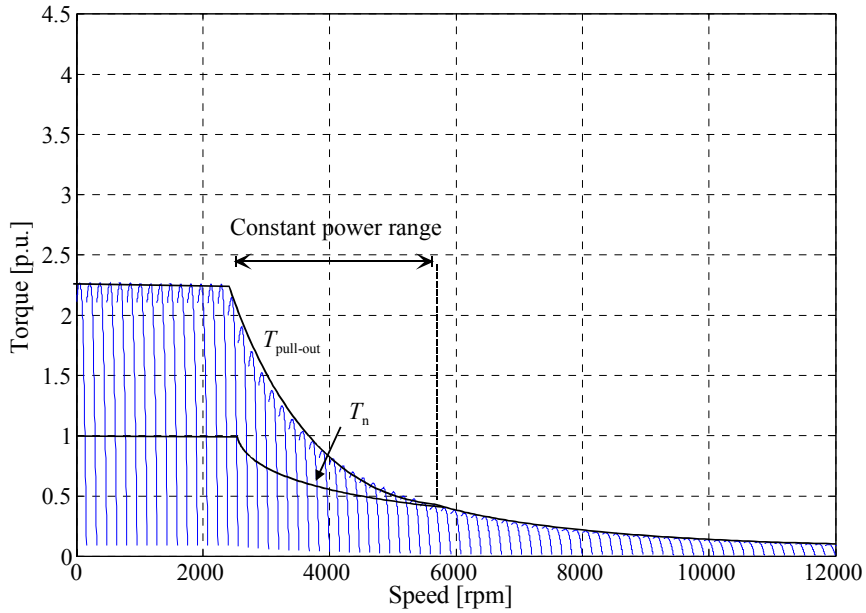

b)

Figure 3.25. Speed-torque curves of the prototype motor with different supply frequencies calculated analytically. a) Prototype motor and b) the same motor with all the slot radial dimensions doubled and tangential ones cut into half. Constant power range of the motor in Fig. a) extends to four times the base speed, while the power range in Fig. b) reaches only slightly above twice the base speed. The figures are in the same scale for visual purposes.

Figure 3.25 shows the substantial effect of an induction machine's leakage on the pull-out torque, and further, on the field weakening characteristics, since these two are closely related. By properly

designing the machine to have a low leakage, a high pull-out torque and a long constant power range can be achieved, both being favourable characteristics in motion control applications.

3.3 Torque-to-current ratio

With PMSM, by controlling the d-axis current, either the unity power factor or a minimum current operation can be achieved. The latter one represents the $i_d = 0$ control principle, where all the current is on the machine's q-axis to produce torque. When the inductances in both directions are small, the armature reaction in the q-axis direction is also small, and both the maximum T/I ratio and high power factor will result. With the $i_d = 0$ control, the stator flux linkage can be expressed as a sum of the flux set by the magnets ψ_{PM} and the q-axis armature reaction $L_{sq}i_{sq}$

$$\psi_s = \sqrt{\psi_{PM}^2 + \left(\frac{T_{em} L_{sq}}{\frac{3}{2} p \psi_{PM}} \right)^2} \quad . \tag{3.31}$$

As it can be seen in Eq. (3.31), if the q-axis inductance is high, the angle between the PM and the stator flux linkages becomes high with the $i_d = 0$ control, and accordingly, the power factor is poor. In addition to a poor power factor, the high q-axis armature reaction causes the stator flux linkage amplitude to increase, which means that as a result, also the stator voltage has to be increased. This will decrease the speed range of the motor, or consequently, leave a smaller voltage margin, both of which might be problematic, should a high-speed operation be required. With PMSM servos having a low L_d (+ low L_q) value, it is practical to use $i_d = 0$ – control. When the $i_d = 0$ control is applied, the inverter current is somewhat higher than the motor current due to the lagging power factor, and also the stator voltage is somewhat higher due to higher stator flux linkage. If an equal *stator* current is applied with unity power factor control, the inverter current will be lower, but the motor produces a lower torque, as part of the current goes for the PM-flux demagnetization. Furthermore, as the voltage is also lower with the unity power factor control, the inverter losses are somewhat lower. However, as the motor produces less torque, the effect on the inverter efficiency may be negligible. The fundamentals of unity power factor and $i_d = 0$ controls were discussed in Chapter 2, and in the following, flux control principles for an induction motor in order to increase its running characteristics are introduced.

3.3.1 Induction motor flux optimization

As the torque production capability of an electric motor is proportional to the air gap flux density squared, it is beneficial to use high flux densities, particularly in high torque machines. This is especially important in servomotors, where a high pull-out torque is required. Further, a high air gap flux density also causes the induction motor to run at a lower slip, which increases the dynamic response during transients and decreases the rotor losses. With servomotors, the maximum air gap flux density can be chosen to be near 1.0 T, while with standard motors, it is typically lower, 0.5−0.9 T. High flux levels, however, decrease the magnetizing inductance due to the saturation of iron, and a higher proportion of the current is required for magnetization instead of torque production. This can be seen in lower power factor values and in the poorer torque-to-current ratio. Also high flux densities cause excessive iron losses in addition to higher stator copper losses due to the higher magnetization current. These drawbacks, however, can be avoided

by properly adjusting the induction machine flux level, depending on the operation point. The main idea is to lower the flux density level, when the motor operates below its maximum loadings. Only when a high overloading is required, for example during acceleration or deceleration, the flux level is increased to its maximum value to provide an adequate torque. It must be noted, however, that this applies especially for induction machines having a high magnetic loading (high flux levels), such as the prototype motor.

The expression for the electromagnetic torque of an induction motor can be derived from the single-phase equivalent circuit, where the stator flux linkage can be expressed as

$$\boldsymbol{\psi}_\mathrm{s} = L_\mathrm{s}\boldsymbol{i}_\mathrm{s} + L_\mathrm{m}\boldsymbol{i}_\mathrm{r} = L_{\mathrm{s}\sigma}\boldsymbol{i}_\mathrm{s} + \boldsymbol{\psi}_\mathrm{m} \quad , \tag{3.32}$$

where $\boldsymbol{\psi}_\mathrm{s}$ is the stator flux linkage vector, L_s the stator inductance, L_m the magnetizing inductance, $L_{\mathrm{s}\sigma}$ the stator leakage inductance, $\boldsymbol{i}_\mathrm{s}$ the stator current vector, and $\boldsymbol{\psi}_\mathrm{m}$ the magnetizing flux linkage vector. The rotor current can be solved from a similar equation of the rotor flux linkage

$$\boldsymbol{i}_\mathrm{r} = \frac{\boldsymbol{\psi}_\mathrm{r} - L_\mathrm{m}\boldsymbol{i}_\mathrm{s}}{L_\mathrm{r}} \quad , \tag{3.33}$$

where $\boldsymbol{i}_\mathrm{r}$ is the rotor current vector, $\boldsymbol{\psi}_\mathrm{r}$ is the rotor flux linkage vector, and L_r the rotor inductance. The electromagnetic torque can therefore be expressed with the cross-field principle

$$\boldsymbol{T}_\mathrm{em} = \frac{3}{2}p\boldsymbol{\psi}_\mathrm{s} \times \boldsymbol{i}_\mathrm{s} = \frac{3}{2}p\left[L_\mathrm{s}\boldsymbol{i}_\mathrm{s} + \frac{L_\mathrm{m}}{L_\mathrm{r}}\left(\boldsymbol{\psi}_\mathrm{r} - L_\mathrm{m}\boldsymbol{i}_\mathrm{s}\right)\right] \times \boldsymbol{i}_\mathrm{s} = \frac{3}{2}p\frac{L_\mathrm{m}}{L_\mathrm{r}}\boldsymbol{\psi}_\mathrm{r} \times \boldsymbol{i}_\mathrm{s} \quad , \tag{3.34}$$

where p is the number of pole pairs. Equation (3.34) simplifies into the latter form, as the cross-product of the current vector $\boldsymbol{i}_\mathrm{s}$ with itself is zero. In a synchronously rotating rotor reference frame, the flux linkage vector $\boldsymbol{\psi}_\mathrm{r}$ and the stator current vector $\boldsymbol{i}_\mathrm{s}$ may be divided into components, and the torque can be expressed in the form

$$T_\mathrm{em} = \frac{3}{2}p\frac{L_\mathrm{m}}{L_\mathrm{r}}\left(\psi_{\mathrm{rd}}i_{\mathrm{sq}} - \psi_{\mathrm{rq}}i_{\mathrm{sd}}\right) \quad . \tag{3.35}$$

If the co-ordinate system is fixed to the rotor flux linkage vector, no q-axis component will be present, $\psi_{\mathrm{rq}} = 0$. The latter term in Eq. (3.35) vanishes. Steady-state rotor voltage equation can be expressed

$$\begin{aligned} u_{\mathrm{rd}} &= R_\mathrm{r}i_{\mathrm{rd}} + \frac{\mathrm{d}}{\mathrm{d}t}\left(\psi_{\mathrm{rd}}\right) - \left(\omega_\mathrm{r} - p\Omega\right)\psi_{\mathrm{rq}} = 0 \\ u_{\mathrm{rq}} &= R_\mathrm{r}i_{\mathrm{rq}} + \frac{\mathrm{d}}{\mathrm{d}t}\left(\psi_{\mathrm{rq}}\right) + \left(\omega_\mathrm{r} - p\Omega\right)\psi_{\mathrm{rd}} = 0 \end{aligned} \quad , \tag{3.36}$$

and because $\psi_{\mathrm{rq}} = 0$, this simplifies into form

$$R_{\mathrm{r}} i_{\mathrm{rd}} + \frac{\mathrm{d}}{\mathrm{d}t}\left(\psi_{\mathrm{rd}}\right) = 0$$
$$R_{\mathrm{r}} i_{\mathrm{rq}} - \left(\omega_{\mathrm{r}} - p\Omega\right)\psi_{\mathrm{rd}} = 0 \quad , \tag{3.37}$$

where R_{r} is the rotor resistance, ω_{r} the electric angular speed, and Ω the mechanical angular speed. The no-load time constant of the rotor is long compared to the stator time constant, typically 0.15−1.5 s depending on the induction motor size. During a fast torque transient, the fast dynamic response with vector control is obtained by rapidly changing the stator flux linkage, while keeping the rotor flux linkage constant. The rate of change, at which the stator flux linkage of an induction motor can be altered, depends on the available voltage reserve, and on the stator transient inductance L'_{s}, defined according to Vas (1998) as

$$L'_{\mathrm{s}} = L_{\mathrm{s}\sigma} + \frac{L_{\mathrm{m}} L_{\mathrm{r}\sigma}}{L_{\mathrm{r}\sigma} + L_{\mathrm{m}}} = L_{\mathrm{s}} - \frac{L_{\mathrm{m}}^2}{L_{\mathrm{r}}} \quad , \tag{3.38}$$

where $L_{\mathrm{s}\sigma}$ and $L_{\mathrm{r}\sigma}$ are the stator and the rotor leakage, respectively, and L_{m} is the magnetizing inductance. L_{s} and L_{r} are the stator and the rotor inductances, respectively.

According to Eq. (3.37), constant rotor flux linkage means that $i_{\mathrm{rd}} = 0$, and the angle between the rotor current and flux linkage vector is 90º. The direct-axis rotor flux linkage in the steady-state therefore becomes

$$\psi_{\mathrm{rd}} = L_{\mathrm{r}} i_{\mathrm{rd}} + L_{\mathrm{m}} i_{\mathrm{sd}} = L_{\mathrm{m}} i_{\mathrm{sd}} \quad . \tag{3.39}$$

By substituting this into Eq. (3.35), the equation of the torque can be given in the form

$$T_{\mathrm{em}} = \frac{3}{2} p \frac{L_{\mathrm{m}}^2}{L_{\mathrm{r}}} i_{\mathrm{sq}} i_{\mathrm{sd}} \quad . \tag{3.40}$$

According to Eq. (3.40), the maximum value for the torque is achieved when the stator q- and d-axis current components are equal, $i_{\mathrm{sq}} = i_{\mathrm{sd}}$. This, however, applies only to unsaturated conditions, and when the motor operates in saturation, the q-axis current component should be chosen larger than the d-axis one. This can be explained by the fact that when the motor is saturated, increasing the flux-producing current i_{sd} increases the motor flux only slightly (proportionally to the vacuum permeability in full saturation), and more torque can be produced by increasing the torque producing current i_{sq} instead, since its effect on the torque remains linear regardless of the saturation. In order to maximize the motor dynamic performance during all operating conditions, the Ψi-curve of the motor must be known to determine the degree of the saturation of the motor. Determination of the Ψi-curve can be performed by using FEM, or with measurements. The method for determining the magnetization curve of an induction motor has been described by Levi (2000). For the saturated motor, optimal torque producing currents from the motor's Ψi-curve are pre-calculated for example as a function of the stator current, and they are then implemented for the motor controller for example in the form of a look-up table. After this, the control strategy that maximizes the torque is straightforward:

- For unsaturated conditions, set $i_{sq} = i_{sd} = \frac{\sqrt{2}}{2} i_{s,max}$
- For saturated conditions, choose optimal $i_{qs,opt}$ and set $i_{sd} = \sqrt{i_{s,max}^2 - i_{sq,opt}^2}$

In practice, i_{sd} component corresponds to the magnetizing current, and the i_{sq} to the rotor current, the stator current being the sum of these. In practice, the balancing of the rotor and the magnetizing current can be carried out by varying the flux level of the machine. When the flux level is decreased, the slip will increase thereby increasing the rotor current, but consequently decreasing the magnetizing current and vice versa. A high flux level results in a high overloading torque and in a low rated slip, which both are important regarding the dynamic performance of the motor. Figure 3.26 shows the different current components of the prototype motor as a function of slip at the rated torque calculated using the equivalent circuit (unsaturated motor model). By varying the stator flux level, the minimum value for the stator current can be found. For the unsaturated motor, this is the point, at which the rotor and the magnetizing currents are equal

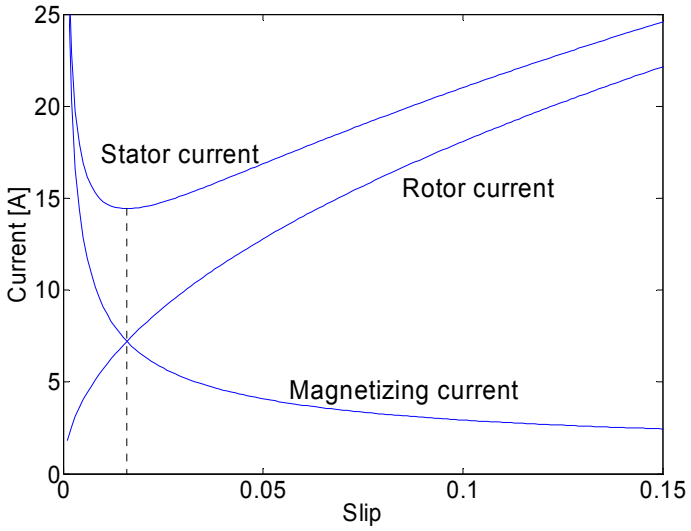

Figure 3.26. Current components of the prototype motor calculated analytically (unsaturated motor) at 15 Nm constant load. The stator current is minimized at the point, where the rotor and the magnetizing current values are equal. In practice, the slip is varied by controlling the flux of the machine. In the figure, zero slip would correspond to an infinite flux, and the flux decreases as the slip increases.

By minimizing the current with an optimal flux reference, both the stator copper and the inverter losses are minimized. Stator copper losses are typically dominating, especially with small induction machines, and thus the effect on the total losses can be significant. Lower winding temperature also increases the lifespan of the motor. The effect of the flux optimization on the iron losses depends on whether the machine is dimensioned to a lower or higher flux level than the optimal flux that minimizes the current. In the latter case, also the iron losses are decreased when the flux level is optimized. This can easily be checked by slightly decreasing the flux level of the motor during operation; if the current decreases, the motor is dimensioned to a higher flux level than the optimal one, and vice versa. For induction servomotors, it might be practical to use a somewhat higher flux than necessary, as the torque increases proportionally to the air gap flux density squared. A higher flux level will result in a better dynamic performance, for example

during a stepwise torque demand. After all, the efficiency is usually a less critical parameter than the dynamic performance with servomotors. When a lower flux level is applied to optimize the current, the dynamic response deteriorates, and thus such a flux optimization should be applied only when the drive cycle is known, and no unexpected torque changes – which might endanger the stability of the drive – will occur. During constant speed running, it is therefore very convenient to drive the motor with such a flux reference that minimizes the current at a given torque. With servomotors designed for high flux densities, this means that the flux of the motor should be decreased when the motor operates at nominal loads, and when the pull-out torque is to be utilized, the flux level is increased to a maximum value. Finite element analysis is applied to take into account the saturation of the machine; Fig. 3.27 shows how the stator current, the efficiency, and the power factor of the prototype motor depend on the input voltage at the rated torque and speed.

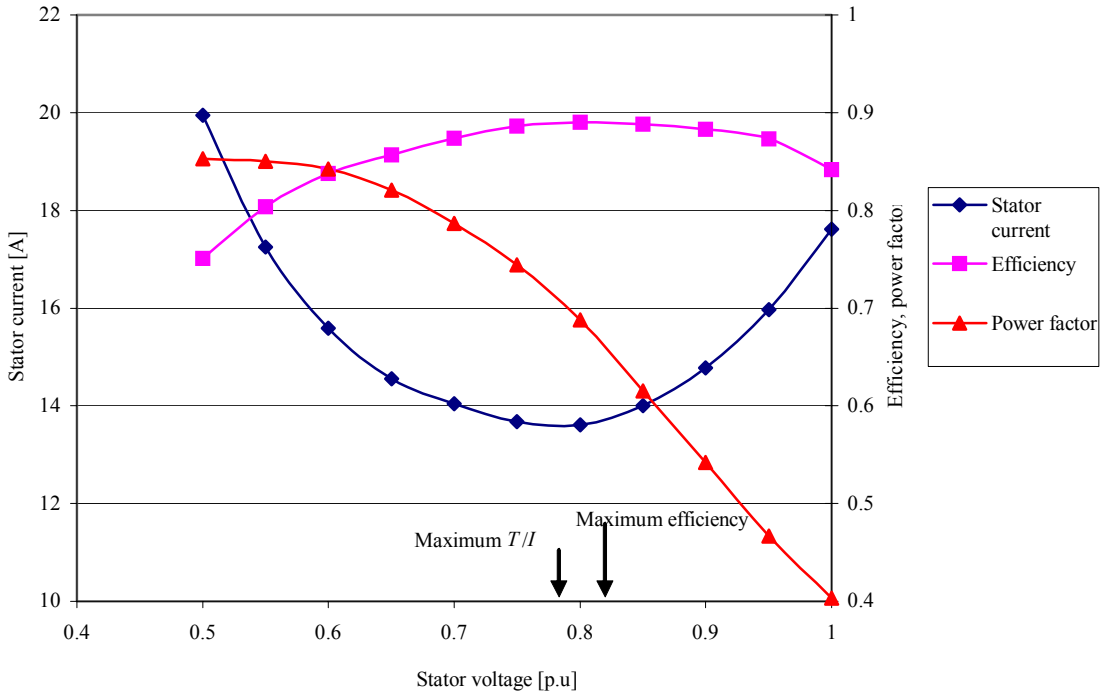

Figure 3.27. Stator current, efficiency, and power factor as a function of the stator voltage with constant load T_n calculated with FEM. The input voltage has a significant role on the running characteristics of the motor. The difference between the maximum T/I and the maximum efficiency is relatively small with this motor due to its high magnetic loading. The rated current of the PMSM is 8.7 A.

Figure 3.27 shows that by decreasing the air gap flux in this motor by approx. 20 %, the current can be significantly decreased (to a minimum value) and consequently, both the efficiency and the power factor are increased. Further, the flux that minimizes the current is almost the same that maximizes the efficiency, too. When the flux is decreased from the rated value, the iron losses are decreased almost in proportion to the flux density squared, and the stator copper losses are decreased proportionally to the current squared. However, due to the decreased air gap flux, a higher slip is required to obtain the rated torque, and the rotor losses are increased. However, the stator copper and iron losses have a far greater effect compared to the rotor losses, and the efficiency is thus increased.

The effect of the flux level on the motor current was verified in the laboratory with the prototype motor by carrying out extensive measurements by measuring the motor current at ten different loading levels from 10 % torque up to the rated torque. At each load, the flux was decreased to a value where the current was minimized (and slightly further). The results are shown in Fig. 3.28. The motor was supplied with an ACS600 frequency converter, with a Magtrol Vibrometer dynamometer (eddy-current brake) as a load.

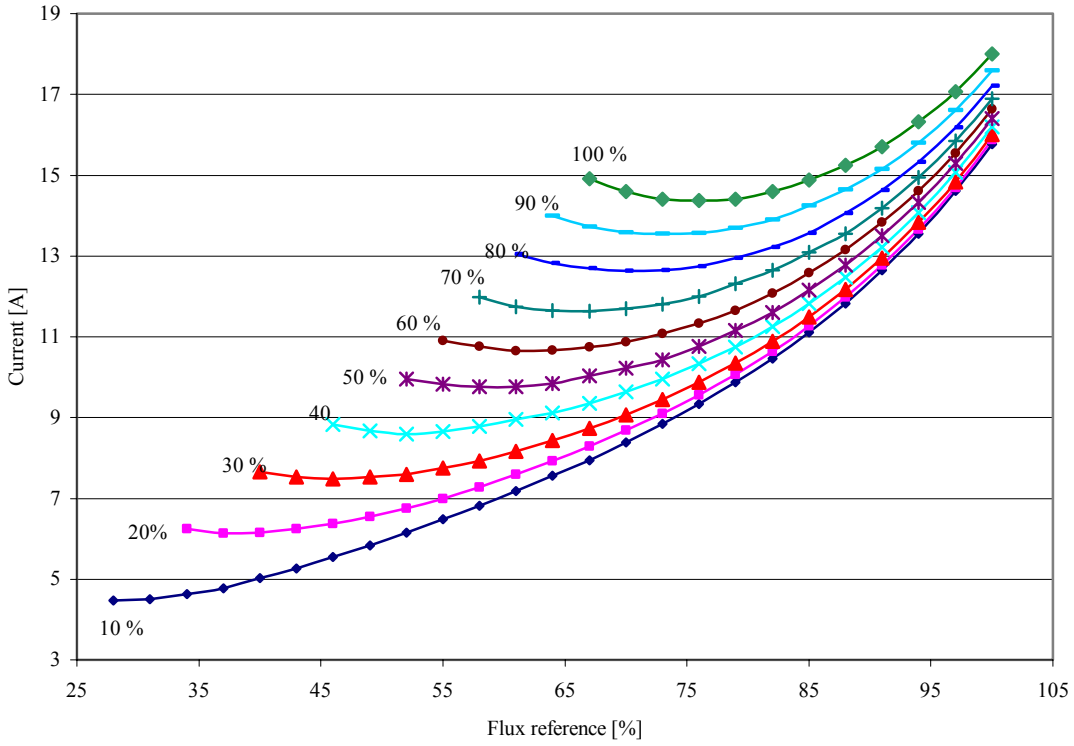

Figure 3.28. The currents of the prototype motor torque as a parameter fed with an ABB ACS600 frequency converter measured with Yokogawa PZ4000 power analyzer. The flux linkage level has a significant effect on the motor current especially at partial loads.

Figure 3.28 clearly shows the significance of the flux level on the induction motor current, especially at partial loads. The stator current can be even 50 % less if the flux level is chosen properly. This certainly has an effect on the efficiency of the machine, as the stator copper losses are usually the dominant loss component in small induction machines. According to measurements and FEM simulations, the flux level should be increased as the load torque increases in order to minimize the stator current. The minimum currents as a function of torque are shown in Fig. 3.29, both calculated with FEM, and measured with the prototype. The FEM results agree quite well with the measured ones. The material of the electrical steel used in the machine – and consequently the exact *BH* curve – were unknown, which may cause slight errors in the FEM results, although there is probably no significant difference in the magnetic characteristics of the most common materials. M400-50A steel was used in the FEM calculations as the core material. Figure 3.29 also shows the current values at the rated flux; the gap between these two set of curves (rated flux and optimal flux) is significant.

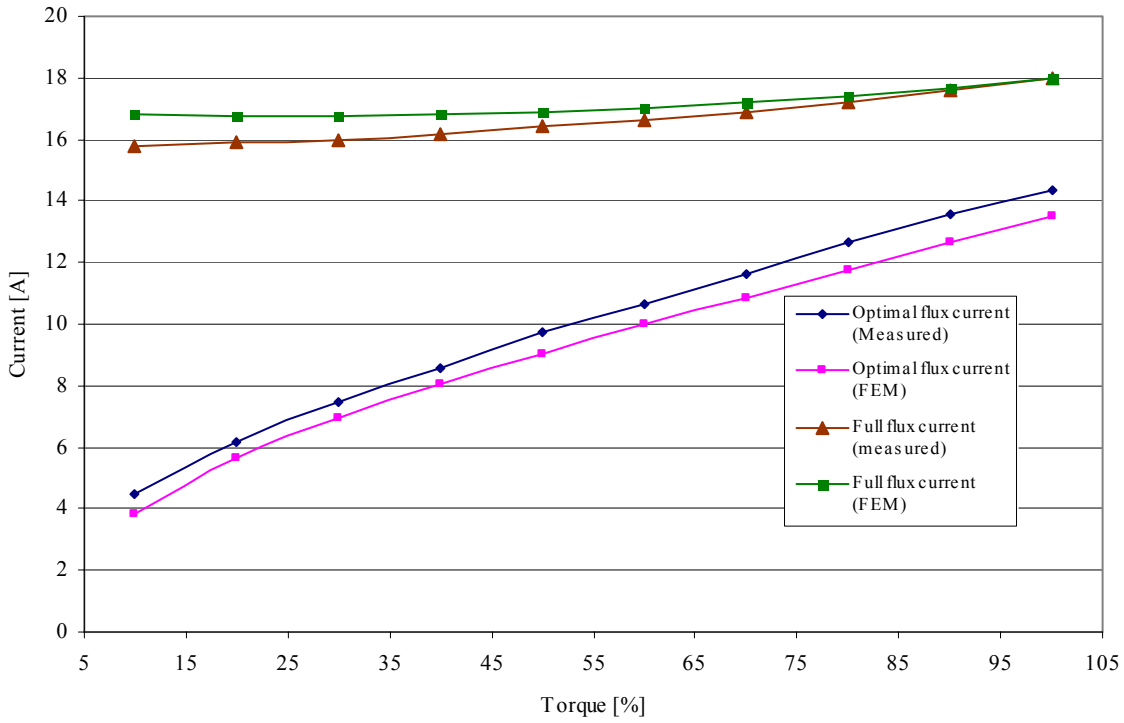

Figure 3.29. Currents at the rated flux and at the current-minimizing flux measured with the prototype and calculated with FEM. The difference between these two flux conditions (rated flux and optimal flux) is significant.

Simulations and measurements imply that in order to obtain the minimum current, the flux level should be increased as the load torque increases. Figure 3.30 shows the current-minimizing flux references as a function of the torque, calculated both analytically using the single-phase equivalent circuit and with FEM. Also measured values are given. The analytical model seems to agree surprisingly well to the measured values, until the motor saturates. At the rated flux and torque of the original PMSM, the stator current of the prototype is nearly twice the current of the original PMSM, and therefore, care must be taken to prevent a thermal failure of the winding, even though pressurized air was blown through the air gap of the prototype motor for cooling.

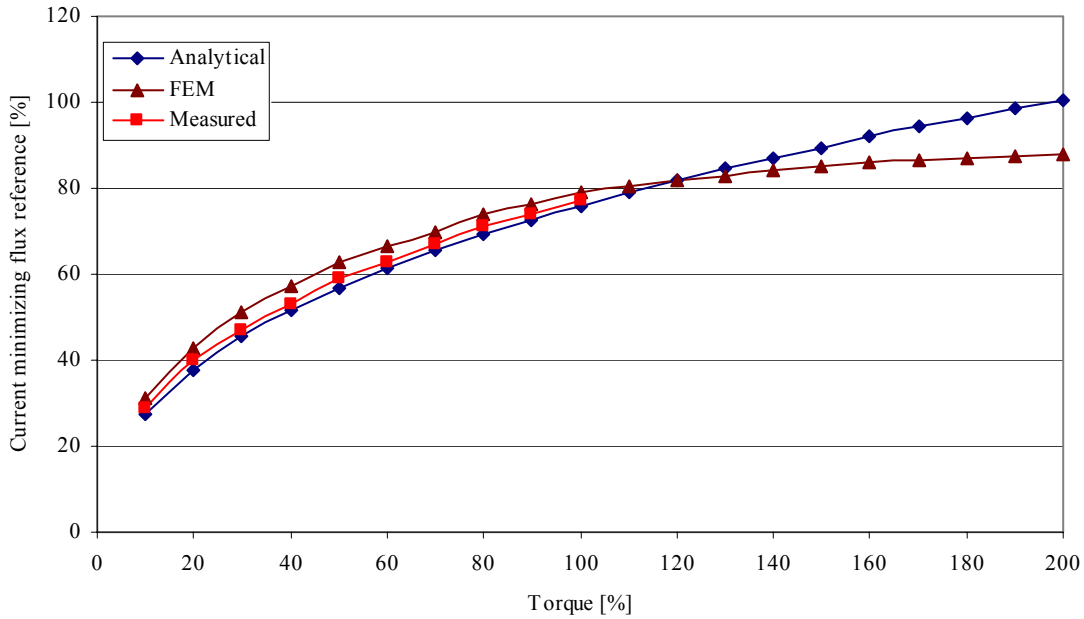

Figure 3.30. Flux reference that minimizes the stator current measured with the prototype and calculated both analytically and numerically. The analytical model gives good accuracy at lower flux levels, but saturation causes excessive errors, as it is not taken into account in the model. Measurements beyond 100 % load torque were not possible due to the test setup performance limitations and also because of the motor thermal limitations due to excessive stator currents.

The motor flux also has a significant effect on the magnitude and the distribution of the loss components. A high flux level causes high core losses, but as the machine then runs at a low slip, the rotor copper losses are low, and thus there is a trade-off between these two loss components. As the flux level has a great influence also on the stator current, and thereby on the stator copper losses, it is clear that the flux level strongly affects the efficiency of the machine. As there is an optimal flux level that minimizes the current, also an optimal flux reference for the efficiency of the motor can be found. The efficiency curves of the prototype motor calculated with FEM are shown in Fig. 3.31 as a function of the flux reference at different load torques. Separation of the different loss components is studied in more detail in Chapter 4.

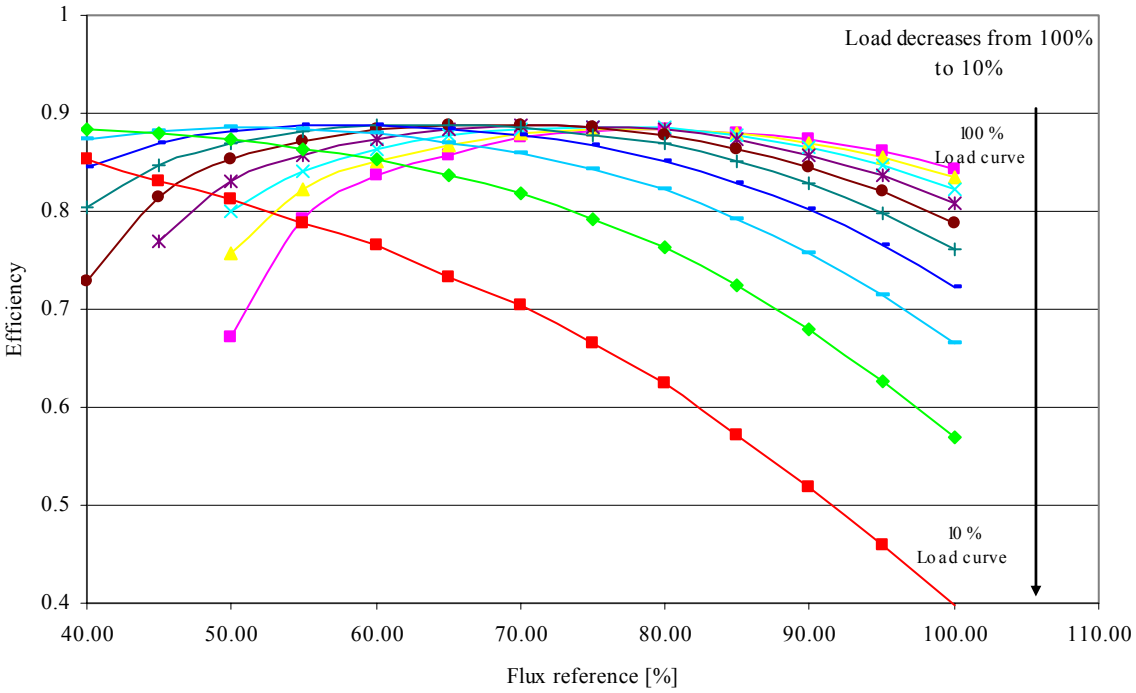

Figure 3.31. Efficiencies at the nominal operating range of the prototype motor calculated with FEM (mechanical losses are not taken into account). The influence of the flux level is significant on the motor efficiency especially at partial loads.

Although the flux level has some effect on the efficiency near the nominal load, the effect is notably greater at partial loads (and also during over loadings). The flux references that maximize the efficiency are quite close to those in Fig. 3.30 that minimize the current for a given torque, which results from the fact that the dominating loss component is the stator copper loss. Figure 3.31 clearly implies that a decreased voltage should be used at nominal load and below, and again, the voltage should be increased towards higher loadings. Figure 3.32 shows the flux references that minimize both the stator current and the total losses at a given load.

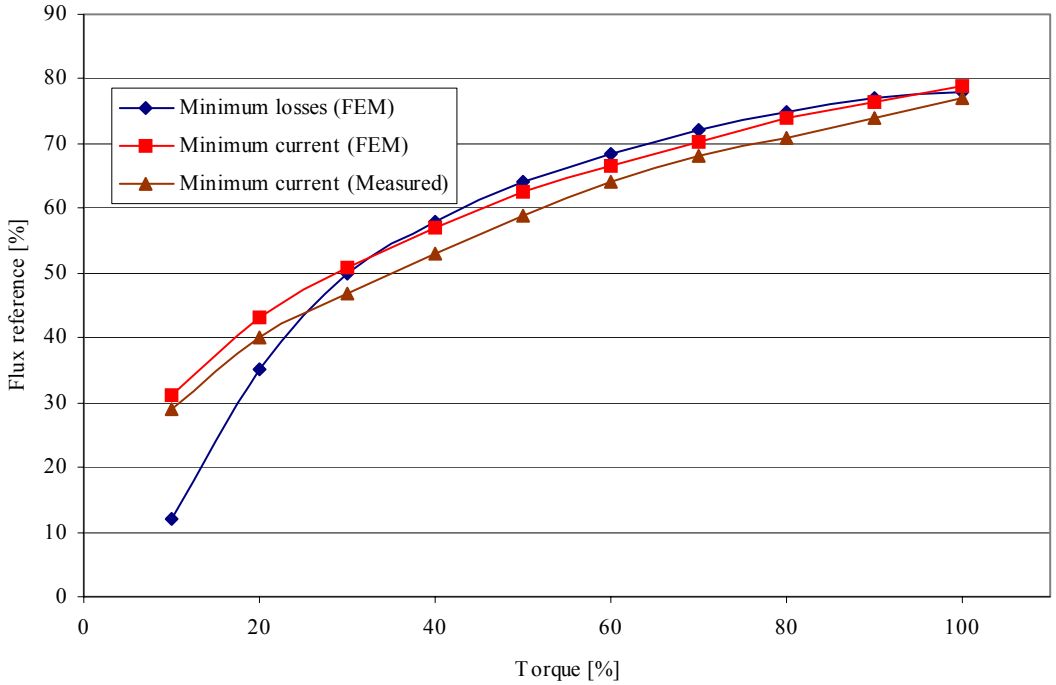

Figure 3.32. Behaviour of the current and loss-minimizing flux references as a function of torque. With the exception of the lowest loads, the gap between these two flux references is fortunately quite small. The measurements gave slightly lower values for the flux than the simulated results.

3.4 Conclusion

In this chapter, the characteristics of an induction motor and a permanent magnet synchronous motor in motion control applications were analyzed. Design methods for the induction motor that optimize the overloading capability – and consequently the field weakening characteristics – were presented. It is possible to obtain adequate overloading capability with an induction motor by minimizing the major leakage inductances, and by dimensioning the motor for a high air gap flux density level. Field weakening characteristics of such a motor are significantly better than with a surface-magnet PMSM, which makes it an attractive alternative in applications requiring high-speed operation. Because of the requirement of high magnetization current of a high-flux machine, the drawbacks of such a motor are a low power factor, lower efficiency, and lower torque-to-current ratio, which results for instance in a larger frequency converter. Therefore, if possible, flux level should be controlled as a function of the load torque; the full flux should be applied only when very high overloading torque is required. It was shown that it is possible to significantly improve the running characteristics of a highly saturable motor this way. Figure 3.33 summarizes the various interactions due to different design methods, which must be adopted to optimize the dynamic performance of an induction motor.

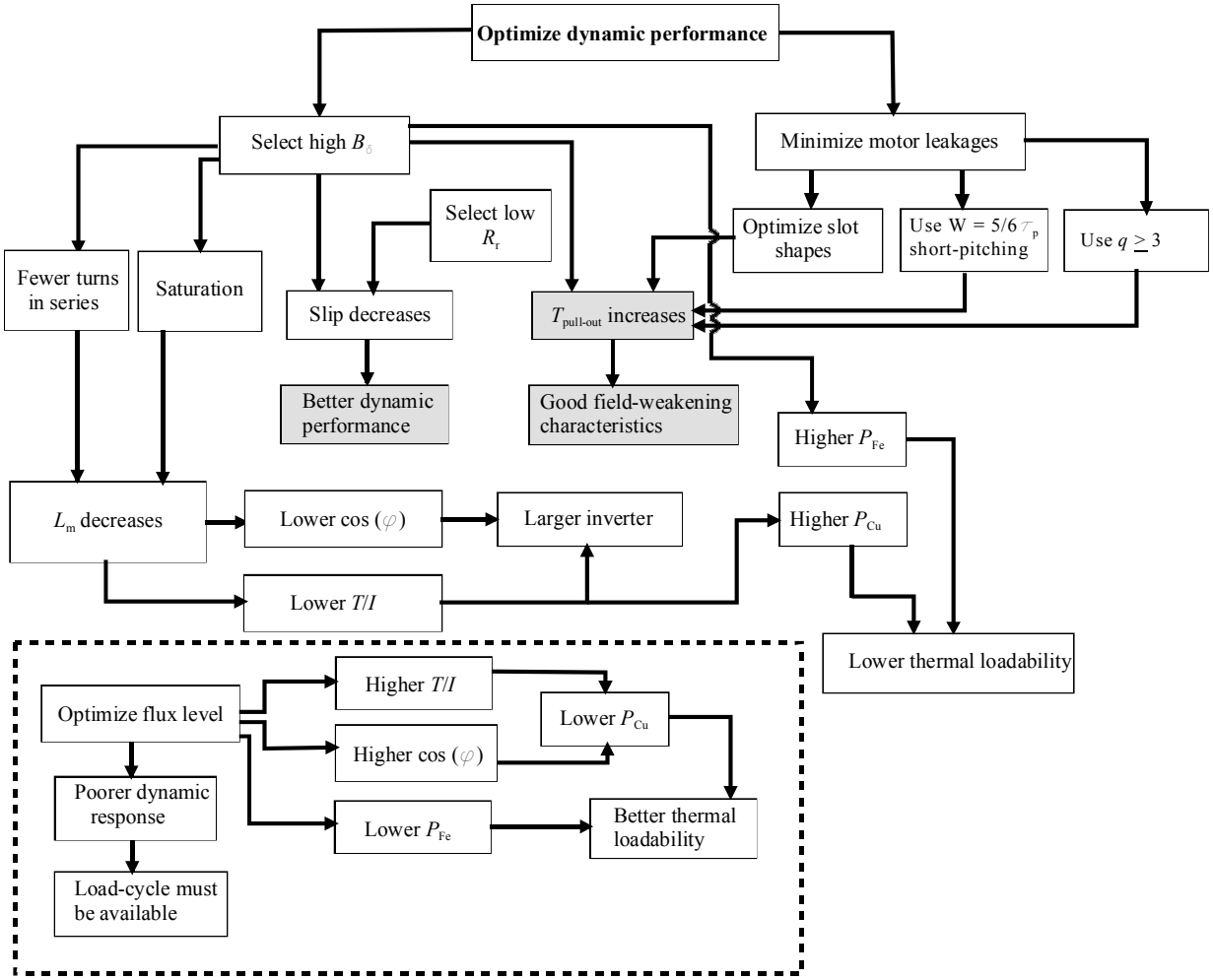

Figure 3.33. Interactions during the optimization process of the dynamic performance of an induction motor, discussed in this chapter.

4. DYNAMIC THERMAL ANALYSIS WITH COUPLED ELECTROMAGNETIC−THERMAL MODEL OF AN INDUCTION MOTOR

It is extremely important to model the heat transfer behaviour in electrical machines properly at least to some degree, as it defines the cooling capability, and consequently the nominal power of the machine. Accurate modelling of heat transfer is practically impossible without the finite element analysis due to the complex three dimensional geometries. Despite the fact that faster and faster microprocessors are available, 3D FE analysis is yet too time consuming (for dynamic thermal analysis), and often different kinds of analytical methods are applied to model the heat transfer in the machine instead. Majority of the industrial electrical machines run continuously in S1 duty cycles, or at least in cycles, where the steady-state temperature is reached. Such applications are for example power plant generators, different kinds of conveyors, air conditioning motors, propulsion motors, and so on. This has led to the fact that very often the heat transfer is studied in the steady-state only, and the heat capacitances of the machine are neglected in the model. Such a model is adequate enough for properly estimating the steady-state temperature rise of the machine; however, it cannot model the heat transfer mechanisms during the loading variations. Servomotors, on the other hand, are applications, in which the heat capacitances are utilized during heavy over loadings, such as in acceleration to slow down the heating of the machine. High over loadings mean high losses, and consequently the temperature gradients are high. Therefore, in this chapter, analytical heat transfer model for the motor is built, and the main interest is focused on the transient heat transfer mechanism during the loading variations. The model should be flexible and computationally fast, but still be able to calculate the temperatures fairly accurately.

Very often in thermal analysis, the whole modelling is carried out with numerical methods, or at least the inputs for the thermal (network) model are calculated with FEM, as it is the most accurate one and suits well in steady-state analysis. Thermal models for the induction motor, where the entire modelling is carried out with FEM, have been introduced for example by Rajagopal et al. (1998) and by Liu et al. (2005). A coupled model, in which the electromagnetic part is calculated with FEM and thermal part analytically, has been proposed for example by Mezani et al. (2005). However, as the FEM is very time-consuming, and the simulation of different torque-speed profiles with commercial codes is not possible, the dynamic simulation is practically impossible with FEM. Due to the long thermal time constants, the calculation of the motor quantities should be as fast as possible, because the simulated time (i.e. the real time) could be even hours, which is not possible with FEM. Also the model should be capable of adapting in different torque-speed profiles, and it has to take into account the effect of temperature increase on the motor thermal and electromagnetic parameters, as the resistance dependent parameters of the motor, such as the slip, the pull-out torque, and currents strongly depend on the temperature. Therefore, in order to increase the calculation accuracy, the simulation model was realized as a coupled electromagnetic−thermal model, so that the electromagnetic quantities are calculated in the electromagnetic part of the model, and the electromagnetic information is then used to calculate the temperatures of the machine. A dynamic model that calculates the currents, the speed, and the electromagnetic torque of the motor with given torque-speed references was constructed for the induction motor in the stator reference frame from the single-phase equivalent circuit and motor flux linkage equations. From these outputs, the losses of the machine are calculated, and then fed for the thermal model, which calculates the temperatures in different machine parts. As the motor dynamic characteristics (i.e. the slip and the pull-out torque) and the loss generation depend on the

temperature, there has to be a feedback-loop that updates the necessary resistance parameters as a function of temperature. Parameters that are updated are the stator and the rotor electric resistance and the thermal resistance for the radiative heat flow from the frame to the ambient. Figure 4.1 illustrates the block diagram of the model with the signal routing.

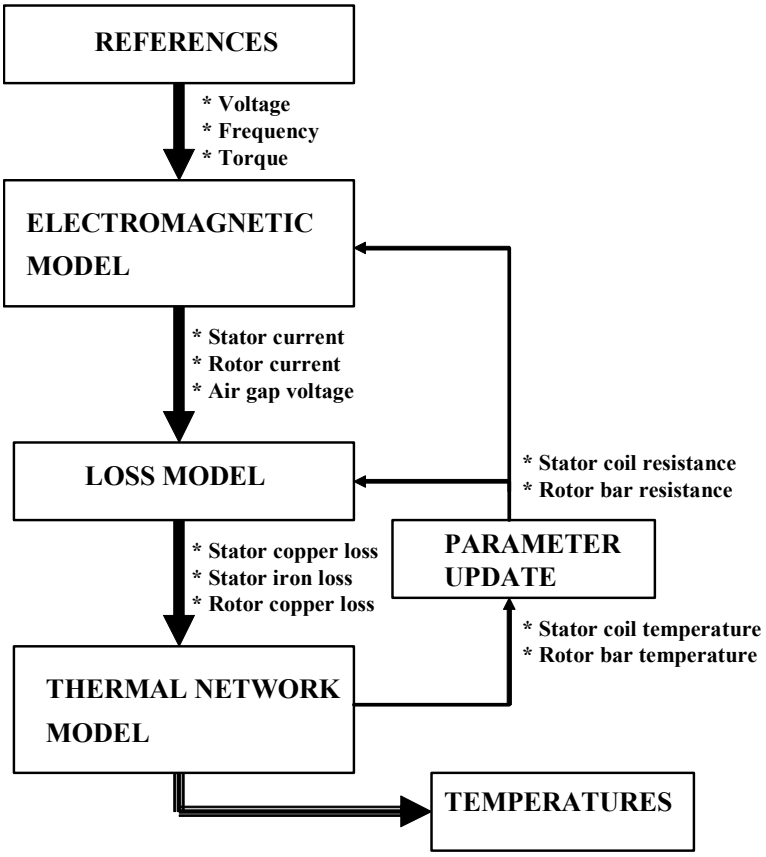

Figure 4.1. Block diagram of the coupled electromagnetic−thermal model of an induction motor.

The model was implemented in Matlab/Simulink™ environment, which makes the model user interface very user friendly, and the model convertibility good. In addition, different speed-torque profiles can be easily generated in the reference block, which makes the simulation of different applications possible. The construction and verification of the model is presented in this chapter, while the focus is on the thermal part, and the electromagnetic part is only briefly introduced. The different blocks are introduced in logical order (according to Fig. 4.1). Also the simplified thermal model is suggested at the end of the chapter, which can be applied when the complete motor dimensional and material data is not available.

4.1 Electromagnetic model of an induction motor

The electromagnetic part of the model is based on single-phase equivalent circuits in stator co-ordinate system in the d- and q -directions, shown in Fig. 4.2.

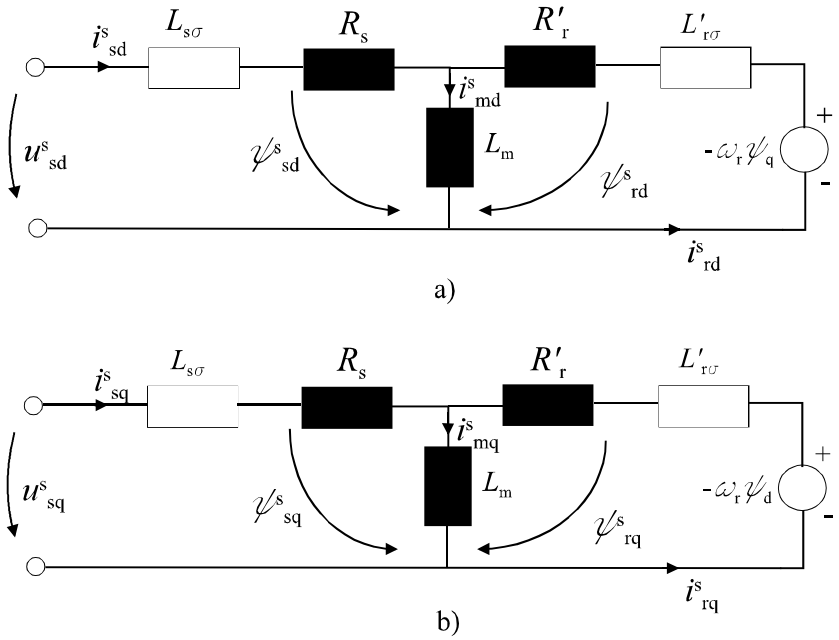

Figure 4.2. Single-phase equivalent circuits of an induction motor a) in the stator d-axis, and b) in the stator q-axis.

From Fig. 4.2, equations for the stator flux linkages and voltages can be written in the form (Bose 1997)

$$\psi^{s}_{sd} = L_s i^{s}_{sd} + L_m i^{s}_{rd} \quad , \tag{4.1}$$

$$\psi^{s}_{sq} = L_s i^{s}_{sq} + L_m i^{s}_{rq} \quad , \tag{4.2}$$

$$u^{s}_{sd} = R_s i^{s}_{sd} + \frac{d}{dt}\left(\psi^{s}_{sd}\right) \quad , \tag{4.3}$$

$$u^{s}_{sq} = R_s i^{s}_{sq} + \frac{d}{dt}\left(\psi^{s}_{sq}\right) \quad , \tag{4.4}$$

and similarly for the rotor voltages and flux linkages

$$\psi^{s}_{rd} = L_r i^{s}_{rd} + L_m i^{s}_{sd} \quad , \tag{4.5}$$

$$\psi^{s}_{rq} = L_s i^{s}_{rq} + L_m i^{s}_{sq} \quad , \tag{4.6}$$

$$0 = R'_r i^{s}_{sd} + \frac{d}{dt}\left(\psi^{s}_{rd}\right) + \omega_r \psi^{s}_{rq} \quad , \tag{4.7}$$

$$0 = R'_r i^{s}_{sq} + \frac{d}{dt}\left(\psi^{s}_{rq}\right) - \omega_r \psi^{s}_{rd} \quad , \tag{4.8}$$

The superscripts in Eqs. (4.1)-(4.8) denote that the values are referred to the stator. The stator and the rotor inductances in Eqs. (4.1)−(4.6), L_s and L_r, can be expressed as

$$L_\mathrm{s} = L_{\mathrm{s}\sigma} + L_\mathrm{m} \quad , \tag{4.9}$$

$$L_\mathrm{r} = L_{\mathrm{r}\sigma} + L_\mathrm{m} \quad . \tag{4.10}$$

The electromagnetic torque $\boldsymbol{T}_\mathrm{em}$ of the machine can be expressed with the cross-field principle in the form

$$\boldsymbol{T}_\mathrm{em} = \frac{3}{2} p \boldsymbol{\psi}_\mathrm{s}^\mathrm{s} \times \boldsymbol{i}_\mathrm{s}^\mathrm{s} \quad , \tag{4.11}$$

and by dividing this into components

$$T_\mathrm{em} = \frac{3}{2} p \left(\psi_\mathrm{sd}^\mathrm{s} i_\mathrm{sq}^\mathrm{s} - \psi_\mathrm{sq}^\mathrm{s} i_\mathrm{sd}^\mathrm{s} \right) \quad . \tag{4.12}$$

The mechanics of the system is modelled with the following equation

$$T_\mathrm{em} - T_\mathrm{load} = J \frac{\mathrm{d}}{\mathrm{d}t} (\Omega) \quad , \tag{4.13}$$

where T_load is the load torque, J the inertia of the motor and load, and Ω the mechanical speed, which can be solved as

$$\Omega = \frac{1}{J} \int \left(T_\mathrm{em} - T_\mathrm{load} \right) \mathrm{d}t \quad . \tag{4.14}$$

The inputs for the electromagnetic motor model are the frequency, the voltage, and the torque, and the model outputs are the RMS currents and voltages, the electromagnetic torque, and the slip. From the currents and the voltages, the different loss components of the machine are calculated in a loss calculation block connected between the electromagnetic and thermal parts of the model. The equations for the losses are presented later in this chapter, after the thermal part.

The analytical models very often assume a magnetically linear machine, and the saturation is not taken into account. As it is clear from the previous chapters, servomotors are often designed for a very high air gap flux density to provide high pull-out torque and hence adequate dynamic performance. Saturation of the iron significantly increases the magnetizing current of the machine, and therefore the modelling of the saturation is vital with such motors. Modelling of the saturation is most straightforward and simplest to take into account by modelling the magnetizing inductance as a function of the flux level. Both the measured and the FEM calculated magnetizing inductances of the prototype motor are shown as a function of the flux level (air gap voltage) in Fig. 4.3.

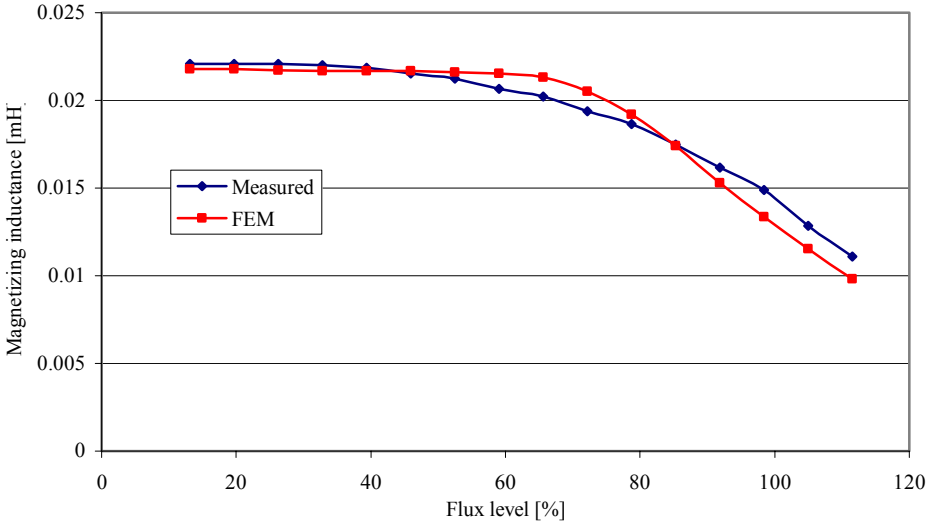

Figure 4.3. Measured and simulated magnetizing inductances as a function of the flux level.

Figure 4.3 shows how deep the saturation is at the rated flux level, but as it was discussed in Chapter 3, the rated flux should be applied only when heavy overloading is required. In order to take the saturation in to account in the model, the magnetizing inductance−flux curve shown in Fig. 4.3 was implemented in the electromagnetic part of the model.

4.2 Heat transfer methods

In general, there are three mechanisms to dissipate the heat energy due to losses in electrical machines; convection, conduction, and radiation, of which the last one is usually of least significance, especially in the case of motors with forced cooling, as the frame temperature remains low. With self-cooled motors, the frame temperature may reach values, at which the radiation cannot be neglected any longer. With the prototype motor, the effect of the radiation was emphasized, as the frame was matt black, having thus high emissivity.

4.2.1 Convection

By convection, heat is transferred from solid to either gas or liquid through the surface layer, always from the higher temperature to the lower. Convection can be either natural or forced convection, depending on whether there is an external device, such as a fan or a pump, which forces the gas or cooling liquid to flow. In natural convection, heat transfer is caused by the gravity acting on the density variations near the boundary section of the two medium. Dissipated power due to convection can be expressed

$$P_{\text{conv}} = h_{\text{c}} A \Delta T \,, \tag{4.15}$$

Where A is the area, T is the temperature, and the coefficient h_{c} is the convection heat transfer coefficient (also known as the boundary film coefficient), which depends on many variables, such as the shape and dimensions of the surface, flow characteristics, temperature, and material

characteristics of the fluid. In electrical machines, heat transfer by convection occurs mainly in three regions

- •Convective heat transfer between the frame and the ambient air
- •Convective heat transfer between the end windings and the end-region air
- •Convective heat transfer between the stator or the rotor and the air gap

Typically, the frame of electric machines is equipped with cooling fins, which makes the calculation of convective heat transfer from the frame to the ambient very difficult, and this coefficient is usually determined by experimental tests. The convective heat transfer coefficient from the frame to the ambient can be found by running the motor continuously so that the steady-state temperature is reached, and by measuring the frame outer surface temperature and the total machine loss. Similarly, the accurate calculation of the convection heat transfer from the end windings is practically impossible, as the geometry of the end winding is too complex. The convective heat transfer from the end winding can also be determined experimentally.

Also the heat transfer from the rotor to the stator across the air gap is extremely difficult to model, due to the slotting of the stator (and sometimes also the rotor) that cause fluid disturbances in the air gap, the accurate modelling of which is practically impossible. Originally, Taylor (1935) solved the convective heat transfer between two rotating concentric smooth cylinders, but due to slotting, these equations cannot be directly applied. For example, Gazley (1958) suggests that the slotting increases the heat flow by approximately 10 % in the air gap. However, in most of the research reports, convective heat transfer across the air gap is solved based on Taylor's work, with some modifications depending on the author.

Convective heat transfer coefficient in the air gap is obtained from Nusselt's number by first defining Taylor's and Prandtl's numbers for the air gap. A dimensionless Taylor's number is obtained from Couette Reynold's number (for enclosed cylinder), defined as

$$Re_{\delta} = \frac{\rho v_{\mathrm{circ}} \delta}{\mu} \quad , \tag{4.16}$$

where ρ is the density of the fluid, v_{circ} the circumferential speed of the rotor, δ the radial air gap length, and μ the dynamic viscosity of the fluid. Now Taylor's number can be obtained from

$$Ta = Re_{\delta}^2 \frac{\delta}{r} \quad , \tag{4.17}$$

where r is the radius of the rotor. Equation for Prandtl's number can be expressed as

$$Pr = \frac{\mu c_{\mathrm{th}}}{\lambda_{\mathrm{air}}} \, , \tag{4.18}$$

where c_{th} is the specific thermal capacity and λ the thermal conductivity of the fluid. As the peripheral speed of the rotor is low below rated speed (below 10.5 m/s), and the air gap is very

short (0.3 mm), Taylor's number becomes low. This means that the air flow in the air gap can be assumed laminar, and according to Boglietti (2002), Nusselt's number is then $Nu = 2.0$. If the air gap flow would be turbulent, the following equation given by Boglietti could be used

$$Nu = 0.386 \frac{1}{\sqrt{r_\delta \delta}} Pr^{0.27} \tag{4.19}$$

Finally, a convective heat transfer coefficient in the air gap, h_δ, can be calculated from

$$h_\delta = \frac{Nu \lambda_{\text{air}}}{\delta} \ . \tag{4.20}$$

The value for the thermal resistance used in the calculations that describes the convective heat transfer across the surface, can be calculated as

$$R_{\text{th,conv}} = \frac{1}{Ah} \tag{4.21}$$

4.2.2 Conduction

Conduction is the mechanism that transfers the heat inside the solid medium. In general case, conduction can be described with the diffusion equation based on Fourier's law

$$\frac{\partial T}{\partial t} = \frac{1}{\rho c} \left[\frac{\partial}{\partial x} \left(\lambda_{\text{x}} \frac{\partial T}{\partial x} \right) + \frac{\partial}{\partial y} \left(\lambda_{\text{y}} \frac{\partial T}{\partial y} \right) + \frac{\partial}{\partial z} \left(\lambda_{\text{z}} \frac{\partial T}{\partial z} \right) + p \right] \ , \tag{4.22}$$

where T is the temperature, t the time, ρ the density, c the specific thermal capacity, λ the thermal conductivity, and p the generated power density. Eq. (4.22), however, cannot be directly applied, due to complex boundary value problems arising due to complex and unknown geometries in different machine parts. In thermal circuit modelling, heat transfer is solved in one dimension at a time, and thus Eq. (4.22) can be re-written in the x-direction to yield the heat flux Φ_{th}

$$\Phi_{\text{th}} = -\lambda A \frac{\text{d}T}{\text{d}x} \approx -\lambda A \frac{\Delta T}{x_2 - x_1} \ , \tag{4.23}$$

and by introducing the thermal resistance R_{th} due to conduction

$$R_{\text{th}} = \frac{\Delta T}{\Phi_{\text{th}}} = \frac{x_2 - x_1}{\lambda A} \ . \tag{4.24}$$

Heat transfer can thus be modelled in a manner that is analogous to Ohm's law. This is very convenient, since commercial circuit simulators can then be applied to model the heat transfer.

4.2.3 Radiation

Heat flux dissipated by radiation can be expressed with Stefan-Boltzmann equation

$$\Phi_{\text{th}} = \varepsilon\sigma_{\text{SB}}\left(T_1^4 - T_2^4\right) \ , \tag{4.25}$$

where ε *is* the emissivity, σ_{SB} Stefan-Boltzmann's constant (5.67×10-8 J/s/m^2/K^4), and T the temperature. Emissivity ε varies from 0 of a "transparent" material to 1 of a black body. In practice, however, emissivity for a painted black surface is typically around 0.9. In this analysis, radiation only from the frame to ambient is taken into account, and radiation for example inside the machine is neglected. As the emissivities for typical machine materials, such as copper and steel are low, in addition to small surface areas inside the machine, this assumption is justified, as the convective and conduction heat transfer dominate inside the machine. Thermal resistance of the radiation from the motor frame to the ambient can be calculated

$$R_{\text{th}} = \frac{T_{\text{frame}} - T_{\text{amb}}}{\varepsilon\sigma_{\text{SB}} A_{\text{frame}}\left(T_{\text{frame}}^4 - T_{\text{amb}}^4\right)} \ . \tag{4.26}$$

4.3 Thermal network of an induction motor

Because there is a full analogy between electric and thermal circuits, the heat transfer can be solved by using similar circuits, where thermal resistance corresponds to electric resistance, heat flux corresponds to current, and temperature difference corresponds to voltage. Also, thermal capacitances are required in the model, as the main focus is on the dynamic modelling. Different thermal network models for induction machines in the literature have been introduced for example by Kylander (1995) and Mellor (1991). Thermal network is constructed by first dividing the motor into separate geometrical sections, which are connected to neighbouring sections through thermal resistances. As the main interest of the study is in the transient heat transfer, thermal capacitances are added to all the sections comprised from the solid material. Internal heat generation is added for all those components, in which the losses are generated. Individual sections that comprise the model are

1. Frame (C_{th})
2. Stator yoke (C_{th}, P_{loss})
3. Stator teeth (C_{th}, P_{loss})
4. Stator winding (in slots) (C_{th}, P_{loss})
5. Air gap
6. End winding (C_{th}, P_{loss})
7. End cap air
8. Rotor winding (C_{th}, P_{loss})
9. Rotor iron (C_{th})
10. Shaft (C_{th})

C_{th} after the component denotes the thermal capacitance and P_{loss} the internal heat generation due to the losses. The modelling is carried out by presenting these 10 components as cylindrical components, symmetrical to the shaft and the radial plane of the machine. Cylindrical components are modelled with the so-called two-node configuration, where the two nodes represent the radial and axial heat flow. In such a way, the independent modelling of radial and axial heat flows is most straightforward. The simplified thermal model presented at the end of this chapter is constructed by using a common single-node configuration. Four assumptions are required to justify the modelling of individual machine sections as cylindrical components (Mellor 1991):

1. Heat flows in radial and axial directions are independent.
2. A mean temperature T_{ave} defines the heat flow in both axial and radial directions.
3. There is no circumferential heat flow (except from stator teeth to stator iron).
4. Thermal capacitance and heat generation are uniformly distributed.

Figure 4.4 a) depicts the simplified cylindrical component, its dimensions and temperatures, and Fig. b) the equivalent thermal circuit.

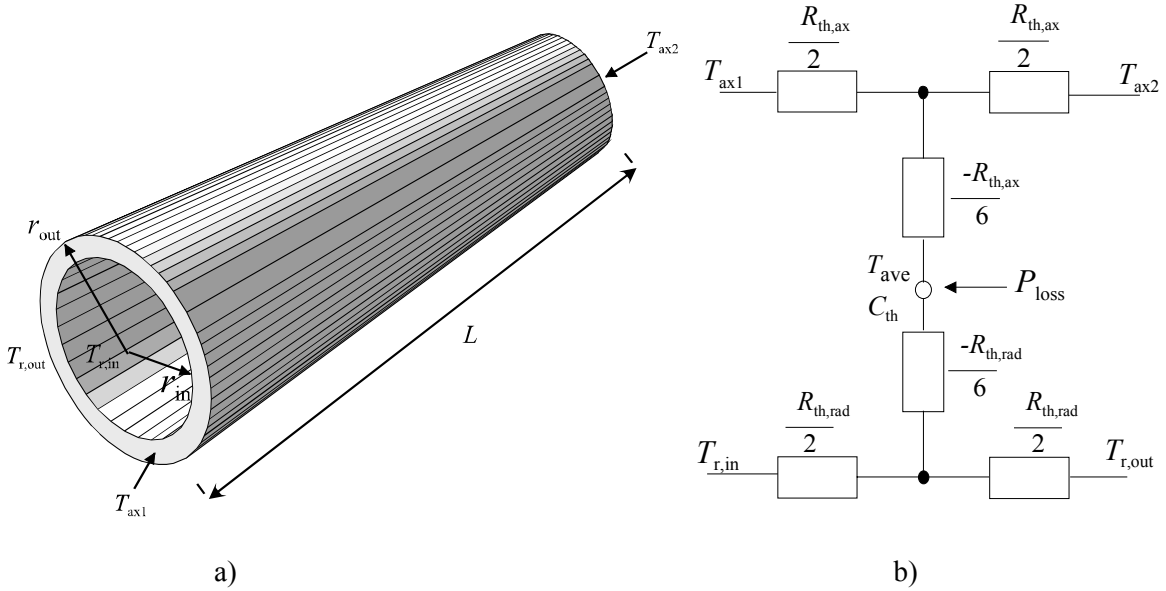

a) b)

Figure 4.4. General cylindrical component and its equivalent thermal circuit.

In Fig. 4.4, the temperatures in the radial directions $T_{r,out}$ and $T_{r,in}$ are the temperatures on the outer and inner surface of the cylinder, respectively, and the temperatures in the axial directions $T_{ax,1}$ and $T_{ax,2}$ are the temperatures at both ends. $R_{th,rad}$ denotes the thermal resistance for the radial heat flow, and accordingly $R_{th,ax}$ for the axial heat flow. The model therefore takes in the account the different heat flow characteristics in radial and axial directions, for example, in the iron due to laminations. Thermal resistance in radial direction can be expressed as

$$R_{th,rad} = \frac{\ln\left(\frac{r_{out}}{r_{in}}\right)}{2\pi\lambda L} \quad , \tag{4.27}$$

and the thermal resistance in axial direction

$$R_{th,ax} = \frac{\lambda\pi\left(r_{out}^2 - r_{in}^2\right)}{L} \quad . \tag{4.28}$$

The upper and lower part in Fig. 4.4 b) represent the one-dimensional heat flow in the axial and radial directions, respectively, and as these two one-dimensional models are connected from the node where the heat is generated, a two-dimensional model for the cylinder results. If there is internal heat generation in the element, a negative-value resistance must be added between the

point of the heat generation and the central node (black spots in Fig 4.4 b)) of each one-dimensional model. This is due to fact that without this negative interconnecting resistance, superposition of internal heat generation would result in average temperature of the element T_{ave} that is lower than the value given by the central node (Mellor 1991). Values for the thermal capacitances can be calculated

$$C_{th} = c_{th} m \quad , \tag{4.29}$$

where c_{th} is the specific heat capacitance and m the mass. Two-dimensional thermal networks for each ten elements are built, and these separate networks are then connected through thermal resistances of each boundary section. The thermal network model for the whole motor is shown in Fig. 4.5, and the explanations of different thermal resistances are listed in Table 4.1.

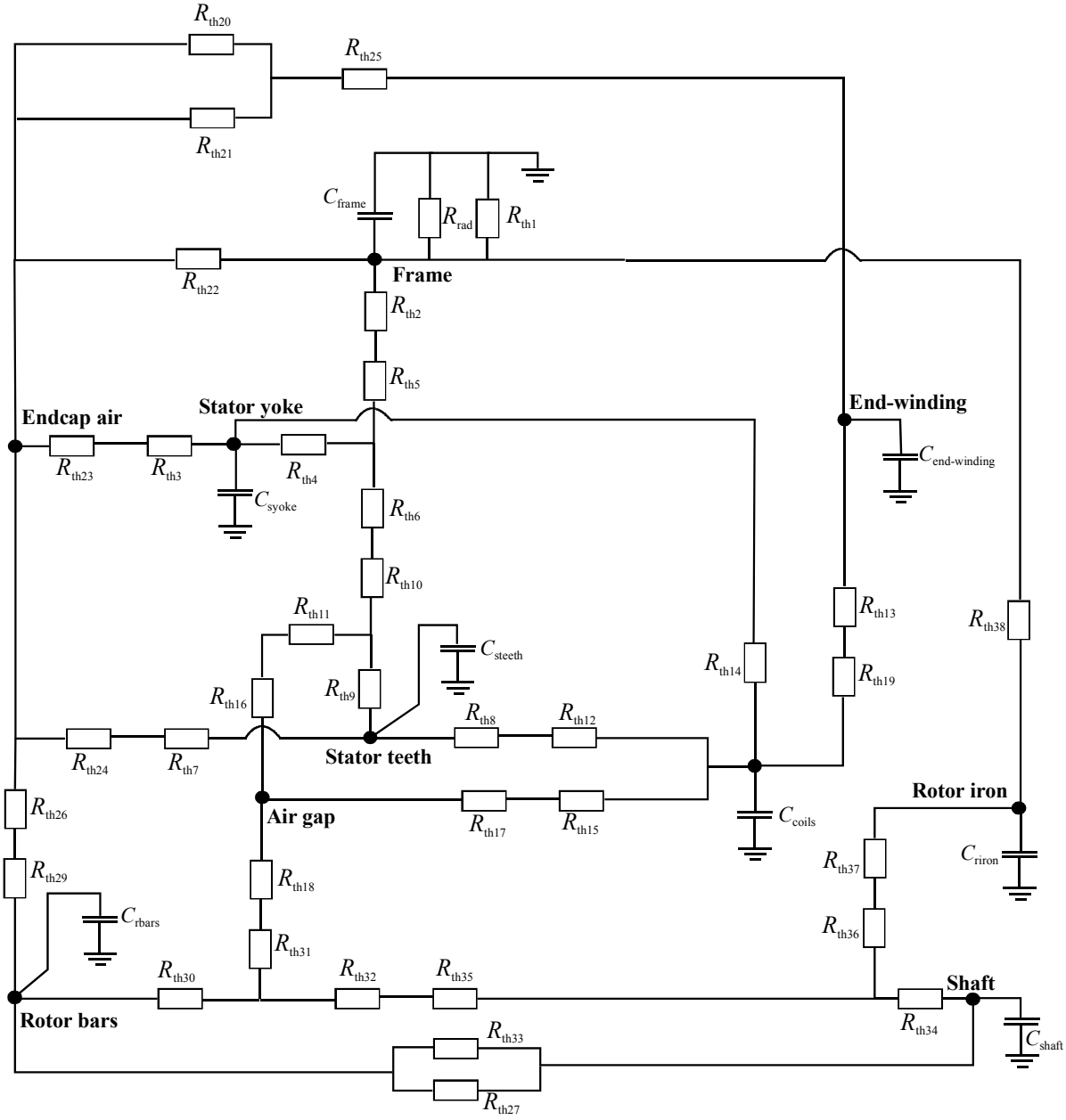

Figure 4.5. Thermal network of an induction motor based on a cylindrical component representation

Table 4.1 Thermal resistances and their explanations of the network

Comp.	Explanation
R_{th1}	Measured resistance from frame to ambient
R_{th2}	Measured radial resistance from frame to stator yoke
R_{th3}	Axial resistance from stator yoke to end cap air
R_{th4}	Radial interconnecting resistance of the stator yoke
R_{th5}	Radial resistance from the stator yoke to frame
R_{th6}	Radial resistance from the stator yoke to stator teeth
R_{th7}	Axial resistance from stator teeth to end cap air
R_{th8}	Radial/circumferential resistance from stator teeth to stator winding
R_{th9}	Radial interconnecting resistance of the stator teeth
R_{th10}	Radial resistance to from the stator teeth to stator yoke
R_{th11}	Radial resistance to from the stator teeth to air gap
R_{th12}	Radial/circumferential resistance from the stator coils to stator teeth
R_{th13}	Axial resistance to from the stator coils to end-winding
R_{th14}	Radial resistance from the stator coils to stator yoke
R_{th15}	Radial resistance from the stator coils to air gap
R_{th16}	Radial resistance from the air gap to stator teeth
R_{th17}	Radial resistance from the air gap to stator coils
R_{th18}	Radial resistance from the air gap to rotor bars
R_{th19}	Axial resistance from the end-winding to stator coils
R_{th20}	Resistance from the end-winding to end cap air (“legs”)
R_{th21}	Resistance from the end-winding to end cap air (“toroid”)
R_{th22}	Axial resistance from the end cap air to frame
R_{th23}	Axial resistance from the end cap air to stator yoke
R_{th24}	Resistance from the end cap air to stator teeth
R_{th25}	Resistance from the end cap air to end-winding
R_{th26}	Resistance from the end cap air to rotor end-rings
R_{th27}	Resistance from the end cap air to rotor iron
R_{th28}	Resistance from the end cap air to cooling holes (if present)
R_{th29}	Axial resistance from the rotor bars to end cap air
R_{th30}	Radial interconnecting resistance of the rotor bars
R_{th31}	Radial resistance from the rotor bars to air gap
R_{th32}	Radial resistance from the rotor bars to rotor iron
R_{th33}	Axial resistance from the rotor iron to end cap air
R_{th34}	Radial interconnecting resistance of the rotor iron
R_{th35}	Radial resistance from the rotor iron to rotor bars
R_{th36}	Radial resistance from the rotor iron to shaft
R_{th37}	Radial resistance from the shaft to rotor iron
R_{th38}	Axial resistance from the shaft to frame through bearings
R_{rad}	Radiation resistance from the frame to the ambient

4.4 Losses of the motor

Inputs in the thermal network model are the electrical losses of the motor, which can be divided into four groups:

- Copper losses P_{Cu}
- Iron losses P_{Fe}
- Additional losses P_{Add}
- Friction and windage losses P_{Mech}

Since the servomotors are always fed with a frequency converter, there are always voltage and current harmonics present (time harmonics), which increase the motor losses, and therefore the model must be able to take into account also the losses due to harmonics. Harmonics are also caused by the discrete distribution of the slots (winding harmonics), and by the slot openings, where there is a local permeance minimum under the slots (permeance harmonics).

4.4.1 Fundamental wave losses

The different loss components and their equations caused by the fundamental wave are briefly introduced below.

Copper losses

Copper losses form the largest proportion in machine total losses; they are generated in the stator and rotor windings according to Ohm's law

$$P_{\mathrm{Cu}} = mRI^2 \quad , \tag{4.30}$$

where m is the number of phases, R the resistance and I the current. Copper losses change with temperature, as the resistance increases directly proportional to temperature

$$R = R_{\mathrm{DC}}\left(1 + \alpha\Delta T\right) \quad , \tag{4.31}$$

where R_{DC} is the DC resistance, α the resistance temperature coefficient, and T the temperature. Stator copper losses must be separated into copper losses occurring in the copper in the slots and those in the end windings. A length of a single stator turn of a small low-voltage machine, required for resistance separation, is approximately (Jokinen 1979)

$$l_{\mathrm{turn}} = 2L + 2.4\tau_{\mathrm{p}} + 0.1 \quad , \tag{4.32}$$

where L is the stack length and τ_{p} the pole-pitch. Similarly, the separation of the rotor copper losses between the bars and the end ring must be done. Separation can be done with the following equation (Kylander 1995)

$$\frac{P_{\mathrm{bar}}}{P_{\mathrm{ring}}} = 2\sin^2\left(\frac{\pi p}{Q_{\mathrm{r}}}\right)\frac{l_{\mathrm{b}}A_{\mathrm{r}}}{l_{\mathrm{r}}A_{\mathrm{b}}} \quad , \tag{4.33}$$

Where Q_r is the number of the rotor bars, l_b and A_b are the length and the area of a rotor bar, respectively, and l_r and A_r are the length and area of a ring segment between two bars.

Iron losses

Iron losses are generated in the conducting core laminations, and they can be divided into hysteresis, eddy-current and excess (known as anomalous) losses. An empirical equation for the iron losses per unit volume in the stator laminations is written as (Cedrat 2001)

$$P_{\mathrm{Fe}} = \left(k_{\mathrm{h}} \hat{B}^2 f_{\mathrm{s}} + \pi^2 \frac{\sigma d^2}{6} \left(\hat{B} f\right) + k_{\mathrm{e}} \left(\hat{B} f\right)^{1.5} \cdot 8.67 \right) k_{\mathrm{f}} \quad , \tag{4.34}$$

where k_h and k_e are the hysteresis and the excess loss coefficients for the laminations, respectively, and k_f is the lamination stacking factor. B is the flux density, f the frequency, σ the lamination conductivity, and d the lamination thickness. They are usually provided by the steel manufacturer, or they can be determined experimentally, for example with the Epstein-frame setup. The values of 153 $\mathrm{Ws/T^2/m^3}$ for hysteresis loss coefficient k_h and 2.32 $\mathrm{W(T/s)^{-1.5}/m^3}$ for the excess loss coefficient were used in calculations. The value of $4\times10^6\ \Omega^{-1}\mathrm{m}^{-1}$ was used for the lamination radial conductivity and 0.97 for the stacking factor.

Since in speed controlled induction motor drives the motor always operates on the linear part of the torque-speed curve, where the rotor frequency is low, typically few Hertz for the low-speed machines, it is justified to neglect the rotor iron losses for the fundamental frequency. During the field weakening, the rotor frequency can increase up to tens of Hertz, but as the flux density decreases correspondingly, the iron losses are further decreased, as the effect of the flux density is greater than that of the frequency for the iron losses. Rotor iron losses were thus neglected in this work. As all the iron losses are caused by the magnetizing flux, the flux densities in different parts of the machine, required in Eq. (4.34), can be calculated from the cross-sectional areas and the magnetizing flux

$$\hat{B} = \frac{\hat{\phi}_{\mathrm{m}}}{A} \approx \frac{\sqrt{2} U_{\mathrm{m}}}{\omega_{\mathrm{s}} \xi N A} \quad , \tag{4.35}$$

where $\hat{\phi}_{\mathrm{m}}$ is the magnetizing flux peak value, A the area, U_m is the air gap voltage, N the number of turns, ω_s the angular frequency, ξ the winding factor, and A the area.

Additional losses

Iron and eddy current losses caused by the leakage fluxes and by the high-frequency flux pulsations are called additional losses (or the stray-load losses), that are according to IEC 60034-2 standard defined as a fraction of the machine input power

$$P_{\mathrm{stray}} = 0.005 P_{\mathrm{in}} \quad , \tag{4.36}$$

There are basically six mechanisms that cause additional losses in the machine (Sen and Landa 1990)

- Eddy current loss in the stator copper due to slot leakage flux
- Loss in the motor end structures due to end leakage flux
- High-frequency rotor and stator surface losses due to tooth-tip leakage flux
- Tooth pulsation and rotor copper losses due to tooth-tip leakage fluxes
- Rotor copper losses due to circulating currents induced by the leakage fluxes
- Iron losses with skewed motors due to skew-leakage flux

Even if the stator voltage is fully sinusoidal, there are always space harmonics present in the air gap flux due to permeance fluctuations caused by the slotting and the discrete winding distribution. These space harmonics induce eddy currents on the stator laminations and on the rotor bars (especially when fully open rotor bars are used to minimize the slot leakage), that are not included in either the fundamental iron or copper losses.

Mechanical losses

Mechanical losses may be divided into friction and windage losses. Friction losses are generated in the bearings, and they can be approximated analytically as (Gieras 1997)

$$P_{\mathrm{b}} = 3\frac{k_{\mathrm{b}} m_{\mathrm{r}} \Omega}{100\pi} \quad , \tag{4.37}$$

where k_{b} is a factor with value 1-3, m_{r} is the mass of the rotor, and Ω is the mechanical speed. Windage losses are generated at the air gap by the friction of the air, and also on the fan integrated to shaft, if there exists one. Windage losses for the machines of this frame size are very small compared to other loss mechanisms due to relatively small peripheral speed, and thus they are neglected here. Further, it would be very difficult to accurately divide the windage losses between the rotor and the stator.

4.4.2 Harmonic losses of the motor due to inverter supply

When the inverter supply is used, the voltage contains different harmonic frequencies, due to power stage switching operation, and the voltage can be expressed as

$$u(t) = \sqrt{2}\left[U_1 \sin(\omega t) + \sum_{k=2}^{n} U_{\mathrm{k}} \sin(k\omega t + \theta_{\mathrm{k}}) \right] \quad , \tag{4.38}$$

Where U_1 is the fundamental RMS-voltage, U_{k} the k^{th} harmonic RMS-voltage, θ_{k} is the harmonic phase angle, and n=0,1,2… Although Eq. (4.38) applies only for the synchronic pulse width modulation (PWM), where the switching-frequency is a fundamental frequency multiplied by an integer, it can be applied also for other modulation techniques as well (e.g. DTC), without making a significant error. Harmonics of the order [3n+1] rotate in the same direction as the main flux creating a positive torque, and those of the order [3n+2] rotate in the opposite direction creating a negative torque. Harmonics of the order [3n+3] produce no rotating mmf, and therefore they have no effect on torque. Besides that harmonic frequencies create harmful torques, they also have a disadvantageous impact on the machine losses, which causes that frequency converter supplied

motors can withstand less continuous torque than the same motor with a sinusoidal supply. The slip s_k at the k^{th} harmonic is

$$s_k = \frac{kn_s \pm n_r}{kn_s} = \frac{kn_s \pm (1-s)n_s}{kn_s} = \frac{k \pm (1-s)}{k} \quad , \tag{4.39}$$

Where n_s is the synchronous speed, n_r the speed of the rotor, and s the fundamental slip. The $\pm$ sign indicates that different harmonics rotate in different directions. Eq. (4.39) shows that the harmonic slip is approximately unity apart from the first two harmonics. The rotor thus appears almost stationary to harmonic frequencies, which means that the impedance of the magnetizing branch is much greater than the rotor impedance. Therefore the equivalent circuit similar to locked-rotor equivalent circuit, where the magnetizing branch is neglected can be used for the harmonics (Fig. 4.6).

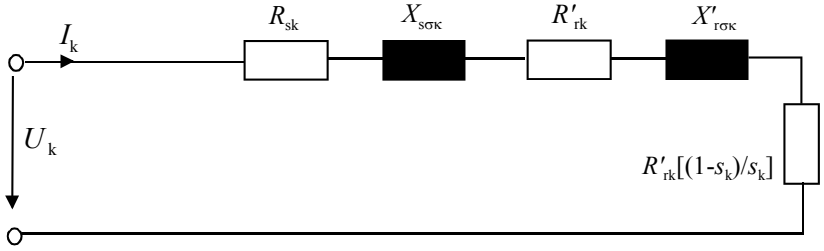

Figure 4.6. Equivalent circuit used in the harmonic loss calculation

The harmonic current of k^{th} order is according to Fig. 4.6 therefore

$$I_k = \frac{U_k}{\sqrt{\left(R_{sk} + \frac{R'_{rk}}{s_k}\right)^2 + \left(X_{s\sigma} + X'_k\right)^2}} \quad . \tag{4.40}$$

Harmonic voltages increase the saturation of the magnetic paths, thus increasing the iron losses. Iron losses for the harmonics can be calculated with Eqs. (4.34) and (4.35) by substituting the harmonic voltages U_k and the corresponding frequency. It is assumed that the hysteresis and eddy current coefficients k_h and k_e remain the same for all frequencies. There is no significant effect on the stator resistance R_s of a small diameter, round-wire machine due to harmonics, since the skin effect is negligible, and the total stator copper losses can be calculated with Eq. (4.30) by substituting the value of the total RMS current

$$P_{Cu} = R_s I^2_{\Sigma RMS} = R_s \left(I_1^2 + \sum_{k=2}^{n} I_k^2 \right) \quad . \tag{4.41}$$

Since the depth of the rotor bars of induction machines in kW range is usually notably higher than the skin depth, the skin effect can have a significant effect on the rotor copper losses. With induction servomotors, the skin effect is further emphasized, since their nominal frequencies can be hundreds of Hertz. The influence of the skin effect on the resistance is taken into account with the skin effect factor k_r

$$R = k_{\mathrm{r}} R_{\mathrm{DC}} \quad . \tag{4.42}$$

When the geometry of the rotor bars is simple, for example rectangular as with the prototype machine, the skin effect factor k_{r} can be calculated

$$k_{\mathrm{r}} = \frac{h_{\mathrm{slot}}}{\delta} \frac{\sinh\left(2\frac{h_{\mathrm{slot}}}{\delta}\right) + \sin\left(2\frac{h_{\mathrm{slot}}}{\delta}\right)}{\cosh\left(2\frac{h_{\mathrm{slot}}}{\delta}\right) - \cos\left(2\frac{h_{\mathrm{slot}}}{\delta}\right)} \ , \tag{4.43}$$

Where h_{slot} is the height of the slot and δ is the skin depth, calculated as

$$\delta = \sqrt{\frac{\rho}{\pi \mu_0 f}} \ , \tag{4.44}$$

where ρ is the resistivity, μ_0 the vacuum permeability, and f the frequency. As the frequency of the rotor current during normal operating conditions is small, the skin effect is relatively small. For example at the nominal point of the prototype induction motor, the increase of the resistance of the rotor bars is only approx. 0.03 % due to fundamental frequency. Even when the motor occasionally operates at higher slip values during overloading, the skin effect is typically approx. 1 % at maximum, and thus it can be neglected for the fundamental wave. However, as the rotor appears almost stationary for all the harmonics, and the rotor frequency equals the harmonic frequency, all the stator harmonics create a strong skin effect on the rotor bars thus increasing the rotor bar resistance and rotor copper losses. For example, the rotor resistance of the prototype motor for the 7$^{\mathrm{th}}$ harmonics is over four-times the DC resistance value according to Eq. (4.42)

Iron losses caused by the harmonic frequencies can be approximated with the same equation as the fundamental wave losses, with the assumption that the hysteresis and eddy-current coefficients remain the same also at harmonic frequencies. Basically this is the case also with additional losses occurring at higher frequencies, but as their proportion is very small, they are neglected here. Also the inclusion of the additional losses at harmonic frequencies would require too profound investigation to be carried out in this study. Figure 4.7 shows the measured 30 first current and voltage harmonics of the prototype at the rated operation point (125 Hz). The measurement was carried out with the Yokogawa PZ4000 power analyzer in harmonic mode, and the motor was supplied with the ACS600 frequency converter.

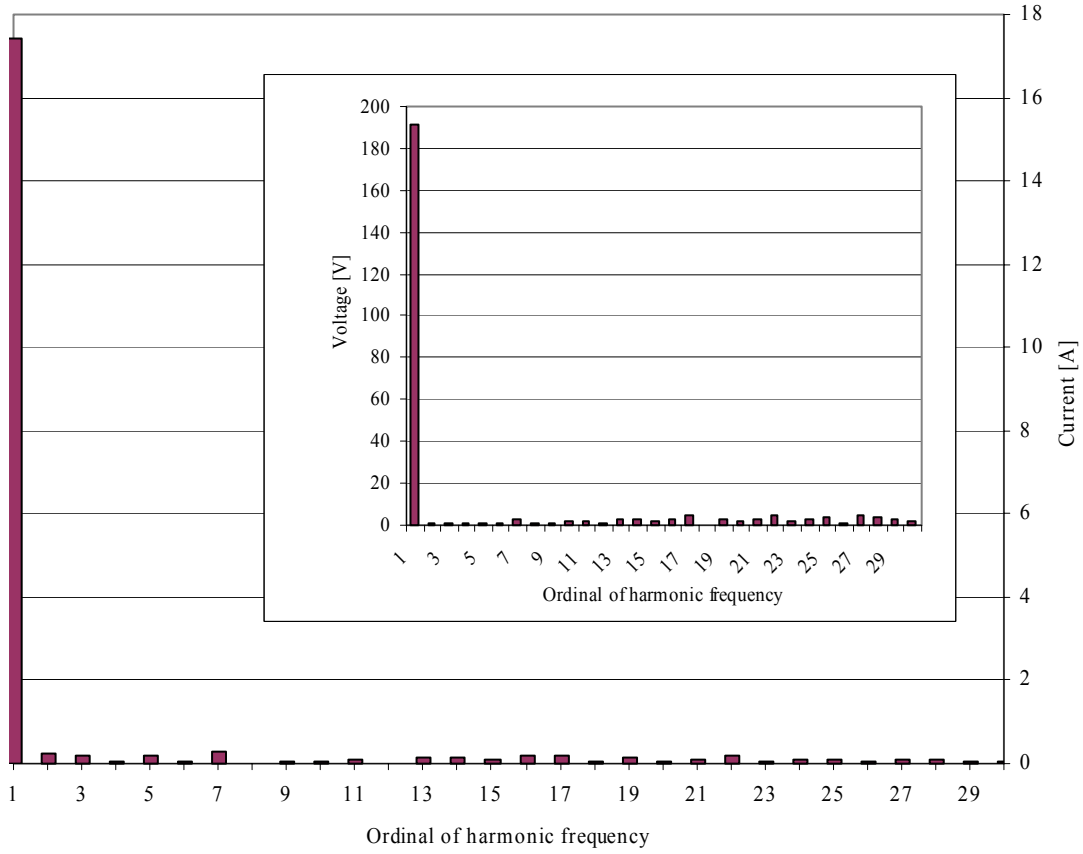

Figure 4.7. Measured current and voltage harmonics (30 first) of the prototype motor. The fundamental frequency was 125 Hz.

4.5 Thermal model calibration

Although the majority of components in thermal model can be calculated within good accuracy due to known dimensions and material data, there are a few components that need more careful study. For example, the stator winding is a complex system containing several materials, both heat conductors and insulators, and in addition, its geometry is too complex to be modelled, at least with random wound windings. In addition, the convective heat transfers between different boundary sections are difficult to calculate accurately, and therefore some thermal resistance parameters need to be determined experimentally with tests. In this work, there were chosen to be four such thermal resistance parameters:

- R_{th} from the stator winding to the stator iron
- R_{th} from the stator yoke to the frame
- R_{th} from the frame to the ambient
- R_{th} from the end windings to the end cap air

Resistance from the stator winding to the stator iron

Heat resistance from the stator winding to the stator iron is typically the most critical parameter in modelling of the thermal behaviour of electrical machines, since large proportion of the heat is

generated in the stator winding, and has to be dissipated to a large degree through this boundary section. Since there are number of insulated conductors in the slot, possibly a resin to fill the rest of the slot and cavities in the resin, and finally a slot liner between the slot and the stator iron, accurate thermal modelling of the slot sections is impossible, and some considerable simplification must be done. It is a common method to model the winding in the slots as a cylindrical rod, containing the copper, the varnish, and the wire insulation, with a radius equivalent to that of the area in the slot, assuming a 100 % slot fill. In the axial direction, it is assumed that only the copper will conduct the heat, but in the radial direction, the rod has a uniform conductivity, which is directly proportional to the conductivities of the varnish and the enamel, which can be assumed equal. The heat conductivity of the copper in the radial direction is thereby not taken into account at all. The rod equivalent conductivity factor F depends only on the fill factor of the slot; Fig. 4.8 shows the values of the F as a function of the slot fill factor when random-wound small diameter wire is used.

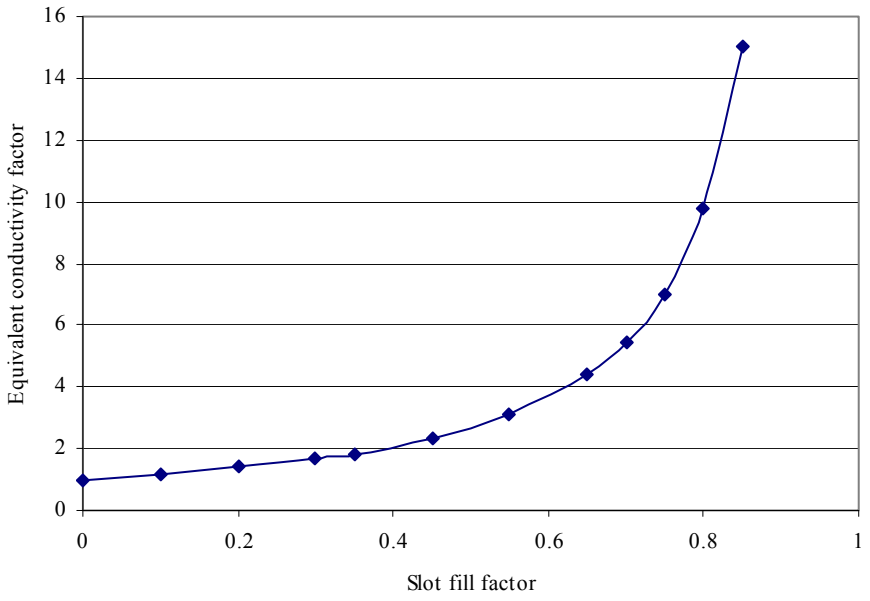

Figure 4.8. Stator winding equivalent conductivity factor as a function of the slot fill factor. With zero fill factor, the factor is unity, and the equivalent conductivity would be equal to that of the insulation. At unity fill factor, the equivalent conductivity would be equal to that of the copper (Downing et al., 2005).

It is impossible to accurately estimate the fill factor of a random-wound electric machine, and it can typically vary between 0.4−0.6, which causes the factor F to vary between 2−4. When comparing the simulation results to measurements, it turned out that a corrected value for F was approx. 2.0, which would correspond to a 0.40 fill factor, which is probably too low a value. Difference could be explained by the manufacturing method of resining; values in Fig. 4.8 are given for a winding with no air bubbles in the resin, which is the case with the (ideal) vacuum impregnation resining. However, if there are air bubbles present in the winding, they will decrease the equivalent thermal conductivity, as the thermal conductivity of the insulators is approximately a decade larger than the conductivity of the air. This virtually decreases the fill factor and consequently the equivalent conductivity factor.

Between the winding and the stator iron, there is usually a slot liner, which is modelled separately in series with the stator winding. Furthermore, the contact between the slot liner and the rough surface of the stator iron contains a lot of air gaps, which must be taken into account in the modelling. These air gaps can be modelled as effective air gaps, and according to Kylander (1995), the typical value for the gap is between 0.17−0.3 mm. Final values for heat resistances are found experimentally from the low frequency thermal test discussed later.

Resistance from the stator yoke to the frame

Heat resistance from the stator yoke to the frame depends mainly on the interface pressure, material hardness, smoothness of the surfaces, and imperfections on the surfaces due to the manufacturing process. The boundary section between the stator yoke and the frame can be modelled with an average air gap, and initial estimates for the model can be found from Table 4.2, which defines thermal conductivities and the average air gap length for the most common solids.

Table 4.2. Heat transfer coefficients and average air gap lengths (moderate pressure and usual finish) (Staton 2005)

Materials	**Heat transfer coefficient** [W/m^{2}K]	**Average air gap** [mm]
Ceramic-Ceramic	500-3000	0.005-0.009
Ceramic-Metal	1500-8500	0.003-0.017
Graphite-Metal	3000-6000	0.004-0.009
Stainless-Stainless	1700-3700	0.007-0.015
Aluminium-Aluminium	2200-12000	0.001-0.002
Stainless-aluminium	3000-4500	0.006-0.009
Iron-Aluminium	4000-40000	0.0006-0.006
Copper-Copper	10000-25000	0.001-0.003

Values given in Table 4.2, however, do not take into account the laminations, and the contact resistance between the yoke and the frame depends to a large degree on the roughness of the lamination of the outer surface, which depends on whether machining of some kind (e.g. turning) is performed before the frame is attached. If the frame and the stator laminations are of different material, also the contact resistance changes with temperature due to different thermal expansion coefficients. The heat resistance values can therefore vary significantly; therefore, they should be used only as initial values, and more accurate values should be found experimentally by passing the known loss through the boundary section and measuring the temperatures on each side.

Resistance from the frame to the ambient

All the heat that is generated inside the machine must ultimately dissipate from the frame to the ambient. Convective heat transfer coefficient can be determined when the motor is run at constant load until thermal equilibrium is reached, and the ambient and the frame temperatures are measured and compared to total machine losses.

Resistance from the end cap air

When the pole number of an electric motor is low, the length of the end turns to the total length of the turn becomes significant. Thereby a large share of total stator copper losses is generated at the end windings, where they have to be dissipated to the end cap air by convection and by conduction to slot regions along the copper itself, as the slot region of the winding is in lower temperature because of the better heat dissipation. With induction machines, there is often an integrated fan on the shaft at the non-drive end to circulate the air in the end regions, and thus to improve the heat dissipation from the end windings. Calculation of the convective heat transfer coefficient for the end windings is extremely difficult due to complex geometries and irregular flow pattern of the cooling air (if there is a fan). Therefore, this thermal resistance is obtained from the low frequency test by measuring the temperatures at the end windings and at the end cap air. The ratio of the length of the end turn to the stack length of the prototype is approximately 0.40, and thus in simulations, it was assumed that 40 % of the total copper loss occurs at the end windings.

4.5.1 Low frequency test

Typically, those thermal parameters that cannot be determined within acceptable accuracy from the geometrical and material data, are usually measured with the so-called DC-test. In the DC thermal test, stator windings are connected in series (or parallel), and DC current is injected to the stator, and thus there are only the stator copper losses present. A problem with the DC-test is that it cannot be applied to star-connected motors with inaccessible star point of the stator winding, as the series (or parallel) connection of the phases is required. In this work, low-frequency current was used instead for heating the machine. As the stator iron losses are approximately proportional to the frequency squared, using for example 10 % of the nominal frequency results only approx. 1 % iron losses compared to the nominal frequency case (if the flux is at the rated value). In this study, 5 Hz frequency was applied (f_N = 125Hz), and thus the iron losses are nearly zero, and can therefore be neglected. The total input power during the low-frequency test was 153 W.

When the motor reached the thermal equilibrium, the input power and temperatures from the frame, the stator yoke, and stator the windings were measured. For example, a thermal resistance between the stator yoke and the frame can then be calculated

$$R_{\text{yoke–frame}} = \frac{T_{\text{yoke}} - T_{\text{frame}}}{P_{\text{in}}} \quad . \tag{4.45}$$

Figure 4.9 depicts the temperatures of the stator winding, the stator yoke, and the frame as a function of the time during the low frequency thermal test.

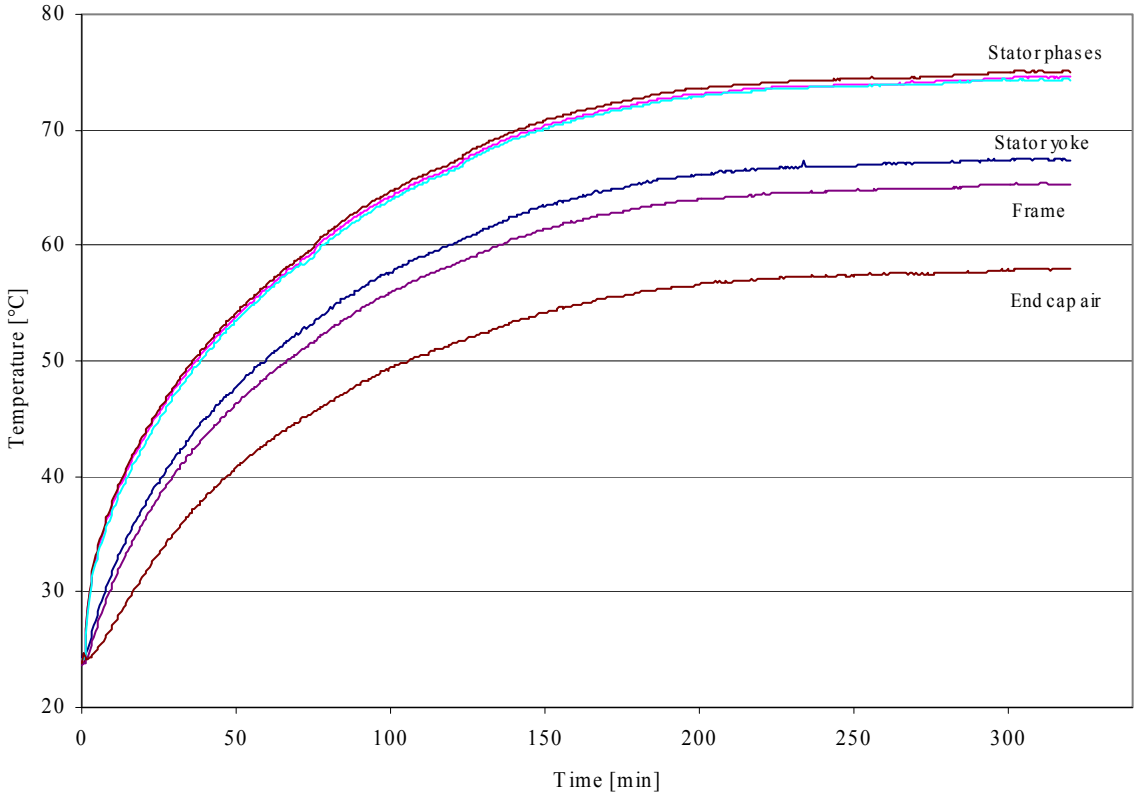

Figure 4.9. Temperature rises of the stator windings, the stator yoke, and the frame during the low frequency test. Steady-state temperatures are: 74.6 °C for the stator winding (average of three phases), 67.4 °C for the stator yoke, 65.3 °C for the frame, and 57.9 °C for the end cap air. Thermal equilibrium was assumed, when the rise of temperatures was less than 0.1 °C in five minutes.

4.5.2 Model verification with prototype motor temperature measurements

Simulation model was verified in the laboratory with the prototype motor connected to an ABB ACS600 frequency converter. The machine was loaded with a Vibro-Meter torque transducer, which is an eddy-current brake connected to the control and measurement equipment. The motor temperatures were measured by using Pt100 temperature sensors, which measure the variation of the resistance due to temperature. Altogether 14 sensors were assembled; one for each phase at both end windings, three for the frame (one in the centre and two at machine ends), and similarly three for the stator yoke and two at the end caps air. Sensors were attached by using heat conducting Araldite glue. Temperature signals were received from the sensors by using Fluke Hydra and a laptop PC equipped with Labview software. The same software was used in obtaining motor currents and voltages from the power analyzer. A minor problem in using Fluke Hydra was its poor suitability for fast temperature transients. When temperatures in five channels were read (e.g. three phases, the frame, and the yoke), the minimum sampling period was approx. 15 s.

Two transient and two static measurements were carried out to verify the validity of the model. Both transient measurements were carried out in overloading conditions, as the overloading of the motor is very common in servo drives. Also a slight adjustment of thermal network parameters

was carried out according to the measurements, although the parameters obtained from pre-calculations and low-frequency tests were surprisingly close to the final values. The biggest source of uncertainty was the radiation resistance from the frame to ambient. Although the emissivity of the matt black frame can be roughly estimated to be approximately 0.8−0.9, it is impossible to estimate the ambient absorptivity even roughly. Therefore, the final value for the radiation thermal resistance was obtained by comparing the simulation data to the measurement data. This value gives a 20 % share of the heat dissipated through radiation, when the motor operates near the maximum winding temperature (where $T_{\text{frame}} \approx 100°\text{C}$).

In first transient measurement, the machine was loaded with the 2.3-fold overload for 15 min, after which the motor was disconnected from both the load and the inverter (zero losses), and the cooling period of 15 min followed. Temperatures were measured within 15 s intervals from the frame, the yoke, and three phases at end windings. The measurement and simulation data is shown in Fig. 4.10.

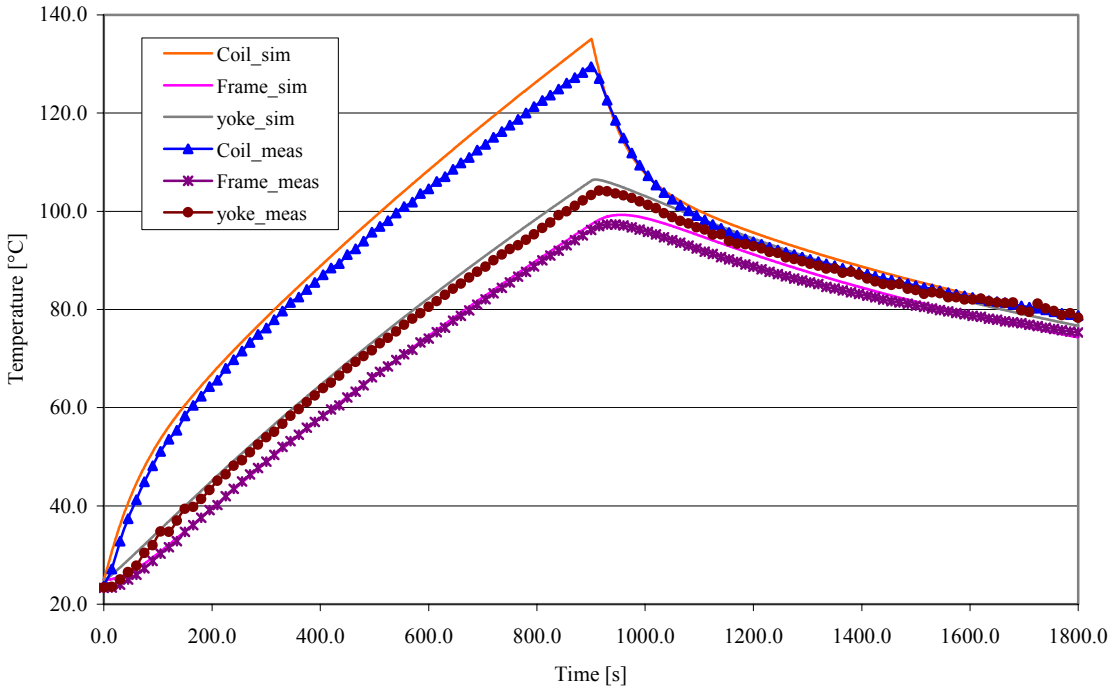

Figure 4.10. Comparison of simulated and measured data, where the cycle consists of 15 min with 2.3-fold overload and 15 min cooling period (no losses). The agreement is very good, although there is a slight error at winding temperatures (4 °C at maximum). The measured temperature of the stator winding is the average value of the three phases.

The second transient measurement was the repeating cycle, where the machine was loaded with the 2.3-fold overload torque for 2 min, which was followed by the 1 min cooling period, and the cycle was repeated again. This measurement is shown in Fig. 4.11.

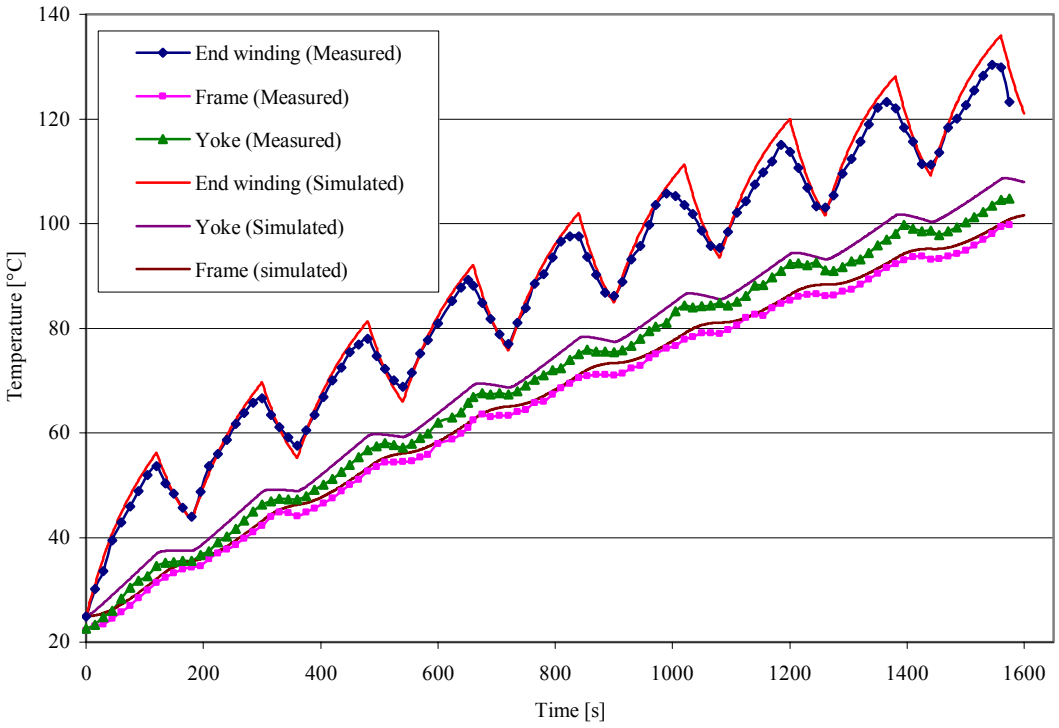

Figure 4.11. Measured and simulated temperatures, when the three minute repeating cycle contains 2 min loading with the 2.3-fold overload and 1 min off-period (zero losses).

As can be seen in Figs. 4.10 and 4.11, the accuracy in the end winding temperature calculations during over loadings is relatively good. At the rated frequency, the frequency converter did not cause any errors to the measured temperatures, as there clearly is no change in temperature after the frequency converter switch-off in Figs. 4.10 and 4.11. However, there seemed to be certain frequencies below the rated one at which the electromagnetic interference of the frequency converter caused significant fluctuations to the temperatures. Temperature sensors were attached by using glue, which has some small thermal capacitance that could slightly smooth out the measured temperatures. Temperature transients in Figs. 4.10 and 4.11 are high, and during such a high transient, the temperature rise rate is to a large degree limited by thermal capacitances that can be calculated accurately, if the complete dimensional and material data of the motor is available. This partially explains the good accuracy in Figs. 4.10 and 4.11. Therefore, also the steady-state accuracy of the model was verified by running the motor with a constant load in two operating points, until the thermal equilibrium was reached. Figures 4.12 and 4.13 show the temperature rise of the motor when loaded with a constant load until the thermal equilibrium is reached (thermal equilibrium was assumed when the temperature rise was below 0.1 °C in 5 min). In Fig. 4.12 the motor is operated at the rated torque and speed, and in Fig. 4.13 both the speed and the torque are 50 % of the rated value. The measurement in Fig. 4.13 was carried out on a hot day in July, when the laboratory temperature was almost 30 °C, which explains the difference between the initial temperatures.

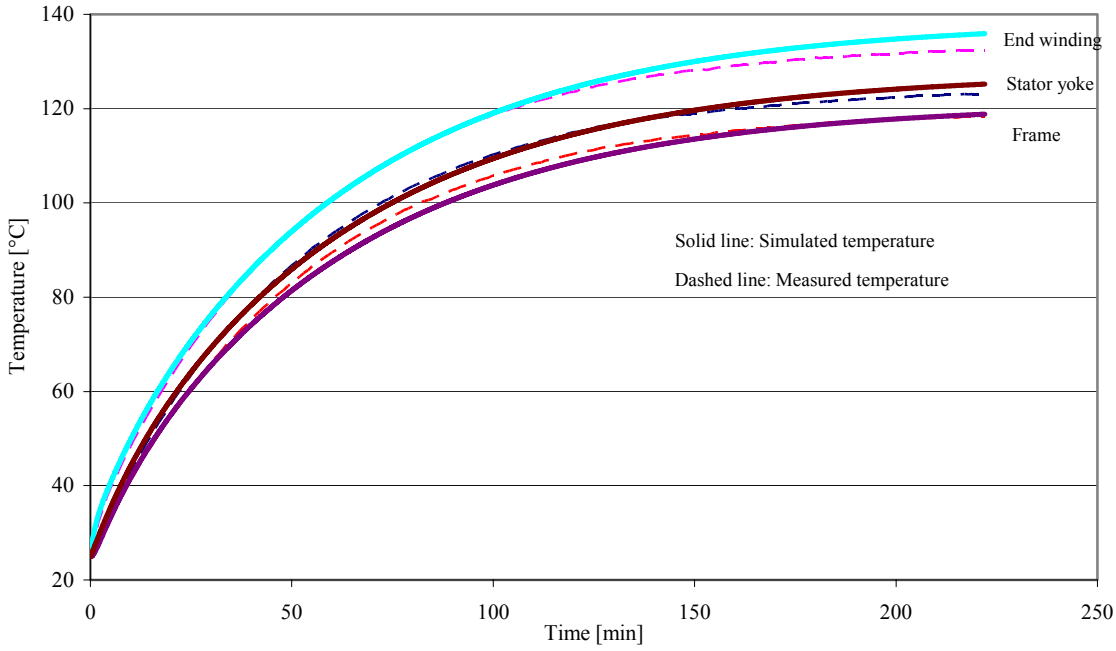

Figure 4.12. Measured (dotted lines) and simulated (solid lines) temperatures of the prototype motor, when it was operating at the rated point.

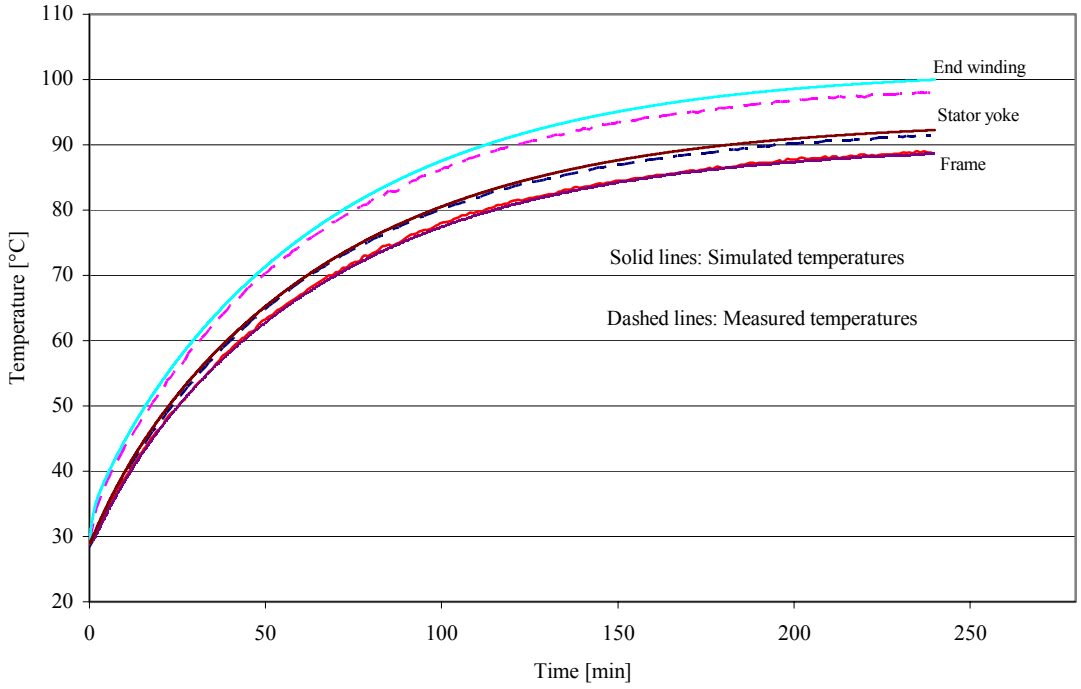

Figure 4.13. Measured (dotted lines) and simulated (solid lines) temperatures of the prototype motor, when it was operating at 50 % of the rated torque and speed.

4.6 Induction servomotor loss distribution vs. thermal behaviour

With industrial induction motors, stator copper losses are typically the dominating loss mechanism, and with small-power machines, they can comprise over 50 % of the total loss. Figure 4.14 shows the typical distribution of the loss components of a four-pole industrial cage-induction motor as a function of power.

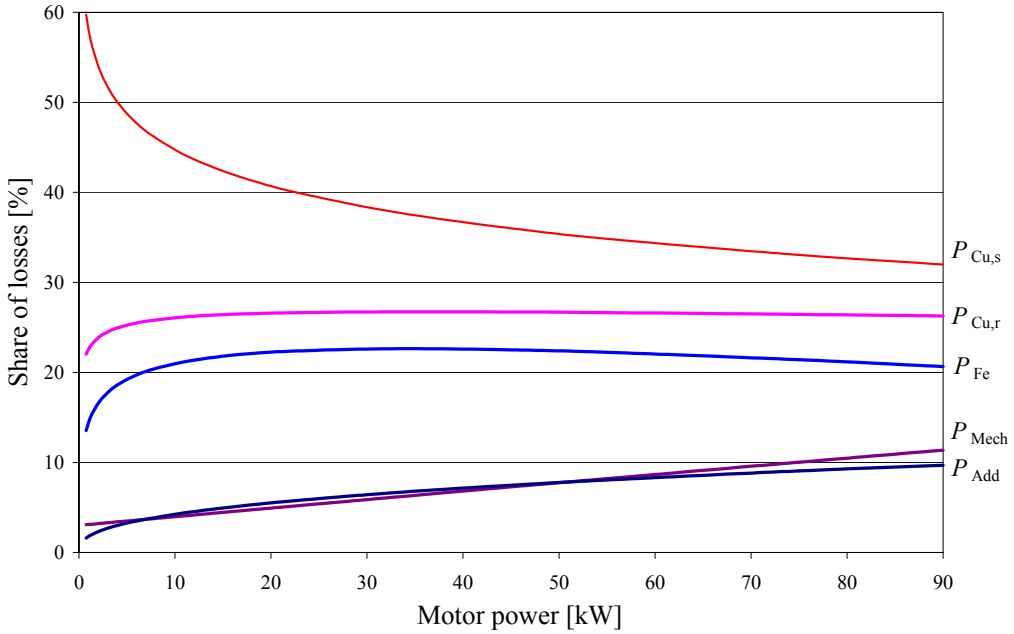

Figure 4.14. Loss distribution of four-pole totally enclosed fan-cooled (TEFC) squirrel cage motors as a function of power (Auinger 1997; Haataja 2003 (modified)).

As the temperature rise of the stator winding insulation is critical from the thermal point of view, the temperature level of the (stator) winding insulation must be kept below value given by the manufacturer, or otherwise the insulation failure and consequently the turn-to-turn or turn-to-ground short-circuit may occur. As almost all the electrical insulators are also thermal insulators, the heat dissipation is very poor from the stator winding to ambient, as the winding is entirely surrounded by several insulation layers. Typically the critical part of the winding is the end-section, as it is fully surrounded by the air and the resin material, and further, it is far away from any conducting section. The heat conductivity of the air is the worst of all the materials present in electrical machines, as can be seen from Table 4.3, which lists the thermal conductivities of the most common materials.

Table 4.3 Heat conductivities of the most common materials used in electrical machines (Kylander 1995).

Material	**Thermal conductivity λ_{th} [W/mK]**
Copper (pure)	395
Aluminium (pure)	237
Construction steel	50
Electrical steel (M600-50A in plane)	38.7
Lamination material	3.7
Epoxy-resin heat conductivity	0.2
Slot insulation varnish	0.2
Air heat conductivity	0.026

As can be seen from Table 4.3, the thermal resistance from the end winding to the conducting parts of the machine – and finally into the ambient – inevitably becomes large as it is surrounded by the air. In the slots, the empty space between the conductors is very often filled with the resin material, which not only mechanically strengthens the winding, but also improves the heat dissipation, as the thermal conductivity of the resin is almost a decade higher than that of the air. Between the winding and the stator iron, there is a slot liner that protects the winding from mechanical shocks, and due to the roughness of the interfacing surfaces, the contact between the slot liner and the stator iron contains lots of cavities. These things together cause that the heat dissipation from the stator winding, especially from the end-section, is very poor, and the loadability of the machine is thereby determined to a large degree by the stator current.

Stator iron losses are easier to dissipate, as the thermal conductivity of the electrical steel is relatively good and there is only one boundary section that the heat flux must pass to reach the frame, which is the section between the stator yoke and the frame. Depending on the manufacturing technique, materials, and the contact pressure, this boundary section also contains cavities that degrade the heat dissipation, but as this section is also included on the heat dissipation from the stator windings to the ambient, it can be said that the thermal resistance from the windings to ambient is remarkably higher than that from the stator iron to the frame. If the load distribution of the motor can be changed in such a way that the stator copper losses are decreased while increasing the stator iron losses (by increasing the flux), the heat dissipation, and thus the thermal loadability of the motor will improve. Increasing the flux level also decreases the rotor copper losses with induction motor, which must be to a large degree dissipated through the stator. With PMSMs having thick magnets, this significantly improves the heat dissipation compared to induction machine, and enables the fully closed construction of PMSM servo. The problem with the induction machine is that although the increase in the flux level decreases the torque-producing stator current, it increases the magnetizing current, especially when the motor is in saturation, and thus the total effect on the stator current can be very small or even the opposite. In Chapter 3, only the behaviour of the total loss (efficiency) as a function of flux density was studied. Figure 4.15 presents the individual loss components of the prototype as a function of flux level (calculated with FEM).

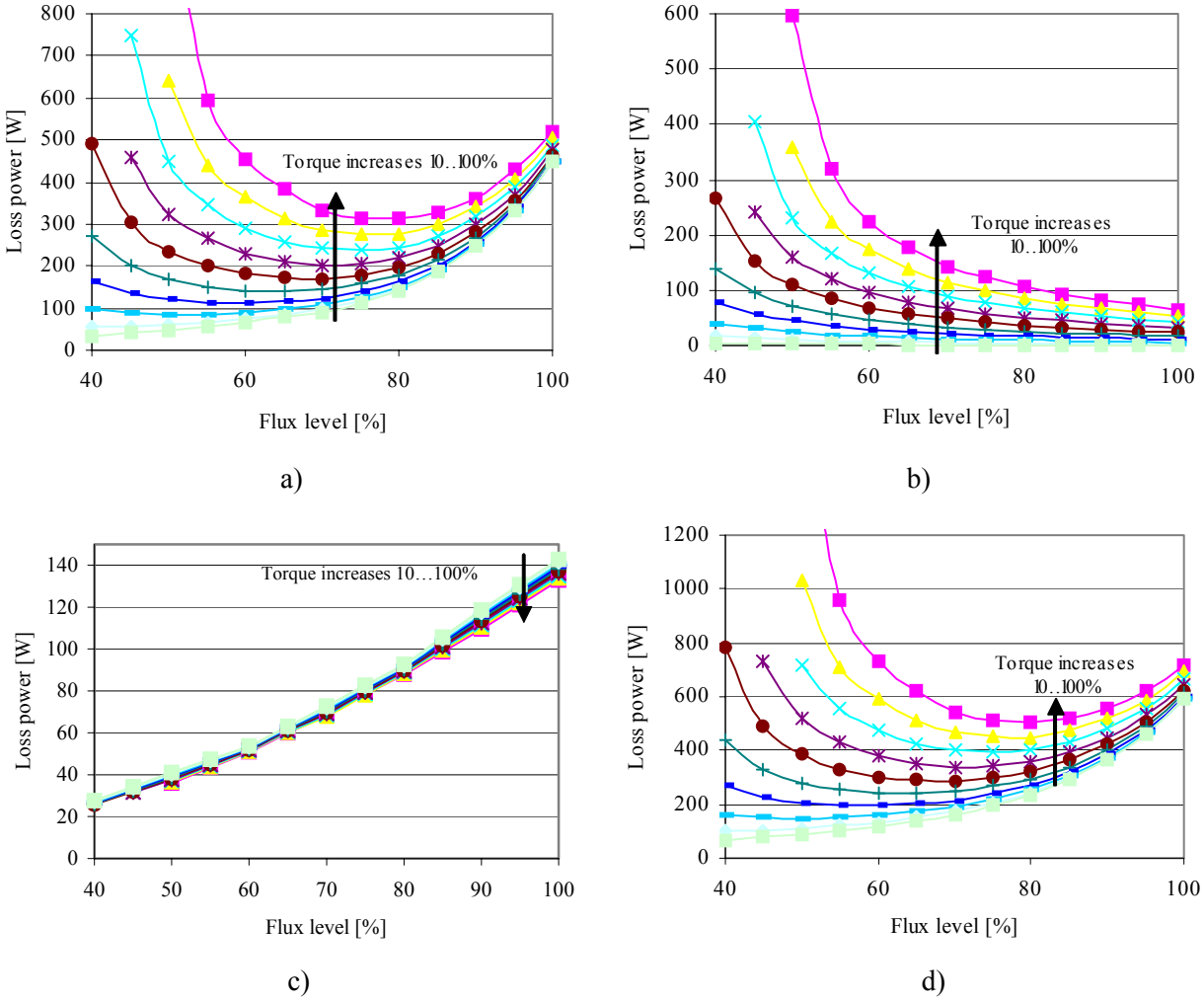

Figure 4.15. Simulated (FEM) fundamental wave losses of the prototype motor as a function of flux level. a) Stator copper losses, b) Rotor copper losses, c) Stator iron losses, and d) Sum of the loss components (total losses).

As can be seen in Fig. 4.15, the flux has a substantial effect on the different loss components, especially the stator copper losses can be reduced substantially by decreasing the flux level. By decreasing the flux at rated torque by approx. 20 %, the total losses can be decreased by approx. 30 %. With smaller loads, the effect is even stronger. Figure 4.16 shows the measured end winding temperature rises of the prototype motor at four different loading levels, and flux level as a parameter.

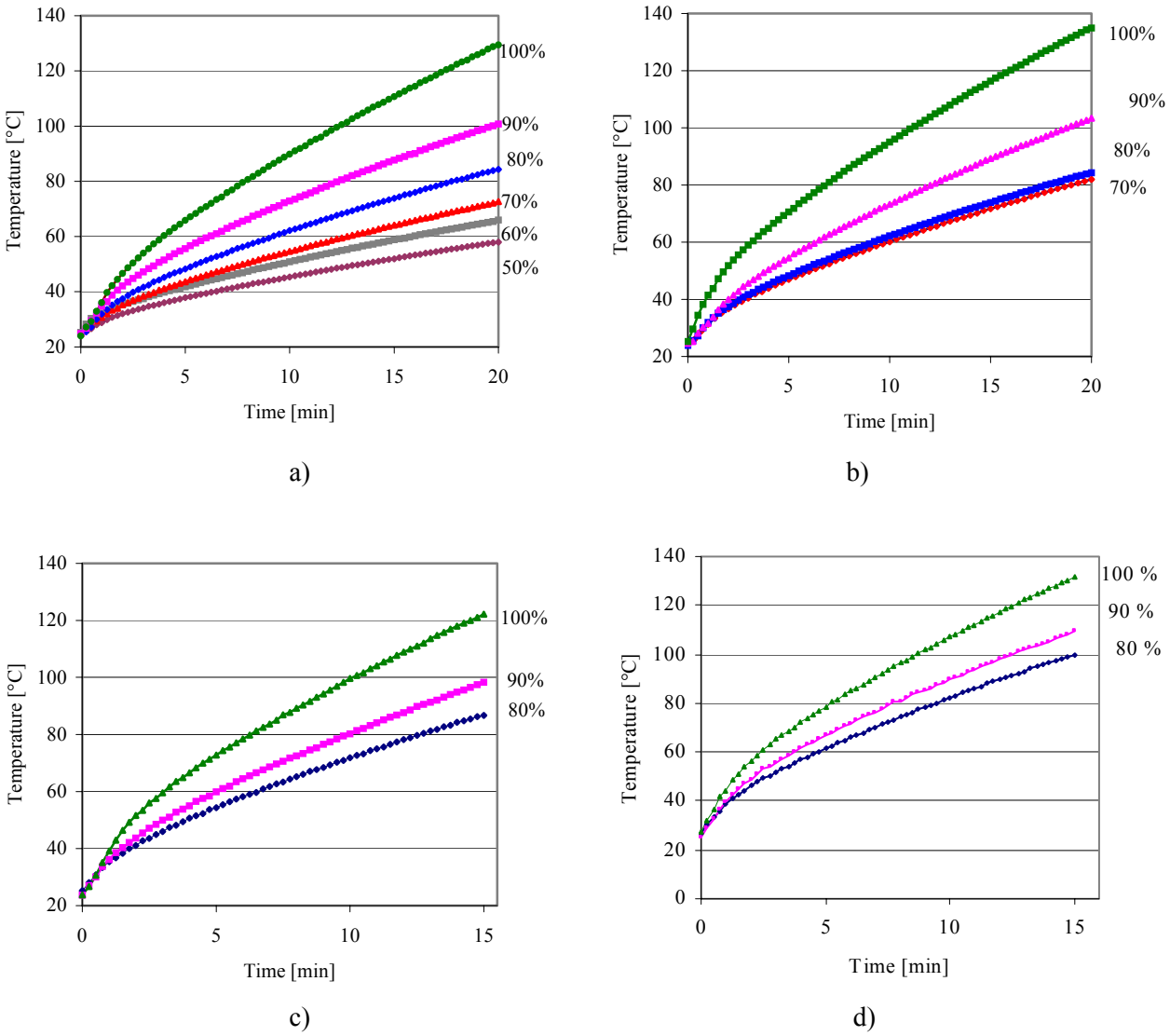

Figure 4.16. Heating of the machine end windings at different flux levels, at 50, 100, 150, and 200 % load torque. a) 50 % of the rated torque, b) rated torque, c) 150 % of the rated torque and d) 200 % of the rated torque. There is a significant difference in the heating at different flux levels, especially at partial loads, although the gap for instance in temperature of the end winding between 80 % and 100 % at rated load is still approx. 30 °C after 15 min loading.

Figure 4.16 shows that the flux level optimization discussed in Chapter 3 has a substantial effect on the heating of the machine, as it could be assumed. By properly controlling the flux level, the thermal loadability can be increased and the lifespan of the windings lengthened. As a drawback, the load cycle must be known to avoid abrupt torque variations. This is because the dynamic stability of the drive diminishes when decreased flux is applied.

4.7 Temperature effects on servo characteristics

Due to a positive thermal coefficient of copper (and the aluminium if used), the stator and the rotor resistances increase with temperature, which has some undesirable effect on the machine. Besides that the resistive losses increase and more heat is generated, more important in servo drives are effects on the overloading capability and dynamic performance due to decreased pull-out torque and increased slip. These two phenomena are briefly discussed below.

4.7.1 Effects on the pull-out torque

It is a common approximation that the pull-out torque of an induction machine depends only on the machine short-circuit reactance, and thus on the sum of the stator and rotor leakage reactances

$$T_{\text{pull-out}} \approx \frac{mp}{2\left(L_{\text{s}\sigma} + L'_{\text{r}\sigma}\right)} \frac{U_{\text{s}}^2}{\omega_{\text{s}}^2} \quad . \tag{4.46}$$

However, the pull-out torque depends also on the stator resistance, and consequently on the coil temperature (Eq. (3.11) in Chapter 3). By substituting the equation for the resistance temperature dependence, Eq. (4.31), into the equation for the pull-out torque (Eq. (3.11)), the equation for the pull-out torque as a function of temperature is given in the form

$$T_{\text{pull-out}}(T) = \frac{mp}{2\omega_{\text{s}}} \frac{U_{\text{s}}^2}{R_{\text{s}}\left[1 + \alpha_{\text{Cu}}\left(T_{\text{ch}} - T_{\text{cc}}\right)\right] + \sqrt{\left\{R_{\text{s}}\left[1 + \alpha_{\text{Cu}}\left(T_{\text{ch}} - T_{\text{cc}}\right)\right]\right\}^2 + \left(X_{\text{s}\sigma} + X'_{\text{r}\sigma}\right)^2}} \quad , \tag{4.47}$$

where T_{ch} and T_{cc} are the temperatures of the stator coil for the hot and cold machine, respectively, and α_{Cu} is the copper resistance temperature coefficient (0.00393 Ω/°C). In Fig. 4.17, the behaviour of the prototype motor pull-out torque is plotted as a function of the temperature at different frequencies.

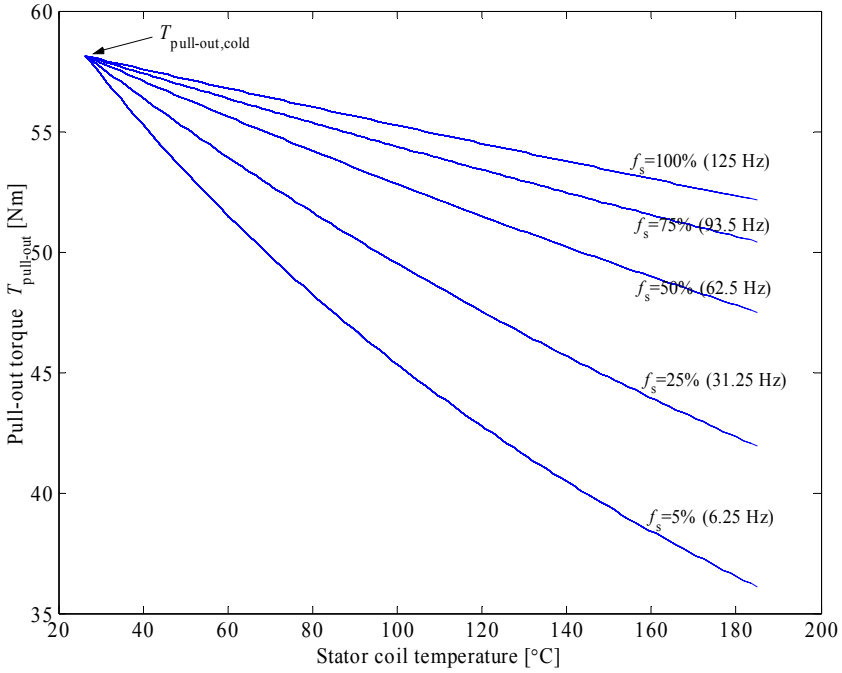

Figure 4.17. Pull-out torques of the prototype motor as a function of the temperature at constant flux. The decrease in the pull-out torque is significant especially at lower frequencies (f_N = 125 Hz). *RI*-compensation is applied to keep the air gap flux constant regardless of the speed. Without it, the pull-out torque would further decrease at lower frequencies due to the stator resistive voltage loss.

Figure 4.17 shows that the decrease in the pull-out torque due to the increased winding temperature is significant, especially at lower frequencies. This due to the fact that at low frequencies, the relative proportion of the reactances decreases, while the resistance remains constant. To be exact, also the stator resistance decreases slightly with the frequency due to skin effect, but especially with small-diameter round-wire, the skin effect is negligible, and can be omitted. To compensate the decreased pull-out torque, air gap flux linkage should be kept constant by increasing the stator voltage similarly to *RI* compensation at lower frequencies. In Fig. 4.18, the prototype motor pull-out torques are plotted as a function of temperature and speed.

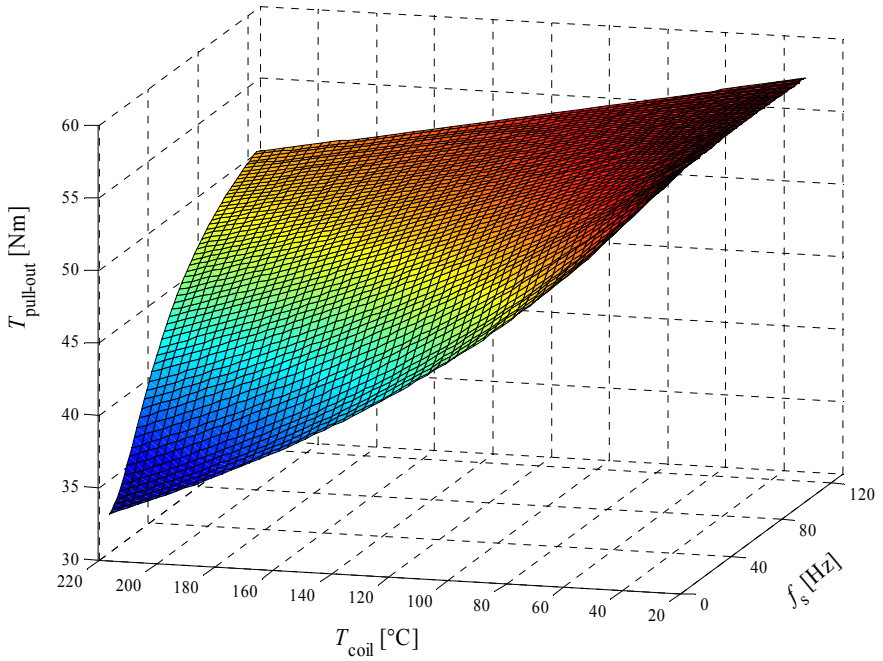

Figure 4.18. Analytically calculated pull-out torques of the prototype motor as a function of the stator frequency and the temperature of the coil. To compensate the decreased pull-out torque, the air gap flux linkage should be kept constant regardless of the speed by increasing the stator voltage towards the lowest speeds.

4.7.2 Slip compensation due to temperature rise with the rotor resistance estimation

As the increase of the stator resistance decreases the pull-out torque, an increase in the rotor resistance increases the slip. An increase of 1 °C of the rotor bar temperature increases the slip approximately by 0.4 %. Figure 4.19 shows how the stator and rotor temperatures affect the motor characteristics. Rotor resistance only affects the slip, while the stator resistance mainly affects the amplitude of the pull-torque, but also slightly the pull-out slip. It must be noted, however, that the temperatures in the rotor and the stator are practically always more or less even, and the case where the one is cold and the other hot rarely occurs. All the four combinations are shown only to illustrate how the two resistance parameters affect the motor characteristics.

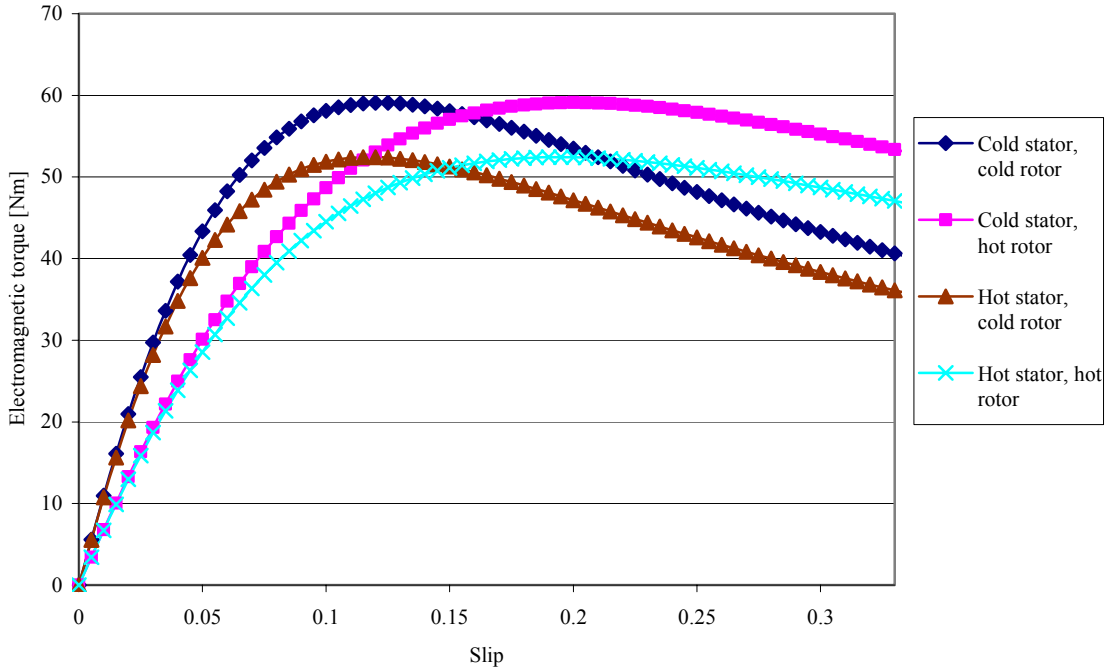

Figure 4.19. Influence of the stator and rotor winding temperatures on the motor torque characteristics at nominal speed. Rotor bar temperature defines the rated and pull-out slip, while the stator coil temperature affects the amplitude of the pull-out torque and also slightly the pull-out slip. A word "hot" refers to 180 °C and "cold" to 25 °C.

An increase of both the stator and the rotor temperatures cause the slip to increase and the pull-out torque to decrease. The increase of the slip consequently increases the rotor copper losses, and decreases the transient performance during fast loading variations, as the torque stiffness reduces. The increase in the rotor resistance can be compensated by increasing the air gap flux of the motor, as the slip is approximately proportional to the inverse of the square of the air gap flux. As the temperature of the rotor bars cannot be directly measured in commercial motors, it can be estimated from the slip. An induction motor can be expressed with the following well-known set of differential equations in the synchronously rotating reference frame

$$\begin{bmatrix} u_{\mathrm{sq}} \\ u_{\mathrm{sd}} \\ 0 \\ 0 \end{bmatrix} = \begin{bmatrix} R_{\mathrm{s}} + \frac{\mathrm{d}}{\mathrm{d}t}(L_{\mathrm{s}}) & \omega_{\mathrm{s}} L_{\mathrm{s}} & \frac{\mathrm{d}}{\mathrm{d}t}(L_{\mathrm{m}}) & \omega_{\mathrm{s}} L_{\mathrm{m}} \\ -\omega_{\mathrm{s}} L_{\mathrm{s}} & R_{\mathrm{s}} + \frac{\mathrm{d}}{\mathrm{d}t}(L_{\mathrm{s}}) & -\omega_{\mathrm{s}} L_{\mathrm{m}} & \frac{\mathrm{d}}{\mathrm{d}t}(L_{\mathrm{m}}) \\ \frac{\mathrm{d}}{\mathrm{d}t}(L_{\mathrm{m}}) & \omega_{\mathrm{slip}} L_{\mathrm{m}} & R_{\mathrm{r}}' + \frac{\mathrm{d}}{\mathrm{d}t}(L_{\mathrm{r}}') & \omega_{\mathrm{slip}} L_{\mathrm{r}}' \\ -\omega_{\mathrm{slip}} L_{\mathrm{m}} & \frac{\mathrm{d}}{\mathrm{d}t}(L_{\mathrm{m}}) & -\omega_{\mathrm{slip}} L_{\mathrm{r}}' & R_{\mathrm{r}}' + \frac{\mathrm{d}}{\mathrm{d}t}(L_{\mathrm{r}}') \end{bmatrix} \begin{bmatrix} i_{\mathrm{sq}} \\ i_{\mathrm{sd}} \\ i_{\mathrm{rq}} \\ i_{\mathrm{rd}} \end{bmatrix}, \tag{4.48}$$

As the thermal time-constants of electrical machines are decades longer than the electrical ones, only the steady-state solutions of Eq. (4.48) are of interest, which means that all the time-derivative terms go to zero, and the equation simplifies into the form

$$\begin{bmatrix} u_{\mathrm{sq}} \\ u_{\mathrm{sd}} \\ 0 \\ 0 \end{bmatrix} = \begin{bmatrix} R_{\mathrm{s}} & \omega_{\mathrm{s}} L_{\mathrm{s}} & 0 & \omega_{\mathrm{s}} L_{\mathrm{m}} \\ -\omega_{\mathrm{s}} L_{\mathrm{s}} & R_{\mathrm{s}} & -\omega_{\mathrm{s}} L_{\mathrm{m}} & 0 \\ 0 & \omega_{\mathrm{slip}} L_{\mathrm{m}} & R_{\mathrm{r}}^{'} & \omega_{\mathrm{slip}} L_{\mathrm{r}}^{'} \\ -\omega_{\mathrm{slip}} L_{\mathrm{m}} & 0 & -\omega_{\mathrm{slip}} L_{\mathrm{r}}^{'} & R_{\mathrm{r}}^{'} \end{bmatrix} \begin{bmatrix} i_{\mathrm{sq}} \\ i_{\mathrm{sd}} \\ i_{\mathrm{rq}} \\ i_{\mathrm{rd}} \end{bmatrix}, \tag{4.49}$$

By solving the rotor quadrature- and direct-axis currents, i_{rq} and i_{rd}, respectively from rows 1 and 2, the rotor resistance R'_{r} can be solved

$$R_{\mathrm{r}}^{'} = \omega_{\mathrm{slip}} \left(\frac{-L_{\mathrm{m}}^2 i_{\mathrm{qs}} \omega_{\mathrm{s}} + L_{\mathrm{r}} R_{\mathrm{s}} i_{\mathrm{ds}} + L_{\mathrm{r}} \omega_{\mathrm{s}} L_{\mathrm{s}} i_{\mathrm{qs}} - L_{\mathrm{r}} \omega_{\mathrm{s}} L_{\mathrm{s}} i_{\mathrm{qs}} - L_{\mathrm{r}} u_{\mathrm{sd}}}{\omega_{\mathrm{s}} L_{\mathrm{s}} i_{\mathrm{ds}} + R_{\mathrm{s}} i_{\mathrm{ds}} - u_{\mathrm{sq}}} \right) . \tag{4.50}$$

Finally, the rotor temperature of the rotor bars can be calculated from the rotor resistance estimate

$$T_{\mathrm{rbar}} = \frac{R_{\mathrm{r}}^{'} - R_{\mathrm{r,cold}}^{'}}{\alpha_{\mathrm{bar}} R_{\mathrm{r,cold}}^{'}} + T_{\mathrm{amb}} \ . \tag{4.51}$$

When the thermal model is connected to the electromagnetic motor model, the d- and q –axis voltages and currents are already available, which makes the implementation of the rotor temperature estimation block very straightforward in the model. Equation (4.50), however, gave approximately 20 % too high value for the rotor resistance compared to the measured value, but as the rotor bar temperature is calculated from the relative variation of the resistance, the absolute value of the resistance is of no interest here. Figure 4.20 compares the rotor temperatures calculated with the thermal network model from the losses, and estimated by Eqs. (4.49)−(4.51) directly from the outputs of the electromagnetic motor model and the motor parameters. It must be noted, however, that the temperature correction for the angular slip frequency ω_{slip} and the stator resistance is required, and thus the rotor temperature estimate cannot be calculated by using only the electromagnetic motor model.

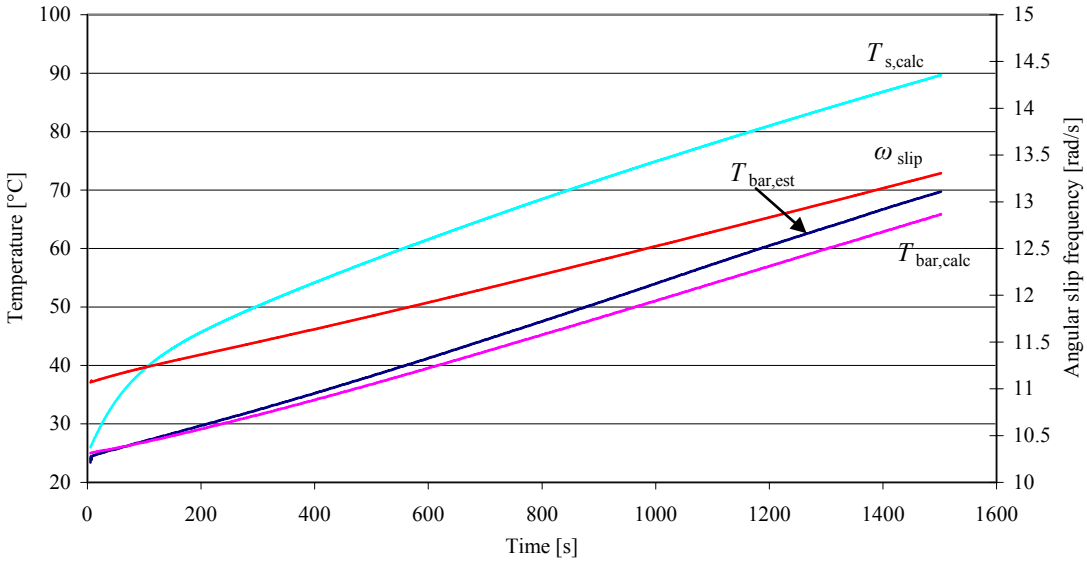

Figure 4.20. Rotor bar temperatures estimated directly from the electromagnetic motor model and calculated from the thermal network model from 0→1500 s. Rotor temperature estimated from the electromagnetic motor model and the corrected angular slip frequency gives within reasonable accuracy the same results as the thermal network model.

Figure 4.20 shows that it is possible to estimate the rotor resistance and temperature within reasonable accuracy from the motor parameters, d- and q–axis currents and voltages, and the slip frequency. Modern AC servodrives are equipped with vector control, as it guarantees the adequate dynamic performance, which means that the required parameters for estimating the rotor resistance are constantly calculated. Temperature corrected value of the stator resistance is required in the pull-out torque compensation due to temperature rise, and the corrected rotor resistance is required if the constant slip is to be kept regardless of the temperature. By keeping the slip low, the dynamic performance during fast load transients remains high, and also the rotor losses can be decreased. Also it should be noted that without the slip compensation due to the temperature, there exists a positive feedback from the rotor temperature. As the increased rotor resistance causes the motor to run at a higher slip, a bigger proportion of the air gap power is transferred into heat at the rotor bars, which further increases the rotor resistance and consequently the slip.

4.8 Thermal model sensitivity analysis and simplified thermal network model

The benefit of an analytical simulation model compared for example to FEM model is the decades lower computation time; a designer can simulate tens of motors per day, while with the FEM model, the accurate computation of a large machine can easily take days, or even weeks if the 3D problem is to be solved. 3D computation is required especially with thermal calculations, as it is very often impossible to reduce the problems in two dimensions, unlike in the case of electromagnetic calculations. Another problem with FEM is the long problem setup time. With the thermal network model, a drawback of the short computation time is the limited accuracy, as the complex 3D heat transfers are modelled only with a few constant parameters. In practice, the designers apply the analytical model to reach the certain accuracy, and after that, the FEM is applied for verification and “fine-tuning”. As the accuracy of the analytical model is limited due to several simplifications, it is yet important to know which parameters are the most sensitive ones so that they can be determined as accurately as possible.

As the temperature of the end windings is the critical part of all electrical machines, it also the main focus of the sensitivity analysis carried out here, and a more detailed analysis would be far beyond the scope of this work. The sensitivity analysis is carried out by increasing each parameter in the thermal network model by 20 %, and comparing the consequent temperatures of the end winding to original temperatures. Also the effect of the motor parameters in the electromagnetic part of the model for the temperature rises of the motor is included. The thermal network in this study comprises 39 heat resistances, 8 heat capacitances, and 4 heat generators as sources of the model. Table 4.4 shows the effect of the parameter variations on the steady-state end winding temperatures of the prototype motor at the nominal point. The description of the each parameter was already given in Table 4.1

Table 4.4. Effect of thermal model parameter variation on the end winding temperature rise. Each parameter was increased by 20 %, and the steady-state temperature of the end winding was compared to the original temperature. Parameters marked grey are used in the simplified model explained below.

Parameter	ΔT end winding [°C]	**Parameter**	ΔT end winding [°C]	
R_{th1}	14.5	R_{th27}	0.03	
R_{th2}	3.32	R_{th28}	0.03	
R_{th3}	1.51	R_{th29}	0.03	
R_{th4}	0.11	R_{th30}	0.04	
R_{th5}	0.12	R_{th31}	0.03	
R_{th6}	0.21	R_{th32}	0.03	
R_{th7}	0.15	R_{th33}	0.03	
R_{th8}	0.05	R_{th34}	0.05	
R_{th9}	0.21	R_{th35}	0.04	
R_{th10}	-0.15	R_{th36}	0.03	
R_{th11}	0.41	R_{th37}	0.05	
R_{th12}	0.03	R_{th38}	0.09	
R_{th13}	0.85	R_{th39}	0.04	
R_{th14}	0.11	R_{rad}	4.1	Radiative resistance from the frame
R_{th15}	0.03	$P_{Fe,s}$	5.28	Stator iron loss
R_{th16}	0.11	$P_{Cu,s}$	24.1	Stator copper loss
R_{th17}	0.12	$P_{Cu,r}$	1.3	Rotor copper loss
R_{th18}	0.13	$d_{insulation}$	2.8	Slot insulation thickness
R_{th19}	0.02	f_{slot}	0.06	Slot fill factor
R_{th20}	0.10	$k_{lamimantion}$	-0.20	Lamination axial heat conductivity
R_{th21}	0.04	$k_{varnish}$	-1.21	Varnish heat conductivity
R_{th22}	0.21	$K_{insulation}$	-2.36	Slot insulation heat conductivity
R_{th23}	0.04	h_{ag}	-0.12	Air gap film coefficient
R_{th24}	0.04	$h_{e\text{-}w}$	-0.28	End-winding film coefficient
R_{th25}	0.05	R	-1.19	Radial conductivity factor
R_{th26}	0.16	W	0.07	Coil hotspot-to-mean temper. ratio

As it can be seen in Table 4.4, there are only a few resistance parameters that significantly affect the temperatures, while the majority has only a minor effect. Therefore, a simplified thermal network model was constructed, which was used to study whether it is possible to estimate the

motor temperatures within reasonable accuracy by only using the most significant parameters. For the simplified thermal network model, some simplifications were made:

- Rotor is modelled as one solid part containing the cage, the rotor core and the shaft
- All the heat generated in the rotor transfers to the stator (through the air gap)
- Stator core is modelled as one solid part where the iron losses are generated

The simplified model was constructed by using ten resistance parameters, marked grey in Table 4.4. In general, these parameters are also the ten most significant regarding the sensitivity analysis. There are, however, some resistance parameters that are also significant, but neglected in the model. For example, the resistance R_{th3} is the fourth most significant parameter, but it is the resistance between the stator yoke and the teeth, and as they are not modelled separately in the model, also the corresponding resistance is not included in the model. Figure 4.21 shows the Simulink™ diagram of the simplified thermal network model. As the figure is in the Simulink form, it also illustrates how the thermal network model can be constructed by using Simulink's circuit simulator ("SimPower Systems"). In the model, losses are fed through the controlled current source blocks, and the temperatures are measured by using the voltage measurement block, as the voltage equals temperature difference. In Fig. 4.21, the nodes correspond to the different sections of the motor.

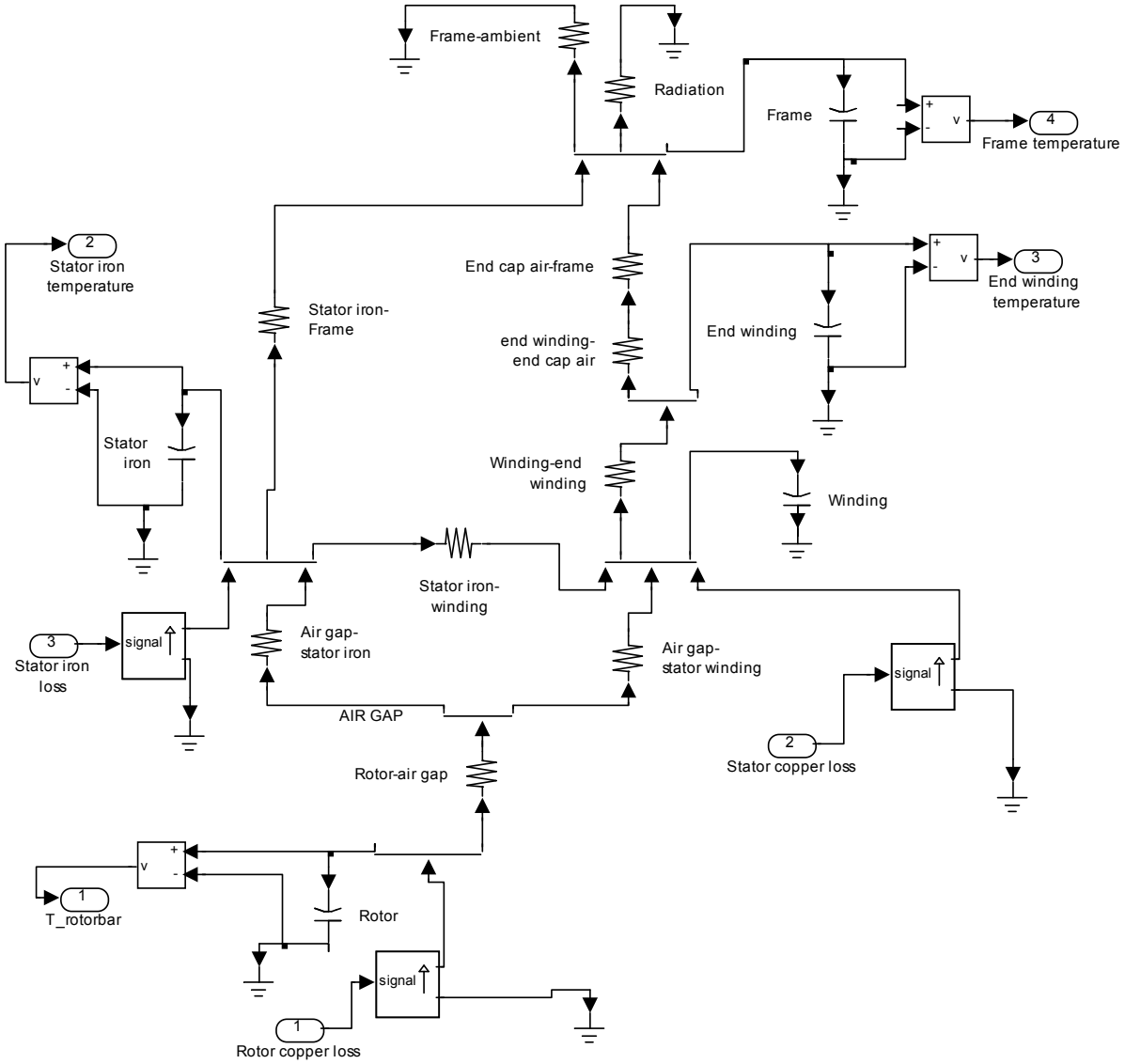

Figure 4.21. Simplified thermal network model in Simulink™.

The comparison of temperatures calculated with the full model and with the simplified one in three different parts of the motor (end winding, frame, and stator iron) are shown in Fig. 4.22. The measured results are not added in the figure, first of all because of clarity, and secondly, it can be assumed that the full model can calculate the temperatures within reasonable accuracy based on the measured results shown earlier. It can be seen in Fig. 4.22 that the steady-state temperature of the end winding is practically the same with both models, although there is some difference in the transient-state temperatures. With the stator iron and the frame, the situation is opposite; the simplified model calculates the transient temperature almost similarly to the full model, but approx. a 10 °C difference exists in the steady-state temperatures. However, as the temperatures of the stator iron and the frame are usually less interesting parameters while the winding temperature defines the rating of the machine, it can be said that the simplified model can be used if the complete dimensional data of the motor is not available.

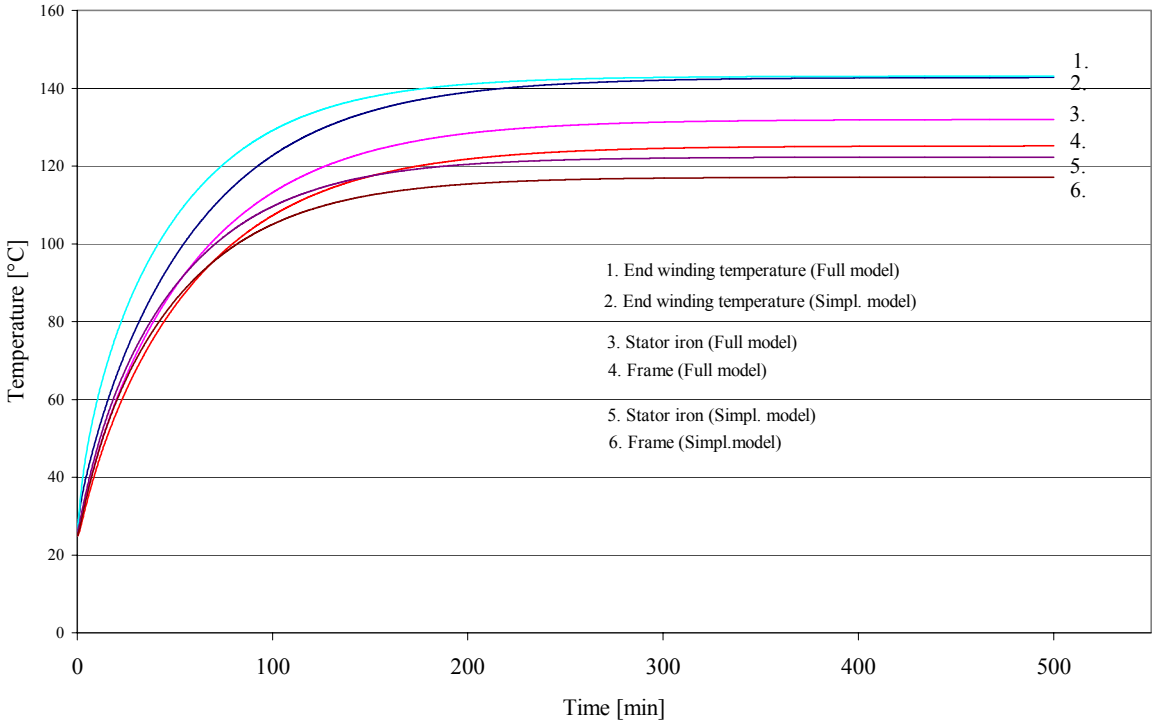

Figure 4.22. Comparison between temperatures calculated with the full model and with the simplified model. Although there is a difference of 10 °C in the frame temperatures and 8 °C in the frame temperature, the difference in the end winding steady-state temperature is less than 1 °C.

4.9 Conclusion

This chapter provided a dynamic thermal analysis of an induction motor with the coupled electromagnetic-thermal model implemented in Matlab/Simulink™. Coupling the two model increases the accuracy, as the model takes into account the changes in the electromagnetic characteristics of the motor due to the temperature rise. The graphical user interface of the Simulink makes the model very user friendly, and the adaptation of different motor drive applications is easy, as the generation of different speed-torque profiles is straightforward. A further benefit of the model is the short computation time, as the model is fully analytical one, at least when compared to the FEM-based methods. The model was verified in the laboratory with the prototype motor controlled with an ACS600 frequency converter and loaded with an eddy-current brake-dynamometer. The correspondence between the measured and the simulated temperatures was quite good in both the transient- and steady-state. The drawback of the model is that it requires a complete dimensional and material data of the motor. Therefore, a simplified thermal network model was constructed to study whether it is possible to properly estimate the motor temperatures by using only the most significant parameters. The simulations with the simplified model showed that the simulation of the winding temperature is possible also with the simplified model, but an error of approx. 5-10 °C resulted in the (steady-state) temperatures of the stator iron and the frame.

5. CONCLUSIONS

This thesis presents and summarizes part of the research work carried out within the "Motion Control" project, funded by ABB Industry. The scope of the project was to study a servo drive system, including the frequency converter, the motor, the load, and the feedback systems. However, the focus of this thesis was only on the motor part of the drive system; the frequency converter part (including the control and the feedback analysis) is currently being studied in two other theses that will be completed during the near future. The two motor types studied in this work are the two most common AC types; the permanent magnet synchronous motor (PMSM) and the induction motor (IM).

5.1 Targets and results of the work

Although both the IM and the PMSM are studied in this thesis, the main focus is slightly on the induction motor. Because of its advantageous characteristics, a PMSM is far more often used in servo applications compared to an induction motor. As the induction motor is therefore clearly a "defendant", the fundamental goal was to analyze its suitability in servo applications and to continuously compare it to the PMSM. The targets of this thesis can briefly be summarized as follows:

1. To study how the electromagnetic design of a servomotor differs from the design of an industrial motor.

2. To study the performance characteristics and the suitability of the IM and the PMSM in dynamically demanding servo applications.

3. To study the design aspects of the induction motor, that have to be adopted to improve its servo characteristics.

4. To develop a computationally fast dynamic heat transfer model for the IM.

The fundamental difference between an industrial motor and a servomotor is the overloading capability required to obtain high dynamic performance. The differences of a servomotor and an industrial motor are studied in Chapter 2, and in addition, a comparison of the induction motor and the permanent magnet synchronous motor is carried out. With the PMSM, high overloading capability can easily be achieved by using surface magnets on the rotor. It seems to be that commercial permanent magnet servomotors typically use a large amount of permanent magnet material in order to achieve a high air gap fundamental flux density and to, simultaneously, get a very low magnetising inductance. The peak values of the fundamental air gap flux density are remarkably higher than in industrial motors of traditional design.

In order to achieve a high overloading capability with the induction motor, the motor has to be designed to have low leakages; furthermore, a fundamental air gap flux density has to be chosen close to 1 T – in the same range as with PM servomotors. According to this study, the following measures turned out to be the most effective ones to minimize the leakage:

- Correct slot dimensioning
- Using at least three slots per pole per phase in the stator
- Using short-pitching

In addition to the above, choosing a high air gap flux density results in a pull-out torque comparable to the values of surface magnet PMSM servos. With the prototype induction motor, the pull-out torque of approx. 4 p.u. using the original permanent magnet motor rated torque as a base value is obtained, which seems to be quite adequate. The pull-out torque of the PMSM typically varies between 4−6 p.u.; the higher the pull-out torque, the heavier the frequency converter over-dimensioning has to be compared to the motor. The optimization of the pull-out torque of an induction motor results in excellent field weakening characteristics, which is the most important benefit compared to the PMSM. Although surface-magnet PMSMs have a high pull-out torque, their constant power range is extremely limited. In applications requiring a wide speed range, choosing the induction motor can substantially reduce the drive sizing. Field weakening and dimensioning of the two motor types in this kind of applications are analyzed in Chapter 3. Lastly, in Chapter 3, the dynamic flux level control strategy for the induction motor is studied. Since the induction servomotors have to be dimensioned to have a high air gap flux density, the saturation of the iron will significantly degrade the motor characteristics, such as the power factor and the efficiency; furthermore, a larger frequency converter is required because of the larger magnetizing current. It is suggested that reduced flux level should be applied when the motor operates below the maximum loads, whereas rated flux level should be applied only when the maximum torque is required. The reduced flux significantly improves certain characteristics of a motor of this kind, such as the efficiency, the power factor, and the thermal loadability. The drawback is the decreased dynamic performance, which in practice means that the load-cycle has to be known a priori to be capable of meeting abrupt torque impacts. The effects of the proposed flux level control are verified by both analytical and numerical methods, and also with measurements with the newly designed prototype motor in the laboratory.

Chapter 4 entirely focuses on the dynamic thermal modelling of the induction motor. An analytical thermal-network model is constructed in the Matlab/Simulink™ environment, and in order to increase the accuracy, the model is coupled with the electromagnetic model of an induction motor. This way, the model properly takes into account the changes in the electromagnetic characteristics of an induction motor due to the temperature variations. As the model is implemented in Simulink™, the user interface is very easy to use, and also the model is very flexible, which makes the generation of different speed-torque profiles (different applications) straightforward. The model is verified in the laboratory with the prototype motor by equipping it with Pt-100 temperature sensors; the agreement between the measured and the simulated temperatures proves to be good. In addition, at the end of Chapter 4, a simplified model containing only the most significant thermal parameters is constructed. With the simplified model containing 10 thermal resistance parameters (39 in the full model), no significant difference is observed compared to the full model. A benefit of the simplified model is that not all the dimensions of the motor are required.

The central scientific contribution of this thesis is the exhaustive discussion and analysis of the design and dimensioning aspects of the permanent magnet synchronous motor and especially of the induction motor in high-performance drives. The results are verified by using both analytical and numerical tools, and also by designing and constructing a prototype motor and carrying out

extensive measurements in the laboratory. Before this study, there was a scarcity of in-depth literature on servomotors, the majority of the existing literature focusing on the control part; in the few surveys that focus on the motor part, the motor types are typically different kinds of PM machines. Therefore, the thesis provides a novel, detailed analysis serving the induction motor design in high performance applications, and compares the suitability of such a motor to a PMSM. In addition, the work presents a *coupled* analytical electromagnetic-thermal model for the induction motor that can be used during the dimensioning stage.

5.2 Subjects of further study

In the near future, two theses will be published within this same project; these works concentrate on frequency converter-related issues, such as the control theory and feedback analysis. Regarding the motor part (studied in this work), a further task could be to design an entirely new induction servomotor, for which all the dimensions and parameters could be freely chosen; in this study, the stator was the existing one from the PMSM. By modifying also the stator slots, the leakage could be further decreased and the pull-out torque increased. The pole number of such a motor would be 4 instead of six to achieve a better torque-to-current ratio. However, a detailed analysis, design, and measurements of such a new motor would have required at least 6 months of further work, and therefore the task had to be left for later consideration. An additional future project could be to develop a thermal model also for the PMSM. The topic was omitted from this study, since there are theses in progress on the subject within the same department at LUT already. Together with the theses in progress at LUT, the present work thus shows some guidelines for the future work on the subject.

REFERENCES

ABB, 2006. ABB Data sheets www.abb.com [cited 3. January 2006].

Andersson, S., 2000. Optimization of a Servo Motor for an Industrial Application. Licentiate thesis, Universitetstryckeriet, Lund University, ISBN 91-88934-15-2

Armstrong Jr, R.W., 1998. Load to Motor Inertia Mismatch: Unveiling the Truth. Drives and Controls Conference, Telford, England.

Auinger H., 1997, Considerations about the determination of the efficiency of electric machines, Energy efficiency Improvements in electrical motors and drives, pp. 284– 304, Springer, ISBN 3-540-63068-6.

Blaschke, F., 1972, The principle of field orientation as applied to the new transvector closed loop control systems for rotating field for rotating field machines, Siemens review XXX1X, No.5. pp 217-220.

Boglietti, A., Cavagnino, M., Lazzari, L. and Pastorelli, M., 2002. A Simplified Thermal Model for Variable Speed Self Cooled Induction Motor, IEEE Transactions on Industry Applications, Vol. 39, Issue 4, July-Aug 2003, p. 945-952

Bose B. K., 1997. Power electronics and variable frequency drives: technology and applications. New York, IEEE Press. 640 p.

Cedrat, 2001. User's guide of Flux2D (version 7.50) finite element program.

Crowder R. M., 1995. Electric drives and their controls, Clarendon Press, Oxford, 238 p.

Deng, F., 1999. An Improved Iron Loss Estimation for Permanent Magnet Brushless Machines. IEEE Transactions on Energy Conversion. Vol. 14, No. 4, pp. 1391-1395.

Downing, S., Reunanen, A., Saari, J. and Arkkio, A. 2005. Losses, Cooling and Thermal Analysis of Electrical Machines, Lecture notes of the postgraduate seminar, Espoo, Otamedia Oy, ISBN 951-22-7991-6

Drury, B., 2001. The Control Techniques Drives and Controls Handbook, Published by The Institution of Electrical Engineers, London, ISBN 0 85296 793 4

Engelmann, R. H,. Middendorf, W. H, 1995. Handbook of Electric motors, New York: Marcel Dekker Inc, 801 p.

Fowler, F.G. (editor), 1988. The Oxford Handy Dictionary, published By Chancellor Press, London, ISBN 1 85152 032 5, 1057 p.

Gazley, C., 1958. Heat transfer characteristics of rotating and axial flow between concentric cylinders, Trans. ASME, p.79-89

Gieras, J.F. and Wing, M., 1997. Permanent Magnet Motor Technology – Design and Applications. New York: Marcel Dekker Inc, p. 444.

Haataja, J., 2003. A comparative performance study of four-pole induction motors and synchronous reluctance motors in variable speed drives. Dissertation, Acta Universitatis Lappeenrantaensis 153, ISBN 951-764-772-7, 135 p.

Heikkilä, T., 2002. Permanent Magnet Synchronous Motor for Industrial Applications – Analysis and Design. Dissertation, Acta Universitatis Lappeenrantaensis 134, ISBN 951-764-699-2, 109 p.

Hendershot Jr, JR., Miller, T.J.E., 1994. Design of Brushless Permanent-Magnet Motors. Magna Physichs Publishing and Clarendon Press, Oxford, ISBN 1-881855-03-1. 574 p.

Jokinen, T., 1979. Pyörivän sähkökoneen suunnitteleminen, Teaching material, Helsinki University of Technology.

Kovács K.P., Rácz I., 1959. Transiente Vorgänge in Wechselstrommaschinen. Budapest, Hungary. Verlag der Ung. Akad., 514 p.

Kurronen, P., 2003. Torque Vibration Model of Axial-Flux Surface-Mounted Permanent Magnet Synchronous Machine. Dissertation. Acta Universitatis Lappeenrantaensis 154, ISBN 951-764-773-5, 123 p.

Kylander, G., 1995. Thermal Modelling of Small Cage induction Motors. Dissertation. Chalmers University of Technology, Sweden, p. 113.

Laurila, L., 2004. Analysis of torque and speed ripple producing non-idealities of frequency converters in electric drives. Dissertation. Lappeenranta. Acta Universitatis Lappeenrantaensis 188. ISBN 951-764-942-8, 124 p.

Levi, E., 1984. Polyphase Motors: a Direct approach to their design, New York, Wiley & Sons, cop, ISBN 0-471-89866-X, 438 p.

Levi, E., 2000. A Method for Magnetizing Curve Identification in Rotor Flux Oriented Induction Machines, IEEE Transactions on Energy Conversion, Vol. 15, No. 2.

Li, T., Slemon, G., 1988. Reduction of cogging torque in permanent magnet motors. IEEE Transactions on Magnetics. Vol. 24, Iss. 6, Nov. 1988, p. 2901-2903.

Liu, H. P., Lelos, V., Hearn, C. S., 2005. Transient 3-D Thermal Analysis for an Air-cooled Induction Motor, IEEE International Conference on Electric Machines and Drives, p. 417-420.

Lorenz, R. D., 1992. AC Induction Servo Sizing for Motion Control Applications via Loss Minimizing Real-Time Flux Control. IEEE Transactions on Industry Applications, Vol. 28, No. 3, June 1992. p. 589-593

Mellor, P.H., Roberts, D. and Turner, D.R., 1991. Lumped parameter thermal model for electrical machines of TEFC design, Electric Power Applications, IEE Proceedings B, Volume 138, Issue 5, p. 205 – 218.

Smezani, S., Takorabet, N., Laporte, B., 2005. A Combined Electromagnetic and Thermal Analysis of Induction Motors, IEEE Transactions on Magnetics, Voil. 41, No. 5, p. 1572-1575

Morimoto, K., Hatanaka, Y., and Tong, Takeda, Y. and Hirasa, T., 1991. High performance servo drive system of salient pole permanent magnet synchronous motor, in Proc. IEEE IAS Annual. Meet., p. 463-468.

Naumanen, V., 2005. Servokäyttöön tarkoitetut kestomagneettitahtimoottorit ja niiden sijaiskytkennän parametrien määrittäminen, Master's thesis (in Finnish), Lappeenranta University of Technology.

Neorem magnets, 2006. Neorem magnets data sheets. www.neorem.fi [cited 19 April 2006].

Nerg, J., Pyrhonen, J. and Partanen, 2004. J. Finite element modeling of the magnetizing inductance of an induction motor as a function of torque, IEEE Transactions on magnetics, Vol. 4. Issue 2, Part 2, p. 2047-2049

Rajagopal, M. S., Seetharamu, K. N., Ashwathnarayana, P. A, 1998. Transient thermal analysis of induction motors, IEEE Transactions on energy conversion, Vol. 13, No. 1, p. 62-69

Richter R., 1954. Elektrische Maschinen IV Die Induktionsmaschinen, 2. Verb. Aufl., Basel/Stuttgart, Verlag Birkhäuser. 440 p.

Salminen, P., 2004. Fractional Slot Permanent Magnet Synchronous Motors For Low Speed Applications. Dissertation, Acta Universitatis Lappeenrantaensis 198, Finland, 150. p.

Sen, P. K., Landa, H. A., 1990. Derating of Induction Motors due to waveform distortion, IEEE Transactions on Industry Applications, Vol. 26, No. 6, p. 1102-1107.

Slemon, G.R., 1994. Electrical machines for variable-frequency drives, Proceedings of the IEEE, Volume 82, Issue 8, p.1123 – 1139

Stemmler, H. 1994. High Power Industrial Drives. Proceedings of IEEE, vol. 82, No. 8. pp.1266-1286.

Staton, D., Boglietti, A., Cavagnino, A., 2005. Solving the More Difficult Aspects of Electric Motor Thermal Analysis in Small and Medium Size Industrial Induction Motors, IEEE Transactions on Energy Conversion, Vol. 20, No. 3.

Taylor, G.I.., 1935. Distribution of velocity and temperature between concentric cylinders', Proc. Roy. Soc., 159, Pt. A, p. 546-578

Wilson, T. G, Trickey, 1962 P.H., DC Machine with Solid State Commutation, AIEE paper CP62-1372

Vas, P., 1998. Sensorless vector and direct torque control. New York, Oxford University Press. 724 p.

Vogt, K., 1996. Berechnung Elektrischer Maschinen. VCH Verlagsgesellschaft mbh Weinheim ISBN 3-527-28391-9. 524 p. (In German)

APPENDIX A.

Table A1. Data of the prototype induction motor

Parameter	**Symbol**	**Value**	**Unit**
Stator outer diameter	D_o	153.0	mm
Stator inner diameter	D_i	80.0	mm
Stack length	L	153	mm
Air gap length	δ	0.3	mm
Number of stator slots	Q_s	36	
Number of rotor slots	Q_r	30	
Number of turns in series in stator	N_s	28	
Connection		star	
Pole pairs	p	3	
Rotor cage material		Copper	
Rated voltage	U_n	330	V
Rated frequency	f_n	125	Hz

ACTA UNIVERSITATIS LAPPEENRANTAENSIS

203. Säädöksiä, systematiikkaa vai ihmisoikeuksia? Oikeustieteen päivät 19. – 21.8.2003. Toim. Marjut Heikkilä. 2004. 350 s.

204. PANTSAR, HENRIKKI. Models for diode laser transformation hardening of steels. 2005. 134 s., liitt. Diss.

205. LOHJALA, JUHA. Haja-asutusalueiden sähkönjakelujärjestelmien kehittäminen – erityisesti 1000 V jakelujännitteen käyttömahdollisuudet. 2005. 201 s., liitt. Diss.

206. TARKIAINEN, ANTTI. Power quality improving with virtual flux-based voltage source line converter. 2005. U.s. Diss.

207. HEIKKINEN, KARI. Conceptualization of user-centric personalization management. 2005. 136 s. Diss.

208. PARVIAINEN, ASKO. Design of axial-flux permanent-magnet low-speed machines and performance comparison between radial-flux and axial-flux machines. 2005. 153 s. Diss.

209. FORSMAN, HELENA. Business development efforts and performance improvements in SMEs. Case study of business development projects implemented in SMEs. 2005. 209 s. Diss.

210. KOSONEN, LEENA. Vaarinpidosta virtuaaliaikaan. Sata vuotta suomalaista tilintarkastusta. 2005. 275 s. Diss.

211. 3rd Workshop on Applications of Wireless Communications. 2005. 62 s.

212. BERGMAN, JUKKA-PEKKA. Supporting knowledge creation and sharing in the early phases of the strategic innovation process. 2005. 180 s. Diss.

213. LAAKSONEN, PETTERI. Managing strategic change: new business models applying wireless technology as a source of competitive edge. 2005. 142 s. Diss.

214. OVASKA, PÄIVI. Studies on coordination of systems development process. 2005. U.s. Diss.

215. YANG, GUANGYU. Control and simulation of batch crystallization. 2005. U.s. Diss.

216. MUSTONEN–OLLILA, ERJA. Information system process innovation adoption, adaptation, learning, and unlearning: a longitudinal case study. 2005. U.s. Diss.

217. SAINIO, LIISA-MAIJA. The effects of potentially disruptive technology on business model – a case study of new technologies in ICT industry. 2005. 205 s. Diss.

218. SAINIO, TUOMO. Ion-exchange resins as stationary phase in reactive chromatography. 2005. 175 s. Diss.

219. CONN, STEFFEN. Software tools to support managers: development and application to new product development and strategic alliance management. 2005. 168 s. Diss.

220. TYNJÄLÄ, TERO. Theoretical and numerical study of thermomagnetic convection in magnetic fluids. 2005. U.s. Diss.

221. JANTUNEN, ARI. Dynamic capabilities and firm performance. 2005. 210 s. Diss.

222. KOLA-NYSTRÖM, SARI M. In search of corporate renewal: how to benefit from corporate venturing? 2005. 190 s. Diss.

223. SARÉN, HANNU. Analysis of the voltage source inverter with small DC-link capacitor. 2005. 143 s. Diss.

224. HUUHILO, TIINA. Fouling, prevention of fouling, and cleaning in filtration. 2005. U.s. Diss.

225. VILJAINEN, SATU. Regulation design in the electricity distribution sector – theory and practice. 2005. 132 s. Diss.

226. AVRAMENKO, YURY. Case-based design method for chemical product and process development. 2005. U.s. Diss.

227. JÄRVINEN, KIMMO. Development of filter media treatments for liquid filtration. 2005. U.s. Diss.

228. HURMELINNA-LAUKKANEN, PIA. Dynamics of appropriability – finding a balance between efficiency and strength in the appropriability regime. 2005. U.s. Diss.

229. LAARI, ARTO. Gas-liquid mass transfer in bubbly flow: Estimation of mass transfer, bubble size and reactor performance in various applications. 2005. U.s. Diss.

230. BORDBAR, MOHAMMAD HADI. Theoretical analysis and simulations of vertically vibrated granular materials. 2005. U.s. Diss.

231. LUUKKA, PASI. Similarity measure based classification. 2005. 129 s. Diss.

232. JUUTILAINEN, ANNELI. Pienen matkailuyrityksen yrittäjän taival. Oppiminen yrittäjyysprosessissa. 2005. 191 s. Diss.

233. BJÖRK, TIMO. Ductility and ultimate strength of cold-formed rectangular hollow section joints at subzero temperatures. 2005. 163 s. Diss.

234. BELYAEV, SERGEY. Knowledge discovery for product design. 2005. U.s. Diss.

235. LEINONEN, KARI. Fabrication and characterization of silicon position sensitive particle detectors. 2006. U.s. Diss.

236. DUFVA, KARI. Development of finite elements for large deformation analysis of multibody systems. 2006. U.s. Diss.

237. RITVANEN, JOUNI. Experimental insights into deformation dynamics and intermittency in rapid granular shear flows. 2006. U.s. Diss.

238. KERKKÄNEN, KIMMO. Dynamic analysis of belt-drives using the absolute nodal coordinate formulation. 2006. 121 s. Diss.

239. ELFVENGREN, KALLE. Group support system for managing the front end of innovation: case applications in business-to-business enterprises. 2006. 196 s. Diss.

240. IKONEN, LEENA. Distance transforms on gray-level surfaces. 2006. 132 s. Diss.

241. TENHUNEN, JARKKO. Johdon laskentatoimi kärkiyritysverkostoissa. Soveltamismahdollisuudet ja yritysten tarpeet. 2006. 270 s. Diss.

242. KEMPPINEN, JUKKA. Digitaaliongelma. Kirjoitus oikeudesta ja ympäristöstä. 2006. 492 s.

243. PÖLLÄNEN, KATI. Monitoring of crystallization processes by using infrared spectroscopy and multivariate methods. 2006. U.s. Diss.

244. AARNIO, TEIJA. Challenges in packaging waste management: A case study in the fast food industry. 2006. 260 s. Diss.

245. PANAPANAAN, VIRGILIO M. Exploration of the social dimension of corporate responsibility in a welfare state. 2006. 239 s. Diss.

246. HEINOLA, Janne-Matti. Relative permittivity and loss tangent measurements of PWB materials using ring resonator structures. 2006. U.s. Diss.